Proximity and flux pinning effects in superconductor-ferromagnet hybrids

Xavier Palermo

NNT : 2019SACLS231

Thèse de doctorat

Proximity and flux pinning effects in superconductor-ferromagnet hybrids

Thèse de doctorat de l'Université Paris-Saclay
préparée à l'Université Paris-Sud

École doctorale n°564 Physique en Ile de France (PIF)
Spécialité de doctorat : Physique

Thèse présentée et soutenue à Palaiseau, le 30 Septembre 2019, par

XAVIER PALERMO

Composition du Jury :

Dafiné Ravelosona Directeur de recheche, CNRS (C2N)	Président
Anna Palau Cientifica Titular, CSIC (ICMAB)	Rapportrice
Alain Pautrat Chargé de recherche, CNRS (CRISMAT)	Rapporteur
Chéryl Feuillet-Palma Maître de conférences, ESPCI Paris	Examinatrice
Philippe Tamarat Professeur, Université de Bordeaux	Examinateur
Javier Villegas Directeur de recherche, Unité Mixte de Physique CNRS-Thales	Directeur de thèse
Nicolas Reyren Chargé de recherche, Unité Mixte de Physique CNRS-Thales	Co-encadrant

Résumé étendu en français

Introduction

La découverte de la supraconductivité en 1908 (K.Onnes, Leiden [1]) a engendré plusieurs applications, incluant des magnétomètres, de puissants électro-aimants, et d'autres plus inattendues comme des trains qui lévitent (SCMaglev, Japon [2]). Néanmoins, à une exception près [3], les exemples d'ordinateurs supraconducteurs se font plus rares. En effet, ils ont une bien meilleure efficacité énergétique que les architectures conventionnelles, mais requièrent un appareillage cryogénique couteux et énergivore, prohibitif pour un usage grand-public. C'est beaucoup moins le cas pour un supercalculateur, qui est déjà encombrant et énergivore [4, 5]. A titre d'exemple, un tel ordinateur à l'état de l'art consomme environ 13 MW [6, 7], soit la production approximative d'un parc éolien entier (Porte de Champagne, France: 12.3 MW [8]). Utiliser une architecture supraconductrice pourrait la réduire jusqu'à un facteur cent, à puissance de calcul équivalente [9, 4]. En ce sens, plusieurs projets ont été lancés récemment par la Chine [10] et les États-Unis (IARPA [5]). Néanmoins, un des principaux freins provient des mémoires compatibles, assez volumineuses (quelques 100 nm [11], contre environ 10-30 nm pour les mémoires flash [12]). Plusieurs solutions sont envisagées, entre autres l'usage de matériaux ferromagnétiques. Ceux-ci permettraient d'emprunter directement les dispositifs de l'électronique de spin [13], ou d'en concevoir de nouveaux [14, 15, 16].

Dans cette thèse, nous avons étudié ce problème de deux manières différentes. Premièrement, dans des systèmes d'oxydes supraconducteurs/ferromagnétiques à haute température critique, qui présentent des états supraconducteurs exotiques, et *polarisés en spin*. Une seconde cherche à détecter avec un supraconducteur des parois de domaines [17] ou des skyrmions [18], qui sont tous deux envisagés comme possibles support de stockage mémoire.

Effet de proximité aux interfaces YBCO/LCMO

Dans certains couples de matériaux supraconducteur/ferromagnétique, des états dits "triplets" apparaissent aux interfaces à cause d'inhomogénéités magnétiques [19]. Certains d'entre eux sont *polarisés en spin*, et peuvent se propager sur de longues distances dans le ferromagnétique. Ceux-ci permettent également d'obtenir des effets tels que la magnétorésistance géante (GMR [20]) ou le couple de transfert de spin [21],

autrement inaccessibles dans des circuits supraconducteurs. Ce type de structure promet aussi de nouveaux dispositifs, comme les jonctions π-Josephson [14, 15, 16].

De tels courants ont déjà été démontrés dans des matériaux supraconducteurs conventionnels [22, 23, 24, 25]. Néanmoins, il n'y a pas encore de démonstration analogue avec des oxydes à haute-température critique, malgré plusieurs preuves indirectes [26, 27, 28], et un effort de recherche certain [27, 28, 29, 30, 31],

Nous proposons d'y contribuer en étudiant l'effet de proximité dans des hétérostructures d'oxydes en film minces. Celles-ci contiennent un supraconducteur à haute température critique, $YBa_2Cu_3O_7$ (YBCO, T_c=92 K), et un demi-métal $La_{0.7}Ca_{0.3}MnO_3$ (LCMO, $T_{Curie} \approx$ 200K). Ce dernier possède une polarisation en spin théorique de 100% en basse température. Ces couches ont été déposées sur substrat de $SrTiO_3$ (STO) par nos collègues de l'*Universidad Complutense de Madrid*, pour leurs propriétés d'interfaces bien connues [32, 26].

Ces travaux poursuivent ceux de C. Visani dans notre groupe [27, 33]. Ceux-ci montraient déjà des signes de la propagation d'états triplets dans le LCMO par oscillations de conductance différentielle. Néanmoins, le contact électrique inhomogène à l'interface Au/YBCO rendait ambigüe l'interprétation des courants critiques dans la tricouche.

Pour approfondir cette étude, nous avons premièrement amélioré la qualité du contact Au/YBCO *ex-situ*. Pour cela, nous avons recuit les échantillons sous oxygène, dans les conditions que celles du dépôt de l'YBCO. Ceci atténue la désoxygénation du matériau à la surface. Ensuite, un contact d'or (30nm) est déposé dans le même bâti par ablation laser pulsé (PLD) sous vide. Les contacts ainsi déposés sont plus homogènes, et moins résistifs que ceux obtenus précédemment par pulvérisation cathodique (quelques 100 Ω contre plus de 1 kΩ).

La seconde concerne les épaisseurs des matériaux. Nous sommes descendus jusqu'à 6nm de LCMO, contre 9 nm précédemment. À de telles épaisseurs, l'effet des phénomènes d'interface est plus prononcé, et donc plus visible. En complément, les deux couches d'YBCO ont des épaisseurs différentes (20 et 30nm), afin de pouvoir identifier dans laquelle d'éventuelles résonances se produiraient. Le dispositif de mesure est une jonction verticale, qui permet d'étudier le transport électronique perpendiculairement aux interfaces des matériaux.

Dans ces jonctions, nous avons observé des oscillations de conductance similaires à celles vues précédemment [27, 33]. Nos principaux résultats concernent l'analyse du spectre en fréquence des courbes de conductance. Celui-ci comporte plusieurs fréquences caractéristiques, dont nous avons étudié les deux plus intenses.

La plus basse (20-30 V^{-1}) ne change pas en fonction de l'épaisseur de LCMO. En l'interprétant comme des résonances Tomasch [34, 35] dans la couche supérieure d'YBCO (20 nm), nous estimons une vitesses de Fermi d'environ 4.2×10^5 m$\cdot$s^{-1}. Celle-ci coïncide avec les valeurs présentes dans la littérature [36, 37].

La fréquence la plus élevée varie selon l'épaisseur, et peut être interprétée comme des oscillations de McMillan-Rowell (MMR) [38] dans le LCMO. Celles-ci donnent des vitesses de Fermi de $2.5 - 2.9 \times 10^5$ m$\cdot$s^{-1} pour respectivement 12 et 24 nm de LCMO. Ces valeurs sont comparables à celles précédemment observées dans la littérature [27, 39].

Pour l'échantillon de 6nm, les valeurs estimées avoisinent 1.0×10^5 m·s^{-1}. Elles sont donc bien plus basses, mais aussi plus dispersées que pour les deux autres échantillons. La dispersion peut s'expliquer par des variations d'épaisseur, jusqu'à 2nm, dont l'effet est plus prononcé dans un film aussi mince. Néanmoins, la valeur moyenne de la vitesse ne peut pas être expliquée seulement par une variation d'épaisseur, ni par d'autres résonances dans l'or ou la couche inférieure d'YBCO. Il s'agit donc sûrement d'oscillations MMR, et donc d'une réduction de la vitesse de Fermi dans le LCMO en couche mince. La réduction observée est sûrement due aux effets de transfert de charge, bien connus aux interfaces YBCO/LCMO [40, 41, 26] Ceux-ci modifient la densité de porteurs près du contact, et créent une couche morte antiferromagnétique d'environ 1nm dans le LCMO. A des épaisseurs aussi réduites, ces effets d'interfaces deviennent prépondérants. Ceci est d'autant plus probable que le LCMO est entouré par deux couches d'YBCO. La présence de résonances MMR indiquent la propagation de corrélations supraconductrices sur un aller-retour dans la couche. Le matériau étant assez épais (jusqu'à 24nm) et fortement polarisé en spin, il s'agit sûrement des états triplets à spin-parallèle que nous mentionnions plus haut.

Nos résultats suggèrent également que l'interface YBCO/LCMO inférieure est au moins partiellement opaque. En effet, nous n'observons pas d'effet Josephson, ni de signes de réflexions d'Andreev à l'interface inférieure. De plus, le mécanisme des résonances MMR implique des réflexions normales à cet endroit. Ces résultats suggèrent que les corrélations supraconductrices pourraient ne pas traverser cette interface.

Pour vérifier cette hypothèse, nous avons fabriqué un prototype de jonction dont le contact supérieur est séparé en deux. Ceci permet de mesurer la jonction en ignorant le contact Au/YBCO. Cette approche a été poursuivie dans notre groupe. Les premiers résultats tendraient plutôt vers un courant critique inhomogène dans la jonction [30]. Cette possibilité est toujours en cours d'investigations, grâce à une collaboration avec l'ESPCI (J.Lesueur) pour mesurer sous micro-ondes. La présence de marches de Shapiro dans ces mesures permettrait d'affirmer un comportement Josephson sans ambigüité.

Couplages magnétiques dans des bicouches supraconducteur/ferromagnétique

Dans un second temps, nous avons cherché à observer l'interaction de vortex supraconducteurs avec des parois de domaines magnétiques, et des skyrmions [18, 42]. Ces derniers sont des structures ressemblant à des bulles, mais chirales et *topologiquement protégées*, ce qui les rend plus stables et plus mobiles. Le type de couplage que nous avons étudié est purement magnétostatique, à travers les champs de fuite. La littérature à ce sujet est assez étendue pour les domaines magnétiques. Elle inclut le confinement de la supraconductivité sous les parois de domaine [43, 44, 45], et les interactions avec les vortex d'un supraconducteur de type II. La présence des champs de fuite provenant du ferromagnétique tend à favoriser leur nucléation [46, 47], mais aussi leur piégeage [48, 49, 47, 50, 51].

Le cas des skyrmions en revanche, n'a été évoqué que très récemment [52, 53, 54, 55, 56]. Ces travaux suggèrent qu'en plus de nucléer et piéger les vortex, il est possible que le réseau de skyrmions puisse être entrainé par leur mouvement [53]. Aucune étude expérimentale à ce sujet n'a été publiée pour l'instant, à notre connaissance.

Pour étudier ces interactions, nous avons choisi un supraconducteur *amorphe*, Mo_4Si ($T_c = 6.5$ K), dans lequel le piégeage intrinsèque des vortex est faible [57]. Pour obtenir des domaines et des skyrmions, nous avons déposé dessus des multicouches magnétiques à anisotropie perpendiculaire, du type $(Pt/Co/X)_n$, où X=Ru,Ir,Pt. Celles-ci présentent des structures de domaines ajustables, mais aussi des skyrmions en choisissant Ir ou Ru et des épaisseurs adéquates [58, 59, 60]. Les structures détaillées des multicouches sont les suivantes :

- Mo_4Si_{60nm} - $AlO_{x,3nm}$ - Pt_{10nm} - $(Co_{0.6nm}/Pt_{1nm})_{\times 5}$ - Pt_{3nm} ;
- Mo_4Si_{60nm} - $AlO_{x,3nm}$ - Pt_{10nm} - $(Ir_{1nm}/Co_{0.6nm}/Pt_{1nm})_{\times 5}$ - Pt_{3nm} ;
- Mo_4Si_{60nm} - Ta_{5nm} - Pt_{8nm} - $(Pt_{1.2nm}/Co_{1.6nm}/Ru_{1.4nm})_{\times 4}$ - Pt_{3nm} ;

Co/Pt comporte uniquement des domaines, plutôt larges (environ 500 nm). Ceux dans Ir/Co/Pt sont plus petits (100-150 nm), et se transforment en skyrmions isolés près du champ de saturation. Dans Pt/Co/Ru, les skyrmions apparaissent plus facilement, et forment des ensembles compacts (80-90 nm environ). Certains échantillons comportent une couche d'alumine (AlO_x) pour atténuer l'effet de proximité, mais nous n'avons pas observé de différence flagrante en son absence. Nous avons ensuite étudié le transport électronique dans ces multicouches de plusieurs manières. Tout d'abord, en mesurant l'influence des domaines/skyrmions sur le courant critique à 3.5 K, puis à 5 K sur les magnéto-résistances longitudinales et transverses au courant appliqué.

Courants critiques

Pour chacun des trois échantillons, nous avons mesuré le courant critique dans plusieurs états magnétiques en suivant le cycle d'hystérèse de la couche ferromagnétique. Nous avons observé une augmentation du courant critique en présence de domaines magnétiques et de skyrmions, par rapport au supraconducteur seul, mais aussi à la même bicouche dans l'état saturé (monodomaine). Puisque le champ extérieur change la structure de domaines, le courant critique évolue également en fonction du champ et devient irréversible. Nous avons pu expliquer la loi d'échelle reliant le courant critique au champ appliqué en utilisant un modèle simple de piégeage magnétique 1D. Quelques différences sont néanmoins à noter. Dans Co/Pt, un pic de courant critique est présent à faible champ (10-20 mT). Il est peut être dû à un effet de commensurabilité entre la taille moyenne des domaines et du réseau de vortex, qui augmente significativement le couplage [51, 61]. Pour Pt/Co/Ru, le courant critique diminue de manière plus marquée qu'attendue lorsque des skyrmions apparaissent. Dans notre cas, les skyrmions, comme les domaines minoritaires ont une polarité opposée au champ appliqué, et donc repoussent les vortex. Nous pensons que ceci est dû

à leur petite taille et leur forme compacte, qui gêne moins le mouvement des vortex que les domaines normaux, plus allongés.

Magneto-résistance et effet Hall

Nous avons également étudié la magnéto-résistance longitudinale (R_{xx}) et transverse (R_{xy}, «effet Hall») dans les bicouches comportant Co/Pt (domaines) et Pt/Co/Ru (domaines et skyrmions). Dans ces échantillons, la présence de domaines magnétiques et de skyrmions diminue la magnéto-résistance (MR). De la même manière que pour le courant critique, une hystérèse magnétique apparaît. Son origine est la même, à savoir le piégeage de vortex par le champ de fuite provenant des domaines. Pareillement, l'irréversibilité magnétique de la structure se transmet à la MR longitudinale.

L'effet Hall (R_{xy}) en champ perpendiculaire comporte aussi une boucle d'hystérèse, en plus d'un arrière-plan parabolique. Néanmoins, ce signal est souvent fallacieux, car il comporte en partie des effets dûs à des imperfections [62, 63, p. 154]. Celle-ci est généralement *paire* en champ magnétique. Une autre composante, plus inhabituelle, apparaît dans nos mesures lorsque le champ est incliné, et est *impaire*. Elle est également hystérétique, et apparaît en présence des structures magnétiques. Elle est reproductible, et n'est pas directement liée à un changement de R_{xx} ou de l'aimantation moyenne, qui ne dépendent presque que du champ hors du plan. Cette composante Hall est maximale pour la gamme de champ à laquelle les skyrmions apparaissent. De plus, son signe change selon le sens dans lequel le champ magnétique est balayé, et non en fonction de la polarité des domaines. De plus, nos images MFM et simulations micromagnétiques indiquent que le champ dans le plan ordonne les domaines et skyrmions parallèlement. Dans ce cas, un effet de guidage des vortex le long des domaines alignés est très probable. Mais pour observer une résistance transverse, ce mouvement doit dévier de la trajectoire imposée par la force de Lorentz, due au courant électrique. Ceci ne se produirait que si les structures sont légèrement inclinées par rapport à la perpendiculaire au courant, ce qui est possible. En revanche, le signe de cette composante s'inverse en changeant le sens de balayage du champ magnétique appliqué. En suivant le scénario précédent, cela implique que l'orientation des structures devrait également s'inverser, ce qui est plus inattendu. Une autre possibilité est que les structures bougent à cause du courant de vortex, ce qui génèrerait cette résistance transverse [53]. Pour l'instant, nous n'avons pas d'explication définitive concernant l'apparition de cette résistance transverse.

Perspectives

La perspective la plus immédiate est la détermination exacte de la structure de domaines sous champ et à basse température. Celle-ci permettrait de vérifier de manière sûre la formation de skyrmions en basse température, ainsi que la structure de domaines précise sous champ incliné. Cette partie est en cours de développement, grâce à une collaboration (MIPT, Fédération Russe). Entra autres, il serait intéressant de savoir si il est possible ici que le flux de vortex puisse entraîner les skyrmions

dans sa course [53]. Nous étudions cette possibilité avec l'aide de collègues théoriciens (LOMA, Bordeaux).

Dans un avenir plus lointain, il pourrait être intéressant d'augmenter la taille des skyrmions [64] ou au contraire, de diminuer celle des vortex en choisissant des matériaux comme Nb_3Si ou V_3Si ($\xi \approx 3$nm, $\lambda \approx 60$nm [65, Ch. 53.3]) dont la taille est plus proche de celle d'un skyrmion. Des signes de mouvement conjoint pourraient être observables dans le transport ou bien par MFM, comme pour les skyrmions seuls [66, 59].

Une possibilité toute aussi intéressante serait étudier l'effet de proximité. Plusieurs propositions ont été faites à ce sujet [67, 68]. De plus, l'aimantation inhomogène en présence de skyrmions pourrait conduire à la formation d'états triplets se propageant dans le ferromagnétique. Des matériaux à skyrmions intéressants seraient soit des multicouches, ou un ferromagnétique chiral comme FeGe en couche mince [69].

Remerciements

Au cours de ces quatre ans à préparer cette thèse, j'ai eu le plaisir de côtoyer et collaborer avec des personnes formidables, que j'ai le plaisir de remercier ici.

Tout d'abord, je souhaite remercier Javier Villegas, mon directeur de thèse, pour son soutien, son enthousiasme, et ses conseils avisés. Merci de m'avoir fait confiance pour mener à bien ce projet. Ensuite, Nicolas Reyren, mon co-directeur de thèse, pour sa bienveillance et son aide précieuse (et pour m'avoir "converti" au micromagnétisme). Je vous suis également reconnaissant d'avoir relu et corrigé le présent manuscrit. Pareillement, merci aux membres du jury, pour avoir accepté d'examiner mon travail de thèse.

Je me dois aussi de remercier ceux qui ont éclairé ma lanterne au cours de cette thèse. En plus de mes encadrants, Vincent Cros et William Legrand pour leurs conseils en matière de skyrmions, Alexandre Bouzdine, A.V. Samokhvalov du côté supraconducteurs, ainsi que *professor* Jacobo Santamaria pour ce qui est des oxydes. Ma gratitude va à Juan Trastoy et David Perconte pour m'avoir transmis leur savoir-faire expérimental, à Sophie Collin, David Sanchez, Anke Sander, et Fabian Cuellar pour avoir fait la croissance des matériaux, ainsi que Karim Bouzehouane et Aymeric Vecchiola pour leurs belles images MFM. À mes collègues de la Cité des Sciences aussi, qui m'ont appris l'art délicat de la médiation scientifique.

Plus personnellement, je remercie chaleureusement mes compères de thèse: Mathieu, Philippe et Steffen (les trois autres "Mousquetaires"), Eliana et ses fous-rires communicatifs, ainsi que Samh, Raphael, Mafalda et Ralph, avec qui refaire le monde était toujours plaisant. Je salue aussi celles et ceux qui ont partagé mon bureau: Victor et ses chansons du vendredi, Laura, Myoung-Woo et Isabella, en plus de ceux déjà cités plus haut. Les blagues absurdes et les chansons du vendredi soir me manqueront. Merci également à Florian, Regina, Adrian, Sophie, Salvatore et Benoît pour la bonne ambiance pendant les expériences. Je remercie tous les membres de l'Unité Mixte de Physique CNRS-Thales, pour leur accueil, et pour l'ambiance bon enfant qui y règne. Si ces quatre ans ont été aussi agréables, c'est en grande partie grâce à vous tous.

Je veux également dire merci à mes amis de l'université : mon "bro" Romain, Aurianne et Baptiste. A mes vieux amis aussi, Thomas, Noëlie, Geoffrey, Manon et Eric. Je remercie aussi les membres du club de boxe de Polytechnique, pour m'avoir remis les idées à l'endroit les mardi et vendredi soirs.

Enfin, mes derniers remerciements (mais pas les moindres) vont à mes parents, qui m'ont très tôt donné goût à la lecture et aux sciences, et m'ont soutenu depuis toujours.

Common acronyms and symbols

The following tables sum up the frequently used abbreviations and symbols, along with their unit (unless otherwise is specified). The formulas in the present thesis use the International System of units (SI). Scalar quantities and norms use normal characters (A), and vectors use bold typography ($\mathbf{A}$). The scalar product is denoted $\mathbf{A} \cdot \mathbf{B}$, whereas the vector cross-product is written $\mathbf{A} \times \mathbf{B}$.

Abbreviation	Meaning
ACF	Auto-correlation function
AHE	Anomalous Hall effect
BCS	Bardeen-Cooper-Schrieffer (theory)
BTK	Blonder-Tinkham-Klapwijk (model)
CMOS	Complementary metal oxide semiconductor
DMI	Dzyaloshinskii-Moriya interaction
DWS	Domain-wall superconductivity
FFLO	Fulde-Ferrell-Larkin-Ovchinnikov, $s_z = 0$ triplets
FFT	(fast) Fourier transform
GL	Ginzburg-Landau (theory)
GMR	Giant magneto-resistance
HTSC	High temperature superconductor
LCMO	$La_{0.7}Ca_{0.3}MnO_3$
LRTC	Long-range triplet correlations, $s_z = \pm 1$ triplets
MFM	Magnetic force microscopy
MMR	McMillan-Rowell resonance
MR	Magneto-resistance
PLD	Pulsed laser deposition
SF, SFB	Superconductor-ferromagnet (bilayer)
SIMS	Secondary ions mass spectroscopy
STO	$SrTiO_3$
TAFF	Thermally-assisted flux flow
TR	Tomasch resonance
YBCO	$YBa_2Cu_3O_{7-\delta}$

Symbol	Quantity	Unit
B	Magnetic induction	T
d_s, d_f	Thickness of the superconductor, and ferromagnet	m
D	Interfacial Dzyaloshinskii-Moriya energy	$\mathrm{J{\cdot}m^{-2}}$
e	Electron charge	1.602×10^{-19} C
E	Electric field	$\mathrm{V{\cdot}m^{-1}}$
F_p	Flux pinning force density	$\mathrm{N{\cdot}m^{-3}}$
h	Planck constant	6.626×10^{-34} J·s
$\hbar$	Reduced Planck constant	1.055×10^{-34} J·s
H	Magnetic field	$\mathrm{A{\cdot}m^{-1}}$
H_c	Thermodynamic critical field	$\mathrm{A{\cdot}m^{-1}}$
H_{c1}, H_{c2}	Lower and upper critical fields	$\mathrm{A{\cdot}m^{-1}}$
H_{ext}	External (applied) magnetic field	$\mathrm{A{\cdot}m^{-1}}$
H_{stray}	Stray magnetic field	$\mathrm{A{\cdot}m^{-1}}$
I	Electrical current (applied)	A
j	Electrical current density	$\mathrm{A{\cdot}m^{-2}}$
j_c	Critical current density	$\mathrm{A{\cdot}m^{-2}}$
k_B	Boltzmann constant	$1.380 \times 10^{-23}\mathrm{J{\cdot}K^{-1}}$
K_{eff}	Effective magnetic anisotropy constant	$\mathrm{J{\cdot}m^{-3}}$
K_u	Uniaxial magnetic anisotropy constant	$\mathrm{J{\cdot}m^{-3}}$
M	Magnetization	$\mathrm{A{\cdot}m^{-2}}$
m	Reduced magnetization	dimensionless
M_s	Saturation magnetization	$\mathrm{A{\cdot}m^{-1}}$
R	DC electrical resistance	Ω
T	Temperature	K
T_c	Superconducting critical temperature	K
V	Voltage	V
v_l	Vortex velocity	$\mathrm{m{\cdot}s^{-1}}$
v_s, v_f	Fermi velocity (superconductor, ferromagnet)	$\mathrm{m{\cdot}s^{-1}}$
Δ	Superconducting gap	eV
ϵ_F	Fermi energy	J
Φ	Magnetic flux	Wb
Φ_0	Superconducting flux quantum	2.068×10^{-15} Wb
κ	Ginzburg-Landau parameter	dimensionless
λ	Magnetic penetration depth (bulk)	m
Λ	Effective magnetic penetration depth (films)	m
μ_0	Magnetic permeability of vacuum	12.57×10^{-7} $\mathrm{N{\cdot}A^{-2}}$
ρ_{FF}	Flux-flow resistivity	Ω·m
ρ_N	Normal state resistivity	Ω·m
ξ	Ginzburg-Landau coherence length	m

Contents

Chapter 1

General introduction

1.1 Historical overview

Attaining temperatures as low as 4 K was made possible due to the first liquefaction of helium in the group of Kammerlingh Onnes in Leiden university, Netherlands (1908). It opened the way to the discovery of superconductivity in 1911, by the same Pr.Onnes, in mercury. He observed that the resistance of mercury was, in his own words, "practically zero" at 4.2 K. This was the exact opposite of what some predictions, like Lord Kelvin's in 1902, were expecting. He later observed persistent currents flowing for an hour in a superconducting ring without perceptible dissipation while trying to estimate how low the residual resistance was [1].

Superconductivity is not at all an exotic property: in the periodic table alone, more than 30 elements are superconducting at a finite temperature. Nonetheless, these temperatures are only a few Kelvin, which requires a cryogenic setup to be reached. Once cooled below its *critical temperature* T_c, the material enters the superconducting state and the electrical resistivity completely vanishes (perfect conductivity). In that state, all magnetic fields are expelled from the bulk (perfect diamagnetism, or *Meissner-Ochsenfeld effect*, 1933). The latter property distinguishes superconductors from ideal conductors, that would just trap the magnetic fields inside. It is also responsible for the magnetic levitation phenomenon shown in Fig.1.1, in which a magnet is repelled by a superconducting cuprate plate, and floats above it.

In 1935, the first theory of superconductivity was formulated by the London brothers, based on the Maxwell equations. Although it is elementary, it manages to explain the perfect diamagnetism with surface screening of the field by superconducting currents. Later, in 1950, Ginzburg and Landau (GL) proposed a phenomenological theory that describes superconductivity as a second-order phase transition. That theory recovered many properties of superconductors, and is still widely used. But the microscopic origin of superconductivity still remained mysterious until the celebrated theory of Bardeen, Cooper and Schrieffer (BCS, theory, 1957 [70]). It explained superconductivity in terms of pairing of electrons (the so-called *Cooper pairs*, mediated by strong *electron-phonon* interaction. These pairs are strongly correlated and behave as a single macroscopic quantum state, as assumed earlier in GL theory.

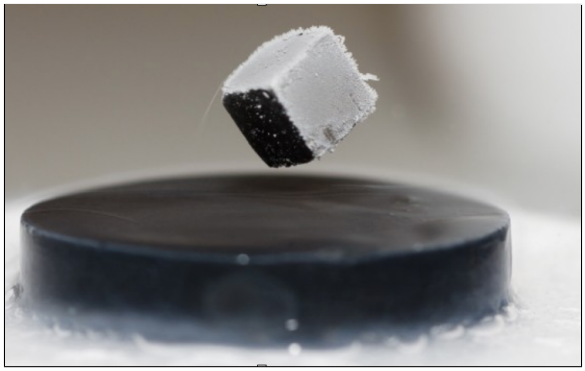

Figure 1.1: **Magnetic levitation in cuprate $YBa_2Cu_3O_7$**
Below its critical temperature, the superconducting cylinder repels magnetic fields. A small magnet placed above floats due to diamagnetism.

The critical temperature of superconductors according to BCS theory was supposed not to exceed 30 K, considering reasonable values of electron-phonon coupling in materials. This was proven wrong by the discovery of high-temperature superconductivity (HTSC) at IBM by Bednorz and Muller in cuprates (T_c = 35 K in LaBaCuO, IBM) [71], in which the measured electron-phonon couplings cannot explain the value of T_c. It was revolutionary, for scientists as it challenged the universality of BCS theory, as well as for applications since these can operate above the boiling point of liquid nitrogen (77 K). The current world record at ambient pressure is held by $HgBa_2Ca_2Cu_3O_8$, which is superconducting up to 135 K [72]. Other HTSC compounds were discovered after, like iron pnictides (thin $FeSe/SrTiO_3$, $T_c > 100$ K [73])or H_3S, which has the highest critical temperature (T_c = 203 K) ever observed, but requires pressures around 200 GPa, accessible only in a diamond anvil [74]. The existence of high-T_c superconductivity challenged the universality of the BCS mechanism as a source of pairing. At the time of writing, the origin superconductivity in cuprates is still an open question.

1.2 Superconductors for high-power computing

The discovery of superconductivity has led to several notable applications. These include very sensible magnetometers (SQUID), particle detectors, high-field electromagnets for research and medical imaging, and even levitating trains (SCMaglev, Japan [2]). Nonetheless, aside from D-Wave's controversial supercomputer [3, 75], no other practical superconducting computer has been built yet. As these typically operate below 10 K, requiring costly and cumbersome cryogenic setups, they are not really suitable for day-to-day applications. That statement is not so true for high power computers, that already require space and large scale cooling [4, 5].

In November 2018, the state of the art supercomputer was IBM's *Summit* architecture. It has a peak calculation power of 200 petaflops (2×10^{17} floating point operations per second), which makes it the world's most powerful computer at the time of writing [6]. On the other hand, it requires around 13 MW to operate [76, 7].

As a comparison, it is approximately the nominal production of the entire wind farm of Porte de Champagne (France, 12.3 MW [8]). This is already a lot, and is not likely to go down, as Intel recently announced Aurora, the first exaflop computer (10^{18} flops) to be delivered by 2021 [77].

At that scale, superconductors become interesting as their high energy-efficiency and speed compensate the increased refrigeration cost [9, 4]. Overall, the estimations shown in Fig.1.2 predict at least a tenfold reduction of the power consumption between equivalent CMOS and superconducting architectures.

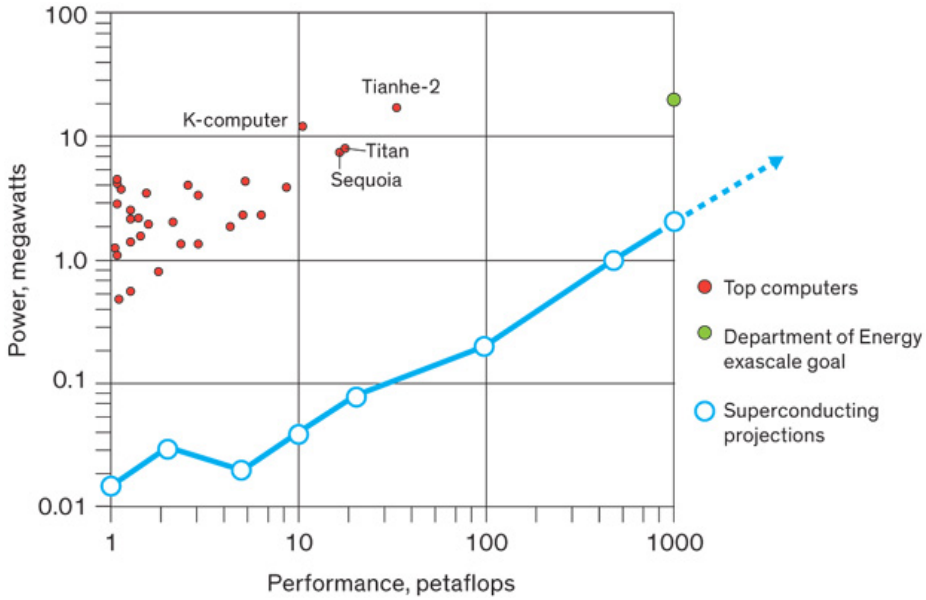

Figure 1.2: **Efficiency of supercomputers [9]**

Several countries like China [10] and the USA intelligence agency IARPA [5] have announced projects of superconducting computers. The latter program, *Cryogenic Computing and Complexity* (C3), plans to build a working computer by 2020. In their roadmap, the said computer would have a 100 petaflop capacity for of 200 kW, which is much more efficient than CMOS equivalents. These are based on niobium technology ($T_c \approx 7$K), and the hallmark device of superconducting electronics : the Josephson junction.

One of the impediments of superconducting computers comes from the memories. The current compatible memory elements involve features of several 100nm [11], which are rather large compared to the few tens of nanometers per cell in semiconductor memories [12]. A possible solution is to include layers of ferromagnetic materials. This is not intuitive, as magnetism and superconductivity are usually at odds with each other. Several approaches exist, like directly adapting basic elements from spin electronics [13], or using new phenomena as in π-Josephson junctions [16].

1.3 Motivations

In the present thesis, we study two different approaches to superconductor-ferromagnet (SF) hybrid devices. The first one involves creating currents that are both *spin-polarized* and *resistanceless* in ferromagnetic Josephson junctions. That uncanny combination may appear in stacks of superconductors and ferromagnets due to interface effects. In addition, this type of junctions may also naturally be π-junctions [78]. Josephson effects have been demonstrated several times in SF systems, but those often involved low-temperature materials. To the author's knowledge, there is still no direct demonstration involving high-temperature compounds, despite its technological interest. Here, we investigate these effects in oxide structures containing the high-temperature cuprate $YBa_2Cu_3O_7$ and the strong ferromagnetic manganite $La_{0.7}Ca_{0.3}MnO_3$. We continue the work previously done in our group on these materials [27, 33], that evidenced superconducting correlations propagating in the magnetic layer. However, likely due to the defects and high resistances of the contacts, no Josephson effects were observed. Here, we propose ways to improve the fabrication techniques to circumvent the latter issues, and attempt to observe superconducting currents across the ferromagnet. These results are presented in Chap.4.

The second approach follows proposals of novel non-volatile memories involving magnetic domain-walls and skyrmions as information bits [18, 17]. They have a width of only a few ten nanometers, and are promising candidates for making high density memory elements that could be adapted to superconducting circuits. In Chap.5 and Chap.6, we investigate whether these could be detected (and eventually manipulated) using a superconductor. To that end, we measured magneto-transport in bilayers containing the low-temperature superconductor Mo_4Si and several ferromagnetic multilayers that host domains and skyrmions.

1.4 Organization of the manuscript

The present thesis articulates in three parts. First, we introduce the core concepts of superconductivity and magnetism employed in this work. We also give a quick overview of how superconductivity and ferromagnetism interact, and how it may be used to make devices. A chapter is also dedicated to the materials and device fabrication techniques we used. The following chapters present the results of our experiments. The first one is dedicated to the study of high-temperature oxide systems. The second and third are about the interplay of magnetic structures and superconductivity in metallic multilayers. One of them focuses on critical currents, whereas the other one tackles unexpected Hall effects that appear in the bilayer due to the presence of the ferromagnet. Each of the experimental chapters starts with a short, more specific literature review on the topic, and may be read independently from the others. The last chapter of the thesis summarizes the results and perspectives of the present work. The Appendices include the detailed fabrication recipes the devices, and some extra experiments or modeling that did not fit in the experimental chapters.

Chapter 2

Basics of superconductivity and ferromagnetism

2.1 Type-II superconductors

2.1.1 Basic phenomenology of superconductivity

As mentioned earlier, superconductivity has two hallmark properties. First, below T_c, electrical currents flowing in the material are resistanceless ($R = 0$). Second, all internal magnetic fields are expelled from the bulk of the material ($B = 0$ in the bulk). The superconducting state, according to the BCS theory, originates from pairing of electrons at low temperatures. Due to local lattice vibrations (*virtual phonons*), there is an effective attractive interaction called *Cooper pairing*, that couples electrons of equal and opposite momenta and spin. The pair having a net spin of zero, it can condense with all the others into the superconducting state, as long as the pairing interaction is stronger than the thermal energy k_BT and the electron scattering mechanisms in the material. This opens a gap 2Δ in the density of states (DOS) of the superconductor (see Fig.2.1a), which can be seen as the binding energy of a Cooper pair. Below T_c, that gap energy is larger than that of scattering mechanisms in the material. Hence, they do not break the pairs, and superconducting current flow without resistance. The DOS in BCS theory writes as in Eqn.2.1, where N_0 is the DOS in the normal state at the Fermi level, and ϵ the energy relative to the Fermi level.

$$N(\epsilon)/N_0 = \frac{\sqrt{\epsilon^2 - \Delta^2}}{|\epsilon|} \tag{2.1}$$

The superconducting gap is small, of the order of 1 meV, and is easily broken by thermal excitation. This is why the critical temperatures of conventional superconductors are low ($T_c < 30$ K). As the temperature increases, the gap is progressively weakened, and vanishes upon approaching T_c, as represented in Fig.2.1b. Close

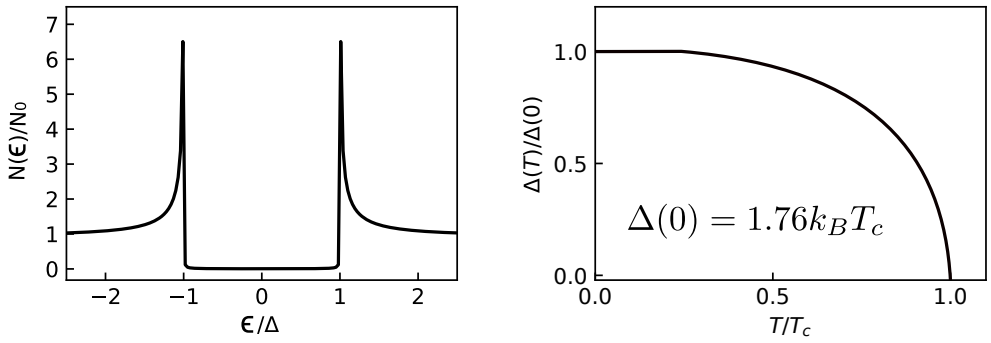

(a) BCS density of states (b) Temperature dependence

Figure 2.1: **Superconducting gap and temperature dependence**

enough to the transition, it may be approximated by Eqn.2.2, where $\Delta_0 \approx 1.764 k_B T_c$ is the gap at zero temperature [63, p. 63]. Near T_c, it can be approximated by Eqn.2.2.

$$\frac{\Delta(T)}{\Delta(0)} \approx 1.74(1 - T/T_c)^{1/2} \quad ; \quad T \to T_c \tag{2.2}$$

Superconductivity is a collective phenomenon : according to the GL theory, all the superconducting pairs can be described as a single macroscopic wave function called the *order parameter* Ψ. It usually writes as in Eqn.2.3 at position $\mathbf{r}$, with $|\psi(r)|^2$ being the local Cooper pair density, and ϕ is the *macroscopic phase* of the condensate.

$$\Psi(\mathbf{r}) = |\Psi(\mathbf{r})| e^{i\phi(\mathbf{r})} \tag{2.3}$$

The order parameter is usually weakened by the defects in the material, like impurities, normal inclusions, or grain boundaries. However, there is a minimal length over which it can be completely suppressed, which is the Ginzburg-Landau *coherence length* ξ [1].

As hinted by the phase factor in Eqn.2.3, the superconducting state is also *phase-coherent*. An important consequence is *fluxoid quantization*, in which the *fluxoid* [2] going through a superconducting loop is quantized in units of $\Phi_0 = \frac{h}{2e}$. The latter quantity is called the *superconducting flux quantum*. An interesting discussion of that phenomena and its discovery is given by Einzel [79]. Coherence effects in superconductors are fundamental, as they lead to multiple effects like the propagation of superconducting correlations in normal materials, even in absence of a pair potential (*proximity effect*, see Sec.2.4).

Superconductors cannot sustain arbitrarily high superconducting currents. At some point, the kinetic energy acquired by the superconducting electrons exceeds the

[1] It has to be distinguished from the Cooper pair size ξ_0 in BCS theory, both being related by $\xi = \sqrt{\xi_0 l}$, where l is the mean-free path in the material.

[2] The sum of the external field flux and the flux due to superconducting currents in the loop.

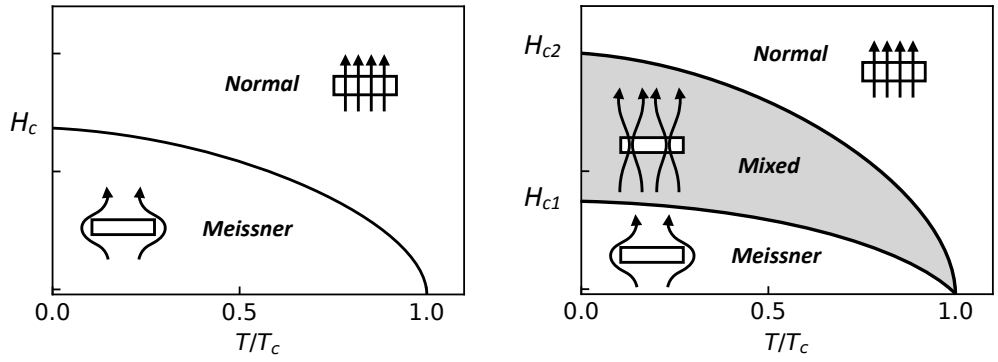

(a) Type I (b) Type II

Figure 2.2: **Field-temperature phase diagram of superconductors**

pairing interaction and separates the pairs. It is represented by the depairing *critical current*, at which superconductivity is destroyed [80].

Usually, the superconducting state is weak to magnetic fields, that tend to align the spins whereas Cooper pairing requires them to be opposite. This leads to a finite *critical magnetic field* H_c, at which the magnetic energy is enough to separate the pairs, reverting the material to the normal state.

Below H_c, the material is a perfect diamagnet and expels all internal magnetic fields. This is called the *Meissner effect*. External magnetic fields are also screened exponentially from the surface by superconducting currents. This occurs over the *magnetic penetration depth* λ, as in the London theory. In films of thickness d_s lower than λ, the field penetration perpendicular to the layer is eased, as superconducting currents become two-dimensional. In that case, the relevant screening length is the *effective* (Pearl) penetration depth $\Lambda = \lambda^2/d_s$ [81]. A consequence of the Meissner effect is that superconducting currents are forced to flow at the surface. This happens since electrical currents generate magnetic fields, which are expelled from the bulk. Nonetheless, the perfect diamagnetism is common to all superconductors only at low fields. For stronger values, some materials locally allow the field to penetrate, as we shall see in 2.1.2.

2.1.2 Type-II superconductors

The perfect diamagnetic behavior described previously is valid for all superconductors only in the limit of small magnetic fields. Outside of that range, the sign of the interface energy between normal and superconducting regions dictates the response of the material to the field. This is characterized by the *Ginzburg Landau parameter* $\kappa = \lambda/\xi$, which allows to distinguish two categories of superconductors.

For *type I* superconductors ($\kappa < 1/\sqrt{2}$) the interface energy is positive and favors large normal/superconducting domains. As shown in the phase diagram of Fig.2.2a, they are always perfect diamagnets below the critical field H_c. Above, they transition to the normal state.

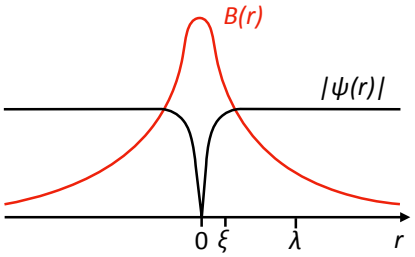

(a) Structure of a vortex [63]

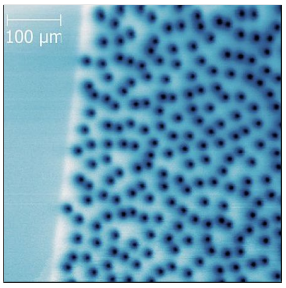

(b) Abrikosov lattice in YBCO [83]

Figure 2.3: **Vortices in superconductors**
Vortices consist of a normal core through which the field penetrates (2.3a). They can form lattices when the field is high enough (2.3b, scanning SQUID image).

Type II superconductors ($\kappa > 1/\sqrt{2}$), on the other hand, have a negative interface energy. This favors many small normal domains instead of a large one. Consequently, the flux can penetrate the material in the form of *flux-lines* called *superconducting vortices*. The material stays perfectly diamagnetic only below a *lower* critical field H_{c1}, at which the first vortex nucleates. The number of vortices then increases with the external field, up to the *upper* critical field H_{c2} at which the vortex cores overlap, and the whole material turns normal. This yields the phase diagram of Fig.2.2b. The vortex state between H_{c1} and H_{c2} is called the *mixed state*. The thermodynamic field H_c still exists between H_{c1} and H_{c2}, but does not determine the transition to the normal state anymore.

The detailed structure of a vortex consists in a normal core of radius ξ, around which screening currents circulate on a typical radius λ. They carry *exactly* one flux quantum Φ_0, which is the minimum allowed by fluxoid quantization. The order parameter and magnetic field in a vortex are given by Eqn.2.4 and 2.5 respectively [82, p.1471], where K_0 is a zero-order modified Bessel function. These are represented in Fig.2.3a.

$$|\psi(r)|^2 \approx \frac{1}{1 + 2\xi^2/r^2} \tag{2.4}$$

$$B(r) \approx \frac{\Phi_0}{2\pi\lambda^2} K_0 \left(\frac{(r^2 + 2\xi^2)^{1/2}}{\lambda} \right) \tag{2.5}$$

The existence of vortices was first proposed by Abrikosov in 1957 [84]. Vortices with the same polarity repel each other and can form dense lattices like the one shown in Fig.2.3b. These can also show hexagonal ordering, given that disorder is not too important in the material. They can move as well, for example due to applied electrical currents, and are hindered by the material defects. Flux pinning strongly influences the electrical properties of type II materials. It also modifies the penetration and escape of the flux, as we shall see in Sec.2.1.3.

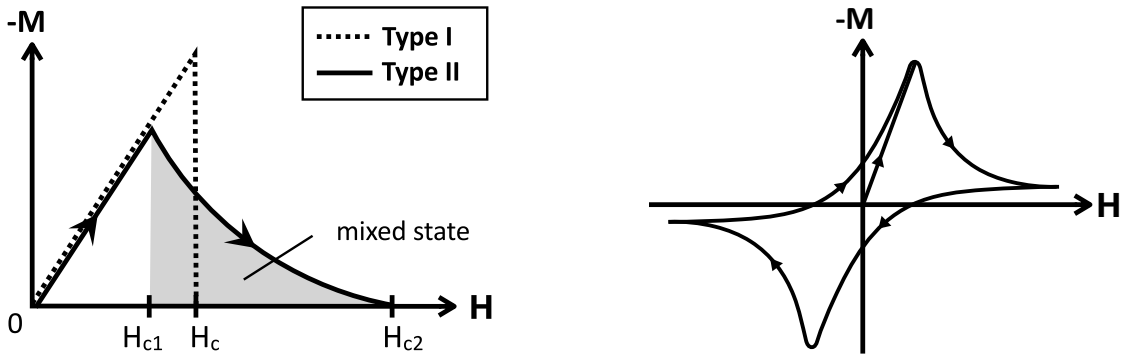

(a) Type I and II materials

(b) M(H) irreversibility [82, p. 1534]

Figure 2.4: **Magnetization curves in superconductors**

2.1.3 Penetration and escape of the flux

The presence of vortices influences the magnetic properties of type II superconductors. In Fig.2.4a, we present a sketch of magnetization curves for type I and II materials. For type I superconductors, it always opposes the field ($H = -M$), so that the field is screened in the bulk ($B = 0$, Meissner effect). It breaks down at H_c, when superconductivity is destroyed. In type-II superconductors, the same behavior is observed up to H_{c1}, at which the first vortex enters. Then, as their number increases, the magnetization drops progressively until the field exceeds H_{c2}, turning the sample normal.

Vortices usually enter at the borders of the sample and diffuse to the center as they are repelled by other appearing vortices. Upon decreasing the field, they exit the material in the reverse way. Still, the flux tends to accumulate at the borders, due to several energy barriers preventing the entry and exit of vortices [85]. Surface effects [86] and flux pinning on defects also prevents their diffusion away from the edges, or escape from the material. This often makes the magnetization curves irreversible in type II superconductors, as represented in Fig.2.4b.

2.1.4 Vortex motion and dissipation in type-II superconductors

Superconducting vortices can move due to time-varying magnetic fields, temperature gradients [87], or electrical currents [88]. That motion is responsible for the onset of electrical resistance between H_{c1} and H_{c2}, and usually dictates the electrical properties of the material.

Applying a current exerts a *Lorentz-like* force density $\mathbf{j} \times \mathbf{B}$ on the vortices [82, 89]. It drives them *perpendicularly* to the current with a velocity $\mathbf{v_l}$. The motion then dissipates due to the currents crossing the normal core region [88], and the retarded recovery of superconductivity after the passing of the vortex [90]. It results in an electric field $\mathbf{E} = \mathbf{B} \times \mathbf{v_l}$, that is perpendicular to the vortex velocity [91].

In the case when pinning is negligible, the vortex motion is opposed only by a *viscous drag* force due to due to friction of normal electrons in the core on the crystal lattice ions [88]. It writes $-\eta \mathbf{v_l}$, where $\eta = \mu_0 \Phi_0 H_{c2} \sigma_N$ is the viscosity coefficient, and σ_N the normal state conductivity. We neglect transverse forces, that are discussed in Sec.2.1.6. In the steady state, the equation of motion simply writes as :

$$\mathbf{j} \times \mathbf{B} - \eta \mathbf{v_l} = 0 \tag{2.6}$$

This is the *flux-flow* regime. Bardeen and Stephen [88] demonstrated that the resulting *flux-flow resistivity* ρ_{FF} in a clean superconductor writes as in Eqn.2.7.

$$\rho_{FF} = \rho_N \frac{H}{H_{c2}} \tag{2.7}$$

It linearly depends on the normal state resistivity ρ_N and the applied field. Interestingly, the flux-flow resistivity *never vanishes* in the presence of vortices. Thus, any finite current should move the flux-lines and create dissipation. Hopefully, in real materials, vortices are pinned on defects, preventing their motion. Consequently, the observed critical current in type II superconductors is a *depinning* current. It is often much lower than the *depairing* critical current discussed in Sec.2.1.1. When pinning is no more negligible, other effects like thermal activation enter into account. These affect the vortex dynamics, as we shall see next.

2.1.5 Thermally activated vortex motion

In the case where the pinning force is not negligible, the motion of vortices is strongly hindered. As explained by Anderson and Kim [92, 93, 94], it becomes thermally activated. Additionally, the long range vortex-vortex repulsion largely disfavors the motion or pinning of single vortices, as it abruptly changes the local flux density. Instead, one has to consider bundles of vortices of a size λ for pinning and transport. A point defect will still directly pin one vortex, but by interacting with the others, it will also prevent the surrounding vortices to move. Thus, the pinning of a single center is distributed among all the vortices in the bundle. The whole flux lattice can still be disordered by the vortex motion, but not on a scale smaller than λ. This is the *flux creep* regime.

Let's consider a single vortex bundle in a simple one-dimensional washboard potential, as shown in Fig.2.5b. The bundle attempts to jump to neighboring pins with a thermally activated frequency $\nu_0 e^{-\frac{U}{k_B T}}$, where U is the depth of the pinning potential. Applying a current biases the hopping probability, and creates a net motion of the vortices. The resulting electric field writes as in Eqn.2.8. Here, j_c is the critical current at $T = 0$, and x_{hop} is the mean distance between adjacent pins [95, 82].

$$E = 4 B x_{hop} \nu_0 e^{-\frac{U}{k_B T}} \sinh\left(\frac{U}{k_B T} \frac{j}{j_c}\right) \tag{2.8}$$

Vortex dynamics and pinning make the current-voltage curves of type-II superconductors strongly non-linear, as shown in Fig.2.5a. In the limit where $j \ll j_c$,

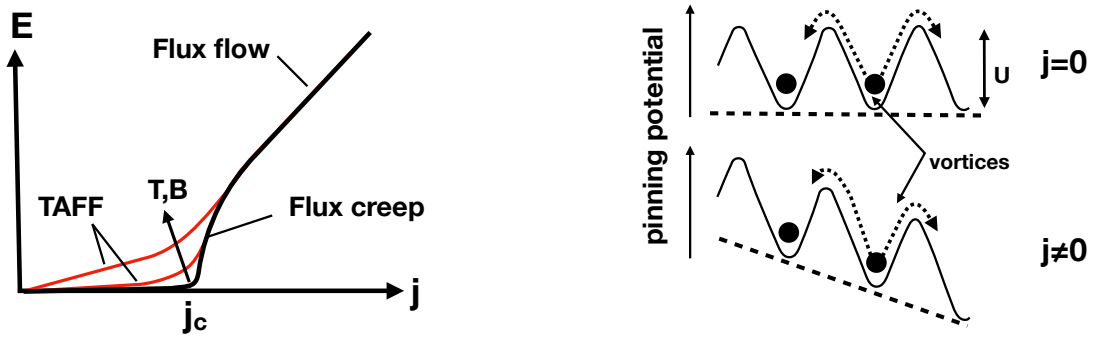

(a) **Current-voltage curves** (b) **Thermally-activated motion**

Figure 2.5: **Transport in type-II superconductors**

the expression of Eqn.2.8 can be linearized. This is the *thermally activated flux-flow* regime (TAFF), in which vortex bundles hop from pin to pin. The intermediate region, where $j \approx j_c$, corresponds to *flux creep*. Here, the flux lattice manages to move by shearing around the pins. It is responsible for rounding the transition to the *flux-flow* regime. In the latter ($j \gg j_c$), pinning becomes negligible and the expression has to be replaced by the formula $E = \rho_{FF}(j - j_c)$ [96, 97], where ρ_{FF} is the flux-flow resistivity from Eqn.2.7.

The TAFF and creep regimes are prominent mostly in low-pinning [98] or high-temperature superconductors [99]. As mentioned by Anderson and Kim, the model is valid only far from H_{c1} and H_{c2}, so that the vortices repel each other, but their cores do not interact. Up to now, we described pinning without considering any detailed mechanism. These are discussed next, in Sec.2.1.6.

2.1.6 Pinning mechanisms

As stated earlier, any local inhomogeneity of superconductivity acts as a pinning center for vortices. Depending on their nature and size, the centers can pin the flux-lines by interacting either with their *core* or their *magnetic field*.

Core pinning is due to inhomogeneities of the *order parameter* and acts on a scale comparable to the coherence length ξ. It generally comes from material defects like voids, surface inhomogeneities, or strains [89, 100, 101], as they locally depress the order parameter [89, p. 338]. In contrast, *magnetic* pinning occurs only through electromagnetic interactions, due to inhomogeneities of the *magnetic field*. These act on a range comparable to the magnetic penetration depth λ [89, p. 339].

The pinning force density F_p of a given mechanism generally obeys a scaling law with parameters like the magnetic field [102] or the crystalline strain [101]. The scaling with the magnetic field can usually be written as in Eqn.2.9, where p and q are characteristic exponents of the mechanism, and $b = H/H_{c2}$ is the reduced magnetic field [103]. As an example, the scaling for the lattice shearing around hard pins has

exponents p=1, q=2. It was originally introduced by Kramer [102], and is represented in Fig.2.6a.

$$F_p/F_{p,max} = b^{p/2}(1-b)^q \tag{2.9}$$

One may notice that the density of pins and their strength are contained in the amplitude $f_{p,max}$, not the scaling itself. These laws are mostly phenomenological though, and identifying the exact source of pinning quickly becomes inextricable if several mechanisms are competing.

Pinning centers can also be made artificially, by using ion irradiation [104], thickness modulations [105], or etched holes [106]. These allow to control the density and strength of the pinning centers in the superconductor, usually to enhance the critical current.

Moreover, cleverly engineering the pins also allows to add new functionalities to the vortex transport in the material, like *ratchet* effects [107, 108] or geometrical frustration [109]. A common one is to make periodic arrays of pinning centers [110, 111]. In these, several geometrical effects are observed due to the periodicity. Among them, strong critical current enhancements are observed at specific magnetic field values at which the periodicity of the vortex lattice and the defect array match [61], as shown in Fig.2.6b. These usually use magnetic dots instead of normal ones, to enhance the pinning force. These effects are covered in Sec.2.3.2. Also, one can *guide* the motion of the vortices by having a shorter period in one direction, like in rectangles [112], along which vortices will hop more easily.

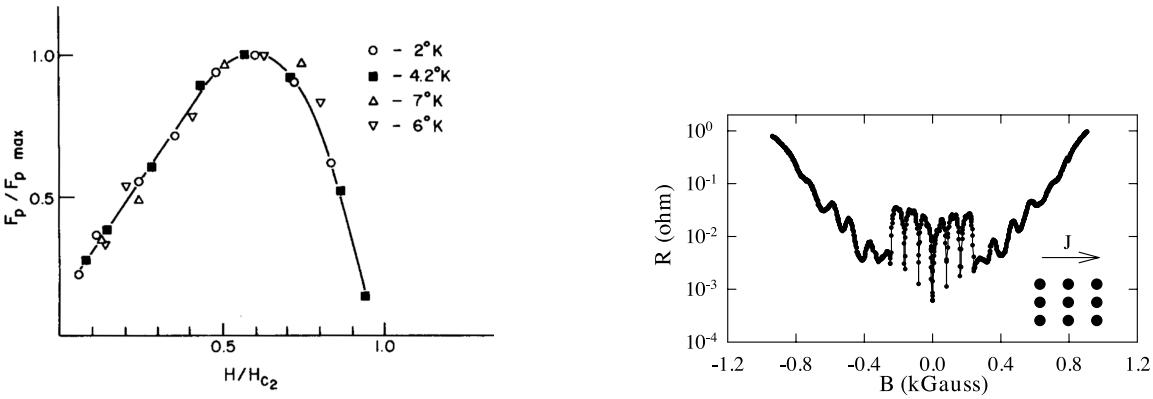

(a) Kramer scaling [102]

(b) Periodic pinning [61]

Figure 2.6: **Scaling of the pinning force and geometrical effects**

Transverse voltages in superconductors

In Sec.2.1.4, we neglected transverse forces acting on the vortices. These are usually small, but still exist and deviate the vortices from the course imposed by the Lorentz force. Consequently, a voltage transverse to the applied current is measured. These forces have several possible origins.

One of them is the Magnus force, in analogy with fluid mechanics, that acts on the moving vortices [113, 114, 115]. It is written as in Eqn.2.10, where $\mathbf{v_s}$ and $\mathbf{v_l}$ are respectively the superconducting current and vortex velocities, and N_e the density of superconducting electrons.

$$F_m = n_s e \left(\mathbf{v_s} - \mathbf{v_l}\right) \times \mathbf{B} \tag{2.10}$$

That expression may be derived by using fluid mechanics [113], or topology arguments [116]. That force comes from the electrostatic field due to the current flow around the vortex, and quasiparticle scattering in the core. However, it is often very small outside of the *superclean* limit. It remained a controversial subject for long, especially with sign reversal effects that were observed in amorphous superconductors like Mo_3Si [117] and cuprates [118]. Some explanations point towards pinning [119, 120], although it may not stem from the same causes in both [121].

In addition, the measurement of these transverse voltages is often ambiguous. As the signals are small, they are often shrouded by parasitic voltages due to defects, or sample asymmetries [122, 123, 124]. Transverse voltages may also originate from guided motion of vortices, either due to unwanted anisotropy of the sample [63], or engineered pinning, that purposefully orients the vortex motion. In the latter case, preferred directions can be observed by measuring simultaneously the longitudinal and transverse electric fields [125, 126, 127]. These usually have the same symmetries as the artificial pinning potential.

2.2 Ferromagnetism and spintronics

2.2.1 Ferromagnetism

In this section, we introduce the other type of materials used in the present work : ferromagnets. These are materials in which neighboring spins tend to align with each other, due to the *exchange interaction*. As a result, a ferromagnetic material can form regions called *magnetic domains*, in which the magnetization is uniform. Thus, the net magnetization $\mathbf{M}$ of the material can be zero if those of the domains cancel each other, or finite if they do not. The latter case can be obtained by applying an external magnetic field, that will tend to orient the magnetic moment of the domains along. The resulting magnetization may also hold when the field is decreased, leading to hysteresis effects. Ferromagnets have found a wide range of applications, from simple fridge magnets to state of the art electronic devices. These are especially interesting for making high-density and non-volatile memories, which is what superconducting circuits lack for now. In the following sections, we review the basic phenomenology of ferromagnetism, including exchange, anisotropy, and domain structures. Then, we present approaches to make memories with ferromagnets that could be adapted to superconducting circuits.

The exchange interaction

Ferromagnetism itself comes from the exchange interaction. For two neighboring spins $\mathbf{S_1}$ and $\mathbf{S_2}$, the corresponding Hamiltonian writes as $\hat{\mathcal{H}}_{ex} = -2J_{ex}\mathbf{S_1} \cdot \mathbf{S_2}$, where J_{ex} is the exchange integral. That interaction can be ferromagnetic ($J_{ex} > 0$, aligned spins) or antiferromagnetic($J_{ex} < 0$, antiparallel spins), depending on the material [128, p. 128]. If the energy reduction of having parallel spins is greater than the cost of modifying the energy bands, the material becomes ferromagnetic. In elemental metals, it occurs only in Fe,Co, and Ni, as their DOS is peaked near the Fermi level. The ferromagnetic state is highly ordered, and is weakened by thermal effects. Below the *Curie temperature*, exchange starts to prevail, and the spins progressively align parallel to each other.

Exchange in ferromagnets also creates a spin-splitting of the bands by ϵ_{ex} (see Fig.2.7b). This leads to an imbalance between the two spin populations, as they have different DOS at the Fermi level ϵ_F. Hence, an electrical current in the material will also carry a *spin current*, and a net *spin polarization* P. It is expressed in terms of the density of states of each spin population $N_\uparrow$ and $N_\downarrow$ as in Eqn.2.11.

$$P = \frac{N_\uparrow(\epsilon_F) - N_\downarrow(\epsilon_F)}{N_\uparrow(\epsilon_F) + N_\downarrow(\epsilon_F)} \tag{2.11}$$

The generation and control of spin-polarized currents is the foundation of spin electronics (*spintronics*), and is covered in Sec.2.2.3.

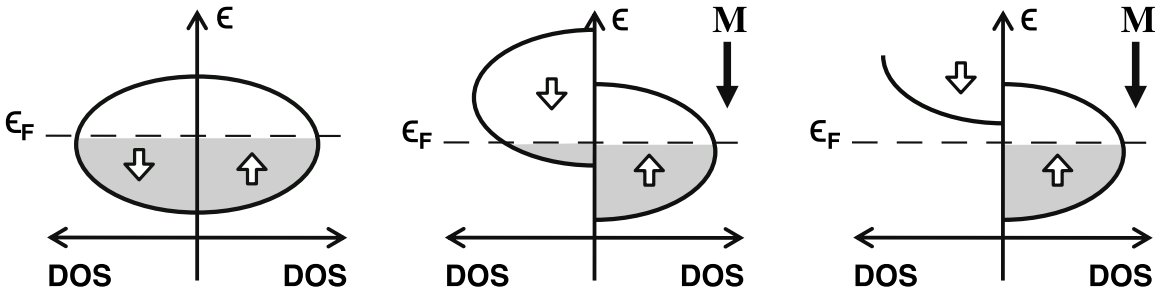

(a) Normal metal (b) Ferromagnet (c) Half-metal

Figure 2.7: **Bands in non-magnetic metals and ferromagnets**[129, Ch.5]
The exchange energy splits the bands in a ferromagnet. The half-metal is an extreme case in which only one band is partially filled.

Half-metals

The extreme case of spin polarized materials is the *half-metals* [130]. These are metallic for one spin orientation, and insulating for the other. This is possible only if $N(\epsilon_F) = 0$ for one of the two bands, as in Fig.2.7c. Consequently, currents going through are fully spin polarized ($P = 1$), at least at zero temperature. Several classes of compounds belong to that category like Heusler alloys, manganites like $La_{1-x}Ca_xMnO_3$, or chromium oxide CrO_2. These materials attracted interest for

making *giant* or *tunnel* magnetoresistance devices [131, p. 373], and possibly induce *Majorana edge states* [132] in superconductors. The latter are sought-after in quantum computing for their higher coherence lifetimes [133, p. 17].

2.2.2 Magnetism in ferromagnetic multilayers

In that section, we discuss what dictates the orientation and spatial distribution of the magnetization. We focus on magnetic multilayers with perpendicular anisotropy, since they are used in a significant portion of the present thesis. We deal with magnetic anisotropy, and the interactions that make the magnetization inhomogeneous in these layers. They lead to the formation of domain structures, helical or cycloidal orders and magnetic skyrmions as well.

Magnetic multilayers

As mentioned, ferromagnets can acquire a finite magnetization due to an external field, and retain it when the field is decreased. As shown in Fig.2.8a, it makes the magnetization curves in ferromagnets irreversible. We also observe two characteristic fields. One is the *saturation field* H_{sat} required to fully magnetize the ferromagnet : $M/M_s = \pm 1$ along the direction of the field, where M_s is the saturation magnetization. The other is the *coercive field* H_{co} that one has to apply to cancel the magnetization ($M/M_s = 0$). Another thing is the orientation and profile of that magnetization, which is determined by the *magnetic anisotropy*. It stems from a competition of volume energies, favoring in-plane orientations, against surface effects that tend to favor out-of-plane ones. It results in directions along which the magnetization lies preferably (*easy axes*) and others that are avoided (*hard axes*), as in Fig.2.8a.

Magnetic multilayers are materials specifically designed to enhance the interface effects and obtain out-of-plane magnetizations. They consist in repetitions of very thin magnetic layers (typically 1 nm) separated by similarly thin layers of non-magnetic metals. Perpendicular anisotropy in multilayers was first demonstrated by Carcia in the late 1980's [134, 135]. They quickly found applications to magnetic reader heads in and magneto-optical memory bits [136].

To see how the anisotropy changes from in-plane to out-of-plane, one has to consider the effective anisotropy energy K_{eff} of the magnetic multilayers (in $\mathrm{J{\cdot}m^{-3}}$). It can be separated into contributions from the *volume* K_v, due to dipolar fields and magneto-crystalline anisotropy, and from the surfaces K_s. That interface contribution originates from various sources, including spin-orbit, strain, or surface roughness, that will not be detailed here. For metallic multilayers, one can approximate $K_v \approx -\frac{1}{2}\mu_0 M_s^2$, which is the contribution of dipolar fields. Considering the top and bottom interfaces to be equivalent, one can express K_{eff} as in Eqn.2.12, where d_f is the thickness of a single ferromagnetic layer [128, 136, p. 252].

$$K_{eff} \approx -\frac{1}{2}\mu_0 M_s^2 + \frac{2K_s}{d_f} \tag{2.12}$$

The sign of K_{eff} then gives what interaction prevails, and hence, the preferred orientation of the magnetization. An example for Co/Pd multilayers is presented in Fig.2.8b. For thick layers, the volume term dominates, so that $K_{eff} < 0$ and the magnetization lies preferably in-plane. For thinner layers, K_{eff} becomes positive and favors out-of-plane magnetizations.

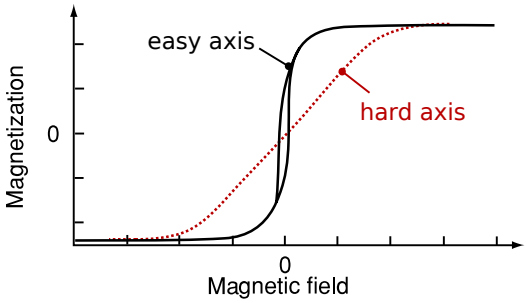

(a) Magnetic anisotropy [128, p. 274] p274

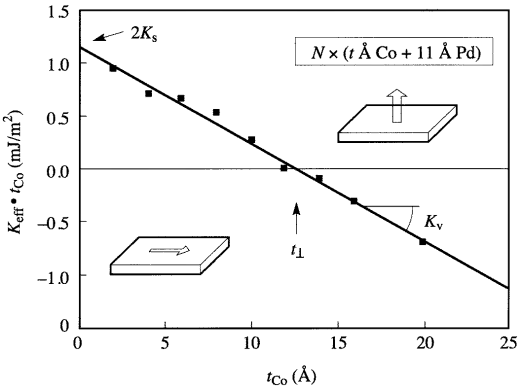

(b) **Anisotropy constant** [136]

Figure 2.8: **Hysteresis and effective anisotropy constant in multilayers** *The ferromagnet is more easily magnetized along some directions thanks to magnetic anisotropy. Its strength and orientation is given by the effective constant K_{eff} (in or out-of-plane).*

Domains, domain-walls

The exchange interaction favors all the spins aligned in a single direction. However, a homogeneous magnetization creates strong demagnetizing fields outside of the sample boundaries. These cost a lot of energy, and compete with the gain provided by exchange. To minimize the energy, the magnetization is often fractioned into *magnetic domains* with different orientations. A sample image is presented in Fig.2.9a for yttrium iron garnet (YIG), where the contrasts indicate alternating out-of-plane domains. At the domain boundaries, the magnetization reverses by tilting from one orientation to the next, forming *domain-walls*. The size of the magnetic domains then depends on the field energy saved by forming domains (proportional to their volume) compared to the cost of forming walls (proportional to the wall area). The nature of these domain-walls can be of two different types, as shown in Fig.2.9b. In *Bloch walls*, spins rotate perpendicularly to the domain boundary, whereas they do it parallel to the interface in *Néel* walls. Bloch walls are the most common, whereas Néel ones are stable only in layers thinner than the wall width [128, p.240-243]. They can also be favored by effects like the Dzyaloshinskii-Moriya interaction, which is presented in the next section.

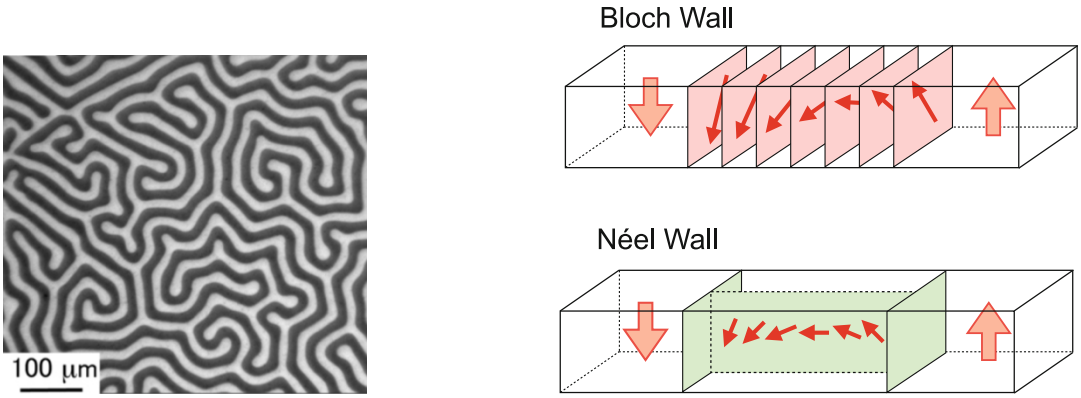

(a) Domain structure in YIG [137]

(b) Bloch and Néel walls [138]

Figure 2.9: **Magnetic domains and domain walls**
Out-of-plane domains in yttrium iron garnet (MOKE image, 2.9a), and structure of Bloch and Néel domain walls (2.9b).

Dzyaloshinskii-Moriya interaction and skyrmions

In the presence of strong spin-orbit coupling and central symmetry breaking, adjacent spins might tilt from one another. This is due to an indirect exchange coupling called the Dzyaloshinskii-Moriya interaction (DMI) [139, 140]. The resulting Hamiltonian writes as in Eqn.2.13, where the coupling strength $\mathbf{D}_{12}$ is given by symmetry arguments. It favors perpendicular spins, and thus competes with ferromagnetic exchange.

$$\hat{\mathcal{H}}_{DM} = -\mathbf{D}_{12} \cdot (\mathbf{S}_1 \times \mathbf{S}_2) \tag{2.13}$$

A simple picture of DMI is a set of three atoms in which two bear spins and the third has strong spin-orbit coupling. In magnetic multilayers, it is essentially an interface phenomenon, as represented in Fig.2.10a. Due to that interaction, spins next to each other are tilted by an angle proportional to the D_{12}/J_{ex} ratio, given that the anisotropy and external field are small enough.

However, if the stacking is symmetrical like in $(\mathrm{Pt/Co/Pt})_n$, the top and bottom DMI are equal and opposite, and cancel out. To have a net DMI in the film, one has to select two different materials that induce non-canceling couplings. Such materials can be $(\mathrm{Ir/Co/Pt})_n$, in which there is an appreciable net interfacial DMI [58].

In these films, DMI helps to stabilize magnetic skyrmions [18], like that shown in Fig.2.10b. These are chiral bubble-like magnetic textures that are *topologically protected*. This means that a skyrmion cannot be, in theory, deformed continuously to a state with a different topology like a uniform magnetization [60, p.4], and reciprocally. It was suggested that even in real systems, the topological "protection", which is not absolute anymore, makes the skyrmion more difficult to nucleate, but also more stable than trivial magnetic bubbles. This is still a matter of debate, and advanced techniques to determine the potential barrier height for nucleation and annihilation are necessary [141]. The small sizes of skyrmions allow them to circumvent

local defects in tracks for example. Unlike domain walls, skyrmions do not deform (much) under various forces, thus the applied torques conserve their efficiency. These properties make them good candidates as information medium for non-volatile and high-density magnetic memories.

Like domain-walls, skyrmions of Bloch and Néel type exist, as represented in Fig.2.10b. In ultrathin multilayers like $(Ir/Co/Pt)_n$, DMI tends to favor Néel walls, as well as Néel skyrmions [58, 59]. Bloch skyrmions are more often found in chiral magnets like MnSi [42] or FeGe [69]. Using multilayers offer the advantage of tunable anisotropy and DMI by changing the materials and thicknesses. They also host room-temperature skyrmions, which is rarely the case in bulk crystals.

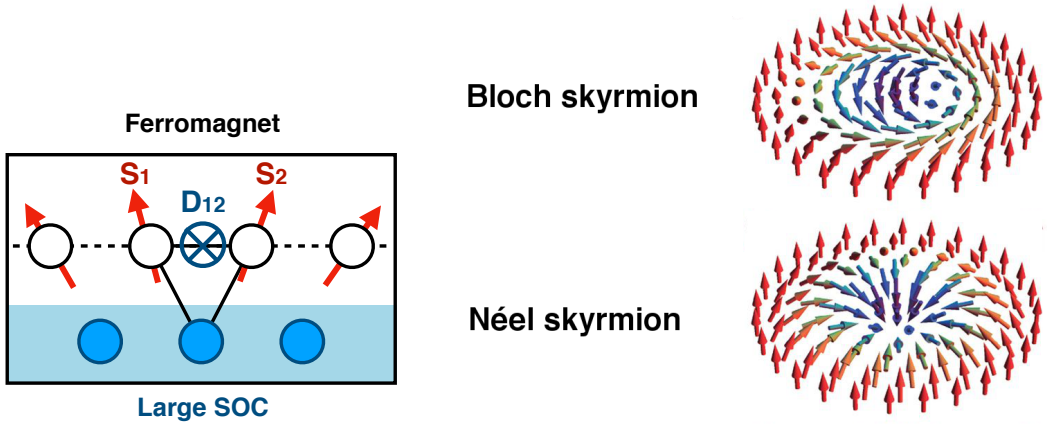

(a) Interfacial DMI [18]

(b) Magnetic skyrmions [142]

Figure 2.10: **Dzyaloshinskii-Moriya interaction and magnetic skyrmions**

The Hall effects in ferromagnets

In ferromagnets, in addition to the normal Hall effect, several transverse voltages may appear due to the total magnetization or the presence of topological structures like skyrmions. We consider three contributions to the total transverse resistivity, which we define as $\rho_{xy} = E_y/j_x$.

The first contribution is the normal Hall effect common to all materials. Consider a slab of material, in which flows a current density j. Applying a magnetic field B_z perpendicular to the material will exert a Lorentz force on electrons, that will deflect and accumulate them on one side of the sample. Consequently, a transverse electric field will build up and oppose further charge accumulation. In the steady state, it is given by $\frac{-B_z}{n_e e} j_x$, and is proportional to the electron density n_e. Hence, it is widely used to estimate the carrier density and sign in materials [143, p. 11].

A second contribution, the *anomalous* Hall effect, comes from the magnetization. It creates a voltage that is proportional to the out-of-plane component of the magnetization M_z, by a constant R_s. That effect originates from spin-orbit coupling and spin scattering, which deflects up and down spins in opposite directions relative to the

local magnetization [144]. In the presence of domains, their individual contributions are summed, resulting in a "net" anomalous Hall effect that mimics the out-of-plane magnetization curves. In ferromagnets with out-of-plane anisotropy, it is useful to deduce the M_z/M_s ratio through electrical measurements.

A third contribution is the *topological* Hall effect, that may appear in the presence of topological textures like skyrmions. It originates from an additional phase acquired by electrons going through these structures. It adds a contribution ρ_{THE} that is proportional to the number of topological objects in the material, and allows their electrical detection [145, 146], although is not systematically observed [66].

The total transverse resistivity then writes as in Eqn.2.14.

$$\rho_{xy} = \frac{-B_z}{n_e e} + R_s M_z + \rho_{THE} \tag{2.14}$$

2.2.3 Spintronics and magnetic memories

The discovery of giant magnetoresistance by Fert [20] and Grünberg [147] has led to the development of *spintronics* [148]. In that approach, the electron *spin* is exploited alone or in complement of their *charge*. That differs from conventional electronics, in which only charge effects are used. Its development resulted in the technologies that currently equip our computers now, and probably in the future too, although the materials and architecture will likely be different [149]. Spintronics offers efficient designs of non-volatile memories, that could be adapted to superconducting electronics.

Spintronics and GMR effect

An effect central to spintronics is the *giant magnetoresistance effect* (GMR), discovered by Fert and Grünberg. It can be explained by Mott's simple two-resistance model. In ferromagnets, the scattering also depends on the spin of electrons. The conduction of each spin orientation occur in separate channels put in parallel [128, p.283]. Electrons with spins aligned to the magnetization experience a small resistance r, whereas those with opposite spins experience a larger one R. Microscopically, this is due to the lower DOS available to scatter into for spins parallel to $\mathbf{M}$ (see Fig.2.7). Of course, this neglects all spin-flip scattering events.

Due to that, the resistance of two stacked ferromagnetic layers decoupled by a metallic spacer depends on the relative orientation of the magnetizations. As sketched in Fig.2.11, for parallel magnetizations ($\uparrow$ in the figure), the resistance for $\uparrow$ spins is lower and shorts the $\downarrow$ spin channel. If the two magnetizations are anti-parallel, the total resistance is higher since both channels conduct equivalently. This is the principle of *GMR spin-valves*, that equip the reader head of hard drives. In real devices, the magnetization of one layer is fixed, either through coercivity or antiferromagnetic coupling. The other is the *free* layer, of which the magnetization can be switched using magnetic fields or spin-polarized currents [149]. In more recent architectures, the metallic spacer of spin-valves is replaced by a tunnel barrier, to exploit the *tunnel magnetoresistance* effect (TMR, [128, p.287]) and obtain higher resistance ratios.

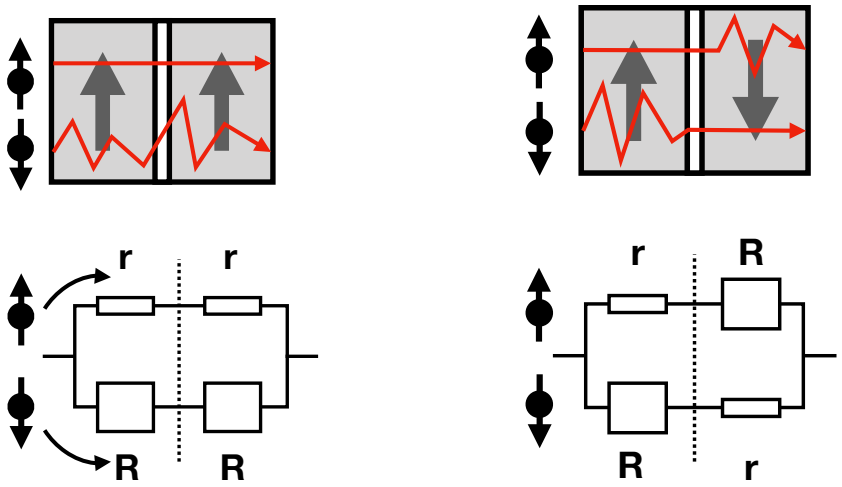

(a) Parallel (b) Anti-parallel

Figure 2.11: **GMR effect and spin-valves**

Magnetic memories

The desire to further reduce the size of memories led to the development of novel magnetic memory designs. Here we briefly present two that could potentially be adapted to superconducting circuits. *Magnetic Random-access memories* (MRAM) are a spintronic memory design that was developed in the late 1980 [150]. The memory element uses several spin-valves connected by perpendicular arrays of conducting tracks, as shown in Fig.2.12a. The information is encoded in the resistance state of the valve, set by the magnetizations due to TMR (parallel or antiparallel). It is read by measuring in the two perpendicular tracks that intersect at the desired element. The magnetization is then controlled with currents pulses, through *spin-transfer torque* [21]. These are non-volatile storage, have high endurance, and high density, but require higher currents than other designs. Current commercial MRAM typically have only a few tens megabytes of memory, but could be used as a universal memory element in the future [149, 151].

Other approaches aim to replace the uniform magnets by magnetic inhomogeneities to carry the information. The domain-walls and magnetic skyrmions we reviewed earlier are strong contenders, as these can reach small sizes (a few tens of nanometers) and be moved by magnetic fields and electrical currents [152, 66]. The latter property has led to the proposal of the *racetrack* memory design [17, 18], which is reminiscent of the bubble shift register memory invented in the 1970's [153]. As its name suggests, the domain or skyrmion continuously moves along a track. These could lead to faster and more energy-efficient memory cells. In terms of power consumption, moving trains of domain-walls or skyrmions at equivalent speeds requires similar current densities, around $10^{11} - 10^{12}$ A·m^{-2}. However, skyrmions are much less sensitive to pinning on defects, and become more interesting than DW at lower currents and velocities [154].

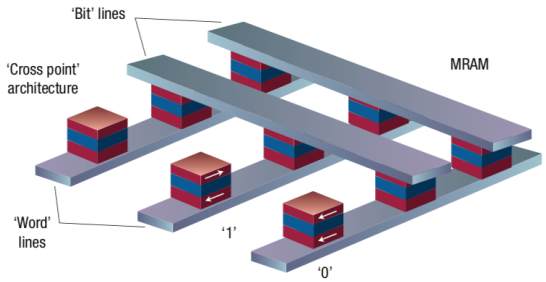

(a) MRAM design [149]

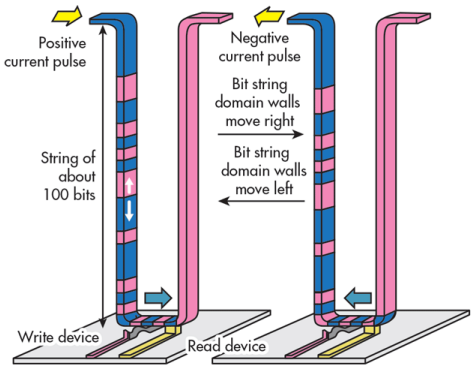

(b) Racetrack memory design [17, IBM]

Figure 2.12: **MRAM and racetrack memory designs**

2.3 SF bilayers without proximity

Now that we have introduced superconductors and ferromagnets, we can show how they interact with each other. For now, we discuss a superconductor-ferromagnet bilayer (SFB), in which the two layers are insulated from each other. Thus, we only consider electromagnetic interactions (no proximity effect). The superconducting and ferromagnetic layers are separated by a distance a that corresponds to an insulating layer, or a non-magnetic buffer for example. The superconductor is assumed to be thin ($d_S \ll \lambda$) and strongly type-II ($\lambda/\xi \gg 1$). In that case, it is sensible only to the out-of plane magnetic field component. The ferromagnet layer has perpendicular magnetic anisotropy, and a magnetic domain structure that is wide compared to the film thickness d_f. The presence of the magnetic domains creates stray magnetic fields that can affect the superconductor. These may induce inhomogeneities of the order parameter, and favor the nucleation and pinning of vortices. These phenomena influence the transport properties of the bilayer, as we shall see now.

2.3.1 Domain-wall superconductivity

The presence of domains in the ferromagnetic layer results in stray fields that appear close to the domain boundaries. These fields locally weaken the order parameter, and even destroy if they exceed H_{c2}. This leads to confinement of superconductivity, generally below the domain walls. Hence, it is called *domain-wall superconductivity* (DWS) [155]. Fig.2.13a shows a schematic of the process, where the grey areas represent the normal regions.

The typical stray field below the domains b_z^* exponentially depresses the order parameter over a length $l_b* = \sqrt{\frac{\Phi_0}{2\pi|b_z^*|}}$. Thus, one must have $l_b^* < W/2$ to turn at least the center of the domains normal and develop DWS [155, p. 9].

The domain morphology and M_s mostly determine the detailed field profile. It has maxima close to the domain walls, and increases in the center for narrower domains. A sample 1D profile is sketched in Fig.2.13. It also depends on the spacing between

the S and F layers, that rounds the features and lowers the amplitude (see Ref.[156] and Sec.5.3.4). Superconductivity is then confined in the regions where $H < H_{c2}$. That picture is valid if ξ is smaller than the scale on which the field profile varies, though. Otherwise, determining where the order parameter nucleates becomes more subtle [157, 158].

Such effects were observed in experiments, either by measuring magneto-resistances [43, 44] or the (T, H) phase diagram [159]. Some of these results are shown respectively in Fig.2.14a and Fig.2.14b. In both, superconductivity is depressed around zero field due to DWS. If an external field is applied, one has to consider the minima of the total field $H_{stray} + H_{ext}$ instead. Thus, superconductivity may re-enter if the external and stray fields compensate. This occurs below the domains opposite to the field, and is labeled as « domain superconductivity » (DS) in the figure.

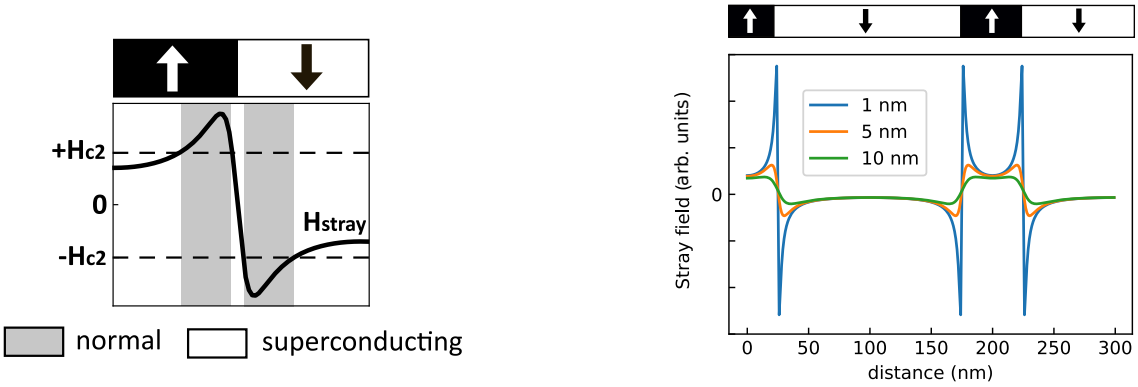

(a) Domain-wall superconductivity

(b) Stray-field from a distance a

Figure 2.13: **Domain-wall superconductivity and stray magnetic field**
Superconductivity nucleates where the field is below H_{c2} (2.13a). The stray field profile depends on the domain size, and on the spacing a between the ferromagnet and the superconductor (2.13b).

2.3.2 Vortices in superconductor/ferromagnet bilayers

Nucleation of vortices and magnetic instability

In type II superconductors, vortex physics play a large role in the transport properties. This is also true for SF bilayers. If the magnetization is large enough, it is likely to induce, or at least favor the nucleation of superconducting vortices and anti-vortices[3], even in the absence of an external magnetic field [160, 156].

Aside from the stray field, there is also a magnetic coupling $-\mathbf{M} \cdot \mathbf{\Phi_0}$ between domains and flux-lines, where $\mathbf{\Phi_0}$ is a vector of magnitude Φ_0 oriented along the vortex flux. That coupling is negative for vortices and domains of same polarity, favoring the apparition of vortices. This is valid even in the saturated state (monodomain), despite the absence of demagnetizing fields. If the net vortex energy $\epsilon_v = \epsilon_{v0} - \mathbf{M} \cdot \mathbf{\Phi_0}$ becomes

[3] Anti-vortices are vortices of opposite polarity.

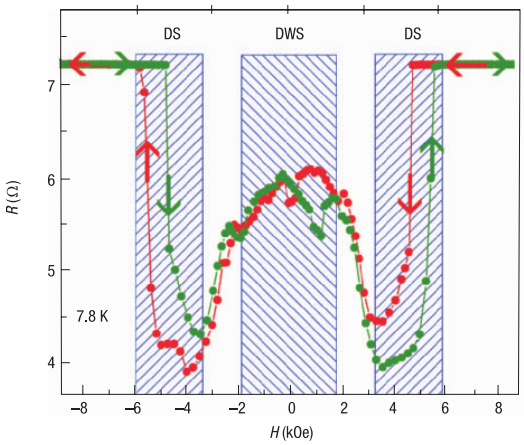

(a) Magneto-resistance in $Nb/BaFe_{12}O_{19}$ [43]

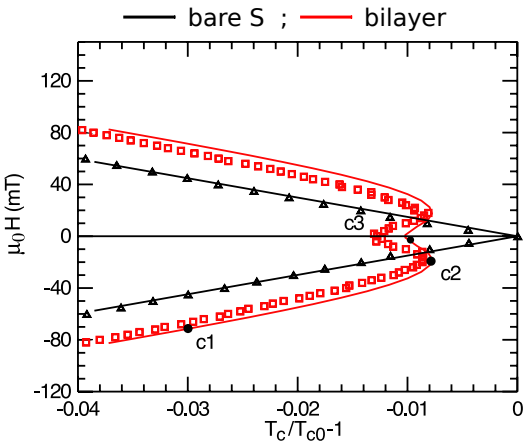

(b) (T_c,H) diagram in $Nb/(Co/Pd)_{10}$ [159]

Figure 2.14: **Domain-wall superconductivity in experiments**
At low fields, superconductivity is confined below the walls (DWS). At higher values, the external field compensates the stray-field below the opposite domains, leading to domain superconductivity (DS) and re-entrance effects.

negative, combined vortex/domains arrangements could even appear spontaneously due to instability[161].

Induced chains of vortices in bilayers were already observed by magnetic force microscopy (MFM) [46, 162]. As shown in Fig.2.15b, stable vortex/anti-vortex pairs are induced in Nb by the demagnetizing field of stripe domains in a permalloy (Py) layer.

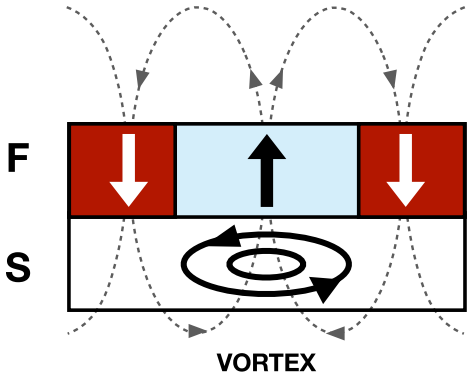

(a) Coupled vortex/domain

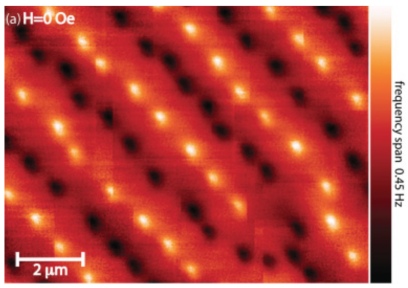

(b) Vortices on stripes in NiFe/Nb [46]

Figure 2.15: **Coupled vortices and magnetic domains**
*Vortices nucleate and lie preferably below the domains with **M** parallel to the flux 2.15a. Induced (or pinned) vortices may form chains on top (2.15b, MFM image).*

Pinning on magnetic domains

The stray field also influences the vortex motion through pinning [163, 156]. This is either due to a local reduction of the order parameter (similarly to DWS), or through magnetic pinning of the flux. Vortices will preferably go below domains of the same polarity due to the stray magnetic fields. The arguments for that are the same as for nucleation, as discussed Sec.2.3.2.

Consequently, the presence of magnetic domains creates vortex pinning. It enhances the critical current in the mixed state, as compared to that when the magnetic layer is saturated (single domain). This was observed in conventional superconductors [48, 164, 165, 51] as well as high-temperature ones [166, 167, 47]. If the applied field is strong enough to affect the domain structure, the pinning potential then becomes field-dependent. It makes the critical current and the magneto-resistance hysteretic, as in Fig.2.16a. In these curves, the resistance is lower in the presence of domains than when the sample is saturated. One also observes a resistance increase with in-plane fields, due to vortex nucleation by the stray fields.

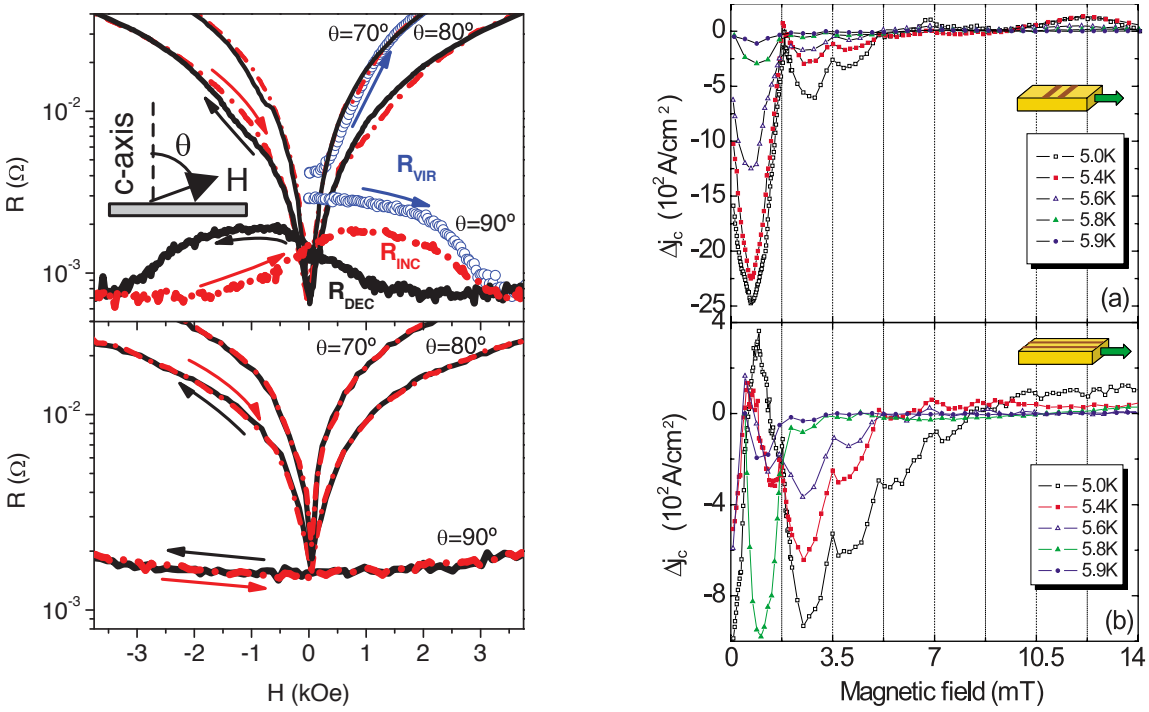

(a) Hysteresis in YBCO-$(Co/Pt)_5$ (b) Matching effects in MoGe/NiFe

Figure 2.16: **Hysteresis and matching effects in SF bilayers**
Figure (a) adapted from Visani [47] and (b) from Belkin [51].

The physics behind pinning on domains are the same as those with magnetic dots [110], despite the very different fabrication. Dots offer many possible configurations as their arrangement, shape and size are set by lithography. Geometrical effects like matching fields are usually strong in these [168, 169]. On the other hand, dot arrays

are not as reconfigurable as plain layers, in which the domain size and shape can be changed or erased [165, 164, 44, 47, 170].

However, as the domain structures are less ordered, geometrical effects in plain bilayers are much weaker than with arrays of dots [163]. Still, they are observed when the densities of domains and vortices match in the case of isolated bubbles [48], or parallel stripes [51, 164, 171]. In the latter case, the pinning force becomes anisotropic [172]. It is higher across the stripes than parallel, due to *guided motion* along the walls. As shown in Fig.2.16b, weak matching effects were observed when the periodicity of the vortex lattice and the stripes are commensurable, in both orientations.

2.4 Proximity effect and tunneling into superconductors

Another kind of interaction occurring at the interfaces with normal materials is the *proximity effect*. Originally defined as a "leakage of Cooper pairs" in the normal region [173], it results in the weakening of superconductivity at the interface, and the propagation of superconducting correlations into the normal side. In this section, we review the core concepts of proximity effect, and tunneling from normal materials into superconductors. We emphasize on *d-wave* superconductors, as they are the subject Chap.4.

2.4.1 Proximity effect and Andreev reflection

At the interface of a normal-superconductor (NS) bilayer, the phenomenon that governs the conversion of currents from normal to superconducting is the *Andreev reflection* [173]. It is sketched in Fig.2.17a. In that process, a normal electron with an energy below the gap enters the superconductor at an angle θ_i. As there are no quasi-particles states within the gap (at least at zero temperature), it has to pair with another electron. This leaves behind a hole excitation, with opposite spin and momentum as the incoming electron. That hole is then rejected into the normal side at an angle $\theta_r = \theta_i$, due to momentum conservation. A frequent picture is that the electron is "reflected as a hole".

Until scattering occurs, that hole remains phase coherent with the paired electron. Hence, it propagates superconducting correlations in the normal side, despite the absence of a pairing interaction there. This is called the *proximity effect*. These correlations decay over a coherence length ξ_N in the normal material. It is defined as $\sqrt{\hbar v_F/k_BT}$ in a clean superconductor, and $\sqrt{\hbar\Gamma/k_BT}$ in a diffusive one, where Γ is the diffusion coefficient. Note that if the thermal scattering k_BT is not the dominant scattering energy, one has to replace it in the formula by the highest one available [173, p.599]. On the superconducting side, the order parameter is also weakened over the superconducting coherence length ξ. Nevertheless, it occurs only if the interface is transparent. If there is scattering, proximity effect and Andreev processes are inhibited.

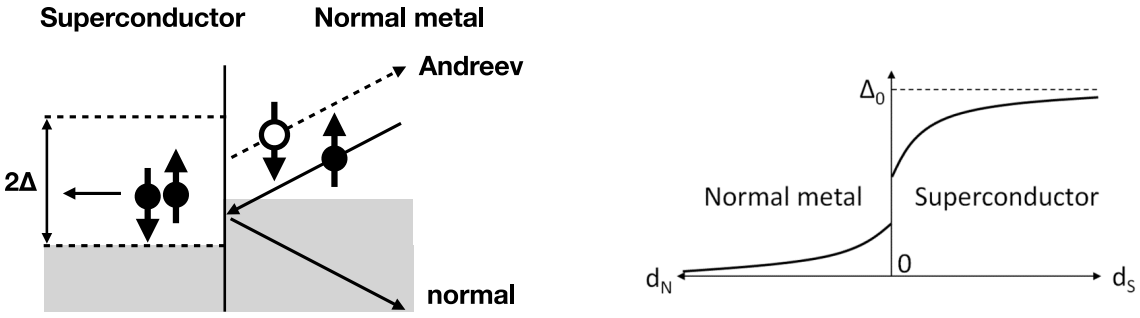

(a) Andreev reflection (b) Proximity effect

Figure 2.17: **Andreev reflection and proximity effect**
Normal electrons are converted into a Cooper pair and a reflected hole at the interface due to the Andreev reflection (2.17a). The reflected hole propagates superconducting correlations in the normal side (proximity effect, 2.17b).

2.4.2 Tunneling into superconductors

In that section, we review the effect of interface transparency on the conductance of a normal-superconductor contact. We first present the theory in the case of conventional superconductors, then the more specific case of *d-wave* materials.

Conductance of a Normal-Superconductor contact

In the case when the interface is not perfect, normal scattering occurs and inhibits the Andreev processes. The resulting differential conductance was calculated by Blonder, Tinkham and Klapwijk (BTK) [174]. They considered, in addition to the Andreev process, the normal reflection due to impurities at the interface and the transmission of quasiparticles above the gap energy.

By modeling an infinitely thin barrier located at the NS interface, then matching the incident, reflected, and transmitted wave functions at the interface, they obtained the differential conductance of the junction in the form of Eqn.2.15. In that formula, A and B are respectively the probabilities of Andreev and normal reflection, and G_N the normal state conductance. The transparency of the contact is modeled by the parameter Z, which goes from transparent ($Z = 0$) to opaque (tunnel regime, $Z \gg 1$). The exact expressions of A and B will not be detailed here, but are found in [174].

$$\frac{dI}{dV} = G_N \left[1 + A(eV, Z) - B(eV, Z)\right] \tag{2.15}$$

If the interface is transparent, the conductance is doubled below the gap. This is due to Andreev reflection, that "converts" a current e into $2e$. Conversely, scattering favors normal reflections and reduces the conductance. For an insulating contact, we retrieve the BCS density of states, as expected for a tunnel barrier.

A limitation of the BTK model is that it does not consider the band structure in the normal metal, and is formulated at zero temperature. However, it is easily

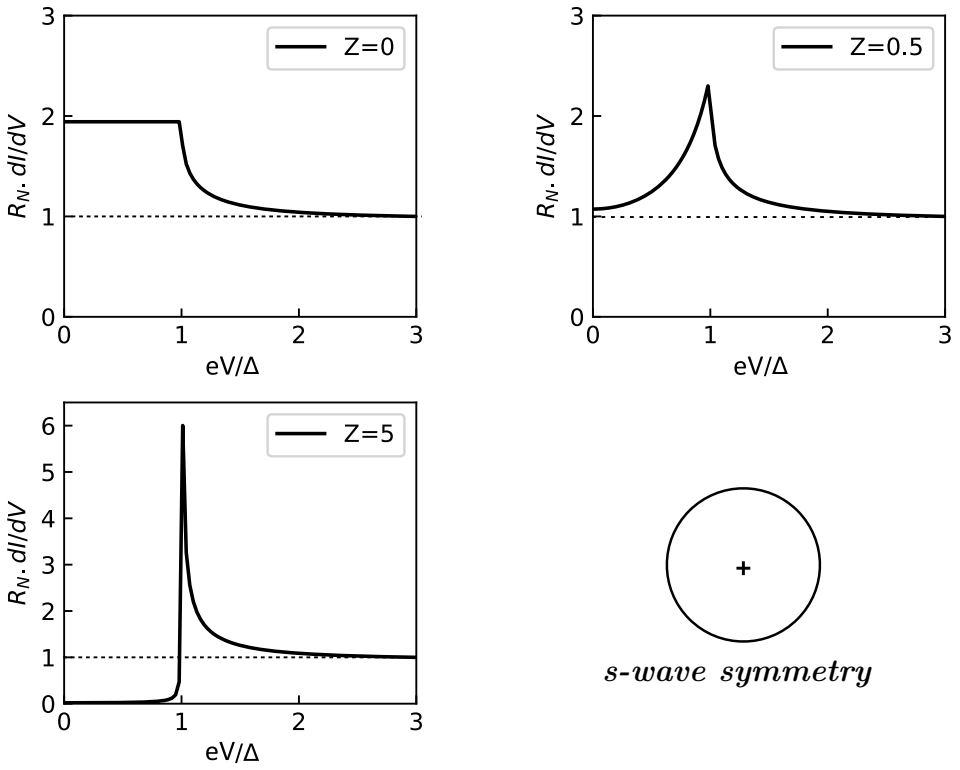

Figure 2.18: **Normal metal-superconductor contact (s-wave)**

adaptable to various situations like finite temperatures [175], finite quasiparticle lifetimes [176], or *d-wave superconductors* [177]. The latter case being relevant to the present thesis, we discuss it in more detail hereafter.

Tunneling into *d-wave* superconductors

Following the discovery of HTSC, several experiments tried to figure out the pairing symmetry in these through tunneling experiments [175]. This motivated the development of a theory for tunneling into $d_{x^2-y^2}$-wave superconductors. Unlike *s-wave* superconductors that have a spherical symmetry, those with *d-wave* symmetry like in $YBa_2Cu_3O_7$ have highly anisotropic orbitals. These are sketched in Fig.2.19 (see Sec.3.2.2 for the crystalline structure). This also makes the gap anisotropic : it is maximum along the *a-axis*, and vanishes along the diagonal direction. The gap then writes as in Eqn.2.16, where θ is the incidence angle of the electron with the *a-axis*.

$$\Delta(\theta) = |\Delta| \ \cos(2\theta) \tag{2.16}$$

To account for the various available tunneling data, Kashiwaya and Tanaka developped an extension of the BTK model to include the anisotropy [177, 178]. The general result can still be written in the form of Eqn.2.15, but the coefficients become dependent on the orientation of the interface relative to the crystalline axes. Also, due to the gap node along the diagonal of the *a-b* plane, bound states may form at the NS interface [179]. These states form in the barrier whenever the quasiparticles

have a momentum component along the nodal direction. They are called *Andreev bound-states*, and often lead to zero-bias conductance peaks (ZBCP) in the tunneling spectra [175].

In the case of *c-axis* tunneling, electrons can be injected with any momentum component in the (a, b) plane [180]. Consequently, the tunneling DOS has to be integrated over θ. This yields the tunneling spectra of Fig.2.19. In the high Z limit, it gives a v-shaped gap, which corresponds to the bulk material DOS. ZBCP can also occur in *c-axis* tunneling if there is a step defect on the surface [175], and are enhanced for a diffusive interface [181].

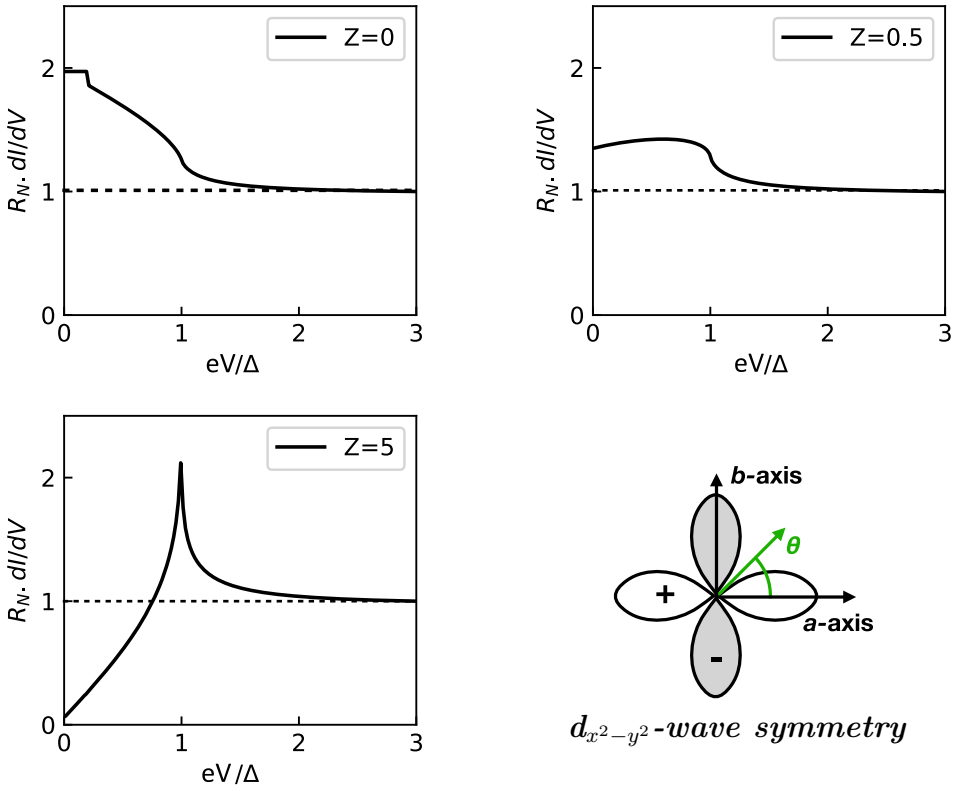

Figure 2.19: **NS contact conductance ($d_{x^2-y^2}$-wave, *c-axis* tunneling)**

2.4.3 SNS junctions

In the case of an SNS junction with a normal barrier shorter than its proximity effect length, coherence effects are frequently observed. Due to Andreev reflection, several resonances or subgap harmonic peaks due to coherence effects may be observed. These are described in Sec.2.4.3, 2.4.3 and 2.4.3. In addition to that, if the NS interfaces are clean enough, a superconducting current may propagate through the normal metal by proximity effect. This leads to the Josephson effect, which is presented in Sec.2.4.4.

Multiple Andreev reflections

Given that the two NS interfaces of an SNS junction are clean enough, quasiparticles in the barrier may be repeatedly Andreev-reflected from one side to the other. These resonances are *multiple Andreev reflections*, and lead to sub-gap peaks in the conductance of the junction. The positions of the peaks are given by Eqn.2.17, where n is a positive integer[182].

$$eV = \frac{2\Delta}{n} \quad ; \quad n \in \mathbb{N} \tag{2.17}$$

Tomasch resonances

In tunneling experiments on a superconductor in contact with a normal metal, quasiparticles in the superconducting layer may be scattered back from the interface if there are local inhomogeneities of the gap (due to impurities for example[183]). Since quasiparticles in superconductors have mixed electron-hole properties, the incident and reflected waves can interfere. This leads to conductance oscillations called *Tomasch resonances*[34, 35]. The process is sketched in Fig.2.20a. The position of the peaks are given by Eqn.2.18, where v_s is Fermi velocity in the superconductor. Each peak indexed by n corresponds to an interference after n round-trips across the superconductor thickness (hence the $2d_s$ dependency).

$$V_n = \sqrt{\Delta^2 + \left(\frac{nhv_s}{2d_s}\right)^2} \quad ; \quad n \in \mathbb{N} \tag{2.18}$$

(a) Tomasch resonance (b) McMillan-Rowell resonance

Figure 2.20: **Interference effects in SNS junctions**

McMillan-Rowell resonances

Another type of quasiparticle interference called *McMillan-Rowell resonances* can occur in the normal layer of a NS or SNS junction [38]. It is due to Andreev reflection, and is sketched in Fig.2.20b. Due to Andreev reflection, an electron incident to an

NS contact can be "reflected" as a hole, and propagates back to the other side. Given that the interface there is reflective, it will be deflected towards to the superconductor, and undergo Andreev reflection again. That second process gives an electron that propagates back, and can interfere with the original incident electron. In total, it requires two round trips in the normal metal, since electrons and holes do not interfere there. These also yield oscillating patterns in the conductance, with a periodicity ΔV given by Eqn.2.19, where v_n and d_n are respectively the Fermi velocity and thickness of the normal metal.

$$\Delta V = \frac{h v_n}{4 d_n} \tag{2.19}$$

2.4.4 Josephson effect and junctions

In the case of an SNS junction in which the barrier is shorter than ξ_n, the Andreev-reflected hole and paired electron stay phase-coherent across the junction. Consequently, a superconducting current flows through the normal metal interlayer [184]. The metal is then called a *weak link*, and the trilayer a *Josephson junction*. Weak links in general are regions in which superconductivity is weakened. That includes proximitized materials, weaker superconducting interlayers, or even a simple constriction in a wire.

Below the Josephson temperature $T_j < T_c$, a resistanceless current can flow through the junction, as shown in Fig.2.21b. Above the *critical current* of the junction I_c, it becomes ohmic (normal). That critical current depends on the macroscopic phase difference $\phi_1 - \phi_2$ between the two superconducting reservoirs, and writes as in Eqn.2.20.

$$I_s = I_c \sin(\phi_1 - \phi_2) \tag{2.20}$$

This is the *DC Josephson effect*. An applied magnetic field in the barrier will also affect that phase difference. Consequently, the critical current oscillates as a function of the number of flux quanta Φ/Φ_0 in the junction, as in Eqn2.21. That pattern is often called the *Fraunhofer pattern* of the junction [63, p.216], as it resembles that of optics. It is represented in Fig.2.22a.

$$I_s^{max} = I_c \left| \frac{\sin(\pi\Phi/\Phi_0)}{\pi\Phi/\Phi_0} \right| \tag{2.21}$$

Another effect occurs when the junction is biased in voltage. The phase difference in the junction becomes time-dependent following $d\phi/dt = 2eV/\hbar$. It results in oscillations of the Josephson current in time at a frequency $2eV/h$. This is the *AC-Josephson effect*. As it is independent of the junction characteristics, that effect is used in metrology to define the Volt standard [185]. In a Josephson junction irradiated with microwave photons of frequency f, the DC current-voltage curve will exhibit voltage steps separated by $\Phi_0 f$. These are *Shapiro steps* [186], that occur due to the coupling of the superconducting currents with the microwaves. A typical step pattern is shown in Fig.2.22b. The Fraunhofer pattern and Shapiro steps are

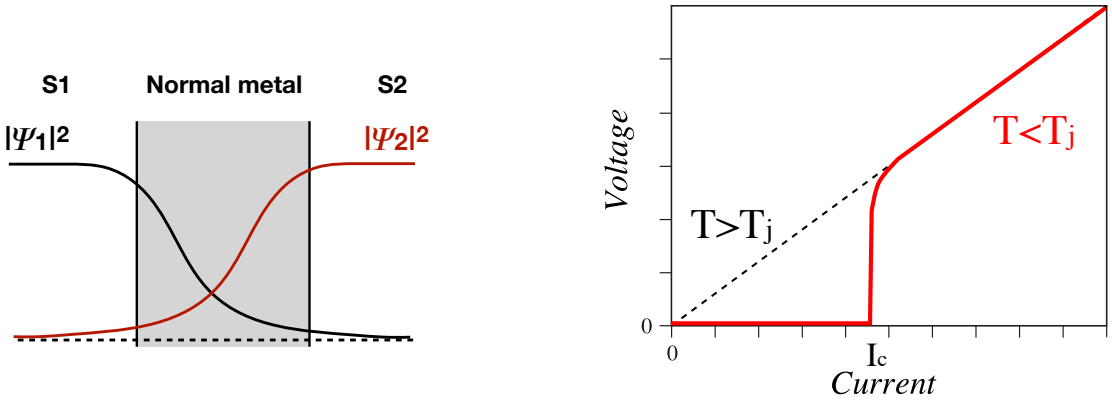

(a) Josephson junction (b) I-V curve of a Josephson junction

Figure 2.21: **Josephson junction and IV curve**

usually the two hallmarks of a Josephson behavior. These junctions are the basic blocks of superconducting circuits, the most well-known application being SQUID magnetometers.

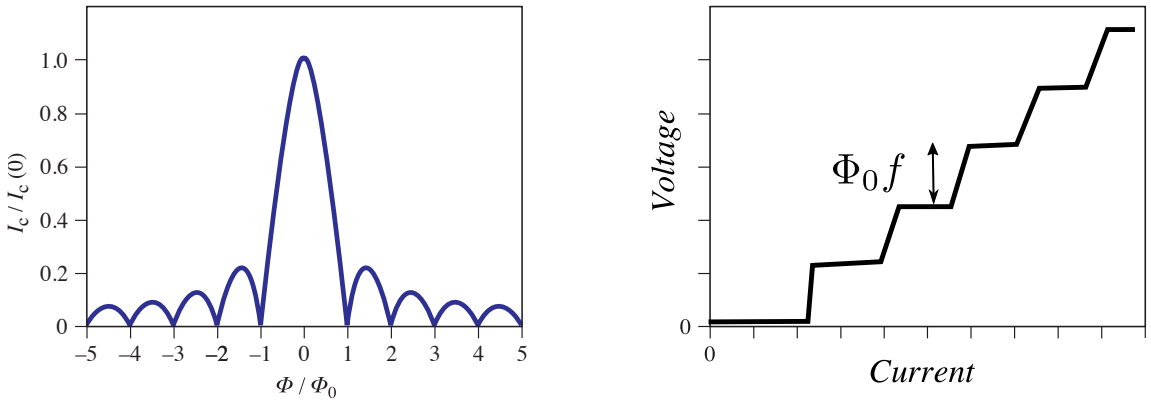

(a) Fraunhofer pattern [187] (b) Shapiro steps [188]

Figure 2.22: **Fraunhofer pattern and Shapiro steps**

2.5 Proximity effects with ferromagnets

2.5.1 Singlet proximity effect in ferromagnets

In the case of a ferromagnet/superconductor contact, superconducting correlations penetrate over approximately $\xi_f = \hbar v_f / 2\epsilon_{ex}$ (or $\sqrt{\hbar\Gamma/2\epsilon_{ex}}$ for diffusive materials), where v_f is the Fermi velocity in the ferromagnet, and E_{ex} the exchange energy. That length is only a few nanometers in weak ferromagnets, and even less for stronger materials. This is much shorter than in non-magnetic metals, where they can reach a few 100 nm for noble metals [189]. Thus, proximity effect is often inhibited in ferromagnets.

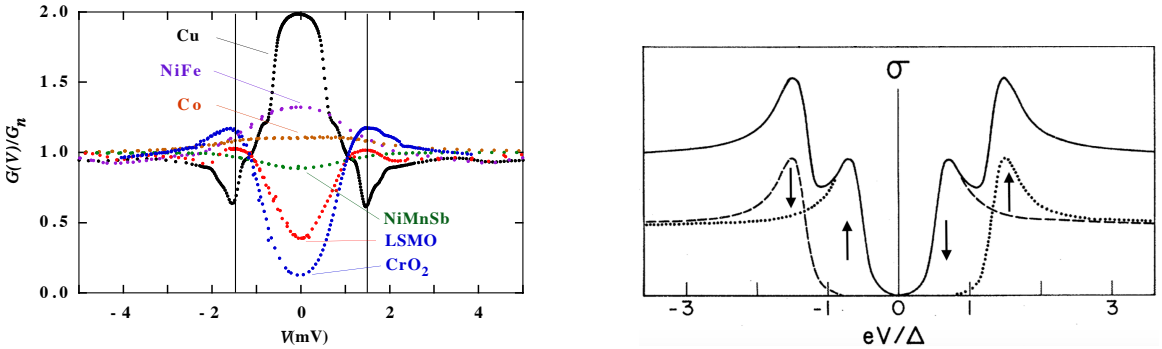

(a) Andreev inhibition [190]

(b) DOS splitting [191]

Figure 2.23: **Conductance of an S/F interface**
Andreev features are reduced proportionally to the spin polarization of F. The DOS peaks seen in tunneling are splitted due to exchange.

Andreev reflection at the interface also reduces with the increase of spin polarization in the ferromagnet [190]. This is due to the lower density of states for the minority spin, which limits the process. As represented in Fig.2.23a, the conductance curves go from well developed Andreev features in Cu (non-magnetic, $P = 0$) to a tunneling regime for half metals like LSMO and CrO_2 ($P \approx 1$). Thus, it is a possible method to assess the the spin polarization, given that the contact is clean. In the case of an opaque interface, the spin-splitting in the ferromagnet also affects tunneling in superconductor. The DOS peaks become splitted (dotted and dashed lines in Fig.2.23b), leading to multiple peaks in the tunneling conductance (plain line). This may be used to quantify the exchange splitting in the ferromagnet [191].

These phenomena describe homogeneously magnetized ferromagnets, though. The presence of a domain-wall in the ferromagnet may allow Andreev reflection locally (*cross-Andreev reflection* [192]). In addition, we considered only "conventional" singlet pairing. Triplet states may also form at the interface, and strongly change how proximity effect occurs in the ferromagnet. These states are one of the subjects of the present thesis, and are covered in the following sections.

2.5.2 The triplet state

Until now, we only considered the proximity effect with *singlet* pairing symmetry $\uparrow\downarrow - \downarrow\uparrow$, which is the conventional pairing of superconductivity. However, in proximity with a ferromagnet, other symmetries may appear due to inhomogeneities of the magnetization at the interface. As proposed by Bergeret [19], BCS theory only requires the overall parity of the pair to be odd. This allows the following pairing symmetries :

- $s_z = 0$ singlet : $\uparrow\downarrow - \downarrow\uparrow$, even momentum and frequency
- $s_z = 0$ triplet : $\uparrow\downarrow + \downarrow\uparrow$, even momentum, odd frequency
- $s_z = \pm 1$ triplet : $\uparrow\uparrow$ or $\downarrow\downarrow$, odd momentum, even frequency

The first one is the usual *singlet* pairing of BCS. The other two are called *triplet states*, and may appear at the interface between superconductors and ferromagnets. Due to the exchange splitting, the penetrating pairs acquire a finite momentum $Q = k_\uparrow - k_\downarrow \neq 0$. This turns superconductivity into a mix of singlet and spin-zero triplet at the interface. The singlet to triplet conversion is represented in Eqn.2.23 [193].

$$\uparrow\downarrow - \downarrow\uparrow \quad \longrightarrow \quad \uparrow\downarrow e^{i\mathbf{Q}.\mathbf{R}} - \downarrow\uparrow e^{-i\mathbf{Q}.\mathbf{R}} \tag{2.22}$$

$$= \quad (\uparrow\downarrow - \downarrow\uparrow)\cos(\mathbf{Q}.\mathbf{R}) + i(\uparrow\downarrow + \downarrow\uparrow)\sin(\mathbf{Q}.\mathbf{R}) \tag{2.23}$$

The spin-zero triplet is also called the *FFLO* state (Fulde,Ferrell [194] and Larkin, Ovchinnikov [195]). If the material is insulating or strongly spin-polarized, spin-scattering at the interface provides the required phase shift to form FFLO pairs. This is the *spin-mixing* mechanism. Notice that the phase of both singlet and zero-spin triplet pairs depends on the position in Eqn.2.23. Away from the interface, it is inhomogeneous and oscillates in space (see Fig.2.24a). Additionally, they are vulnerable to exchange, and decay exponentially in the ferromagnetic side.

The spin-parallel triplets appear if the magnetization at the interface is misaligned with respect to that in the bulk of the ferromagnet. Due to that, the quantization axis of the spin changes, and the new projection of the FFLO pairs is a mix of the zero-spin component and the equal spin triplets. The latter being also favored by exchange, they propagate over ranges comparable to those in a non-magnetic material. For that reason, they are called *long-range triplet correlations* (LRTC).

If the ferromagnet is strongly spin-polarized, FFLO pairs do not propagate beyond the interface as ξ_f is atomically short. Nevertheless, the formation and propagation of equal-spin triplets occurs through *spin-flip Andreev reflection* [196, 197]. The mechanism is the same as the conventional Andreev process, but includes a spin-flip event in the interface region. As the reflected particle has the same spin as the incident one, it is allowed to propagate in the ferromagnet. Hence, proximity effect occurs like in non-magnetic materials, as sketched in Fig.2.24b.

Spin-parallel triplets have been observed in several classes of materials, including half-metallic oxides like CrO_2[22] or manganites such as $La_{0.7}Ca_{0.3}MnO_3$ [26, 30], and strong ferromagnets like Co [23]. A schematic of the pairing states present at the interface is provided in Fig.2.24a. In that figure, one can see the short-ranged decay of singlets and FFLO amplitudes, whereas equal-spin triplets propagate over much longer ranges. Since pairing for equal spins can happen without a finite pair momentum, these do not oscillate in space.

2.5.3 π-Josephson junctions

In the previous section we saw that, due to spin splitting, singlet and FFLO pairs (with spin zero) acquire a finite momentum when entering the ferromagnet. This causes the phase of the superconducting order parameter to oscillate in space, depending on the distance away from the interface (see 2.24a). Hence, if there is a second superconducting material on the other side, a natural phase difference will

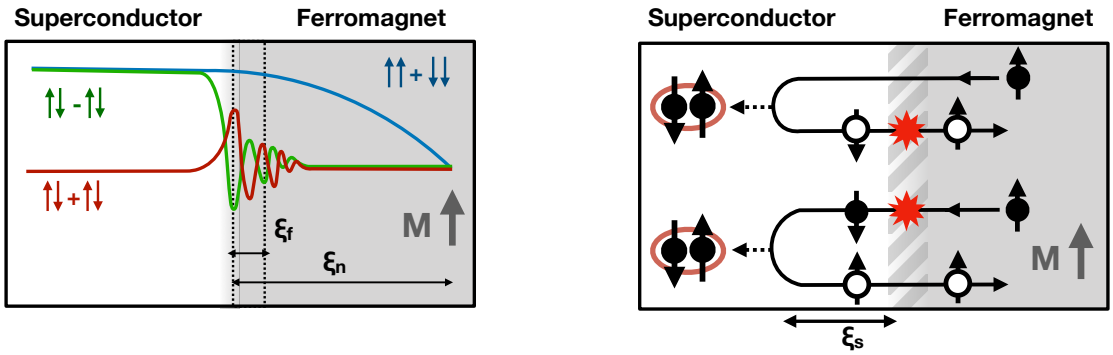

(a) Pairing at SF interfaces [78]

(b) Spin-flip Andreev reflection [197]

Figure 2.24: **Proximity effect in SF hybrids**
Triplets form at the interface, but do not propagate far unless they are spin-parallel (2.24a). If the contact is spin-active, spin-flips allow Andreev reflections (2.24b).

appear between the two superconductors. This makes a Josephson junction, with a built-in phase difference due to the ferromagnetic interlayer. As shown in Fig.2.25a, that phase shift depends on the thickness of the ferromagnet d_f, and can be made to π by choosing d_f adequately. Such a device is called a π-*Josephson junction*, and differs from the conventional junctions of Sec.2.4.4, that have no phase difference in absence of a magnetic field. In addition to the thickness, the $0-\pi$ transition can be triggered with the temperature, as shown in Fig.2.25b. At the transition, the critical current of the junction vanishes, then becomes *negative* in the π state. It is not visible on the figures, since conventional measurements are not sensitive to the sign of I_c.

The $0-\pi$ transition was demonstrated in 2001 by Ryazanov [14] in Nb/CuNi/Nb junctions. The phase shift also leads to a reversal of the junction conductance, as shown later by Kontos [15]. In addition, other works have shown that such a junction leads to spontaneous currents when placed in a superconducting ring [198, 199], or half-integer Shapiro steps [200].

In superconducting circuits, π-junctions could be used to perform logic and memory functions in superconducting circuits [16]. Nonetheless, using FFLO correlations for applications is restrictive. It requires to precisely control the thickness of the magnetic material, as the latter dictates the phase difference across the junction. That constraint is manageable only in weak ferromagnets, in which the coherence length ξ_f is already as short as 10nm. Stronger ferromagnets are excluded, since ξ_f drops to a nanometer or below in these materials. An alternative is to use the equal-spin triplets, which are long ranged (up to a few 100nm), and can provide a phase difference as well. On the other hand, their generation is governed by the magnetism at the interface, which is often delicate to characterize and control. We discuss these in the next section.

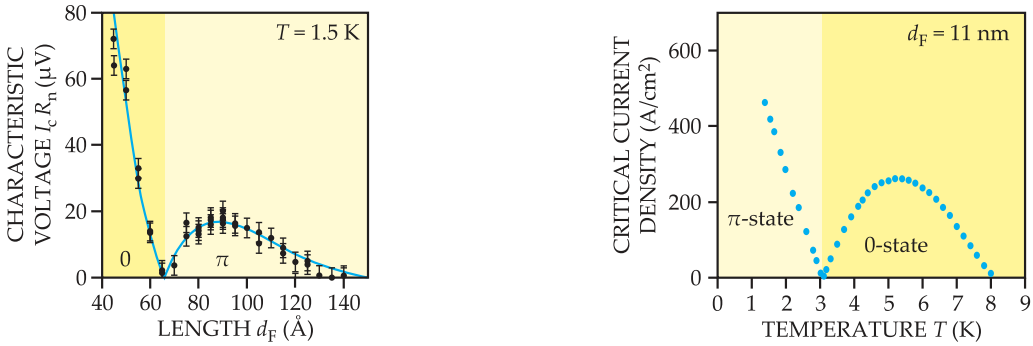

(a) Critical current modulation [201]

(b) Temperature dependence [14]

Figure 2.25: **π-Josephson junction characteristics**
The critical current cancels at the frontier between the 0 and π states. The latter can be achieved by adjusting the ferromagnet thickness d_f, and then switched using the temperature. Figures taken from [78].

2.5.4 Equal-spin triplets devices

Using LRTC instead of FFLO states in Josephson junctions has two immediate advantages. First, they are equal-spin correlations that are not broken by ferromagnetic exchange. Thus, they can propagate over a few 100 nm, even in strong ferromagnets or half-metals. This relaxes the thickness and materials requirements, as compared to the junctions described in Sec.2.5.3. Second, they carry currents that are both *superconducting* and *spin-polarized*. The latter property enables to use spintronic effects like GMR and spin-transfer torque, while conserving the advantages of superconductivity. On the other hand, their generation is governed by the magnetism at the interfaces.

Forming LRTC requires the presence of *magnetic inhomogeneities* at the S/F interface (see Sec.2.5.2 and Ref.[19]). In a Josephson junction, these inhomogeneities must be present on both sides of the magnetic barrier to propagate a superconducting current. A sketch is presented in Fig.2.26a, where inhomogeneities are represented as thin ferromagnetic layers at the interfaces. Tilting their magnetization with respect to that of the thicker middle layer triggers the formation of LRTC. Interestingly, the angle between the interface magnetic moments on both sides of the ferromagnetic layer also influences the Josephson effect. It adds a phase difference across the junction, that goes from 0 (anti-parallel) to π (parallel) [196, 202]. This makes LRTC Josephson junctions good candidates for making π-junctions [203], especially if one manages to control the orientations of the bulk and interface moments separately. These differ from the FFLO-based devices of Sec.2.5.3, as the phase difference here becomes independent of the temperature and the interlayer thickness.

Up to now, we have not considered the nature of the interfacial magnetic inhomogeneities. These may form spontaneously in some materials, for example at NbTiN/CrO2 interfaces [22], or between $YBa_2Cu_3O_7$ (YBCO) and $La_{0.7}Ca_{0.3}MnO_3$ (LCMO) [26, 41]. However, in this case, it is often hard to characterize the nature of these inhomogeneities, which may limit the reproducibility of the devices [24].

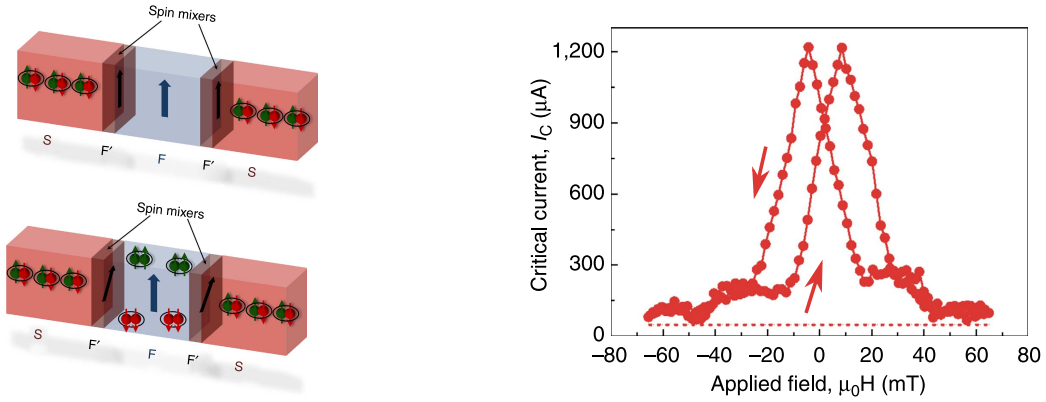

(a) SFS junction with spin-mixers

(b) Fraunhofer pattern of the device

Figure 2.26: **Critical current modulation in SFS with spin-mixer** [204] *Nb/Py/Cu/Co/Cu/Py/Nb Josephson junction. Thin permalloy (Py) layers provide the magnetization inhomogeneity, and Co the "bulk" magnetization. I_c is enhanced when triplets are generated (misaligned magnetizations).*

To circumvent that issue, Houzet and Buzdin proposed to introduce them artificially [205]. Their design is represented in Fig.2.26a, where the inhomogeneity is introduced using thin ferromagnetic layers decoupled from a thicker central layer. These interface layers are called *spin-mixers*, and can consist of weak ferromagnets like permalloy [204] or CuNi [23], as well as conical magnets like holmium [206, 25]. In this, the orientation of the mixers is controlled with an external magnetic field, as shown in Fig.2.26b for a Nb/Py/Cu/Co/Cu/Py/Nb junction. It triggers the creation of LRTC, leading to magnetic hysteresis appearing in the critical current. The phase difference across the junction could also be controlled, if the orientation of the mixers can be changed independently.

Alternative designs are possible as well, like using FNF or FSF spin-valves [207, 208, 189]. These function more like the conventional spin-valves of spintronics (see Sec.2.2.3), as the triplet superconducting current is switched by the relative orientation of the magnetization in the two ferromagnetic layer. It might be simpler to implement than the double spin mixers in systems like heterostructures of YBCO and LCMO, where introducing multiple spacing layers is more complicated because of crystalline matching constraints.

Chapter 3

Materials and Methods

3.1 Introduction

In this chapter, we introduce the materials and devices used in the following experimental chapters. We first review the properties of the different superconductors (Sec.3.2) and ferromagnets we have employed (Sec.3.3), along with experimental characterizations when these are available. We then review the devices and their fabrication steps (Sec.3.4).

3.2 Superconductors

3.2.1 Amorphous MoSi

Molybdenum silicide ($Mo_{1-x}Si_x$) is an amorphous superconductor in which the superconducting properties can be tuned with the silicon concentration of the alloy. It is interesting for extrinsic vortex pinning experiments as it is strongly type-II ($\kappa_{bulk} \approx 70$) and has low intrinsic vortex pinning ($F_p \approx 10^8$ N·m^{-3} at 4.2 K). It can be deposited on various materials due to its amorphous structure and a relatively high critical temperature ($T_c \approx 7$ K) compared to other amorphous superconductors [57, 209].

It is deposited by DC sputtering at room temperature, on Si(001) substrates. To calibrate the deposition, we deposited several MoSi thin films on Si(001) substrates with different concentrations. The concentration is tuned by placing silicon shards on a molybdenum target, and then measured using energy-dispersive X-ray spectroscopy (EDX). We verified that the films were amorphous using X-ray diffraction, in which only the substrate peaks were observed.

We then patterned the samples to measure the resistivity (see Sec.3.4.1). We deposited 60nm films,and measured their exact thickness by reflectometry. We also measured the critical temperature and upper critical field H_{c2} by measuring the temperature and field evolution of the resistance in a He-flow cryostat, with fields up to 7 T.

In Fig.3.1a, we present measurements of the critical temperature for the calibration samples. In that curve, the samples are superconducting for concentrations starting

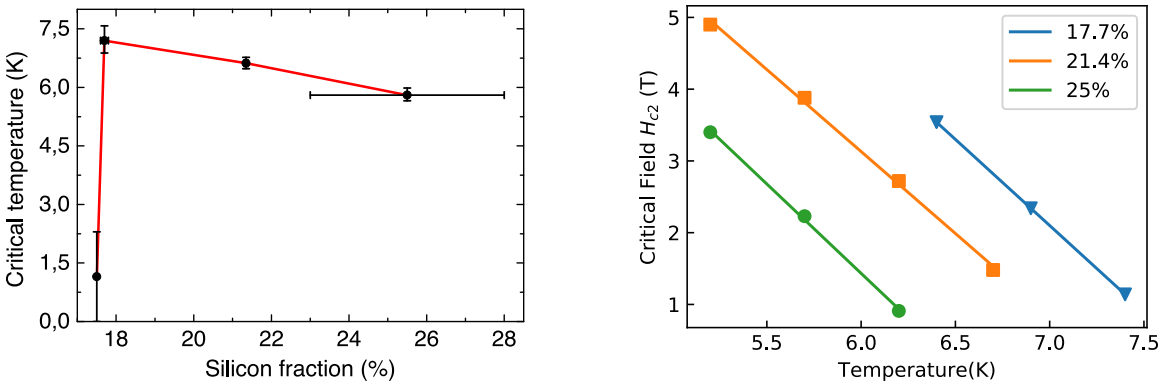

(a) Critical temperature (b) Upper critical field

Figure 3.1: **Measured transition temperature and critical field of $Mo_{1-x}Si_x$** *Error bars show the standard deviation for each set of T_c measurements in y, and the estimated error on concentration in x, by EDX for all the points but the 25% one, which is qualitative.*

from 17.7%. In that range, T_c steadily decreases when the silicon concentration increases, up to 25% which is the highest we measured. At 17.5%, superconductivity breaks down and T_c is below 1.5 K. At that temperature, we observed the onset of the transition, but couldn't go lower to see the end. For the samples that were superconducting, we measured the upper critical field H_{c2} (Fig.3.1b) with magneto-resistances. The fields were applied perpendicularly to the samples. We defined it with the criterion $\rho(H_{c2}) = 0.9\rho_N$, where ρ_N is the normal-state resistivity. For all concentrations, H_{c2} decreases linearly with the temperature, as expected. We fitted the data with GL formulas [63, Chap.4] and the expected dependency of λ_{bulk} in the strong diffusive limit [57] (respectively Eqn.(3.1a) to (3.1c) and Eqn.(3.1d)). The extrapolated values at zero temperature are summed up in Tab.3.1. It is important to note that these values are fitting parameters, as GL theory is valid only close to T_c. However, they are useful for qualitative comparison, and for interpolation at a temperature close to the transition.

$$\xi = \sqrt{\frac{\Phi_0}{2\pi H_{c2}}} \tag{3.1a}$$

$$H_{c1} \approx \frac{\Phi_0}{4\pi\lambda^2}\ln(\lambda/\xi) \tag{3.1b}$$

$$H_{c2}(T) = H_{c2}(0)(1 - T/T_c) \tag{3.1c}$$

$$\lambda[\mathrm{cm}] = 6.42 \times 10^{-3}\sqrt{\frac{\rho_N[\Omega.\mathrm{cm}]}{T_c}}\,(1 - T/T_c)^{-1/2} \tag{3.1d}$$

We later bought a sputtering target for the $Mo_{0.8}Si_{0.2}$ composition (Mo_4Si for simplicity), as it offers a high enough T_c without being too close to the breakdown concentration. Its estimated properties are summed up in the bottom line of the table. Overall, the properties that we obtain are comparable to those found in the

x_{Si} (%)	T_c (K)	$\xi(nm)$	$\lambda(nm)$	ρ_N (Ω·cm)	$\mu_0 H_{c1}(mT)$	$\mu_0 H_{c2}(T)$	κ
17.7	7.8	4.2	306	1.78×10^{-4}	7.6	18.9	73
21.4	7.2	4.4	291	1.48×10^{-4}	8.1	16.8	65
25	6.5	4.5	335	1.77×10^{-4}	6.4	16.4	74
20.0 (target)	6.5	4.4*	183	5.28×10^{-5}	7.9*	17.3*	42

Table 3.1: **Superconducting properties of bulk Mo_4Si extrapolated at T=0 K** *The first three rows are the calibration samples, the fourth is the commercial target. The values marked by an asterisk were interpolated from the calibration samples data.*

literature [57, 209, 210]. As confirmed by the values of $\kappa = \lambda_{bulk}/\xi$, the material is a strong type-II superconductor.

3.2.2 High-temperature superconductor $YBa_2Cu_3O_7$

$YBa_2Cu_3O_{7-\delta}$ (YBCO) is a *high-temperature* superconductor of the *cuprate* family. Its critical temperature is dependent on the oxygen deficit δ, and ranges from 0 up to 92 K for *optimally doped* samples ($\delta = 0.08$). It grows in an orthorhombic structure as shown in Fig.3.2a. That material is promising for applications as it is superconducting at the temperature of liquid nitrogen (77 K), which is easier and much cheaper to produce than liquid helium.

The crystal structure of YBCO is anisotropic, and so is superconductivity in the material. The superconducting gap depends on the orientation of propagation for the Cooper pairs. It is maximal along the *a,b - axes* and vanishes completely along the diagonal [178]. Superconducting currents propagate in the CuO planes and tunnel from plane to plane along the *c-axis* direction.

(a) **YBCO unit cell** [211] (b) **LCMO unit cell** [212]

Figure 3.2: **Unit cells of YBCO and LCMO**

YBCO layers are deposited by sputtering by our collaborators of *Universidad Complutense de Madrid* (D.Sanchez and F. Cuellar), on $SrTiO_3(100)$ (STO) substrates. We preferred their samples instead of homegrown YBCO because of their

controlled and widely characterized interfacial properties in heterostructures (see Sec.3.3.1). In Tab.3.2, we sum up some superconducting properties of optimally doped YBCO, which is the composition used in our samples.

T_c	$B_{c1,ab}$	$B_{c2,ab}$	ξ_{ab}	λ_{ab}
92 K	8.9 mT	850 T	1.6 nm	135 nm

$B_{c1,c}$	$B_{c2,c}$	ξ_c	λ_c	v_F
50 mT	130 T	0.24 nm	894 nm	$4-5\times10^5$ m·s^{-1}

Table 3.2: **Superconducting properties of YBCO (T=0 K)**
The values are taken from Ref. [213], aside from the Fermi velocity and gap that were estimated from Refs. [27, 214].

3.3 Ferromagnets

3.3.1 Half-metallic $La_{0.7}Ca_{0.3}MnO_3$

$La_{0.7}Ca_{0.3}MnO_3$ (LCMO) is a half-metallic oxide that grows in a perovskite structure, as sketched in Fig.3.2b. It shows colossal magnetoresistance (CMR), and theoretically full spin polarization. The latter properties and its relatively high Curie temperature ($T_{Curie} \approx 200$ K) make it interesting for studying proximity effect in heterostructures with YBCO, as they have compatible crystalline lattices. The interfaces are also clean and show no sign of inter-diffusion [26].

Although the proximity effect depresses the magnetic and superconducting properties of both, they still strongly coexist even down to a few unit cells [32]. Fig.3.3a shows that in a superlattice, increasing the thickness of the YBCO layers decreases the magnetization of the 6 nm LCMO layers in between (15 unit cells) [215]. It saturates around 6 YBCO unit cells ($\approx$ 7 nm). Conversely, in Fig.3.3b, increased thicknesses of LCMO also depresses the critical temperature of a 6nm of YBCO layer ($\approx$ 7 nm).

Our LCMO layers were grown by sputtering, as a magnetic interlayer between two YBCO layers. The deposition is done by sputtering at *Universidad Complutense de Madrid*. In Tab.3.3, we sum up some magnetic properties of LCMO [32, 215, 26, 27, 216, 39].

T_{Curie} (K)	M_s (A·m^{-1})	ϵ_{ex} (eV)	v_f(m·s^{-1})
200	4×10^5	3	$2-3\times10^5$

Table 3.3: **Magnetic properties of $La_{0.7}Ca_{0.3}MnO_3$**

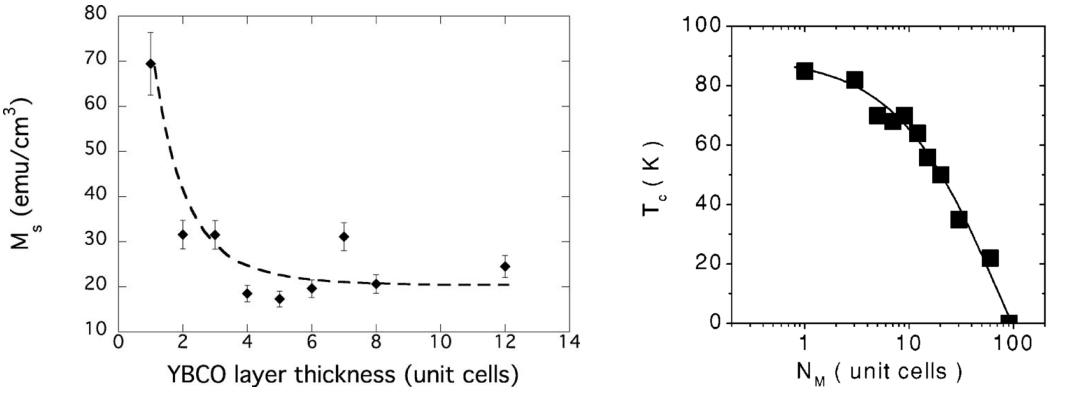

(a) M_s of 6 nm LCMO [215] (b) T_c of 6 nm YBCO [32]

Figure 3.3: **Crystal lattice and Curie temperature of LCMO**
In superlattices, the properties of LCMO (ferromagnetic) and YBCO (superconductor) are weakened due to each other's presence.

3.3.2 Magnetic multilayers

We deposited several ferromagnetic multilayers consisting of repetitions of Pt/Co/X layers, where X=Ir,Ru,Pt. These all have perpendicular magnetic anisotropy. We deposited these by DC magnetron sputtering, with a Pt buffer layer to help having flatter interfaces. It also gives the (111) texture to the stack, which is necessary for perpendicular anisotropy. They are also capped with 3 nm Pt to avoid oxidation. In the following, we present Alternating Gradient Field Magnetometer (AGFM) magnetization measurements in perpendicular field. These were measured at room temperature in patterned samples. Although the M/M_s ratio is precise, the value of M_s is qualitative only ($10-30\%$ error on the value of M_s is realistic given the errors due to the calibration and the sample area measurement).

Co/Pt multilayers

The first layer we deposited is $Pt_{10nm}/(Pt_{1nm}/Co_{0.6nm})_{\times 5}/Pt_{3nm}$. It has perpendicular magnetic anisotropy from 300K to low temperatures. Due to the symmetric stacking, the value of the DMI D is either small or null ($|D| < 0.4$ mJ·m^{-2} [58]). The surface anisotropy is estimated to be around $K_s \approx 0.4$-1.0 mJ·m^{-2} [136, Tab.4], yielding an uniaxial anisotropy constant of $K_u = 2K_s/d_{Co} \approx 1.3$-$3$MJ·m^{-3}.

Ir/Co/Pt multilayers

We also deposited $Pt_{10nm}/(Ir_{1nm}/Co_{0.6nm}/Pt_{1nm})_{\times 5}/Pt_{3nm}$. As shown in Fig.3.5, the sample has perpendicular anisotropy. Also, there is a net DMI in these layers, estimated to be $D \approx 1$ mJ·m^{-2} [58, 66]. It remains finite since the DMI at the Co/Pt interface exceeds that of the Ir/Co one. In that sample, small worm domains shrink into magnetic skyrmions close to the saturation field.

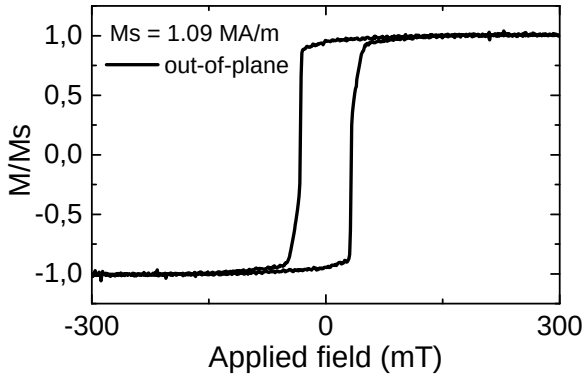

Figure 3.4: **Co/Pt magnetization (AGFM,300K)**

The uniaxial anisotropy constant K_u can be calculated from the area difference method [136], using the formula in Eqn.3.2.

$$K_{eff} \approx \frac{1}{2}\mu_0 M_s(H_{s\parallel} - H_{s\perp}) = K_u - \frac{\mu_0}{2}M_s^2 \tag{3.2}$$

With $\mu_0 H_{s\parallel}$=373 mT and $\mu_0 H_{s\perp}$=48 mT, one gets $K_u \approx 0.5$ MJ·m^{-3}. It is a bit small compared to the $0.7 - 0.8$ J·m^{-3} usually encountered in the literature [58, 59], but realistic. That method is not very accurate though, as it assumes that the magnetization curves are linear with negligible hysteresis.

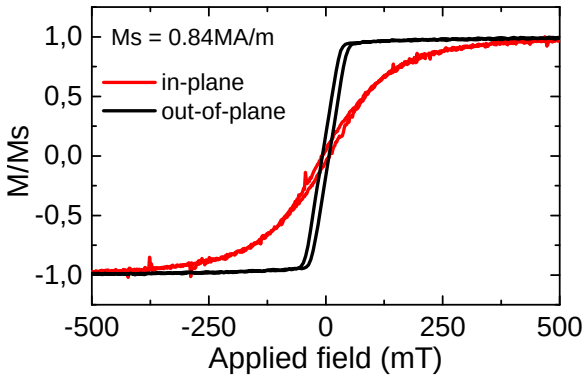

Figure 3.5: **Ir/Co/Pt magnetization (AGFM,300K)**

Ru/Co/Pt multilayers

Another multilayer we used is $Ta_{3nm}/Pt_{10nm}/(Pt_{1.4nm}/Co_{1.6nm}/Ru_{1.2nm})_{\times 4}/Pt_{3nm}$. In magnetization curves of Fig.3.6, the out-of-plane saturation field is lower than the in-plane one, but not by far. This means that the sample also has perpendicular anisotropy, but is close to the transition due to the larger cobalt thickness. It has stripe-like spin spiral domain structures that turn into magnetic skyrmions around $M/M_s \approx 0.5$. The value of M_s is higher than in the others due to the higher cobalt thickness in each layer. The values of the DMI should be around those of Ir/Co/Pt

or a bit higher. Estimating the anisotropy constant using the method in 3.3.2 yields $K_u \approx 1 \text{MJ}\cdot\text{m}^{-3}$ with $\mu_0 H_{s\parallel}$=373 mT and $\mu_0 H_{s\perp}$=48 mT. In these layers, the strength of the DMI should be $D \approx 1.0$ mJ·m^{-2} [60, p.125], similar to that in Ir/Co/Pt.

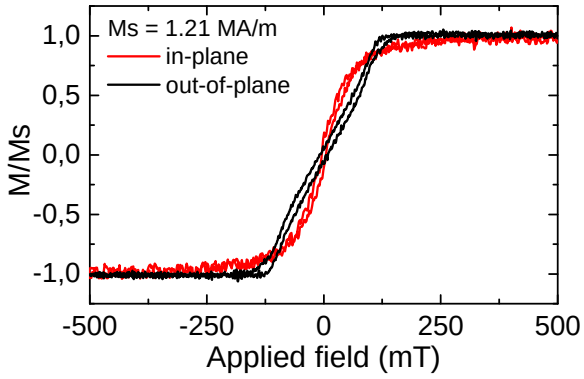

Figure 3.6: **Pt/Co/Ru magnetization (AGFM,300K)**

3.4 Devices

In this section, we review the different device designs that were fabricated for the present thesis. These are used to measure the transport properties of multilayers, either in the layer plane (Sec.3.4.1) or across the interfaces (Sec.3.4.2 and 3.4.3). The device fabrication is done in a clean room, to avoid contamination by particles, as the sizes of the patterns are typically small (1-100 μm). In the following, we will go through the steps of fabrication without entering into the details of the lithography processes. The detailed fabrication recipes are found in Sec.A. For readers unfamiliar with fabrication techniques in microelectronics, please refer to textbooks like that of Jaeger [217].

3.4.1 Hall cross-bridge

To make transport measurements, the geometry of the samples has to be well controlled. To do that, we use the cross-bridge pattern shown in Fig.3.7. The measured regions (one highlighted in blue in the figure) measure 40×200 μm^2. They are designed to make 4-points measurements, in addition to the Hall effect with the transverse contacts. The device fabrication consists in a single UV photolithography, and an ion beam etching step down to the substrate. The detailed recipe is given in App.A.1.

3.4.2 3-point vertical junctions

The multilayers we measured consist in YBCO/LCMO/YBCO trilayers with a 30nm gold capping. To measure the transport across the interfaces, we patterned them into a vertical junction configuration, as shown in Fig.3.8a. In that design, the

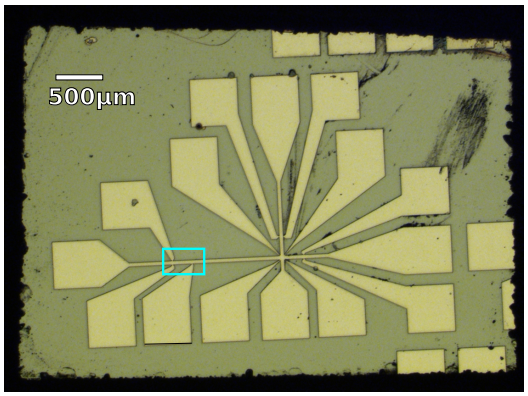

Figure 3.7: **Hall cross-bridge device**

top layers are patterned into a pillar in which the current is injected from the top. The bottom layer is patterned into a wide stripe, to serve as common bottom electrode for several junctions. These are contacted on the top by large gold electrodes, that are insulated from the lower layers by a thick (approximately 1 μm) hardened photoresist. In this layer, holes are opened to contact the pillars. That technique allows to avoid going through an additional insulator deposition and lift-off step. The gold capping on top of the pillars protects the layers during the processes and ensures a good electrical contact. It also helps aligning the structures, as there is little contrast between the different oxide layers.

The main drawback of that geometry is that two parasitic interface resistances are measured : between the evaporated electrode and the capping, and that of the capping with the pillar. In the following, we present the different fabrication steps. The detailed recipe is provided in App.A.2.

(a) 3pts vertical junction cross-section

(b) Top view

Figure 3.8: **3pts vertical junction schematic and top view**

Step 1 : defining the pillars

The first step consists in patterning the pillars in the first layers by UV photolithography (see Fig. 3.9a). As we wanted to define relatively small patterns (1-20 μm), we ensured the best contact between the mask and the resist by doing a border removal first. That step removes the higher thickness resist on the borders of the samples. We then defined the junctions and alignment marks in the photoresist with a second UV lithography, and transferred the pattern to the film with argon ion beam etching (IBE), down to the last layer surface. The etching is monitored using Secondary Ion Mass Spectroscopy (SIMS). We stop the etching when either the LCMO signal drops or the bottom YBCO signal increases. Consequently, there may be residual LCMO here and there, but the YBCO below is kept intact. A finished pillar is shown in Fig 3.9b We then remove the resist mask with an oxygen plasma to clean the superficial burnt resist, and then the rest in acetone and isopropanol.

(a) Pillar definition (b) Top view of a pillar

Figure 3.9: **Pillar definition**

Step 2 : defining the bottom electrode

In that step, we pattern the common bottom electrode in the bottom YBCO layer. A cross section sketch and top view are shown in Fig.3.10. That step is done in one UV photolithography and IBE step. Special care has to be taken to stop the etching as as soon as the signal of the YBCO starts to decreases, to avoid touching the STO substrate with the beam. Otherwise, the STO quickly becomes conducting due to the formation of oxygen vacancies at the surface, that create a highly conducting 2D electron gas [218]. The result is shown in Fig.3.10b.

Step 3 : insulating the device

To insulate the bottom electrode and the sides of the pillars during the top electrode deposition, we pattern holes in a photoresist layer. These are smaller than the pillar, and fall in the center of it, so that the sides are not touched. (See Fig. 3.11a and 3.11b) This requires very precise alignment. The resist is carefully developed,

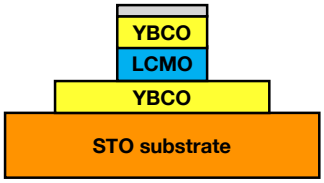

(a) Bottom electrode definition

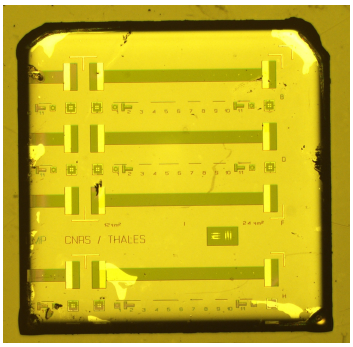

(b) Top view

Figure 3.10: **Bottom electrode patterning**

so that the holes are well opened and no resist remains at the bottom. Once the patterns are satisfactory, the resist is cured at high temperature (170 °C), so that it hardens enough to be resistant to chemicals, etching, and oxygen plasma.

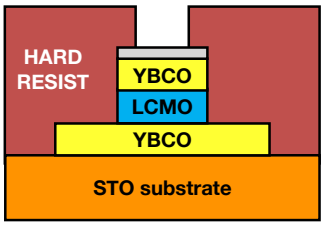

(a) Pillar insulation using resist

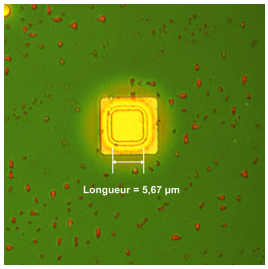

(b) Top view of a pillar under a hole

Figure 3.11: **Insulation of the pillars and bottom-electrode**

Step 4 : top electrode deposition

The last step is to evaporate and pattern the top electrode contact by *lift-off*. For that we spread a resist layer on the surface, and harden it using chlorobenzene, so that the metal sticks on the resist. We then pattern it by UV lithography (see Fig3.12a. The resist is removed where the electrodes should be, as shown in Fig.3.12b. After that, we evaporate a 8nm titanium adhesion layer, then a 150 nm layer of gold on top. Since there is a gold capping on the pillars, the titanium does not de-oxygenate the YBCO. Otherwise, it would fully degrades the devices. After the evaporation, we lift-off the resist in hot acetone to obtain the electrodes, as shown in Fig.3.12b. The device is now finished ready to be measured.

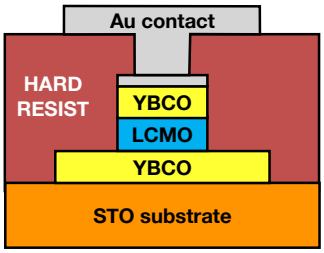

(a) Top contact deposition and lift-off

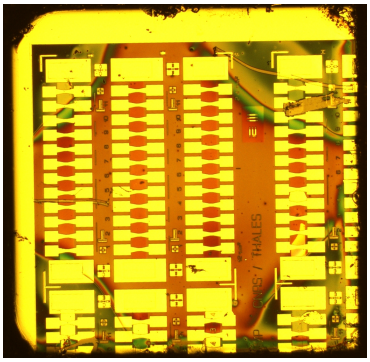

(b) Top view of a finished top contact

Figure 3.12: **Top electrode evaporation and patterning**

3.4.3 4-point vertical junctions

As mentioned earlier, the main drawback of the 3-points configuration is that several interface resistances are measured in addition of those in the oxide stack. These may hide the footprints of a superconducting current or Josephson behavior we are looking for. To circumvent that problem, we adapted the previous design in order to measure in 4-points configuration, as shown in Fig.3.13a. The geometry is essentially the same, but the hole and top contact patterns are split in two. This allows to separate the current and voltage top contacts.

As there is little contrast between the oxide layers, we deposited and patterned a thin Au layer where the alignment marks should be by lift-off at the beginning of the process. These are then pattern along with the multilayers. As the covered areas are small, that process does not significantly affect the SIMS monitoring during the first etching step. The rest of the process is essentially the same as that in 3 pts junction. No Ti adhesion layer was deposited before the evaporation of the gold top electrode, as it would completely de-oxygenate the whole pillar.

Due to a long-lasting technical issue at UCM, we could not test that design ourselves in trilayers. However, it was shown to function by subsequent work in our group.

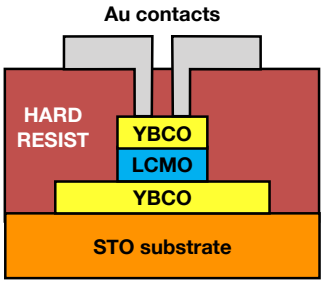

(a) 4 pts device cross-section

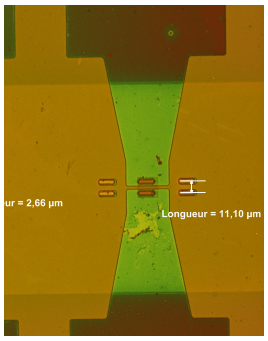

(b) Top view before depositing the top electrode

Figure 3.13: **4 pts vertical junction design and prototype**
The top electrode is separated in two to avoid measuring the contact resistances.

Chapter 4

Tunneling conductance of high-temperature superconductor / half metal SFS stacks

In the present chapter, we study the proximity effect in oxide heterostructures consisting of a half-metallic layer of $La_{0.7}Ca_{0.3}MnO_3$ (LCMO) sandwiched between two superconducting layers of $YBa_2Cu_3O_7$ (YBCO). These materials combine the advantages of high critical temperature superconductivity and high spin-polarization. Several experiments suggest the propagation of spin-polarized superconducting currents across the LCMO layer [26, 27, 28]. Yet, none has directly demonstrated the resulting Josephson effect. To that end, we first enhanced the quality of the electrical contact by an order of magnitude compared to preceding experiments [27, 33]. In the conductance of the trilayers, we found marked oscillations in the superconducting state. These change with the LCMO thickness, the temperature, but not the applied magnetic field. A Fourier analysis of the data yields sets of characteristic frequencies. Some of them can be related to those expected from quasiparticle interference in the superconductor (Tomasch resonances) and in the ferromagnetic barrier (McMillan-Rowell resonances). The presence of these conductance oscillations suggests the propagation of superconducting correlations across the LCMO. Since it is strongly spin-polarized, the correlations are likely spin-parallel triplets. However, enhancing the contact quality by an order of magnitude did not suffice to observe a possible Josephson effect.

4.1 Introduction

The observation of long-range superconducting current propagating through strong ferromagnets due to proximity effect [22, 23, 24, 25] has opened the possibility of merging the fields of superconducting circuits and spintronics. Obtaining currents that are both spin-polarized and superconducting offers access to effects like GMR or spin-transfer torque, that were otherwise inaccessible to superconducting electronics. In Josephson devices, ferromagnetic interlayers also allow to make π-junctions [14, 15]

and superconducting spin-valves (see Sec.2.5.3 and 2.5.4, or Refs. [219, 220]). These could be used to address the lack of high-density and non-volatile storage in superconducting circuits [16, 11].

Several demonstrations of working π-junctions and spin-valves have been achieved [14, 15, 204, 207, 221]. However, they all involve low-temperature materials, like niobium alloys ($T_c \approx$10-25 K). A similar demonstration in cuprates would be an important milestone, since these are high-temperature superconductors (HTSC), that can operate in liquid nitrogen (30-77 K). Several attempts were made to observe Josephson currents in SFS oxide systems [27, 28, 30, 31], but none of them unambiguously demonstrated the Josephson effect.

In the present work, we study trilayers composed of the HTSC cuprate $YBa_2Cu_3O_7$ (YBCO, T_c=92 K) and the half-metallic manganite $La_{0.7}Ca_{0.3}MnO_3$ (LCMO, fully spin-polarized) as the magnetic interlayer.

Evidence of the formation and propagation of *equal-spin* triplets were found in these materials through measurements of magnetization [26], or in conductance spectra as zero-bias peaks [28, 29] and oscillations [27, 33]. However, as stated before, those observations are only indirect. In these systems, due to charge transfer effects, a few nanometers of LCMO become antiferromagnetic [40, 41, 26]. It is strongly supposed to provide the magnetic inhomogeneity required to form triplet states.

In our group, conductance oscillations were observed in YBCO/LCMO/YBCO pillars [27, 33], as shown in Fig.4.1. They were attributed in part to Andreev-related resonances in the LCMO (McMillan-Rowell oscillations, see Sec.2.4.3). The authors argued that it should originate from the propagation of equal-spin triplets, since LCMO is too strongly spin-polarized and thick for singlet proximity effect (10-30 nm of ferromagnet). Though, the apparent critical current in their measurements (inset) produced no Fraunhofer pattern, and was deemed too low to originate from a Josephson effect.

The highly resistive and inhomogeneous Au/YBCO contact impedes the possible observation of Josephson effects in these devices. We propose to improve the contact resistance, and see if it allows to observe a Josephson behavior. In the following, we first present our method and results for optimizing the Au/YBCO capping contact. Then, we show the results of our conductance measurements in the trilayers.

4.2 Materials, devices an measurement methods

4.2.1 Materials

As stated earlier, the materials we employed in this work are the cuprate superconductor $YBa_2Cu_3O_7$ (YBCO, T_c = 92 K), and the half-metallic manganite $La_{0.7}Ca_{0.3}MnO_3$ (LCMO, $T_{curie} \approx$ 200 K). Conveniently, these materials have compatible crystalline structures, and can be grown in heterostructures down to a few unit cells [26, 32].

We measured the transport in trilayers composed of $YBCO_{20nm}/LCMO_{Xnm}/YBCO_{30nm}$, deposited on (001) oriented $SrTiO_3$(STO) substrates. As geometrical resonances in

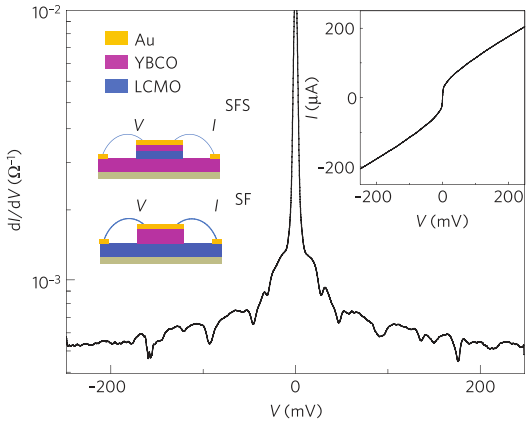

Figure 4.1: **Conductance oscillations in YBCO/LCMO/YBCO [27]**
The oscillating conductance patterns can be tied to Andreev-related resonances across the LCMO. These likely indicate the propagation of triplets across the F layer. However, the apparent critical current is likely not due to Josephson effects, as it shows no Fraunhofer pattern.

the YBCO layers were already reported in such a system [27], the two YBCO layers have different thicknesses to distinguish in which it may occur. We used LCMO thicknesses of 6, 12 and 24 nm for the magnetic barrier. These films were grown at *Universidad Complutense de Madrid* (UCM) by sputtering. On all of them, we deposited a gold capping *ex-situ* by pulsed laser deposition (PLD). The sample is first annealed in oxygen atmosphere (0.36 mbar, 720 °C) for 3 mn, then cooled to ambient temperature in oxygen (800 mbar). Finally, 30 nm of gold are deposited to cap the sample. This annealing is done at the pressure/temperature conditions at which YBCO is usually grown in that setup. It is helps to re-oxygenate the surface of YBCO, from which oxygen may have leaked. That method was found to be the best among those we tried. For the optimization, we used layers of bare YBCO (30 nm) grown at UCM in the same conditions. We present the results of that process in Sec.4.3.1.

4.2.2 Devices and measurement methods

Devices

All the devices were patterned into a vertical junction geometry by UV lithography, following the steps in Sec.3.4.2. Cross-section schematics are shown in Fig.4.2, along with the electrical contacts configuration. That geometry allows injecting the current across the interfaces, to investigate the proximity effect in the LCMO layer. On the other hand, it also measures the interface resistance between the gold and the oxide layers. The junctions are contacted on the top with one aluminum wire, the resistance of which is negligible (around 2 Ω or less vs. a few 100 Ω). The bottom electrode consists in a long strip of YBCO common to several other devices. The

voltage and current contacts are placed on the ends, to separate them and avoid measuring the interface resistance there too.

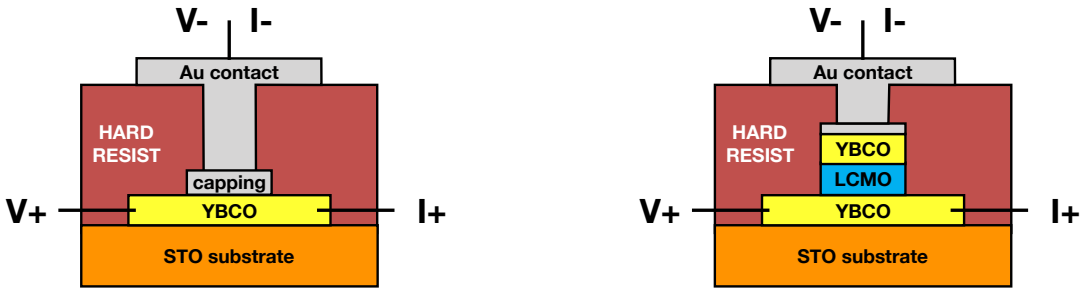

(a) Au/YBCO bilayers junction (b) YBCO/LCMO/YBCO trilayers

Figure 4.2: **Schematics and contact configuration**

Measurement method

The samples are measured in a a liquid helium cryostat, going down to 3 K. Conductance maps were acquired in another setup, which is a closed cycle helium cryostat, allowing to automate the temperature and magnetic field control. Magnetic fields are applied with an electromagnet, and the sample is rotated in the setup to select the field angle. We bias the junctions in current using a stabilized *Keithley 6221* current source, and measure voltages with a *Keithley 2182* nanovoltmeter. The differential resistance is directly measured by linking the two instruments and using the *delta mode* [222, ch. 5]. Differential conductances are then obtained by inverting the measured differential resistance. That method is faster to use than lock-in techniques, and allows much better signal/noise ratios than numerical differentiation of the current-voltage curves. The contact configuration is sketched in Fig.4.2.

4.3 Results

4.3.1 Optimization of the Au/YBCO contact resistance

Before measuring in the trilayers, we wanted to reduce the parasitic contact resistances in the devices. As seen in Fig.4.2a, there are two of them. One is between the oxide multilayer and the gold capping, the other is between the capping and the top electrode evaporated at the end of the fabrication process. These add parasitic resistances in the measurement, and may hide the footprints of proximity effect in LCMO that we are looking for.

The first parasitic resistance to reduce is between the evaporated gold electrode and the gold capping. It is due to dirt and photoresist residues accumulating on top of the capping after each lithography step. If not taken care of, the contact

becomes very resistive, as shown in Fig.4.3. Most of the times, it also creates strongly asymmetric backgrounds in conductance curves. To reduce that resistance, we did plasma cleanings to remove the burnt resist crust that forms after each ion milling step. If one directly dissolves the resist in acetone, that layer sticks on the sample and degrades the contact. Prior to the top electrode evaporation, another plasma cleaning is done to ensure the absence of dirt and resist where the gold will contact the pillars. Below T_c, the resistance of the junctions is reduced from $0.5 - 1$ kΩ to $30 - 150$ Ω (both for an optimized Au/YBCO contact).

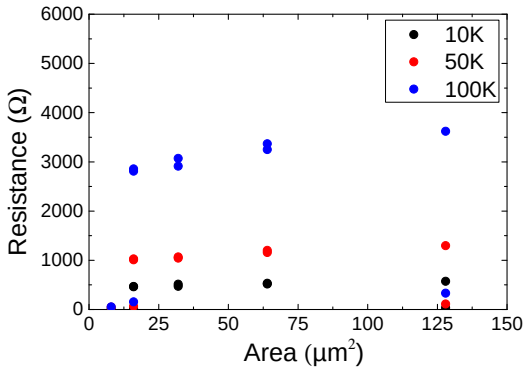

Figure 4.3: **Contact resistance due to dirt during fabrication**
Resist residues accumulate during the fabrication and degrade the contact between the Au electrode and the capping, up to several kΩ.

The second contact resistance to improve is the one at the interface of gold and YBCO. In previous work from our group [27], the gold capping was done directly by sputtering at ambient temperature. Representative data for an Au/YBCO bilayer is presented in Fig.4.4. That method yields large contact resistances, in the kΩ range, that is likely inhomogeneous since it does not depend on the junction area (Fig.4.4b). It was attributed to point defects in the contact shorting the interface resistance, leading to pronounced zero-bias conductance peaks (Fig.4.4a).

We suppose that the high resistance in these devices may be due to YBCO being de-oxygenated at the surface (insulating). Damages to that layer could also lead to the pinhole defects observed in previous work. To enhance the quality of the Au/YBCO contact, we switched to PLD, that provides better contacts than sputtering. Then, we tested several methods, listed below.

- annealing in O_2, then deposition of Au on YBCO;
- oxygen plasma cleaning, annealing in O_2, then deposition of Au on YBCO ;
- regrowth of YBCO, then in-situ Au capping ;

All of them include an annealing in oxygen atmosphere (recipe in Sec.4.2.1) prior to the gold deposition. It should replenish the oxygen content of the surface, since the pressure/temperature conditions are the same as during the growth of YBCO in that

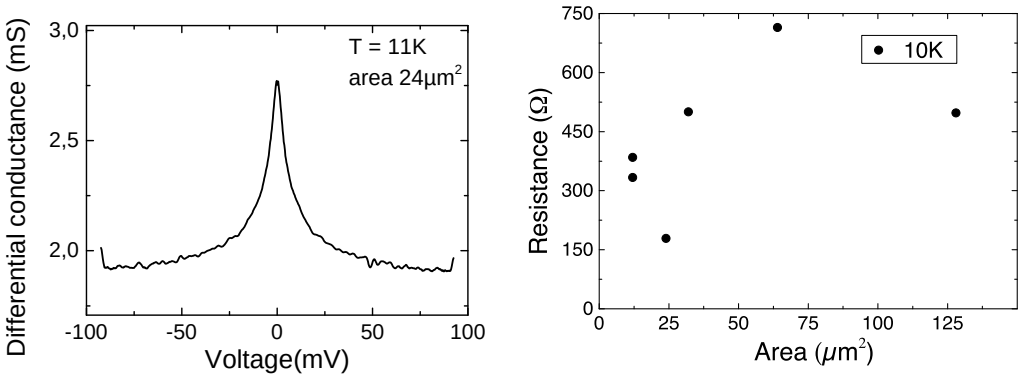

(a) Differential conductance ($24\mu m^2$ area) (b) Area dependency

Figure 4.4: **Au/YBCO contacts from preceding work (sputtering)**
In previous experiments [27], the sputtered Au/YBCO contact is resistive and inhomogeneous. It leads to strong zero-bias conductance peaks 4.4a, and no area dependence of the contact resistance (4.4b).

setup. We then tried capping directly after annealing, doing an oxygen plasma before to clean the surface, and re-growing a few nanometers of YBCO before depositing gold *in-situ*. We used three plain YBCO samples, and measured their critical temperature to be $T_c \approx 90$ K. We then used one for each deposition method, and measured T_c again. An R(T) curve is presented for each sample after the deposition in Fig.4.5.

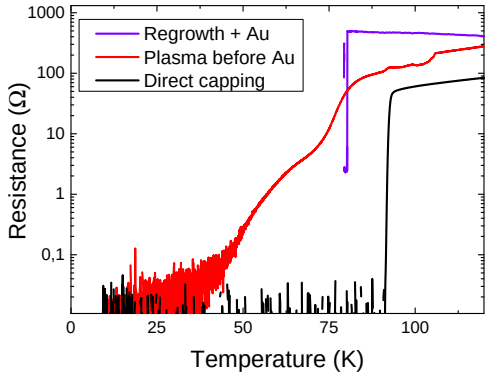

Figure 4.5: **R(T) for several Au capping methods**
Regrowing YBCO or doing a plasma in the PLD degrades the material, whereas only annealing the sample does not degrade the properties.

We found that attempting to regrow YBCO degraded T_c to approximately 80 K, and measured a finite residual resistance of 2.5 Ω at 77 K. Additionally, that resistance increases when lowering the temperature (insulating) whereas it decreased linearly in the bare YBCO (like the black curve). Since it was measured in liquid nitrogen, we could not go to lower temperatures. But these results were sufficient to dismiss this deposition method. The red curve shows that doing a plasma cleaning in the PLD before annealing significantly damaged the superconductor. That method was

abandoned too. Conversely, doing only the annealing in oxygen before depositing gold does not apparently degrade the properties of the material (black curve). We followed that method to fabricate the devices presented in the following sections of the chapter.

In Fig.4.6, we present data in vertical junctions using the PLD annealing and capping method. We observe that these show a parabolic (tunnel) background (Fig.4.6a). There is still a zero-bias feature, but broader and much smaller in comparison to previous results. At low temperatures, the contact resistance is improved by roughly an order of magnitude. As seen in Fig.4.6b, the resistance decreases with the junction area, indicating that the contact is homogeneous. For each temperature, a guide for the eye is drawn with the plot.

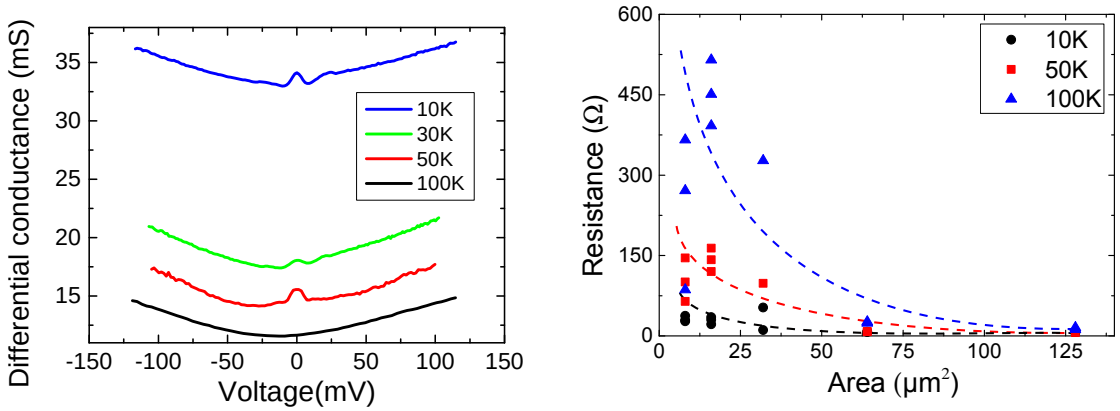

(a) Differential conductance ($8\mu m^2$)

(b) Area dependence

Figure 4.6: **PLD Au/YBCO contacts with O_2 annealing**
Careful cleaning during fabrication and capping in O_2 atmosphere reduces the contact resistance by an order of magnitude at 10 K.

4.3.2 Tunneling conductance in SFS high-temperature stacks

In this section we study the transport across the interfaces in YBCO/LCMO/YBCO trilayers. They are also patterned into vertical junctions, with the geometry being represented in Fig.4.2b.

We measured the differential conductance at several temperatures and magnetic fields in the samples. In the following, we describe the general features of the curves. As some of them showed oscillations, we also present the spectral analysis of these curves, and its evolution with the temperature, magnetic field, and LCMO thickness. We also show that these frequencies can be explained in terms of separate Andreev-related phenomena occurring in the superconducting and ferromagnetic layer.

Conductance tunneling spectra

After optimizing the contact resistance, we went on studying the proximity effect in the YBCO/LCMO/YBCO samples. There are three of them, with LCMO thick-

nesses of 6, 12, and 24 nm. We measured the conductance of these junctions, and found a tunnel behavior for all of them. Several distinct features were observed in some of them, as presented in Fig.4.7. Most of them display a parabolic conductance background typical for tunneling junctions, like that of Fig.4.7d. It is on average more pronounced with increasing LCMO thicknesses. In many of them, oscillating patterns are superimposed. The features in the 6 nm LCMO sample are pronounced, and show zero-bias peaks along with the oscillations (Fig.4.7a). In the 12 nm sample (Fig.4.7b), the tunneling background increases, and sharp dips occur at higher biases. The features in the low-bias part still exist but are much less visible. The 24 nm sample shows mostly features related gold/YBCO tunneling contact (weakly visible gaps, or $Z \approx 0.5$ Andreev structures, see Sec.2.4.2). One junction showed a very clear oscillating pattern (Fig.4.7c). We found no evidence of a possible Josephson behavior in these samples.

For all the measured junctions, we plotted the zero bias conductance value around 3 K in Fig.4.8 as a function of the junction area. On the diagram, one can separate the devices that present conductance oscillations from those that exhibit only a plain tunneling curve. The latter are in the greyed area, and generally have a lower conductance than the others. Zero bias peaks are found for the highest conducting junctions, which were mostly those of the 6 nm LCMO sample. A few ones were observed for the 24 nm sample too (the two points above all the rest), but their occurrence remains marginal.

As these patterns disappeared in the normal state ($T > 90$ K), they originate from superconductivity. If these are caused by the proximity effect, they should be affected by magnetic fields and temperature. In the next section, we investigate these two parameters.

Temperature and magnetic field dependence

In the present section, we investigate how increasing the temperature or applying a magnetic field affects the conductance curves. For selected junctions that showed clear patterns, we measured conductance spectra at several temperatures and magnetic fields. Fig.4.9a and 4.9b map the temperature evolution for the junctions previously presented in Fig.4.7a and 4.7c. In these, the oscillations vanish upon increasing the temperature, and also seem to shift to zero voltages. They disappear before the critical temperature of the YBCO.

Since magnetic fields also affect superconductivity, we also acquired curves and maps as a function of that parameter. As shown in Fig.4.10a, the effect of applying 500 mT is nearly negligible. The oscillation pattern seems to shift a tiny bit to zero voltage, in the same fashion as with temperature. However, the effect is far less important within that field range. To look for a possible Josephson-like modulation, we acquired a detailed map with the field applied in the plane of the junction. It is presented in Fig.4.10b, and shows no noticeable effect. The same conclusion is drawn when mapping the field out-of-plane, which is not shown for brevity. From these results, the strongest effect is that of temperature. The field may be able to shift the

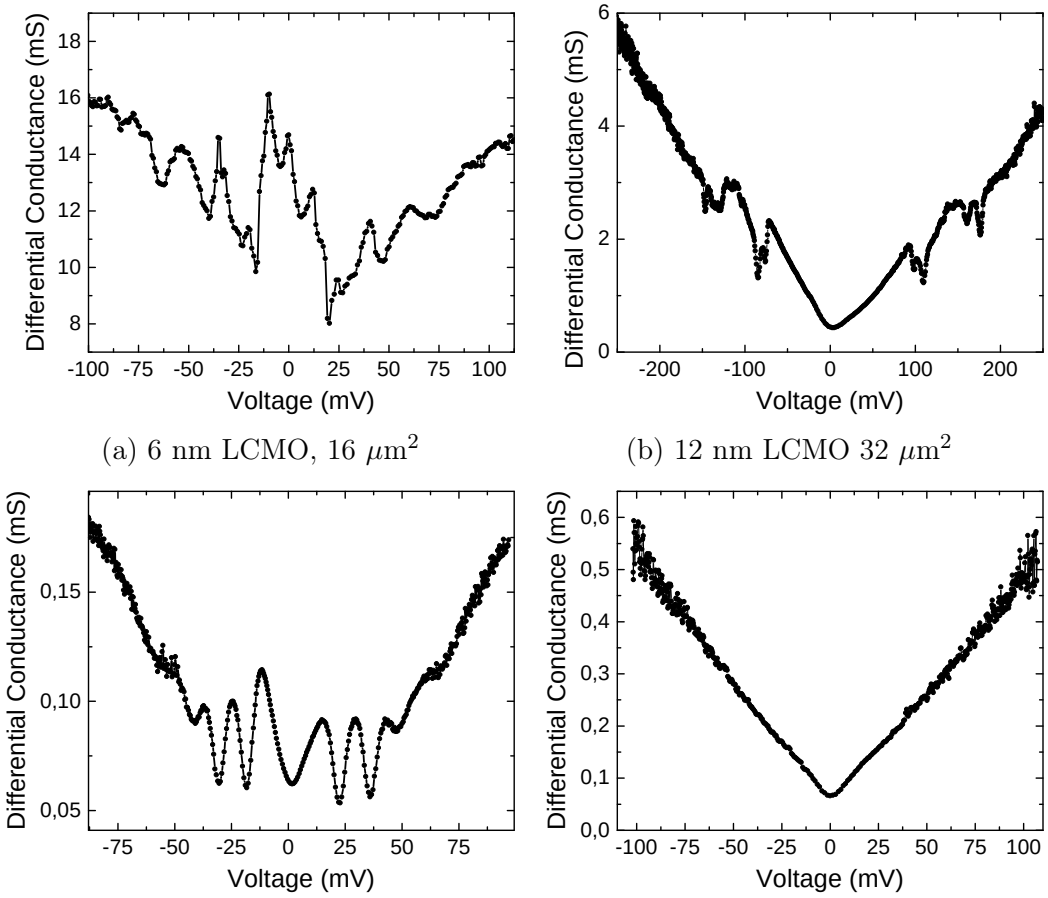

(a) 6 nm LCMO, 16 μm^2

(b) 12 nm LCMO 32 μm^2

(c) 24 nm LCMO, 8 μm^2

(d) 24 nm LCMO, 32 μm^2

Figure 4.7: **Differential conductance of several junctions ($T = 3.5$ K)** *Different oscillating behavior appear depending on the sample and junction. Additional zero bias peaks are seen exclusively in the 6 nm sample (4.7a). Less conducting ones have a more pronounced tunnel (parabolic) background. In the 24 nm sample, one junction shows oscillations (4.7c) whereas others present "basic" YBCO/Au tunneling contacts (4.7d), sometimes with gap features.*

oscillations too, but it is small compared to the critical field of YBCO. We suppose that more pronounced effects could arise for higher values.

Up to now, we have gathered data about how the differential conductance changes depending on thickness, temperature, and magnetic field. However, the patterns are sometimes difficult to interpret. As some of them showed signs of periodicity, we suppose that there might be one or more periodic phenomena that could occur. To find out, we carry a spectral analysis of the data in the next section.

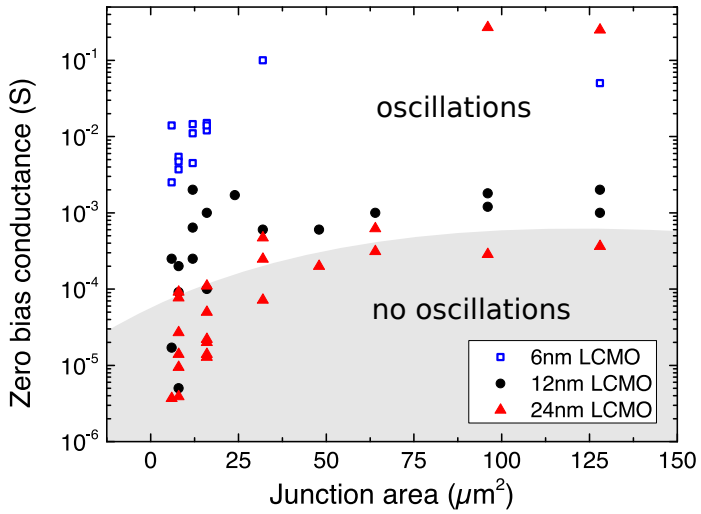

Figure 4.8: **Zero-bias conductance of the junctions(T=3.5K)**
Higher conductance devices show oscillations and Andreev-related features (white). Lower ones present a plain tunneling behavior.

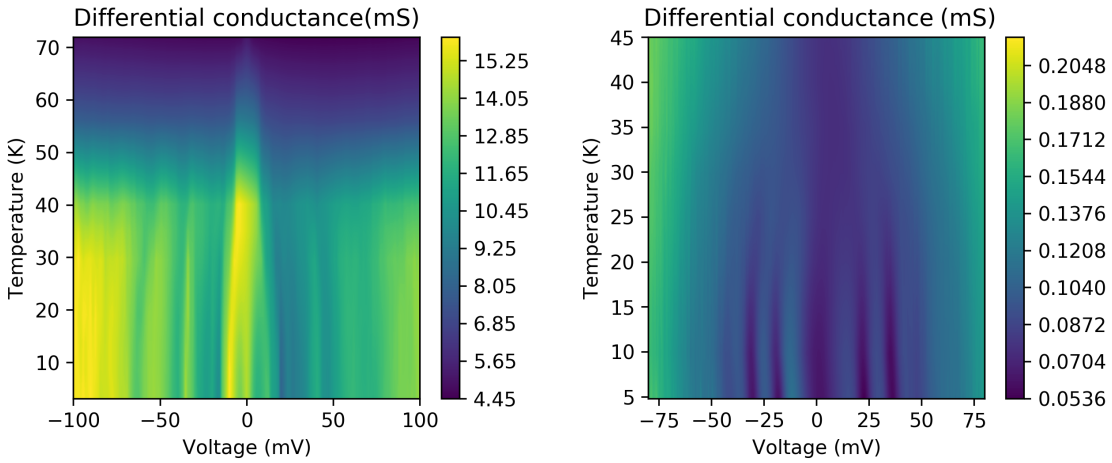

(a) 6 nm LCMO, 16 μm^2 (b) 24 nm LCMO ; 24 μm^2

Figure 4.9: **Temperature evolution of the oscillations**
The patterns shift to zero voltage and vanish upon increasing the temperature.

4.3.3 Spectral analysis of the tunneling conductance

Fourier analysis of the oscillations

Deciphering what composes the patterns that we found in the conductance is often difficult. As we have seen, some of them show clear series of maxima. Others, like that in Fig.4.11a, have more complex shapes that may result from interference (we show only half of the curve, to better see the features). Thus, we decided to analyze the data using the Fourier transform, to retrieve the characteristic frequencies in the

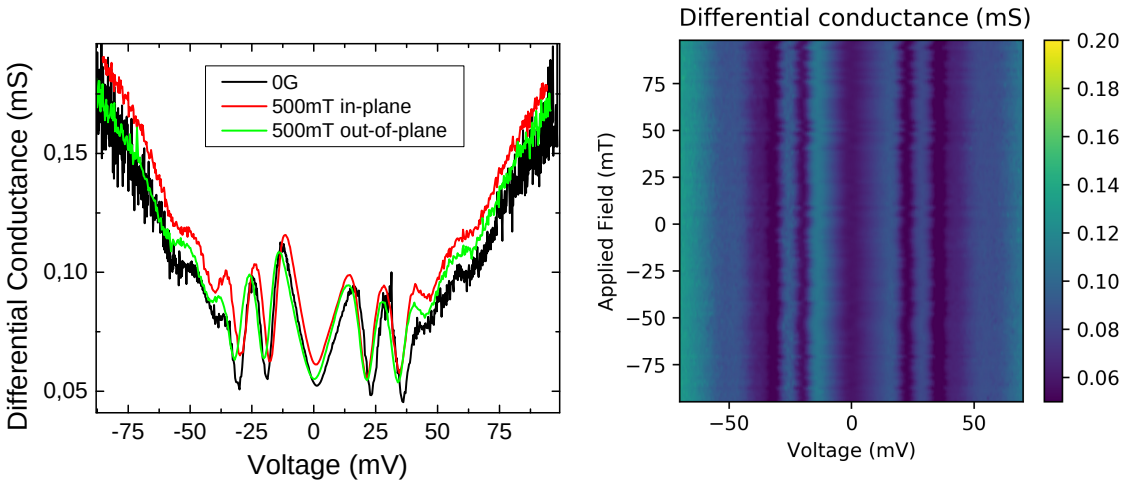

(a) Effect of magnetic field (b) In-plane field map

Figure 4.10: **Field-dependence of the conductance spectra**
The maps are recorded at 3K, for the same device as in Fig.4.9b.

signals. For that, several precautions were taken when processing the signals, to ensure the validity of the analysis. First, as the measurements are biased in current, we interpolated the data to have a regular sampling in voltage, which is a pre-requisite of the *fast Fourier transform* (FFT) algorithm. Second, we applied a Hann (hanning) window before calculating the FFT instead of the "default" rectangle one. This makes the frequency peaks more visible (less power leakage), but also broadened (less resolution). The trade-off is still advantageous, since some small components could be mistaken for noise by using the default rectangle window.

In Fig.4.11b, we plotted the FFT modulus of the full curve in Fig.4.7a. For all the curves, there is a strong zero frequency peak. It originates from the background, as it is present even in the curves that show no particular features. When there are oscillations in the conductance, additional peaks appear in the spectra. The FFT modulus presents peaks that can sometimes be related to a visible series of maxima in the conductance. For example, the 43 V^{-1} peak (23 mV period) likely corresponds to the bumps indicated by the blue arrows in Fig.4.11a graphs. For others like the frequency at 16 V^{-1} (62 mV), it is more difficult to see the corresponding period. Other peaks, like the 83 V^{-1} one, are likely harmonics (approximately two times 43 V^{-1}). These have usually lower amplitudes than the fundamental, and happen because the patterns are not sine waves.

We then used the FFT to analyze the temperature evolution of these patterns. From the conductance maps of Fig.4.9a, we obtained the temperature evolution of the frequency spectrum. The result is presented in Fig.4.12. In that map, the 43 and 83 V^{-1} peaks vanish with increasing temperatures, but do not shift. Since the conductance oscillations do shift to zero voltage, it indicates that only the phase and amplitude are temperature-dependent. The 16 V^{-1} feature broadens when increasing the temperature, then completely disappears around 50 K. Above, the only feature

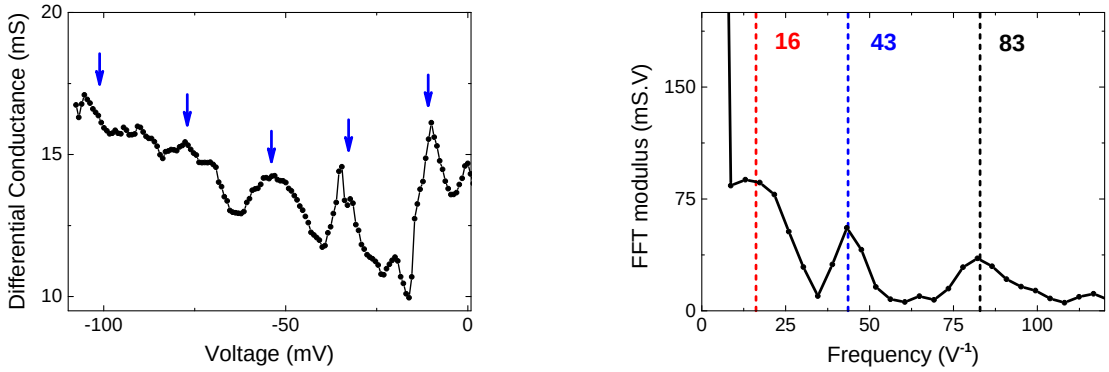

(a) Complicated conductance pattern (b) Fourier transform

Figure 4.11: **Conductance curve and Fourier transform (16μm^2, 6nm LCMO)** *The FFT gives a way to decode the more complex patterns. Some frequencies can be correlated to visible features in the conductance (23mV/43V^{-1}, in blue), whereas others are less obvious (red one, 63mV). Some may be harmonics of lower frequencies (black one).*

remaining is the zero frequency peak. The same behavior is observed when calculating the temperature maps for other junctions.

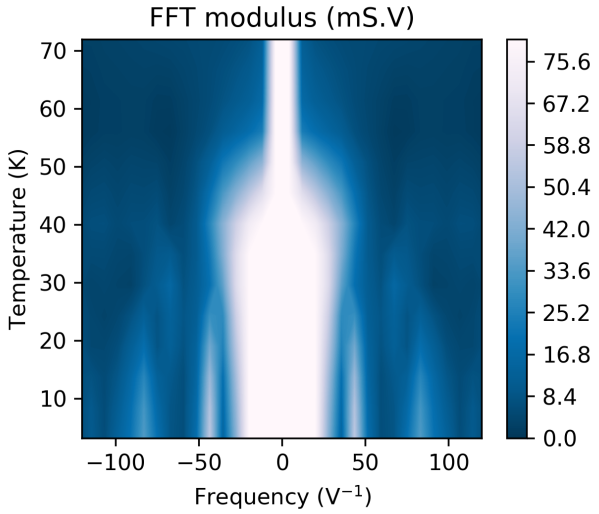

Figure 4.12: **Temperature maps of the frequency (16μm^2, 6nm LCMO)** *Calculated from Fig.4.9a. The visible peaks do not shift with temperature. The one around 20 V^{-1} broadens when the oscillations vanish.*

Now that we have discussed the features of the frequency spectrum in one "typical" junction, we can do statistics using the others and see what happens when the thickness changes.

We carried the FFT analysis for all the junctions that showed oscillations, using the measurements at 3.5 K. In the conductance curves, there is generally a

small asymmetry between positive and negative voltages. It was already observed in cuprates [223, 224], and is not due to heating or defects. Nonetheless, it makes the periodicity on both sides to differ by a few V^{-1}. To check how it influences the spectra, we calculated the FFT for both the full curve and the negative voltage part (measured first). We found that the former better separates the peaks below 30 V^{-1} from the low-frequency background, since it is calculated over more periods. To ensure the validity of the analysis, we compare the two FFT and neglect peaks that were not identified in both spectra. They are plotted in Fig.4.13 against the LCMO thickness. Shapes represent different junctions on the same sample. Filled symbols are assigned to the lowest frequency peak, which often appeared around 20 V^{-1} (50 mV). It is present in both the 6 and 12 nm samples, and is often broader than others. The second one, marked with hollow symbols, has more scattered values, especially for the 6nm samples. The colored areas in the graph correspond to different frequency ranges that are discussed in the next section.

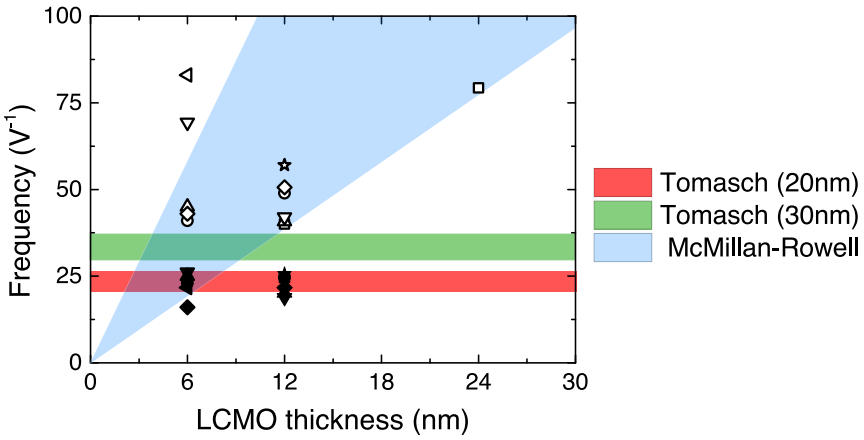

Figure 4.13: **Observed frequencies for several LCMO thicknesses** ($T = 3.5K$) *We selected the two most intense frequencies in the FFT spectra. These can be attributed to Tomasch and McMillan-Rowell resonances, respectively in YBCO and LCMO.*

Interpretation of the conductance pattern

Previous work from our group [27, 33] found similar oscillations in the conductance of YBCO/LCMO/YBCO trilayers, but not in the tunneling regime. These were interpreted as a sum of interfering patterns in the junction. One was attributed to Tomasch resonances in the top YBCO layer (TR, quasiparticles interference), the other to McMillan-Rowell oscillations (MMR, interference of Andreev-reflected particles in LCMO). They are covered more extensively in Sec.2.4. These resonances have conductance peaks at the voltages given by Eqn.4.1 and Eqn.4.2, along with the corresponding frequencies f_{TR} and f_{MMR}. In the formulas, v_s and v_f are the Fermi velocities respectively in YBCO and LCMO, and n, m are positive integers.

$$V_n^{TR} = \sqrt{\Delta^2 - \left(n\frac{hv_s}{2d_s}\right)^2} \quad f_{TR} \approx \frac{2d_s}{hv_s} \tag{4.1}$$

$$V_m^{MMR} = V_0 + m\frac{hv_f}{4d_f}; \quad f_{MMR} = \frac{4d_f}{hv_f} \tag{4.2}$$

From the literature, we estimated the Fermi velocity in YBCO to be v_s =4-5×10^{5}m·s^{-1} [214, 27, 37]. The corresponding TR in the top YBCO layer (20 nm), yields a band of frequencies between 20-26 V^{-1}. We shaded it in red on Fig.4.13, and found that it encompasses most of the first frequency set (filled symbols). It is also possible to have TR in the bottom layer, which is also YBCO. For a 30 nm thickness, the previous values of v_s result in the 30-40 V^{-1} frequency band. It is represented in green in the plot, and does not overlap the points.

Another possible source of oscillations is MMR in LCMO. We found that it covers most of the remaining data points, if one assumes a value of v_f between $v_f = 1 - 3 \times 10^5$ m·s^{-1}. That range is shaded in blue on the figure.

Following that scenario, we evaluated the mean frequencies f and Fermi velocities for each sample and type of oscillation. We also estimated the error on each quantity. For the frequencies, we calculated the standard error σ_f for each type of oscillation, and for each thickness. The error on the frequency is then estimated to by $2\sigma_f$ (95% confidence interval). The error on the thickness, according to our colleagues at UCM, is $\delta d \approx 2$ nm. The relative error on the Fermi velocity $\frac{\delta v}{v}$ is then given by Eqn.4.3.

$$v \sim \frac{d}{f} \implies \frac{\delta v}{v} = \frac{\delta d}{d} + \frac{2\sigma_f}{f} \tag{4.3}$$

The results are summarized in Tab.4.1. In the table, the MMR phase V_0 is computed using the phase of the each FFT curve. We estimated the gap from the first TR peak when it was clearly identifiable, and from the junctions that showed only plain gap features.

d_f (nm)	v_s(×10^5 m·s^{-1})	v_f(×10^5 m·s^{-1})	Δ (meV)	V_0 (mV)
6nm	4.3 ± 0.8	1.0 ±0.5	19.8 ± 0.7	14 ±3
12nm	4.2 ± 0.6	2.5 ± 0.6	21 ± 0.8	12± 1
24nm	-	2.9 ± 0.2	16.3 ± 1.7	12

Table 4.1: **Average Fermi velocities, gaps, and phases**
Errors on v_s and v_f are calculated according to Eqn.4.3. Those on V_0 and Δ are twice the standard error of the data set.

Overall, we find a Fermi velocity around 4.2 × 10^5 m·s^{-1} for YBCO, which is the same as that found in the literature [214, 37]. The values of v_f in LCMO that we obtained from MMR range between 1.0 and 2.9×10^5 m·s^{-1}. In particular, those of the two thicker samples agree well with first principles calculations for LCMO (3.1 × 10^5 m·s^{-1}, found in Ref.[39]). However, for the junctions with 6 nm thick

LCMO, the average velocity is significantly lower and shows a larger dispersion. This is as expected from earlier experiments in our group [27] and could be explained by different reasons discussed below.

4.4 Discussion

First, we managed to enhance the quality of the contact by annealing the sample in oxygen before capping using PLD. It lowered the resistance by an order of magnitude, down to a few tens of Ohms at 10 K. Additionally, the contact is more homogeneous since it is inversely proportional to the area, unlike the previous ones. Zero bias conductance peaks (ZBCP) were significantly reduced, but sometimes still present, especially in the 6 nm sample. Shorts in the tunnel contact are very unlikely, since the junctions show the expected area dependency. According to Ref.[225], ZBCP can also occur due to a step defect at the surface of YBCO.

Our main results concern the analysis and interpretation of the oscillation patterns in the conductance spectra. Tomasch and McMillan-Rowell resonances account for the oscillation frequencies that we observed. These resonances depend on temperature mainly through Δ and V_0, not the Fermi velocity (mostly constant). This explains why we see a decrease in phase and amplitude when approaching T_c, but not in the frequencies (proportional only to the velocity and thickness). The small phase shifts observed up to 500mT indicate that such fields are too weak to noticeably influence the gap of YBCO, as H_{c2} is of the order of several Tesla (see Sec.4.2.1).

The low frequency oscillations, around 20 V^{-1}, do not depend on the LCMO thickness. These agree with Tomasch resonances in the top YBCO layer (20 nm), and yield values of v_s that are very similar to those found in literature [36, 37]. The corresponding FFT peak is expectedly broadened, as TR are only periodic for higher order resonances.

As the bottom YBCO layer has a different thickness (30 nm), resonances could develop there as well (30-40 V^{-1} band). However, we did not find compelling evidence of these being present. It suggests that the bottom interface may not be transparent. This agrees with Ref.[27], where it is shown that removing the bottom YBCO makes no difference in the oscillation frequency. Our values of v_f in LCMO are in the same range as theirs ($v_f \approx 1.8\text{-}2.7\times10^5$ m·s^{-1}), and expectations from the literature [39].

However, we found a Fermi velocity in the 6nm LCMO that is both significantly lower and more variable than for the thicker LCMO (12 and 24 nm). Thickness variations likely play a role, since the 2 nm error on the thickness represents a third of the nominal value. Nonetheless, this is not enough to explain the decrease in v_f ($d_f \approx$15-20 nm without considering anything else).

The most likely is a reduction of v_f for low thicknesses, as the contribution of interface effects becomes prominent. More specifically, a charge transfer phenomena is known to occur with YBCO, creating a dead layer of $\approx$ 1nm at each interface by changing the carrier density [40, 26]. Consequently, we expect more pronounced local changes in the Fermi velocity for thinner LCMO layers.

We also considered other phenomena, but none provided a better explanation. For example, MMR in gold is possible too, and should yield frequencies around 21 V^{-1} (30 nm capping, $v_{Au} = 1.4 \times 10^6$ m·s^{-1} [143, p. 38]). Nonetheless, we have not found evidence of it happening in other trilayers nor in the YBCO/Au samples. Phenomena like de Gennes-Saint James oscillations [226], or crossed-Andreev reflections at domain-walls [227] are also ruled out, since they create features around and below the gap, whereas those in our measurements occur mainly above.

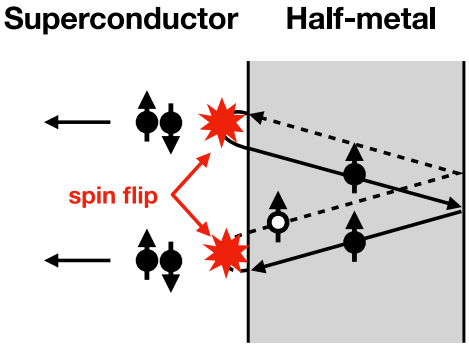

Figure 4.14: **McMillan-Rowell resonances in presence of spin-flip**
Spin-flip at the interface allows Andreev reflections, and the formation of equal spin correlations (red marks). These correlations can propagate in the ferromagnet, leading to McMillan-Rowell resonances.

Finally, the observation of MMR in LCMO implies that superconducting correlations are able to propagate in the ferromagnet. It also means that the Andreev-reflected particles stay coherent for at least one round trip across the ferromagnet. Since the material is half-metallic (or at least, strongly spin-polarized), it is very unlikely that singlets or FFLO triplets could survive that far. Hence, the propagating correlations are likely the spin-parallel triplets. These may be generated by spin-flip events during the Andreev process, due to inhomogeneities of the magnetization at the interface (more details in Refs.[196, 78] and Sec.2.5.2). The whole process of MMR, including spin-flip Andreev reflections, is sketched in Fig.4.14.

Such a process should happen at the top YBCO/LCMO interface, according to the arguments developed earlier. If the bottom interface is really opaque, this means that triplets cannot cross on the other side and mediate the Josephson effect. That possibility requires further investigation, and possibly an alternative take if one wants to make Josephson device.

4.5 Perspectives

Despite the reduction of the contact resistance to a few tens of Ohms, Josephson effects were still not visible. It might be due to either the tunnel Au/YBCO contact hiding the effect, or the bottom LCMO/YBCO interface being opaque. A way to verify the latter hypothesis could be to fabricate tunnel Au/LCMO/YBCO junctions, and look for Andreev features again. In the latter case, observing MMR or not

could help to assess the quality of the interface. Another option is to change the device geometry to 4 points, to completely avoid measuring the Au/YBCO contact resistance. This way, we could directly look for the Josephson effect. This requires to remove the gold capping, that protects the surface, and separating the top electrode into two. The fabrication becomes a bit more delicate, but still manageable. We have developed a prototype device for that, which is detailed in Sec.3.4.3. We did not manage to test it on trilayers though, due to a long-lasting technical issue experienced by our colleagues at UCM. Nonetheless, the activity has been carried on during the writing of the thesis by S. Mesoraca, who could fabricate and test such samples (inset of Fig.4.15a).

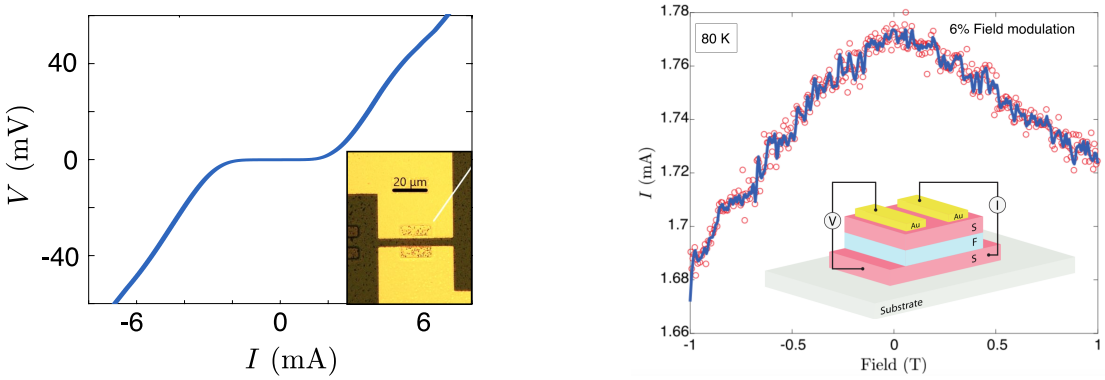

(a) Conductance curve

(b) Critical current

Figure 4.15: **Early 4-points junction result**
Patterning two contacts on top allows to avoid measuring the contact resistance (picture and sketch in insets). The current-voltage curve looks like a Josephson junction (4.15a). Its critical current depends on the field, but shows no Fraunhofer-like modulation (4.15b).

Without measuring the gold/YBCO interface, current-voltage curves that resemble those of a Josephson junction (Fig.4.15a), with a critical current that depends on the applied magnetic field (Fig.4.15b). However, it does not show a Fraunhofer-type modulation, which may be due to inhomogeneities of the critical current in the junction [30]. These results are still under investigation at the time of writing. To settle whether a Josephson current occurs in these heterostructures, Shapiro steps measurements are in progress with our partners at ESPCI. A positive result would be a first step towards realizing π-Josephson junctions and spin-valve devices in full oxide systems. These could help to probe the magnetic inhomogeneity responsible for triplets, as well as making good candidates for high-density, non-volatile superconducting memories.

Chapter 5

Magnetic pinning of vortices in SF bilayers

In the present chapter, we investigate how the presence of magnetic domains and skyrmions in a ferromagnetic film affects the magneto-transport of a strongly type-II superconductor. We found that both types of magnetic textures enhance the critical current and conductivity of the superconductor in a similar fashion. However, the enhancement is lower than expected for magnetic skyrmions compared to regular domains. As sweeping the external field affects the domain structure, we observed magnetic hysteresis appearing as well. The latter scales qualitatively like a simple magnetic pinning model. Though, in the presence of skyrmions, the magnetic pinning appears to be reduced compared to expectations from the model. We discuss the differences in terms of morphology, as skyrmions may hinder the vortices less than stripes or worms.

5.1 Introduction

There is already a vast literature about the interactions of superconductivity with magnetic domains and bubbles in superconductor-ferromagnet bilayers (SFB). In these, the stray magnetic field from the domains can locally destroy the order parameter (*domain-wall superconductivity*) [43, 44, 45], or affect the mixed state of the superconductor. In the latter case, the local field can nucleate vortices [46, 47], or pin the existing ones [48, 49, 47, 50, 51].

More recently, a few proposals were made specifically about magnetic skyrmions. These are magnetization inhomogeneities that are small (only a few 10nm), and more stable than magnetic domain-walls in ferromagnets. This makes them good candidates to carry information bits in novel magnetic memory designs (see Sec.2.2.3).

According to theory, skyrmions could interact with vortices by favoring their nucleation [52, 228], or at least interact with existing ones by inducing currents in the superconductor [55, 229, 52]. Conversely, the localized magnetic flux of the vortex lattice could be used as a template to imprint skyrmions in a ferromagnetic film [56]. Since they emit a stray field resembling that of magnetic dots, we suppose that

skyrmions should pin vortices in the same fashion [110]. Eventually, matching effects between the vortex and skyrmion lattices could occur, given that the latter is regular enough.

To investigate these phenomena, we measured the magneto-transport in several superconductor-ferromagnet bilayers (SFB). In these, different magnetic multilayers were deposited on the same amorphous Mo_4Si superconducting film. The ferromagnetic layers all have perpendicular magnetic anisotropy, with different domain structures of varying morphology and size. Two of them host skyrmions, in more or less dense arrangements. In the following, we study the effect of these layers on the mixed state of the superconductor. We investigate only the coupling through magnetic fields, not proximity effects.

5.2 Materials and methods

5.2.1 Materials

We measured three SF bilayers in which the superconductor is a 60nm layer of amorphous Mo_4Si, deposited on a Si(001) substrate. That superconductor is a strong type-II material, in which the vortices experience low intrinsic pinning [57]. These properties make it attractive to study extrinsic vortex pinning, such as the one due to stray fields from a ferromagnet. The estimated superconducting properties of the alloy at 3.5 K are summed up in Table 5.1.

T_c	$\mu_0 H_{c1}$	$\mu_0 H_{c2}$	ξ_{GL}	Λ
6.5 K	≈ 0.1 mT	7.9 T	6.4 nm	1210 nm

Table 5.1: **Estimated superconducting properties of Mo_4Si at 3.5 K**
Values estimated from the measurements and formulas in Sec.3.2.1. Here, we consider the effective penetration depth of the film $\Lambda = \lambda^2/d_s$.

We deposited three different metallic multilayers on top, consisting of repetitions of Pt/Co/X thin films, where X is Pt,Ir, or Ru. They all have perpendicular magnetic anisotropy. In addition to usual magnetic domains, the stacks containing Ir and Ru host skyrmions. Magnetic multilayers have the advantage of being easier to deposit than bulk materials like helical magnets, that also host skyrmions. They are also more versatile, since one can change the anisotropy and interfacial DMI by changing the materials, thicknesses and periodicity of the stack. The detailed composition of the samples that we used is summed up below.

- $Si(001)/Mo_4Si_{60nm}/AlO_{x,3nm}/Pt_{10nm}/(Co_{0.6nm}/Pt_{1nm})_{\times 5}/Pt_{3nm}$;
- $Si(001)/Mo_4Si_{60nm}/AlO_{x,3nm}/Pt_{10nm}/(Ir_{1nm}/Co_{0.6nm}/Pt_{1nm})_{\times 5}/Pt_{3nm}$;
- $Si(001)/Mo_4Si_{60nm}/Ta_{5nm}/Pt_{8nm}/(Pt_{1.2nm}/Co_{1.6nm}/Ru_{1.4nm})_{\times 4}/Pt_{3nm}$;

The S and F layers are separated by a Pt buffer layer, and for the first two of them, a 3 nm air-oxidized alumina layer. It serves as an insulating layer, to suppress the proximity effect. The absence of that layer does not significantly affect the results, as demonstrated in App.B.2. The Ta layer promotes adhesion, and is not superconducting. The total buffer thickness is 14 nm in all three. The deposition of the superconductor, alumina interlayer, and magnetic multilayers are done *ex-situ*.

5.2.2 Measurement methods

In that section, we review the different methods employed to measure the transport properties of the samples. We also discuss how we characterized the magnetic properties and morphology of the domain structures.

Transport measurements

To measure the layers in a controlled geometry, the samples were patterned by UV lithography into the cross-bridges described in Sec.3.4.1 The measured area is 200 μm long by 40 μm wide.

The samples are measured in 4-points configuration to avoid measuring the contact resistances. The magnetic field is applied perpendicular to the sample plane. A schematic of the measurement configuration is shown in Fig.5.1a. In the experiments, we apply a continuous current using a Keithley 6221 stabilized current source, and measure the voltage with a Keithley 2182 nanovoltmeter. In all the measurements, for a given value of the bias current, the measured voltage is averaged between positive and negative bias (see Eqn.5.1), to remove parasitic voltage offsets.

$$V(H, I) = \frac{V(H, +I) - V(H, -I)}{2} \tag{5.1}$$

To demagnetize the samples, we do magnetic field sweeps between positive and negative setpoints starting from 500 mT, the amplitude of which is reduced by 10% after each sweep. The field is shut down when the amplitude is low enough (1 mT). The magneto-resistance is then measured during field sweeps, done approximately at 100 mT/min. At this sweep rate, no parasitic induction effects were observed in the results. We also measured current-voltage curves for several external magnetic fields. The applied current values are logarithmically spaced to probe all the vortex transport regimes (at least 50 points per decade).

Magnetic force microscopy imaging

For all three layers, we did magnetic force microscopy (MFM) images at ambient temperature. They were done using a TeamNanotech high-coercive magnetic tip in an Asylum commercial AFM setup. The measurements were done in lift mode, at a distance of approximately 30 nm above the surface of the sample. The images are then processed using Gwyddion [230]. We removed the median plane and offset, then aligned the lines and corrected the horizontal marks.

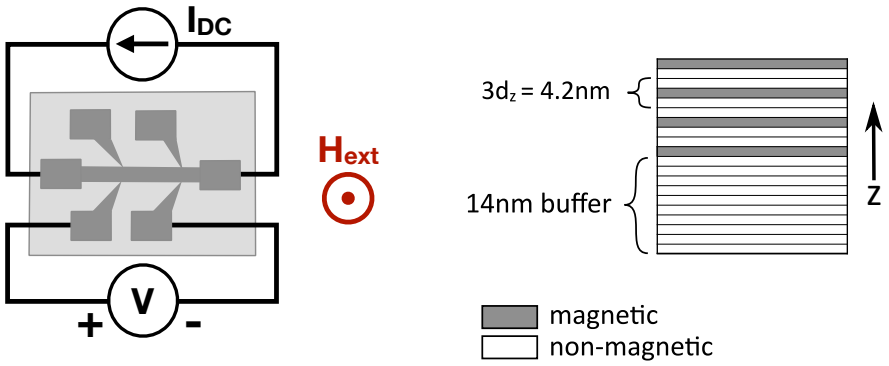

(a) Measurement configuration (b) Micromagnetic model for Pt/Co/Ru

Figure 5.1: **Measurement configuration and micromagnetic simulation** *The sample is measured in 4 pts configuration (5.1a). For micromagnetic simulations, the ferromagnetic multilayer is modeled as magnetic planes (in grey), separated by non-magnetic layers that play the role of the Pt or Ru interlayers, as well as the 14 nm Pt buffer (in white).*

Micromagnetic simulations

To calculate the stray magnetic field from the ferromagnetic layers at the surface of the superconductor, we did micromagnetic simulations with the open-source software Mumax3 [231].

First, we defined the magnetic system by setting its area to a 1000×1000 cells square in the x and y plane, of 2 μm side. The resolution is chosen so that the cell size stays below the exchange length in cobalt (3.8 nm,[232]), while remaining tractable by the computer. This limits the error of the simulation [231]. The thickness d_z of cells in the vertical direction then depends on the sample.

We model the system by magnetic material planes (one cell thick) separated by two layers of non-magnetic material (schematic in Fig.5.1b). The number of repetitions is the same as in the real sample. In Fig.5.1b, we present a schematic of the model sample of Pt/Co/Ru layers. In these, each repetition of the real sample is modeled by three layers, one of them being magnetic (cobalt). The total thickness $3d_z$ is made equal to that of one repetition in the real sample, so that $3d_z = d_{Co} + d_{Pt} + d_{Ir,Ru}$. This is to spare memory, and stay within the capabilities of our computer.

To calculate the stray field at the surface of the superconductor, we also added non-magnetic layers at the bottom to represent the buffer. For the magnetic layers, we considered a saturation magnetization of M_s =1.0 MA·m^{-1} for all the samples. It is that commonly measured at 300 K. That value is then increased by 30% to account for the low temperature [233][p.81], and corrected by d_f/d_{cell} to keep the same magnetization per unit area $M_s d_f$ as in the real sample.

The parameters we used for each system are summed up in Tab.5.2. Aside from M_s, the other parameters are close to those commonly found for these layers [58, 59]. These are not very important, since we only want to relax domain walls of

approximately 10 nm and calculate the demagnetizing field, not find the equilibrium structure. We took the same parameters in the three layers for simplicity.

Sample	M_s(MA/m)	z size (nm)	z cell number (nm)
$(Co_{0.6nm}/Pt_{1nm})_{\times 5}$	1.47	19.73	37
$(Ir_{1nm}/Co_{0.6nm}/Pt_{1nm})_{\times 5}$	0.9	25.1	29
$(Pt_{1.4nm}/Co_{1.6nm}/Ru_{1.2nm})_{\times 4}$	1.49	28	20

Table 5.2: **Micromagnetic simulation parameters**
Parameters common to all layers : $A = 10^{-11}$ $J{\cdot}m^{-1}$, $\alpha = 0.5$, $D_{ind} = 0.6$ $mJ{\cdot}m^{-2}$, *uniaxial anisotropy constant* $K_u = 0.4$ $MJ{\cdot}m^{-3}$ *along (0,0,1)*

The magnetization profile is then obtained using the MFM images. As the images for the Co/Pt sample were larger than 2×2 μm in size, they were cropped to fit the dimensions. All the images were then enhanced to a 1000×1000 resolution to fit that of the simulation. We then smoothed the image with a median filter (5 pixels window) to reduce the aliasing. A binary magnetization profile is then obtained by applying a threshold on the image ($m_z = \pm 1$). That profile was used as an initial magnetization for the calculation. They are input into the solver, and evolved for 10 ps to form approximately 10 nm wide domain-walls.

5.3 Results

5.3.1 Characterization of the magnetic layers

Before measuring how the presence of the ferromagnet affects the transport properties of the superconductor below, we needed to characterize the magnetic domain structure.

We did this first by measuring the magnetization hysteresis loops by anomalous Hall effect to know in what field range the domains are present in the layers. We then observed the magnetic domains with MFM images to obtain their morphology and characteristic size. We then calculated the stray field radiated by the domains with micromagnetic simulations by using the previously acquired MFM images.

Magnetic hysteresis

To know how the magnetization reverses, we measured the Hall effect in the normal state. We then assumed that it is mostly due to the anomalous Hall effect (AHE, see Sec.2.2.2), which is proportional to the mean out-of-plane magnetization of the film M_z. We carried measurements 300 K to correlate MFM images to the cycle, and at 10 K compare how it changes close to T_c. This will help to assess qualitatively what is the domain structure in the superconducting state. From the AHE measurements, we deduced the reduced magnetization $m_z = M_z/M_s$ of the three samples, that are presented in Fig.5.2. In these curves, we see that the coercive

and saturation fields increase strongly upon lowering the temperature in Co/Pt and Ir/Co/Pt layers. In Pt/Co/Ru, the saturation field seems roughly unaffected, and is only weakly hysteretic at 300 K, whereas hysteresis features become well developed at 10 K.

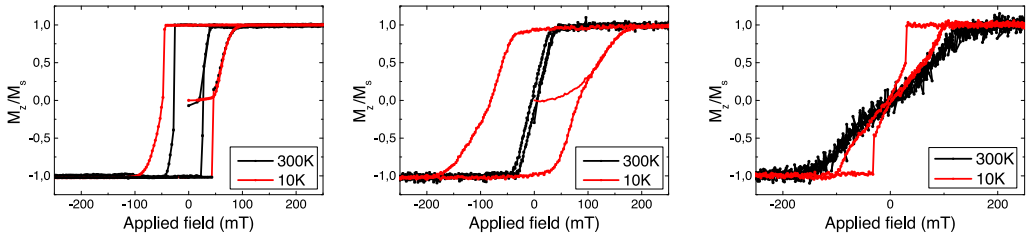

(a) $[Co_{0.6}/Pt_1]_{\times 5}$ (b) $[Ir_1/Co_{0.6}/Pt_1]_{\times 5}$ (c) $[Pt_{1.2}/Co_{1.6}/Ru_{1.4}]_{\times 4}$

Figure 5.2: **Magnetization loops at 10 and 300 K**
Estimated from the Anomalous Hall effect, centered and normalized to resistance value at saturation.

Magnetic force microscopy imaging

Since our MFM setups did not allow us to measure around T_c with high enough magnetic fields, we did images at ambient temperature instead. These were taken in perpendicular and positive field, along the increasing field branch of the magnetization loops. In Fig.5.3, 5.4, and 5.5, we show some selected MFM images of each sample at typical values of m_z. In these images, we observe the magnetization changing through the nucleation and expansion of domains parallel to the field, at the expense of those opposite.

In Co/Pt multilayers (Fig.5.3), the domains are very large, around 500nm at $m_z = 0$. They show disordered stripe-like structures at low $m_z \approx 0 - 0.25$, that get thinner as m_z increases. However, they never form regular stripes or skyrmions.

In Ir/Co/Pt (Fig.5.4), the structures are much smaller, between 100 and 200 nm. As opposed to Co/Pt, they tend to form short worms and isolated skyrmions when the sample is magnetized (from $m_z \approx 0.5$ up to $m_z \approx 1$). The images in that particular sample were noisy, so the presented maps were cleaned with a gaussian filter (5pts) to make the pattern more visible. Despite that, the images at high magnetizations are still hard to read, even if one distinguishes bubbles that could be skyrmions (unrelated to topography features or artifacts).

In Pt/Co/Ru multilayers (Fig.5.5), the patterns are again smaller than in Ir/Co/Pt, around 80 nm in width. It shows well defined labyrinthine patterns at $m_z \approx 0$. More interestingly, upon increasing the magnetization, they progressively turn into magnetic skyrmions. Compared to those seen in Ir/Co/Pt, the skyrmion arrangements are dense. They even show short-ranged hexagonal order over the first few nearest neighbors.

To obtain the typical domain size and periodicity in the images, we calculated the radially-averaged autocorrelation function (ACF) [234, pg. 373]. Sample curves are

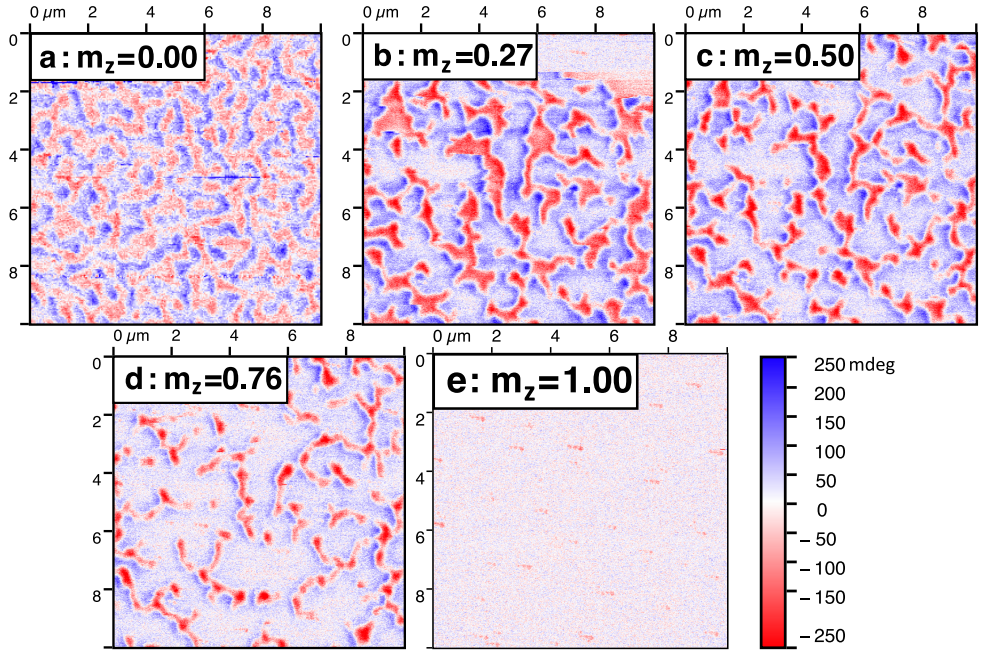

Figure 5.3: **MFM images in Co/Pt**
MFM images for $m_z \approx 0, 0.25, 0.5, 0.75$ *and* 1.

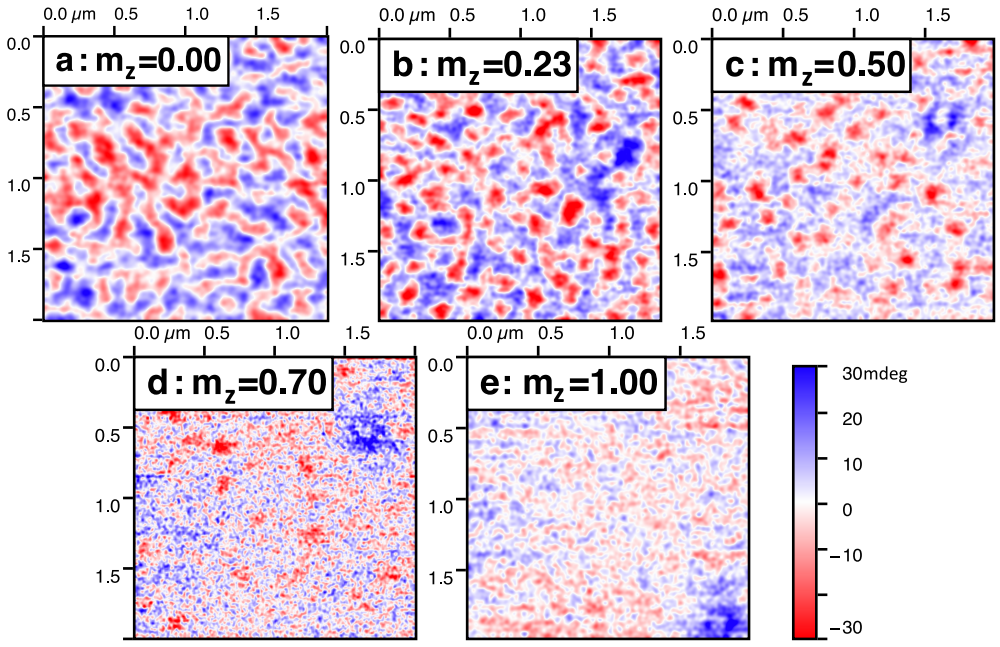

Figure 5.4: **MFM images in Ir/Co/Pt**
MFM images for $m_z \approx 0, 0.25, 0.5, 0.75$ *and* 1.

shown in Fig.5.6 for images in the demagnetized state. In these, the position of the first maxima gives the average domain periodicity. For each figure, the inset represents the evolution of that value with the magnetization. In these plots, we observe that the characteristic length of the ACF evolves with the reduced magnetization. At higher

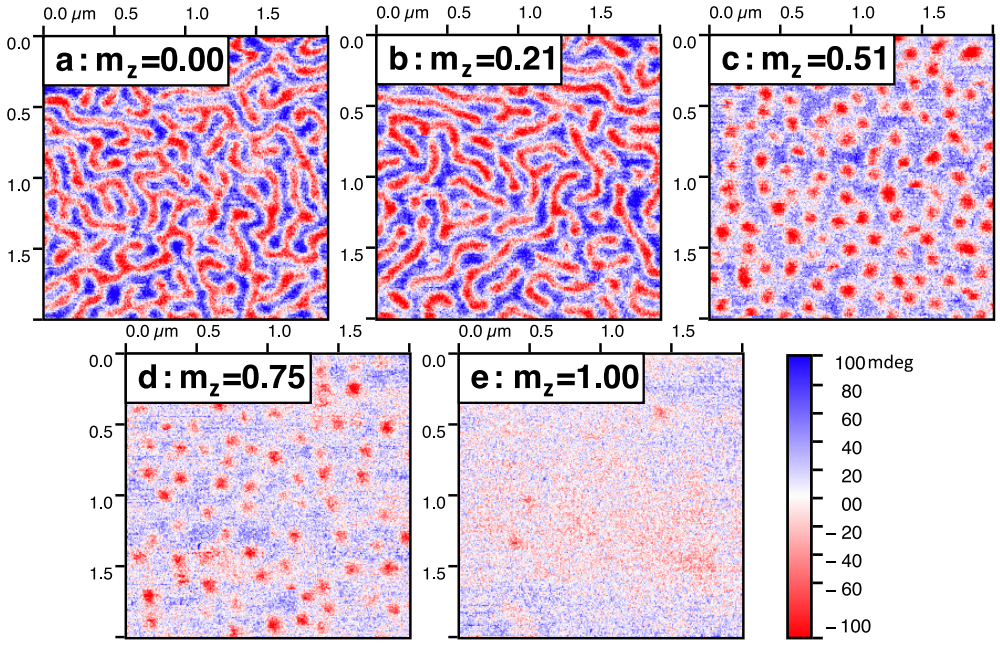

Figure 5.5: **MFM images in Pt/Co/Ru**
MFM images taken $m_z \approx 0, 0.25, 0.5, 0.75$ *and* 1.

values of m_z, it is not as well defined, especially in Ir/Co/Pt due to the noise (no clear peaks above $m_z \approx 0.5$). In Tab.5.3, we present the typical domain size (half the ACF characteristic length). These are coherent to what is seen in the MFM images.

Sample	$(Co/Pt)_{\times 5}$	$(Ir/Co/Pt)_{\times 5}$	$(Pt/Co/Ru)_{\times 4}$
Typical domain size (nm)	470	114	85

Table 5.3: **Characteristic size of the domains at** $\mathbf{m_z = 0}$

Stray-field calculation

To estimate the stray magnetic field from the domain structure, we did micromagnetic simulations by using the MFM images. The detailed method is described in Sec.5.2.2. Then, we extracted the z-component of the stray field at the surface of the superconductor. In Fig.5.7, we show the calculations corresponding to the $m_z = 0$ and $m_z = 0.75$ MFM images. The latter being close to saturation, we see the stray field in the large domains parallel to the applied field, as well as that in small worms and skyrmions.

We observe that the stray fields in Co/Pt are localized close to the walls due to the large domain size. They almost cancel in the center. When the domains shrink, the field becomes homogeneous and stronger in the center of the smaller domains. The stray field values are a bit lower in Co/Pt than in Ir/Co/Pt, which is due to the domains being larger. In Ir/Co/Pt, the field is more homogeneous inside the

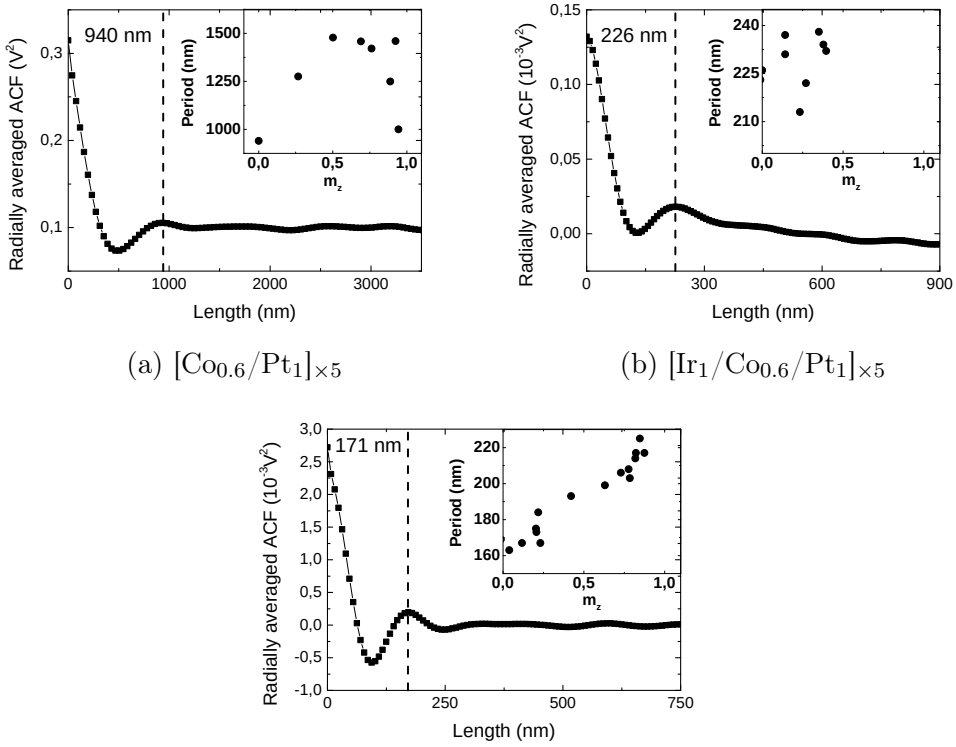

(a) $[Co_{0.6}/Pt_1]_{\times 5}$

(b) $[Ir_1/Co_{0.6}/Pt_1]_{\times 5}$

(c) $[Pt_{1.2}/Co_{1.6}/Ru_{1.4}]_{\times 4}$

Figure 5.6: **Radially averaged autocorrelation function at $\mathbf{m_z = 0}$**
The position of the first maximum in the ACF gives the average periodicity of the image. It generally increases with the magnetization, as the domains reduce in numbers.

domains, and does not seem to vanish in even in those parallel to the applied field. In Pt/Co/Ru, we observe a much stronger stray field inside the domains. This is logical, as the total Co thickness is approximately doubled and the domain size further reduced in that sample. It even reaches values of 100 mT in the small skyrmions.

5.3.2 Magneto-resistance in bilayers

In that section, we present magneto-resistance (MR) measurements of the three bilayers in the superconducting state, at 3.5 K. These were carried with an applied current of 1 mA (4.16×10^8 A·m^{-2} in the superconductor). The MR is measured in cycles : the sample is demagnetized, the field is then swept increasingly above the saturation field, then decreased down to negative values, and finally swept back to positive. The results are shown in Fig.5.8a,b,c. We compare these MR cycles to the magnetization loops at 10 K, represented below.

The measurements start from a demagnetized state, along the blue curve, by increasing the field from zero. The black/red curves correspond to the field decreas-

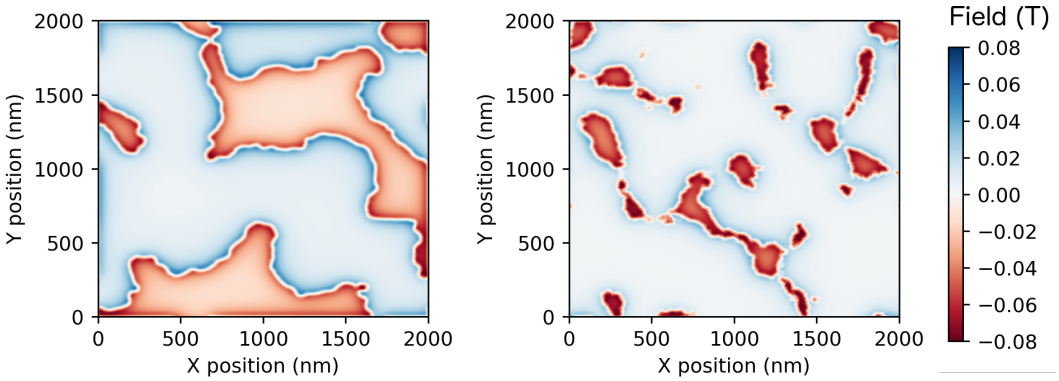

(a) $[Co_{0.6}/Pt_1]_{\times 5}$

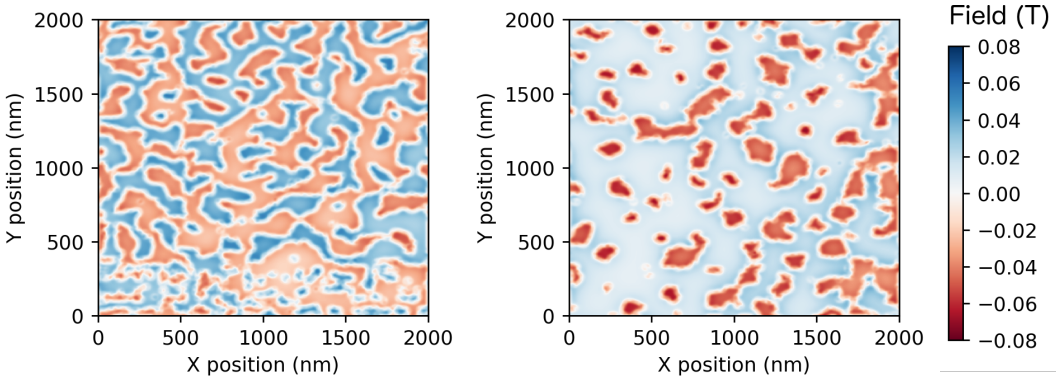

(b) $[Ir_1/Co_{0.6}/Pt_1]_{\times 5}$

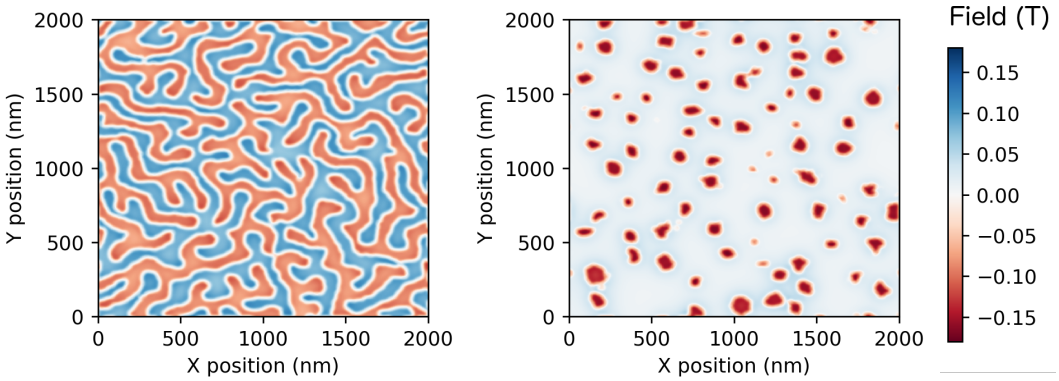

(c) $[Pt_{1.4}/Co_{1.6}/Ru_{1.4}]_{\times 4}$

Figure 5.7: **Stray-field calculations**
Stray-field simulations $m_z \approx 0$ (left) and $m_z \approx 0.75$ (right). For the Ir/Co/Pt sample, we picked the highest readable map, which was for $m_z \approx 0.5$.

ing/increasing branches. We also plotted the MR of the bare MoSi thin film (in green). The same convention is kept until the end of the chapter.

For all three samples, magnetic hysteresis appears in the resistance of the bilayers. It is correlated to the magnetization of the F layer, since the irreversibility occurs in the same field range in which the magnetization reverses. In the presence of magnetic

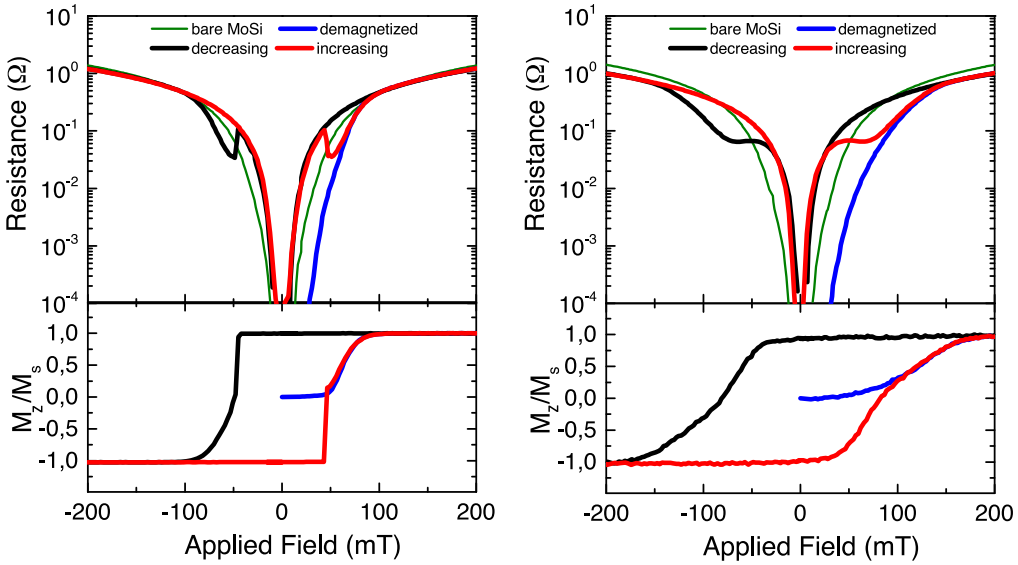

(a) $[Co_{0.6}/Pt_1]_{\times 5}$ (b) $[Ir_1/Co_{0.6}/Pt_1]_{\times 5}$

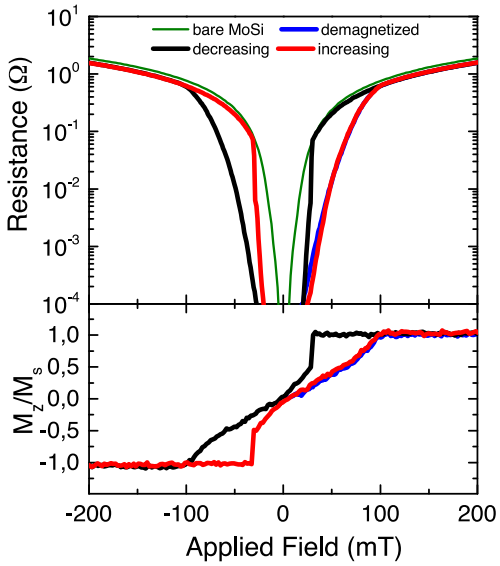

(c) $[Pt_{1.2}/Co_{1.6}/Ru_{1.4}]_{\times 4}$

Figure 5.8: **Magnetoresistances (3.5 K) and magnetization loops (10 K)** *The resistance of the bilayers becomes lower than that of the bare MoSi, and irreversible in the presence of magnetic domains ($|m_z| < 1$).*

domains ($m_z \neq \pm 1$), we observe a significant reduction of the MR compared to that in the saturated state ($m_z = \pm 1$, single domain). When the bilayer starts demagnetized (blue curve), we observe a lower resistance from zero field to saturation.

In addition, it is comparable to the bare MoSi in the saturated state, but only at high enough fields (above 100 mT). Below, in the Co/Pt and Ir/Co/Pt samples,

the bilayer becomes more resistive than the single superconductor for the branches of the cycles where $|m_z| = 1$. This is surprising since there should be no more stray magnetic fields, aside from those at the edges.

In addition, comparing it to the resistance of the bare MoSi reveals interesting features. The MR of the bilayer is systematically lower in the presence of domains. In the absence of domains, we observe that both are similar only at higher fields (above 100 mT). In the Co/Pt and Ir/Co/Pt samples, for lower values, the bare superconductor is less resistive than the bilayer. Since stray fields exist only at the edges when in the saturated state, we expected them to be comparable at all fields, which is not the case. In the Pt/Co/Ru bilayer, that effect is not observable, as the ferromagnet never stays saturated upon decreasing the field below 25 mT.

5.3.3 Critical currents in bilayers

In the previous section, we observed the apparition of irreversibility in the MR of the bilayers in the presence of magnetic domains. As the transport properties of Mo_4Si are due to vortex dynamics [57], we suspected that the hysteresis effect in the MR originate from flux pinning effects. To investigate that possibility, we measured current-voltage curves at 3.5 K for several applied magnetic fields along all the hysteresis loop. Some sample IV curves in the field-increasing branch are presented in Fig. 5.9a, 5.9b, 5.9c, and 5.9d up to values exceeding the saturation field of the layers.

These curves are highly non-linear, as expected from vortex dynamics (see Sec.2.1.5). We observe a linear slope at low currents, followed by a steep increase in voltage around a the critical current, then another linear regime. These correspond to the thermally-assisted flux-flow, frequent in amorphous superconductors [57], flux creep, and flux-flow regimes. However, the effect of the domain structure is not evident by just looking at the curves.

To better compare the effects, we calculated the critical current density. It is obtained by setting a voltage criterion of 5 μV, at which $j = j_c$ (dotted line in the plots). It is chosen to be well above the noise, while staying far from the flux-flow (linear) regime. Changing that criterion does not qualitatively affect the results. We also assume that most of the current goes through the superconductor, as the measured resistances in Sec.5.3.2 are much below the normal state resistance of the bilayers (several tens of Ohms). Thus, the section to calculate the critical current is that of the superconductor, identical in all three samples. The results that we obtain are presented in Fig.5.10.

The critical current in the bilayers depends on the magnetic history in the same fashion as the MR. In the saturated state, it is also similar to that of the bare superconductor (in green) except at low-fields. In the presence of magnetic domains, j_c increases compared to when the sample is saturated, and to the value in plain MoSi. The increase seems to have a similar magnitude in all three layers though, despite the significant change in size and morphology of domains. We strongly suspect that the domain structures create vortex pinning, which would result in similarly irreversible

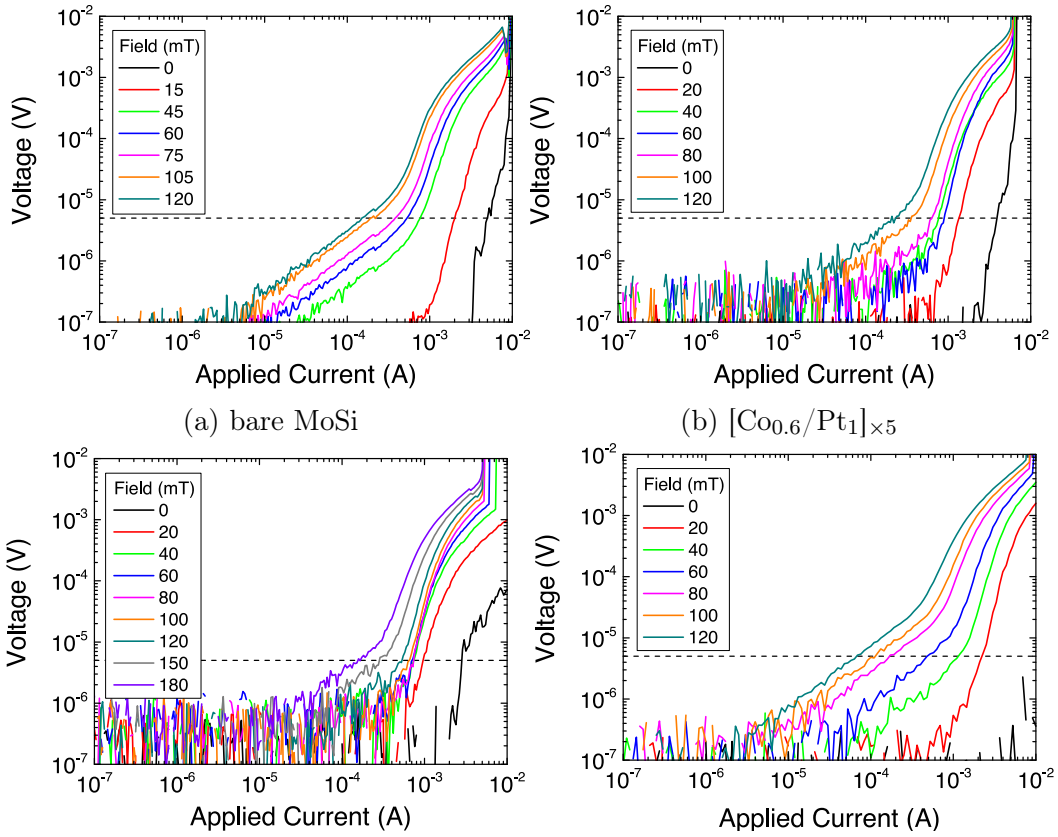

(a) bare MoSi (b) $[Co_{0.6}/Pt_1]_{\times 5}$

(c) $[Ir_1/Co_{0.6}/Pt_1]_{\times 5}$ (d) $[Pt_{1.2}/Co_{1.6}/Ru_{1.4}]_{\times 4}$

Figure 5.9: **Current-voltage curves at 3.5 K**
Sample current-voltage curves taken in the increasing field branch. We observe all three regimes of vortex pinning (TAFF, creep and flux-flow). The dotted line is the $5\mu V$ criterion for calculating j_c.

properties. In the next section, we compare our data to a simple magnetic pinning model in order to find out.

5.3.4 Magnetic pinning model

Model

To assess whether the critical current irreversibility comes from pinning, we used a simple 1D magnetic pinning model in the following. The analytical calculations were made by A. Buzdin[1] and A. Samokhvalov [2]. We then adapted the results to account for how domains changes in magnetic field, and did the numerical calculations.

We consider a superconductor-ferromagnet bilayer as represented in Fig.5.11a. The superconductor has a thickness d_s, and is separated from the ferromagnet by a distance a. We assume that the ferromagnetic layer is thin ($d_f \to 0$). Its domain

[1]LOMA Bordeaux, France
[2]Institute for Physics of Microstructures, Russian Federation

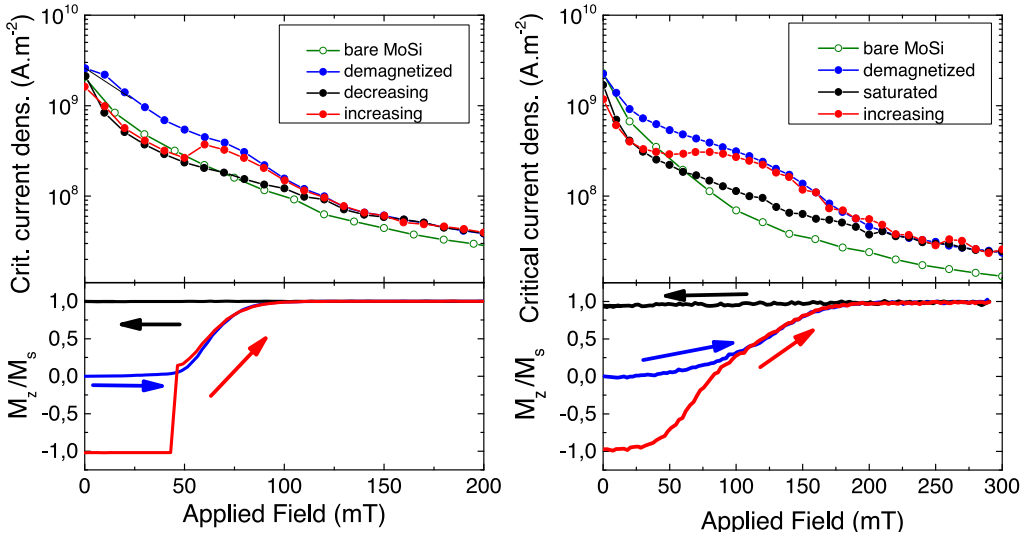

(a) $[Co_{0.6}/Pt_1]_{\times 5}$

(b) $[Ir_1/Co_{0.6}/Pt_1]_{\times 5}$

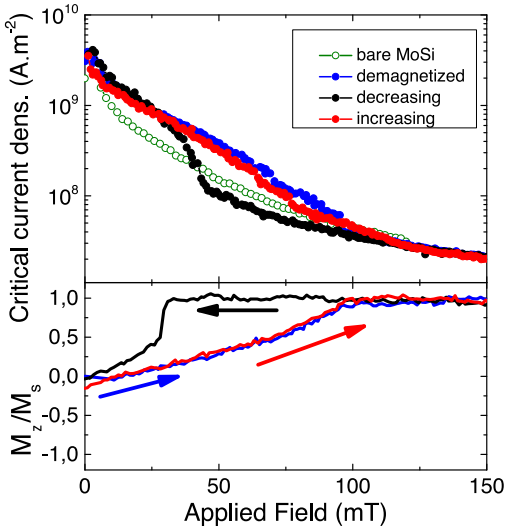

(c) $[Pt_{1.2}/Co_{1.6}/Ru_{1.4}]_{\times 4}$

Figure 5.10: **Critical current density measurements**
Like the MR, the critical current becomes irreversible in the presence of domains. It is enhanced compared to the saturated state and the bare superconductor.

structure consists of parallel stripes along y, with out-of-plane magnetization (along z). The up domains have width $w_+ = w$, and those opposite $w_- = L - w$, where L is the structure's periodicity. We neglect the domain wall width, so that the magnetization writes as a step-like function along x :

$$\mathbf{M} = M(x)\mathbf{e_z} \quad ; \quad M(x) = \begin{cases} M_s, & -w/2 + Ln \leq x \leq w/2 + Ln \\ -M_s, & w/2 + Ln \leq x \leq -w/2 + L(n+1) \end{cases} \tag{5.2}$$

Where $\mathbf{e_x}, \mathbf{e_y}, \mathbf{e_z}$ are the unitary vectors of the Cartesian frame. The Fourier expansion of the magnetization then writes :

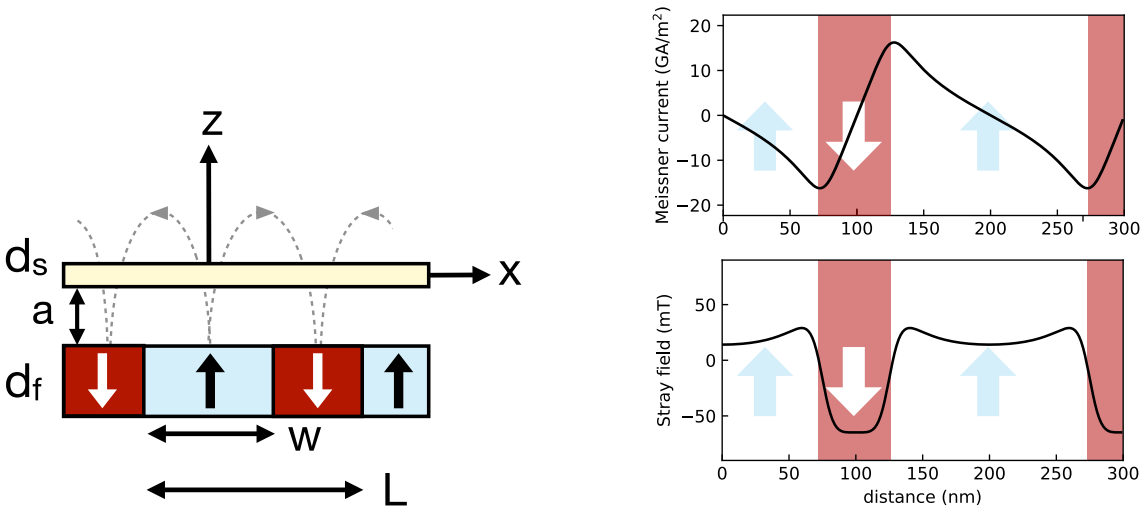

(a) Model schematic

(b) Calculation for $m = 0.5$

Figure 5.11: **Model schematic and sample calculations**
The system consists in thin S and F films of thicknesses d_s and d_f, separated by a distance a. The magnetization is out-of-plane, and represented by the arrows. M_s = 1.4 MA·m^{-1} ; d_f = 6.4 nm ; Λ=1210 nm ; a=14 nm

$$M(x) = \sum_{n=0}^{\infty} M_n e^{iqnx} \quad ; \quad M_n = \frac{1}{L}\int_{-L/2}^{L/2} M(x) e^{-iqnx} dx \quad ; \quad q = \frac{2\pi}{L} \tag{5.3}$$

$$M_{n=0} = M_s\left(\frac{2w}{L} - 1\right) \quad M_{n\neq 0} = \frac{2M_s}{\pi n}\sin\left(\frac{\pi n w}{L}\right) \tag{5.4}$$

Consequently, the magnetization of the F layer can be represented as :

$$\mathbf{M} = M_s \mathbf{e_z}\delta(z+a)\left\{\frac{2w}{L} - 1 + \frac{2}{\pi}\sum_{n\neq 0}\frac{\pi n w}{nL} e^{2i\pi n x/L}\right\} \tag{5.5}$$

$$\delta(z+a) = \int \frac{dp}{2\pi} e^{ip(z+a)} \tag{5.6}$$

Following that, the magnetic *sheet* current density $j_F = d_f \nabla \times \mathbf{M}$ only has a component on y, which is :

$$\mathbf{j_F} = -d_f \mathbf{e_y}\frac{\partial M}{\partial x}\delta(z+a) = -\frac{4iM_s d_f}{L}\mathbf{e_y}\int \frac{dp}{2\pi} e^{ip(x+a)} \sum_{n\neq 0}\sin\left(\frac{\pi n w}{L}\right) e^{i2\pi n x/L}; \tag{5.7}$$

As a result, the vector potential $\mathbf{A_F} = A_F(x,z)\mathbf{e_y}$ due to the ferromagnet is also directed along y and is obtained from the Maxwell equation :

$$\nabla \times \nabla \times \mathbf{A_F} = \mu_0 \mathbf{j_F} \implies -\nabla^2 A_F = \mu_0 j_F \tag{5.8}$$

$$A_F = \int \frac{dp}{2\pi} e^{ipz} \sum_{n\neq 0} A_{Fn} e^{iqnx} \quad ; \quad A_{Fn} = -\frac{2i\mu_0 M_s d_f}{\pi L} \sin\left(\frac{\pi n w}{L}\right) \frac{e^{ipa}}{p^2 - q^2 n^2} \tag{5.9}$$

$$A_F(x,z) = \frac{2\mu_0 M_s d_f}{\pi} \sum_{n\geq 1} \frac{1}{n} \sin\left(\frac{\pi n w}{L}\right) \sin\left(\frac{2\pi n x}{L}\right) e^{-2\pi n(z+a)/L} \tag{5.10}$$

As the effective penetration depth $\Lambda = \lambda^2/d_s$ exceeds the period of the magnetic texture L, we may neglect the screening of the magnetic field of the domains. The stray magnetic field B_F from the domain structure only has components along x and z. In thin film superconductors, we consider only the latter. At the surface of the superconductor ($z = 0$), it writes :

$$B_{Fz}(x,z) = \frac{4\mu_0 M_s d_f}{L} \sum_{n\geq 1} \sin\left(\frac{\pi n w}{L}\right) \cos\left(\frac{2\pi n x}{L}\right) e^{-2\pi n a/L} \tag{5.11}$$

The resulting *sheet* Meissner current density is then given by :

$$j_m d_s = \frac{-d_s}{\mu_0 \lambda^2} A_F(x, z=0) = \frac{-1}{\mu_0 \Lambda} A_F(x, z=0) \tag{5.12}$$

$$j_m(x) d_s = -\frac{1}{\mu_0 \Lambda} A_F = -\frac{2M_s d_f}{\pi \Lambda} \sum_{n\geq 1} \frac{1}{n} \sin\left(\frac{\pi n w}{L}\right) \sin\left(\frac{2\pi n x}{L}\right) e^{-2\pi n a/L} \tag{5.13}$$

In Fig.5.11b, we show a sample calculation of j_m and B_{Fz}, with different domain sizes. The field is mostly homogeneous in the center of the domains. The induced Meissner currents are maximum exactly at the wall, and cancel in the center. As these Meissner currents exert a force on the vortices, the pinning current given by:

$$j_p = max|j_m| \tag{5.14}$$

In the case of a small separation ($w \gg a$), it reduces to Eqn.5.15. Since the computation of the full sum is not resource-demanding, we did not use the reduced formula. However, it shows more clearly that j_p weakly depends on the domain size w. Thus, the results should be qualitatively similar in all the samples.

$$j_m(x) = -\frac{4M_s d_f}{\pi \Lambda d_s} \ln\left(\frac{2w}{\pi a}\right) \tag{5.15}$$

To compare with the experiments, we must account for the field evolution of the magnetic domains. For simplicity, we consider the periodicity of the domain structure L to be independent of m_z. Thus, changes in the magnetization occur by adapting sizes of the domains widths w_+, w_- accordingly. The magnetization of the film then writes as Eqn.5.16.

$$m_z = \frac{w_+ - w_-}{L} \quad ; \quad L = w_+ + w_- \quad \Longrightarrow \quad w_+ = \frac{L(m_z+1)}{2} \tag{5.16}$$

To simulate our bilayers, we set the value of L to that observed in the MFM images at $m_z = 0$. The value of M_s is that measured at 300 K (Sec.3.3.2). At low temperature, it may increase by 20-30% depending on the multilayer [233, p.81-82]. The field evolution of m_z is then given by magnetization curves deduced from Hall effect measurements. Finally, we calculate the pinning current at each point using Eqn.5.13 and Eqn.5.16.

Comparison to experimental data

Now, we compare the results of the model to the experimental data. In the measurements, a significant proportion of the critical current comes from *intrinsic* pinning, that is due to defects. Consequently, we calculate $j_c(bilayer) - j_c(MoSi)$ in order to isolate the contribution due to the magnetic domains. It is presented in Fig.5.3.3, along with the results of the simulation in the middle row. The magnetization curves are also plotted at the bottom, for direct comparison.

Surprisingly, the amplitudes of the theoretical values are between one and two orders of magnitude larger than those measured. But as suggested from Eqn.5.15, the results are comparable in the three samples despite the large differences in domain size. Qualitatively, the scaling with the applied field and the magnetic history of the experimental data and the model mostly coincide. Still, we observe a few differences to be discussed. In the experimental data, the blue dotted line represents the behavior expected from theory.

In Co/Pt, the increasing and decreasing branches behave in good agreement with the theory. In the demagnetized curve though, there is a peak around 10mT whereas a plateau is predicted, as indicated by the blue dashed line. This could be an additional effect, since the curve merges with the field increasing one far from the peak, as in the model (above 50 mT).

The predicted scaling in Ir/Co/Pt on the other hand is remarkably similar to that observed in the experiment.

In the Pt/Co/Ru sample, the j_c hysteresis seems narrower compared to the expectations. It steadily decreases from zero field to saturation in the demagnetized and increasing field curves, whereas those of the model stay on the same level and drop more abruptly close to saturation. The difference with expectations is indicated by the dashed line in the experimental data. In the calculations, as in experiments, the demagnetized and increasing curves superimpose.

In the three samples, we observe negative values at low fields when the ferromagnet is saturated. It is less visible in the Pt/Co/Ru sample though, as the magnetization does not stay homogeneous below 25mT. That feature is similar to what is seen in the MR curves of Sec.5.3.2.

In addition to the critical current, we estimated the pinning force density $F_p = (j_c - j_{c,MoSi})B$ due to the presence of the magnetic layer for both the data and

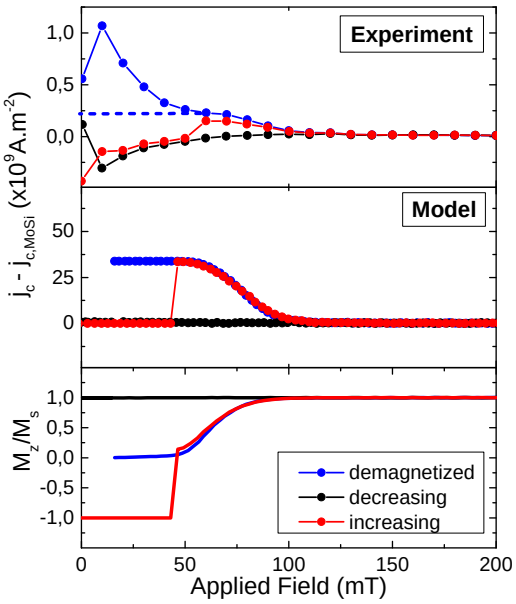

(a) $[Co_{0.6}/Pt_1]_{\times 5}$

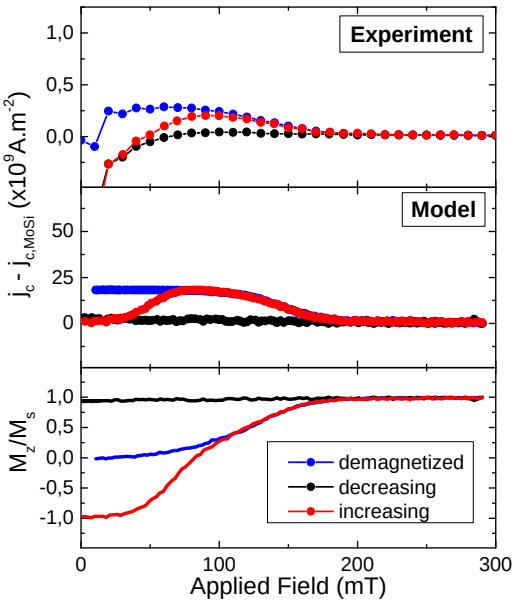

(b) $[Ir_1/Co_{0.6}/Pt_1]_{\times 5}$

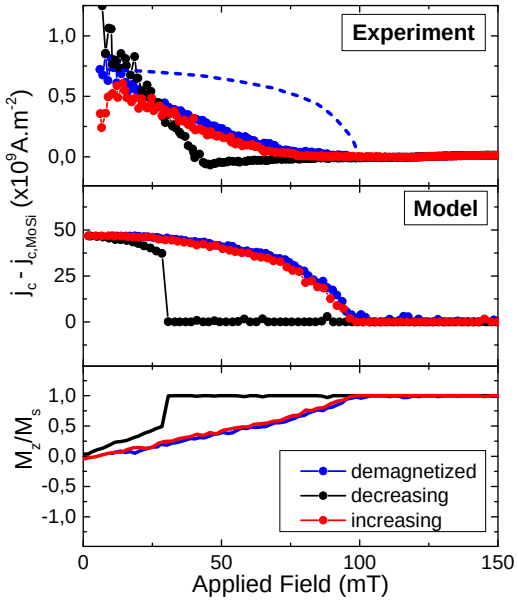

(c) $[Pt_{1.2}/Co_{1.6}/Ru_{1.4}]_{\times 4}$

Figure 5.12: **Critical current enhancement and simulation**

simulations. This yields the data presented in Fig.5.13. In the experimental data (top row), a blue dotted line serves as a guide to where the demagnetized curve should fall according the model (bottom row). We observe that the relative amplitudes of the curves to one another are on good agreement with that predicted by theory. The maximum of the pinning in Co/Pt and Pt/Co/Ru are similar, and slightly below that in Ir/Co/Pt. The scaling in the experimental data mostly agrees with that of the model. The only significant differences are the 10 mT maximum in Co/Pt, and

the shifted maximum in Pt/Co/Ru. In the latter, the decrease in pinning coincides with the change from worms to skyrmions seen in the MFM images (Fig.5.5).

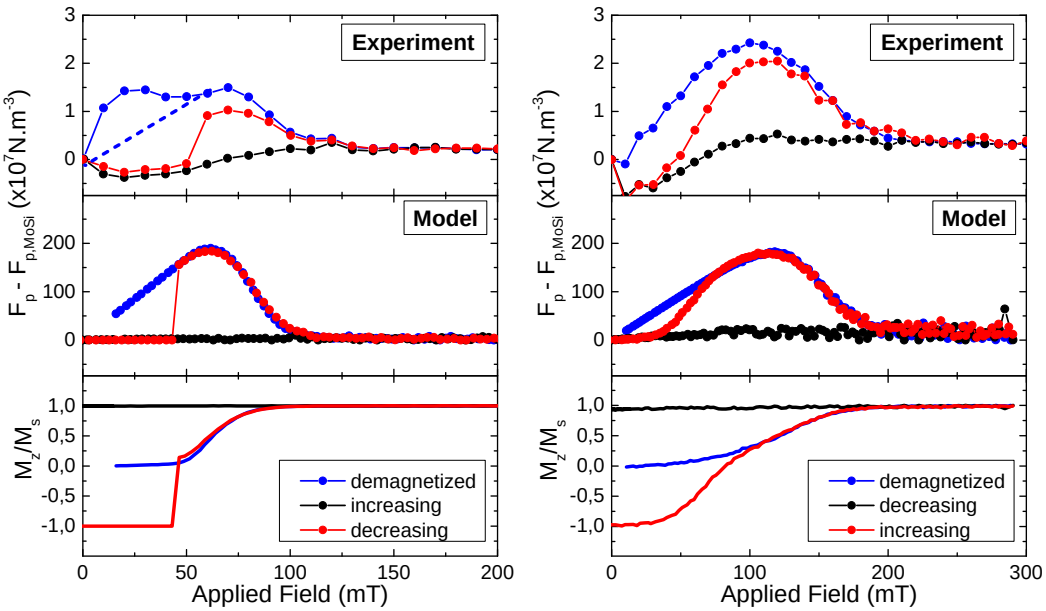

(a) $[Co_{0.6}/Pt_1]_{\times 5}$ (b) $[Ir_1/Co_{0.6}/Pt_1]_{\times 5}$

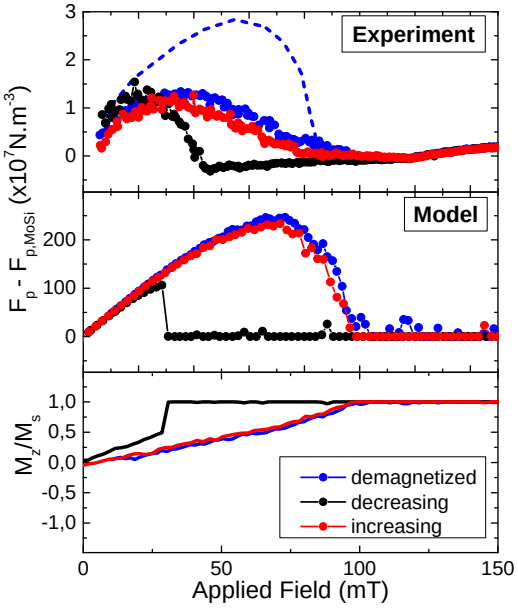

(c) $[Pt_{1.2}/Co_{1.6}/Ru_{1.4}]_{\times 4}$

Figure 5.13: **Scaling of the pinning force of the magnetic structures**

5.4 Discussion

Several phenomena could explain the lower resistances and hysteresis in the presence of magnetic domains. Proximity effect is dismissed, since the three layers behave

the same, and two of them include a 3 nm insulating barrier between the S and F layers (more details in App.B.2). The other possibilities we considered are the destruction of the order parameter by the stray field of the domains (domain-wall superconductivity) or vortex pinning.

To locally destroy superconductivity, the local field must be comparable to the upper critical field H_{c2} [43]. Since the stray field from the domains ranges mostly from 20 mT to 100 mT, the total field $|H_{ext} + H_{Stray}|$ does not exceed 300 mT. Compared to $\mu_0 H_{c2} \approx 7$ T, this is way too low to revert the bilayer to the normal state. This is further developed in App.B.1 using a resistor network toy model.

Flux pinning effects are the most plausible cause of the critical current enhancement and MR irreversibility. The stray field from the domains generating additional pinning explains why the critical current increases (and the MR reduces) in the field range when the magnetization is not homogeneous. Since the latter shows magnetic hysteresis, so do the pinning force and transport properties of the bilayer. Additionally, the scaling with field and magnetic history of j_c and F_p is qualitatively similar to that predicted by our simple pinning model. The peculiarities observed for the Co/Pt and Pt/Co/Ru samples may be explained by geometrical effects. First, the unexpected maximum of the critical current and pinning force occur around 10-20 mT. It may be due to a matching effect, since the average domain size in the images (470 nm) is commensurable with the average inter-vortex distance ($\sqrt{\Phi_0/B} \approx 450$ nm). Such an effect is not observed in the other samples, since the matching field in Ir/Co/Pt (114 nm) and Pt/Co/Ru (85 nm) should be well past their saturation field (150-200 mT or more).

Second, we observed a reduction of pinning in Pt/Co/Ru when the labyrinth domains turn into skyrmions (30-40 mT). This differs from the stripe model, that predicts a maximum around 75 mT. We suppose that it may be due to the circular shape of skyrmions. As the structures are narrow, the field is homogeneous away from the domain walls (Fig.5.5). Hence, vortices are trapped below the domains parallel to field, in which the field is parallel to their flux (imposed by the external field). Those opposite, like worms and skyrmions, repel the vortices as they oppose the flux in the core [235]. One may see the situation as "free" vortices in an array of repulsive pins. Hence, evenly distributed round structures (skyrmions) are easier to bypass than more elongated ones like stripes. This could explain why the estimated pinning force scales lower than the stripe model when worms collapse into skyrmions. In the other two samples, the stripe approximation holds over a broader range of fields, and scales closer to expectations.

As in the model, the enhancements due to the magnetic structures are comparable in the three samples, and weakly depend on the domain size. However, the predicted values are two orders of magnitude above those observed in experiment. Uncertainties on the exact values of M_s at 10 K and λ each reasonably accept a 10-20% relative error, which does not explain such a high difference. Several limitations of the model altogether may explain these. First, it assumes parallel stripes, whereas the real structures are shorter and disordered. They can be locally bypassed, or guide the motion of vortices in the regions where they are not perpendicular to the Lorentz force. Additionally, the model neglected the width of the domain walls, which overestimates

a bit the stray field, and thus j_p. Thermal depinning and vortex-vortex repulsion are also unaccounted for in the model. These are observed in the transport (Fig.5.9), and contribute to weaken the pinning too.

The last point to discuss is higher resistance and lower j_c in the saturated bilayer compared to the bare Mo_4Si. It could originate from additional vortices appearing due to the presence of the ferromagnet. Its magnetization favors the nucleation of vortices with a parallel flux through magneto-static coupling (see Sec.2.3.2 and Ref.[161]). This, added to the demagnetizing fields at the sample edges, could help nucleating vortices, thus increasing the dissipation.

5.5 Conclusion and outlook

To summarize, the magnetic hysteresis appearing in the magneto-resistance and critical currents of our SF bilayers originates from vortex pinning. In the presence of domains, the stray magnetic field pins the vortices, reducing the dissipation compared to the saturated state and the bare superconductor. A simple pinning model on a 1D stripe structure qualitatively explains the observed scaling with magnetic field and history. Overall, the amplitude of the critical current does not strongly depend on the domain size, in both the experiments and the model. A few additional features were observed, which are attributed to the domain morphology. In the presence of dense skyrmion ensembles, we observed a strong reduction of vortex pinning compared to expectations from the stripe model and the other samples. We attribute that to the possibility of vortices to move in between skyrmions more easily than with elongated stripes or worms. Matching effects were not observed, since the skyrmions and vortices have opposite polarities. To observe these, one could use bulk chiral magnets such as FeGe [69], in which hexagonal order is present over much longer ranges. Since we observed that skyrmions hinder the motion of vortices, moving vortices may also drag skyrmions [53]. This could be observed more easily in low-temperature MFM than in transport experiments, given that one can apply a current. In both cases, one might prefer another superconductor in which the vortex flux is more concentrated than in Mo_4Si. Niobium films ($\xi \approx 38$ nm; $\lambda \approx 39$ nm [236, ch.12]) or alloys like Nb_3Si or V_3Si (for both $\xi \approx 3$ nm, $\lambda \approx 60$ nm [65][Ch. 53.3]) are good candidates. These values may vary depending on preparation though, as reported in Refs. [237, 238, 239], and likely require sub-λ thicknesses to prevent intrinsic pinning from masking the magnetic contribution. One might also use materials with larger skyrmions, like Pt/Co/Ta or Pt/Co/MgO multilayers that host skyrmions with radii of 100-200 nm [64], so that the size is commensurate with λ and/or ξ while remaining below a few 100 nm.

Chapter 6

Anomalous transverse resistance of SF bilayers

Hall effects in magnetic materials are often useful to study the magnetization [144], or topology [240] among others. On the other hand, in type II superconductors, they result from vortices moving sideways from the course imposed by the Lorentz force[113]. In the present chapter, we explore the Hall effect of the SF bilayers studied in Chap.5, both in the superconducting and normal states. Specifically, we investigate if there are signs of the apparition of skyrmions in the Hall voltage below T_c. In the superconducting state, we found an unexpected *odd-parity* transverse voltage appearing when the field is tilted from the normal direction of the films. It correlates with the presence of magnetic inhomogeneities in the bilayers, but not only since it exists exclusively for intermediate angles between in-plane and out-of-plane orientations. We then discuss the possible origins of tour observations. These include guided motion of vortices, due to the morphology of the magnetic structures, and the motion of skyrmions due to the superconducting vortex flow.

6.1 Introduction

In type-II superconductors, transverse voltages appear when vortices deviate from the course imposed by the Lorentz force of the current (see Sec.2.1.4). In bare superconductors, they originate from the superfluid Magnus force [88, 113, 114], or other causes like pinning [120]. These are usually *odd* with magnetic field, and can even reverse sign in cuprates [241] and amorphous materials like MoSi [117, 121]. Nevertheless, these effects are very small if observable, and often shrouded by parasitic effects due to inhomogeneities of superconductivity, defects and asymmetries in the measurement device, that deviate the vortex motion [62, 63, p. 154]. These usually create *even* transverse voltages. However, vortices can also be deviated artificially by deliberately making the pinning force anisotropic. In SF systems, it is the case for arrays of magnetic dots [61, 168, 110], or parallel stripe domains in plain films [51, 165, 171]. These deviations of the vortex motion by the magnetic structures also leads to measurable transverse voltages.

In Chap.5, we studied superconductor/ferromagnet bilayers in which the ferromagnetic layer hosts domain structures with various morphologies : mazes, stripes, and interestingly skyrmions. The latter can be detected using the topological Hall effect in ferromagnets [145, 146]. On the other hand, it may be difficult to detect or isolate from the normal and anomalous components [146, 66]. Thus, we investigate whether the formation of skyrmions also leaves footprints in the Hall effect of the superconducting layer. In that case, it would be due to the interaction of skyrmions with moving vortices.

To that end, we measured longitudinal and transverse magneto-resistances (MR) with tilted magnetic fields. We investigate the bare superconductor first, then study the Hall effect in the bilayer. To see whether these relate to changes in domain morphology, we carried MFM imaging at low temperatures and micromagnetic simulations.

6.2 Materials and Methods

In the following, we present the superconductor and the ferromagnetic multilayers that we used. Then, we detail the measurement method, with an emphasis on the orientation of the current and the field. We finally give information about how we characterized the domain structure, both in MFM imaging and simulation.

6.2.1 Materials

The bilayers measured in this chapter are the same as measured in Chap.5. They consist of a 60 nm layer of amorphous Mo_4Si superconductor, on which several magnetic multilayers are deposited. It is a strong type-II material, with low intrinsic vortex pinning [57]. We summed up the properties of the alloy in Tab.6.1, estimated at 5 K from the values of Sec.3.2.1.

T_c (K)	$\mu_0 H_{c1}$ (mT)	$\mu_0 H_{c2}$ (T)	ξ_{GL} (nm)	Λ_{eff} (μm)
6.5	$\approx$1 or less	4.0	9.1	2.4

Table 6.1: **Superconducting properties of Mo_4Si at 5 K**

We considered the two following SF bilayers :

- $Si(001)/Mo_4Si_{60nm}/AlO_{x,3nm}/Pt_{10nm}/(Co_{0.6nm}/Pt_{1nm})_{\times 5}/Pt_{3nm}$;
- $Si(001)/Mo_4Si_{60nm}/Ta_{5nm}/Pt_{8nm}/(Pt_{1.2nm}/Co_{1.6nm}/Ru_{1.4nm})_{\times 4}/Pt_{3nm}$;

Both have perpendicular magnetic anisotropy, but very different domain structures. In Pt/Co/Ru, labyrinthine domains and magnetic skyrmions with a size of 80-90 nm are observed. In Co/Pt, the domains are much larger (around 500 nm at $m \approx 0$), have disordered shapes, and do not form skyrmions as far as we observed (see Sec.3.3 and Sec.5.3.1). It also has a stronger perpendicular anisotropy, which makes it less sensible to in-plane fields.

6.2.2 Transport measurements

We studied magneto-transport in these samples using the planar bridge geometry described in Sec.3.4.1. The measurements are done in 4-points configuration, as shown in Fig.6.1a. The measured area is 200 μm long and 40 μm wide. We applied magnetic fields at several angles θ from the out-of-plane direction. Two geometries were used, one in which the field and current are always coplanar (Fig.6.1c) and another in which they are perpendicular (Fig.6.1b). The samples are biased in current, applied along x, while the longitudinal (V_{xx}) and transverse (V_{xy}) voltages are recorded simultaneously during the field sweeps, using two nanovoltmeters. Each data point was obtained by applying a positive and negative bias, then averaging the measured voltages $V = \frac{V(I)-V(-I)}{2}$ to remove parasitic offsets. Before each field sweep sequence, the sample is demagnetized at the same angle θ as for the measurement. The demagnetization procedure consists in sweeping the field between positive and negative setpoints starting from 500 mT, and reducing the sweep amplitude by 10% each time, until it reaches 1mT.

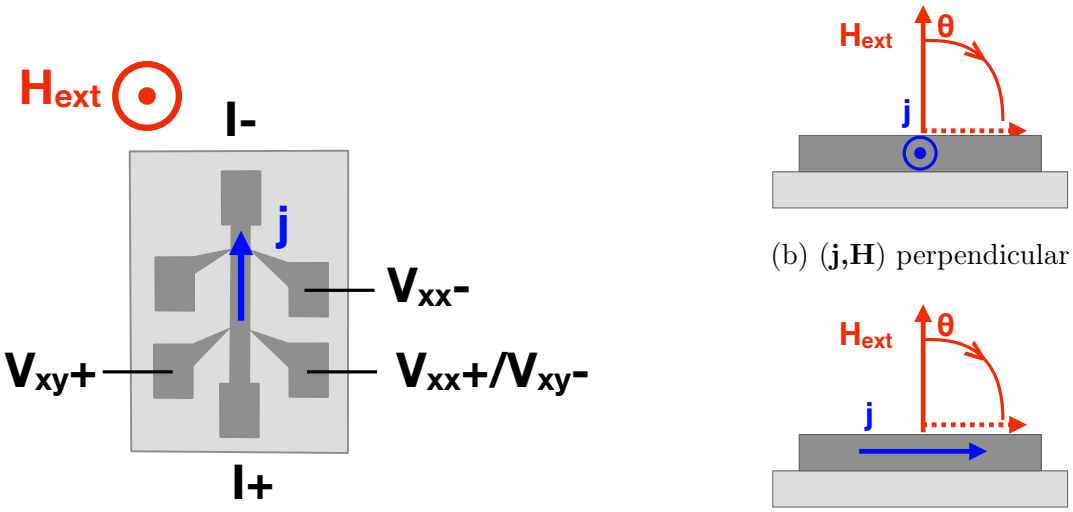

(a) Measurement configuration

(b) (**j**,**H**) perpendicular

(c) (**j**,**H**) coplanar

Figure 6.1: **Contact configuration and field/current orientations**

6.2.3 MFM imaging method

We did low-temperature Magnetic Force Microscopy (MFM) at 77 K using a cryogenic *Attocube* setup, cooled with liquid nitrogen. The setup generates magnetic fields up to 20-30 mT in perpendicular, and up to 200 mT in the sample plane using two separate coils and power sources. In that setup, the samples were put together and measured one after the other. In both measurements, we used a *TeamNanotech* high coercive magnetic tip. Scans are done in lift mode, at a typical height of 30 nm above the sample.

6.2.4 Micromagnetic simulations

In addition to the MFM images, we carried micromagnetic simulations of the multilayers behavior in a tilted fields using the open source software Mumax3 [231].

For both simulated samples, the area is defined as a regular 256×256 cells square of 1 μm side in the x and y directions. In z, we model the multilayers by magnetic material planes (one cell thick) separated by two-cell thick non-magnetic regions (Pt or Ru layers). The periodicity and number of repetitions are then the same as that of the real sample. The z cell size is thus defined as $d_{cell} = (d_{Pt} + d_{Co} + d_{Ru})/3$.

The magnetic parameters used for each are detailed in Tab.6.2. We considered a saturation magnetization M_s =1.0 MA·m^{-1} for the two samples, which is that commonly measured at 300 K. That value is then increased by 30% to account for the low temperature [233, p.81], and corrected by d_f/d_{cell} so that the magnetization per unit area $M_s d_f$ is the same as the real sample. The other parameters are those commonly used for these layers [58, 59], aside from the anisotropy constant K_u in the Pt/Co/Ru sample. Since we could not estimate it properly, we arbitrarily chose it so that the anisotropy is still out-of-plane , but small : $K_{eff} = K_u - \frac{1}{2}\mu_0 M_s^2 \approx 0$. For more details, please refer to Sec.3.3.

Sample	$M_{s,simu}$ (MA·m^{-1})	d_{cell} (nm)	K_u (MJ·m^{-3})	D_{ind} (mJ·m^{-2})
$(Co/Pt)_{\times 5}$	1.29	0.533	1.5	0
$(Pt/Co/Ru)_{\times 4}$	1.49	1.42	1.4	1.0

Table 6.2: **Micromagnetic simulation parameters**
Parameters common to all layers : uniaxial anisotropy along (0,0,1) ; exchange stiffness $A = 10^{-11} J{\cdot}m^{-1}$, Gilbert damping α=0.5

The simulations start from a random magnetization state, which is relaxed at zero field to form the equilibrium domain structure, using the *relax()* method. The field is then incremented, and the magnetic configuration relaxed again. The ramp goes from zero field (demagnetized) to +500 mT then -500 mT. We set the temperature in the simulation to 5 K, as in the measurements.

6.3 Transverse resistance in SF bilayers

In this section, we present the results of magneto-resistance (MR) measurements in the SF bilayers at 5 K. These include the longitudinal and transverse MR, with the field gradually tilted away from the out-of-plane direction. We focus on the observation and discussion of the transverse ("Hall") component R_{xy}, as the behavior and origin of the longitudinal resistance R_{xx} was already discussed in terms of magnetic vortex pinning in Chap.5. We show that R_{xy}, similarly the longitudinal one, it becomes irreversible due to the presence of domains. More interestingly, a signal of *odd parity* with magnetic field appears exclusively when the latter is tilted, and is maximal around 45°. As we shall see, it does not depend only on the value of m_z in

the ferromagnet, since the large changes in R_{xy} are not related to comparable effects in the magnetization curves, as revealed by anomalous Hall effect (AHE) above T_c.

6.3.1 2D behavior of MoSi

Before investigating the bilayers, we studied briefly the longitudinal and transverse MR of the bare Mo_4Si. The measurements were carried out at 5 K, with a bias current of 1 mA (4.17×10^8 A·m^{-2}). The field is swept at an angle θ from the out-of-plane direction. To change the orientation of the in-plane component, we applied the field in the coplanar ($j \parallel H_\parallel$) and perpendicular ($j \perp H_\parallel$) configurations (sketched in Fig.6.1). We present the results respectively in Fig.6.2b and Fig.6.2a, plotted against the out-of-plane field component $H_\perp = H\cos\theta$.

For both configurations, the longitudinal resistance R_{xx} is almost linear with the applied field. All the curves collapse when plotted versus the out-of-plane field. In addition, there are no differences between the coplanar and perpendicular field configuration. We deduce that the in-plane component $H_\parallel$ has no effect on the bare superconductor. The transverse resistance R_{xy} shows an essentially similar behavior. We note that the parity of these curves is *even* with magnetic field. The detailed shape of the curve varies from sample to sample, but is generally parabolic, sometimes with irregularities. This even signal originates from parasitic guided vortex motion [63, p. 175], contacts misalignment, or current redistribution [242] among others. We dismiss them in the rest of the chapter.

6.3.2 Anomalous transverse resistance in SF bilayers

Now, we present MR measurements in the SF bilayer containing Pt/Co/Ru as the ferromagnet. In Fig.6.3, we compare the results with fields angled at 0° and 45°. They are done in the perpendicular (j, H) configuration, at 5 K. We also present $m_z = M_z/M_s$ curves in the bottom row, estimated by AHE above T_c (0.5 mA, 10 K).

In the R_{xx} curves, the resistance is reduced in the presence of magnetic domains, and becomes irreversible like the magnetization loops of the ferromagnetic layer. As the domain structure changes with the applied field, the curves become irreversible. These properties originate from magnetic pinning, as discussed in Chap.5. For R_{xx} and m_z, there are only minor differences between the 0° and 45° measurements. Surprisingly, this is not at all the case for the transverse resistance.

At 0°, the R_{xy} measurement also presents a magnetic hysteresis loop, which is reminiscent of that observed in the R_{xx} curves. Note that it is *even* with the applied magnetic field. The hysteresis shows bumps in the field ranges where $m_z \approx 0.5$ in the magnetization curves. We then measure the same loop, but with a magnetic field angled at 45°. Unlike R_{xx} and m_z, the shape of the R_{xy} curve is significantly altered. It still shows an irreversibility in the presence of domains, but the bumps now seem to point in opposite directions. It looks like the parity is switching to *odd*. On the other hand, the branch that starts from a demagnetized state (in blue) looks similar to that in the 0° measurement.

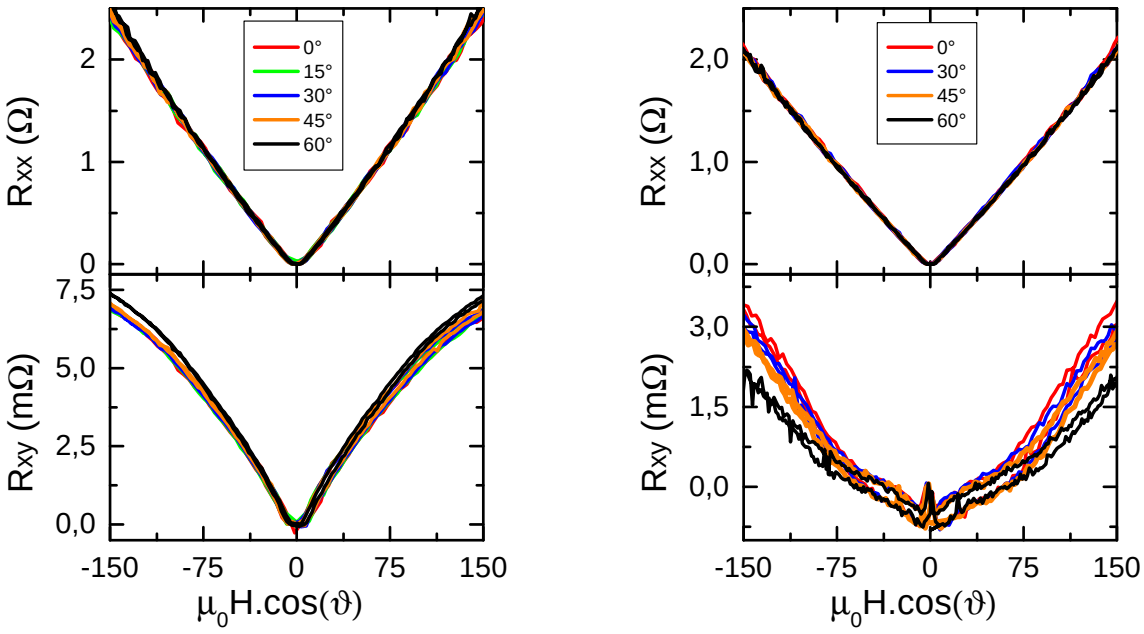

(a) (**j**,**H**) perpendicular

(b) (**j**,**H**) coplanar

Figure 6.2: **Longitudinal and transverse resistances of Mo_4Si films**
The curves in 6.2a and 6.2b are from two separate, but nominally identical samples, hence the different R_{xy} backgrounds. For both configurations, R_{xx} and R_{xy} superimpose when plotted against $\mu_0 H_z$.

In order to extract the odd (Hall) contribution, we decomposed the curves into an *even* and *odd* part [123]. We took care to preserve the hysteresis features by using the formulas in Eqn.6.1 and Eqn.6.2, in which R_{inc} and R_{dec} are the increasing and decreasing branches of the sweeps. The curves in Fig.6.4 present the result for the 0° and 45° measurements.

$$R_{inc,odd}(H) = \frac{1}{2}\left(R_{inc}(H) - R_{dec}(-H)\right) \quad ; \quad R_{dec,odd}(H) = -R_{inc,odd}(-H) \qquad (6.1)$$

$$R_{inc,even}(H) = \frac{1}{2}\left(R_{inc}(H) + R_{dec}(-H)\right) \quad ; \quad R_{dec,even}(H) = R_{inc,even}(-H) \qquad (6.2)$$

In the 0° measurement (Fig.6.4a), there is only the even part, which is identical to the raw data. The odd component is mostly noise. Interestingly, the same analysis for 45° (Fig.6.4b) yields two finite components. The even part is almost identical to that measured at 0°, whereas the odd component now shows a large anti-symmetric loop. In the odd part, there is a large bump for fields swept from zero to saturation, and a peak feature when the sweep reverses back to zero. They occur in the field ranges in which there are domains in the ferromagnet. Additionally, these two features have opposite signs. This is striking, since the sign seems to depend on the magnetic history, rather than the field polarity alone. This strongly suggest that the odd transverse signal is related to the morphology of the magnetic domain structure.

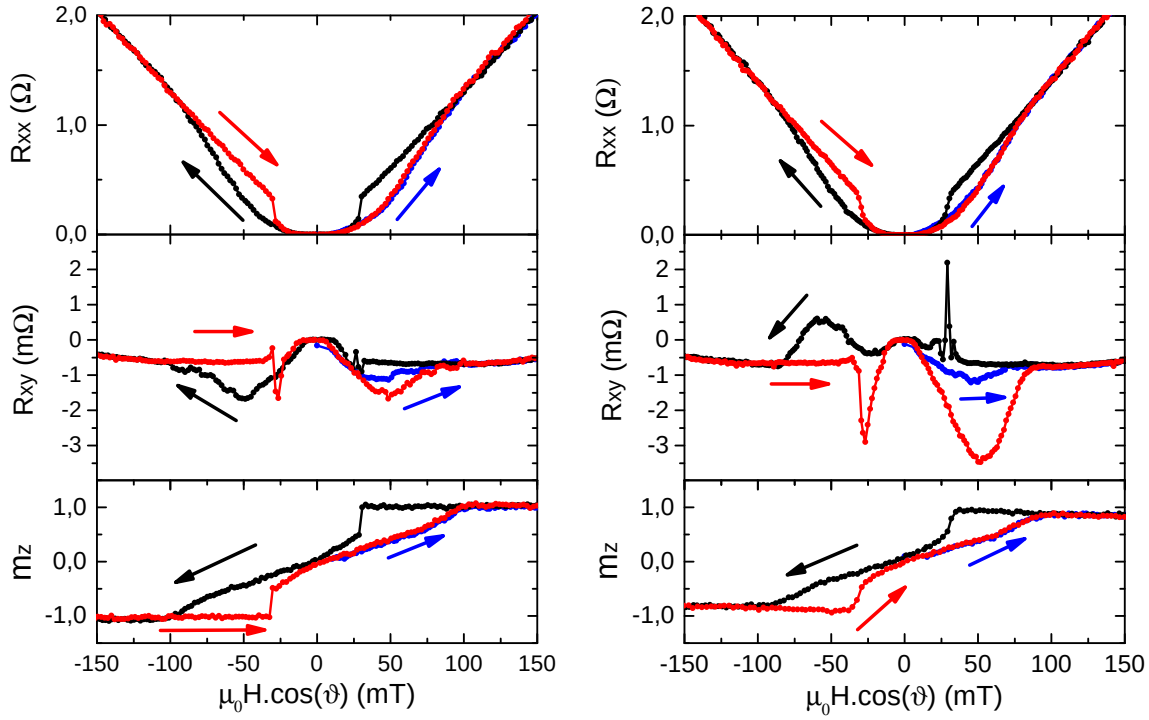

(a) 0° measurement

(b) 45° measurement

Figure 6.3: **Magneto-transport in Mo_4Si -(Pt/Co/Ru)$_{\times 4}$ (5 K ; 1 mA)** *There are no significant differences between the R_{xx} and m_z curves at 0° and 45°. However, the parity of the R_{xy} curve seems to change when the field is angled. The demagnetized curve (blue) on the other hand, looks unaffected.*

6.3.3 Angular dependence

To see how the odd component varies with the angle, we measured sets of R_{xx} and R_{xy} from 0° to 90°. Some selected curves are presented in Fig.6.5. In these, the Hall component appears at all angles between 15° and 60°. For the even component, the loop amplitude tends to reduce when increasing the angle. For each measurement, we calculated hysteresis amplitudes L_{even} and L_{odd}. These are plotted against the angle in Fig.6.6a. As readily seen in the MR curves, the even part monotonously decreases when the field rotates in the plane of the sample. In contrast, the odd part is visible at intermediate angles between 0° and 90°, and completely vanishes for these two values. It is maximum right in between, at 45°. In that configuration, j and $H_{\parallel}$ are perpendicular. We found that switching to the $j \parallel H_{\parallel}$ configuration does not change the results. The corresponding amplitudes are plotted in Fig.6.6b, and follow the same trends as when $j \perp H_{\parallel}$. We also measured at negative angles, to reverse $H_{\parallel}$. No differences are to be noticed in that case either.

From these data, we deduce that the odd R_{xy} requires both H_z and $H_{\parallel}$ to appear, since it vanishes at both 0° and 90°. It is indifferent to whether $H_{\parallel}$ is parallel or perpendicular to **j**.

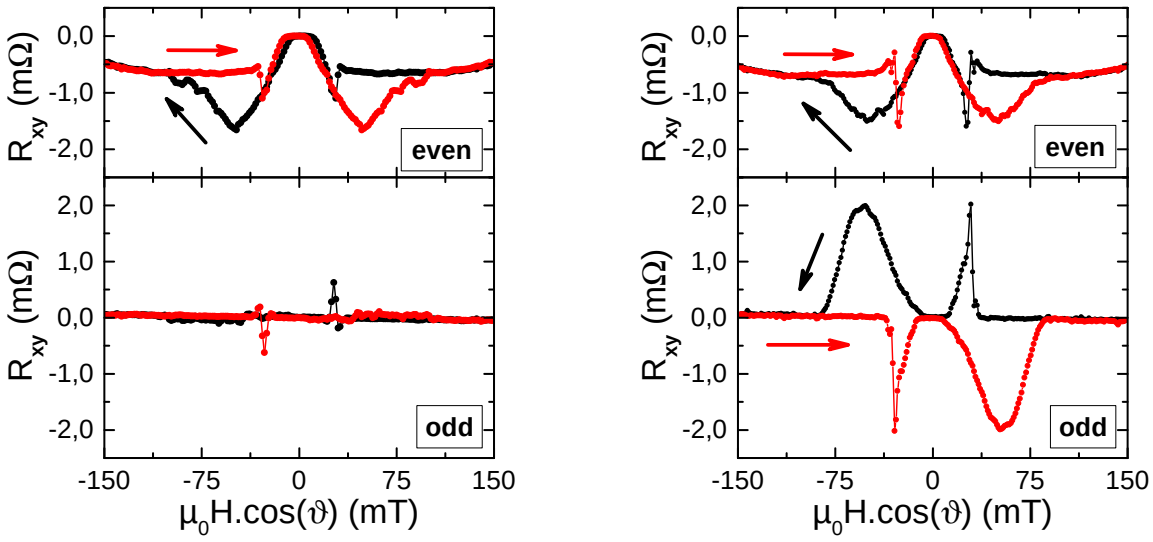

(a) θ =0° (b) θ =45°

Figure 6.4: **Transverse resistance decomposition for** 0° **and** 45°
The even *component remains the same, whereas a larger* odd *signal appears at* 45°.

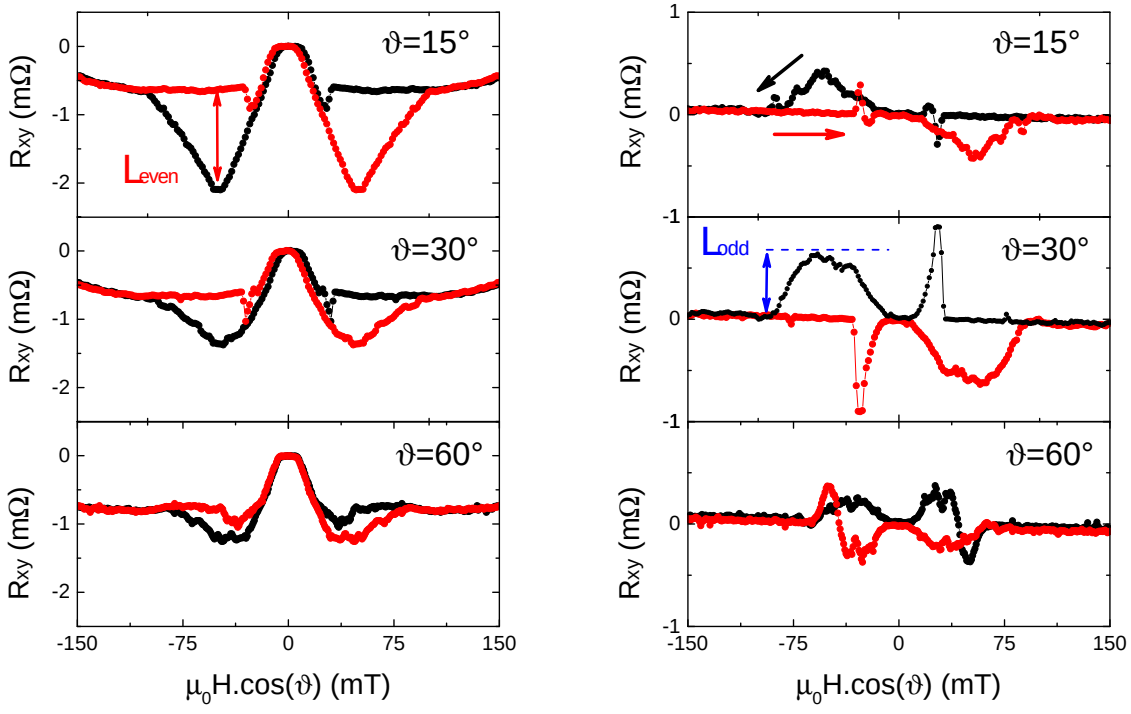

(a) even (b) odd

Figure 6.5: **Angular evolution of** R_{xy} **(H** $\perp$ **j)**
Tilting the field reduces progressively the even *loop, and reveals an* odd *component. The latter is maximum at intermediate angles.*

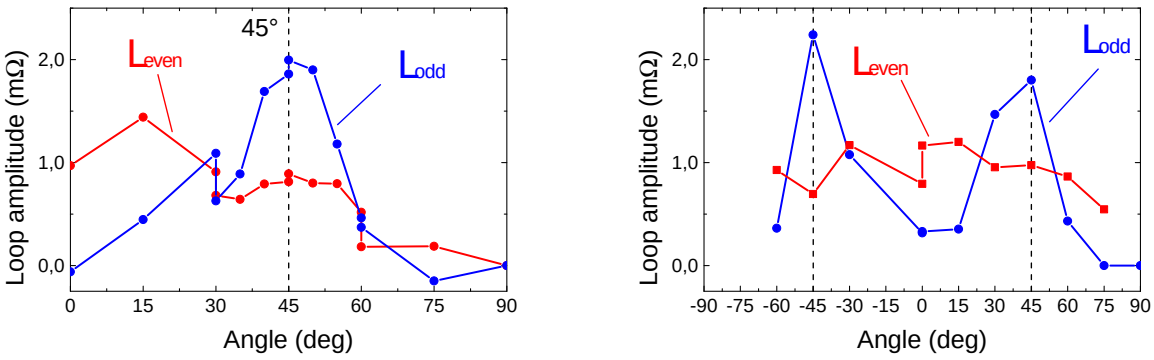

(a) (**j**,**H**) perpendicular

(b) (**j**,**H**) coplanar

Figure 6.6: **Angular dependency of R_{xy} in Pt/Co/Ru**
The odd component is maximum around 45°, whereas the even one gradually decreases as the field approaches the sample plane. Whether $H_{\parallel}$ is parallel or perpendicular to j is seemingly indifferent.

6.3.4 Current dependence

Like most resistances in type II superconductors, the odd R_{xy} component might originate from vortex dynamics. Since these are strongly non-linear with the applied current, it is interesting to study how changing it affects our measurements. For that, we measured field sweeps at 45°, for several values of the bias currents. Some decomposed curves are presented in Fig.6.7a. In these, the background and hysteresis amplitude of the even part seem to flatten when the current increases. The odd component, on the other hand, seems to change mostly in amplitude, not shape. Fig.6.7b shows that both components evolve non-monotonously with the bias current. They are the most pronounced for a few 100 μA, and decay outside of that range. We also checked whether applying higher currents could reveal an odd component at 0°, but did not find one between 100 μA and 4 mA.

6.3.5 Verifications

In order to rule out artifacts, we did several verifications. First, we decomposed the MR of the bare MoSi. As shown in Fig.6.8a, there is no odd component at all in the absence of the ferromagnet. We also ensured that the measurement is reproducible by measuring in two other regions of the sample, presented in Fig.6.8b. In all of them, the same odd R_{xy} component appears when the field is angled at 45°. This is not the case of the even part, that reverses when changing the measurement location, despite the contact configuration being the same. Hence, it may originate from defects like transverse contact misalignment, at least in part.

We also verified that the transverse signals are not caused by alternating $\pm j$ during field sweeps. For that, we measured the positive and negative curves separately at 45°, and did the averaging in post-processing. The results were not changed, which

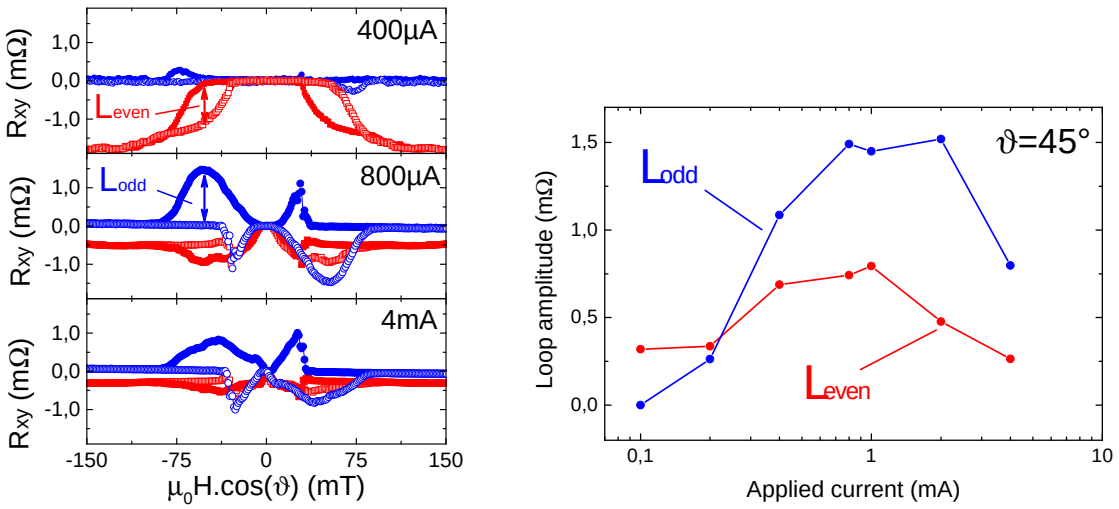

(a) Current evolution

(b) Loop amplitude vs current

Figure 6.7: **Current dependency of R_{xy}**
○ = *increasing field* ; ● = *decreasing field*
The amplitude of the hysteresis loop is maximal for a few 100 µA, and decays if for currents outside that range.

confirms it is not a mathematical artifact of some sort. These are not shown for brevity.

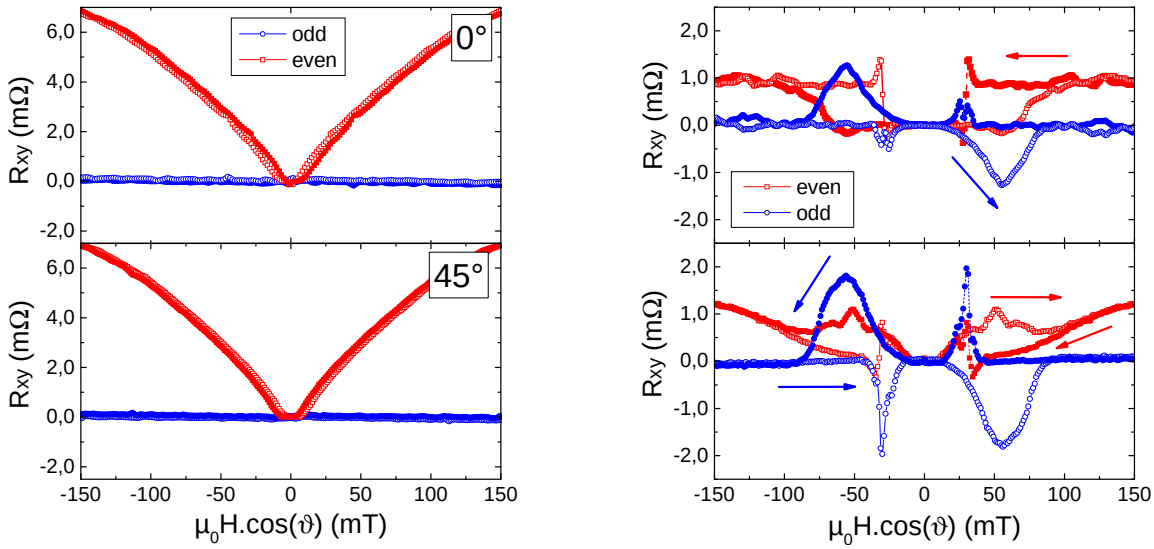

(a) Decomposition in bare MoSi

(b) Measurement in two other regions

Figure 6.8: **Decomposition in bare MoSi and elsewhere in the sample**
○ = *increasing field* ; ● = *decreasing field*
No significant odd component is observed in the bare MoSi. It is observable similarly in several locations of the bilayers, unlike the even component, that sometimes reverses.

6.3.6 Transverse resistance in Co/Pt bilayer

The Pt/Co/Ru sample that we previously studied may host a variety of magnetic structures (see Sec.5.5). Since the perpendicular anisotropy in that sample is not so strong, these are also likely affected by $H_{\parallel}$. We also wanted to see if these phenomena also occur in a "simpler" system, in which we observed only disordered domains. Thus, we measured a bilayer including a Co/Pt instead, that has a stronger anisotropy. It shows larger, disordered domains (Sec.5.3), that should be less sensitive to $H_{\parallel}$.

We similarly measured MR curves in the perpendicular (**j**,**H**) configuration, for several angles. The results for $\theta = 0°$ and 45° are presented in Fig.6.9a and Fig.6.9b respectively. These are also measured at 5 K, but with a bias of 500 μA, for which the features were clearer. Qualitatively, we observe the same behavior as in Pt/Co/Ru. However,R_{xy} strongly resembles the longitudinal MR curves. When the field is angled, the loop in negative field is larger than in positive, unlike that in R_{xx}. It indicates that there is an odd signal here as well, which we extracted.

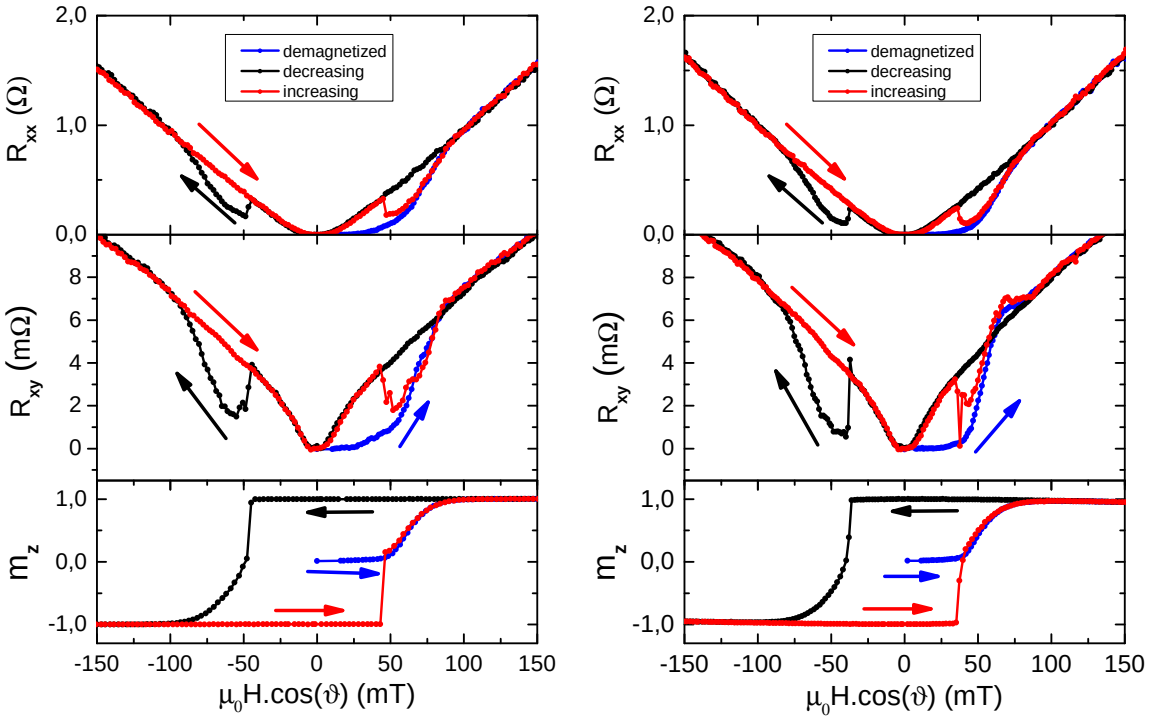

(a) θ =0° (b) θ =45°

Figure 6.9: **Magneto-transport in MoSi - Co/Pt bilayers**
Like in Pt/Co/Ru, there is a deformation of the R_{xy} curve at 45°, whereas R_{xx} does not change much.

The odd/even decomposition of the 45° measurement is shown in Fig.6.10a. It also reveals the presence of an additional odd component. It is upside-down compared to that found in Pt/Co/Ru, for which the bump feature in positive field was negative. This is surprising, but not an error since the contact configuration is the same as in Pt/Co/Ru, and the anomalous Hall effect (m_z curve) has the "correct" sign. Since

the magnetization reverses in a narrower range of fields, the peak and bump features that were present in the other sample are now merged.

In Fig.6.10b, we see that the loop amplitude for both components behaves similarly as those in Pt/Co/Ru. The even one decays when approaching the in-plane position, whereas the odd one is maximum at intermediate angles. However, the maximum is at 60° for that sample instead of 45°. Thus, to have a comparable effect, higher in-plane components are required. This might be consistent, given that Co/Pt has a stronger perpendicular anisotropy.

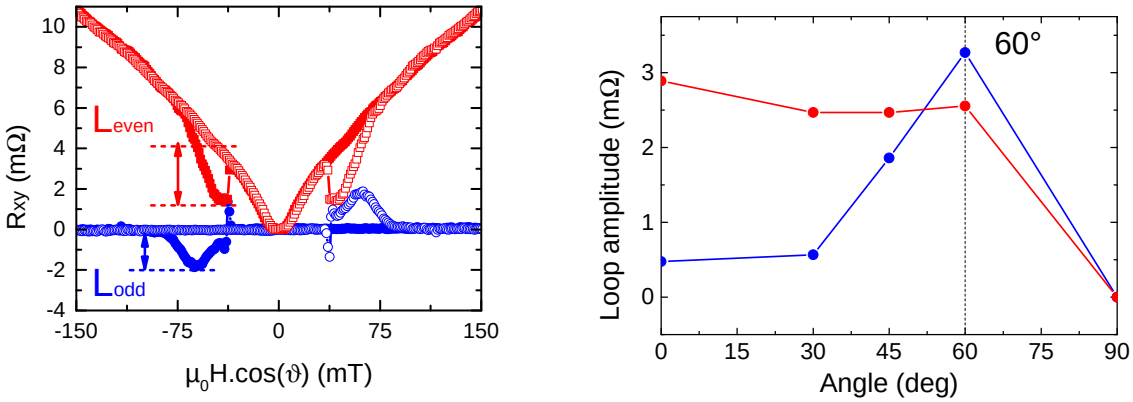

(a) 45° decomposition

(b) Angular dependency

Figure 6.10: **Angular dependency in Co/Pt**
The odd component peaks at 60°*, which is higher than in Ru/Co/Pt.*

6.4 Domain structures at angled magnetic field

In the transport measurement, we found that the odd R_{xy} component requires both $H_{\parallel}$ and $H_{\perp}$ to exist, and is maximum at intermediate angles. We also observed no comparable effect in either R_{xx} or m_z. The latter suggests that the changes may come from domain morphology due to $H_{\parallel}$. In the present section, we probe how the magnetic structures behave when the field is applied obliquely to the sample plane. To that end, we did magnetic force microscopy images at low temperature (Sec.6.4.1), and complemented them with micromagnetic simulations (Sec.6.4.2).

6.4.1 Low-temperature MFM imaging

To observe the domain structure at low-temperatures and angled fields, we made MFM images in a cryogenic setup (77 K). However, due to technical limitations, we could only apply continuous fields up to 20 mT in out-of plane and 150 mT in the sample plane (or 400 mT for few seconds). This does not reproduce the conditions in which the MR are measured, but will suffice to check whether in-plane fields affect the domain structures.

To be able to correlate the images at 77 K to the magnetic state at 10 K, we compared the anomalous Hall effect measurements of both bilayers, shown in Fig.6.11. For each, the two curves are very similar, except from minor changes in the coercive and saturation field. This suggests that the magnetic structures should behave similarly at 77 K as they do at 10 K.

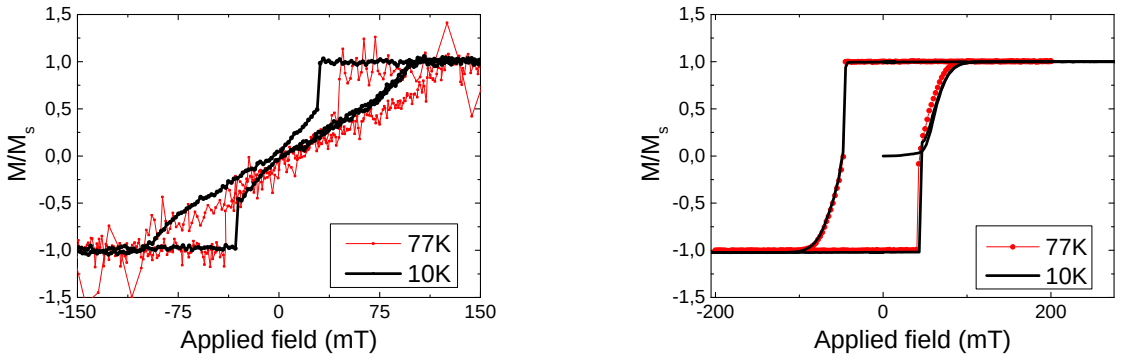

(a) $(Pt_{1.2nm}Co_{0.6nm}Ru_{1.4nm})_{\times 4}$ (b) $(Co_{0.6nm}Pt_{1nm})_{\times 5}$

Figure 6.11: **Anomalous Hall effect at 10 K and 77 K**

The magnetic layers were demagnetized by oscillating the field in perpendicular prior to the experiment. This is to ensure the presence of magnetic domains at zero field in both samples. Images of the Pt/Co/Ru layers are presented in Fig.6.12. At zero field, we observe large and disordered domains. However, the labyrinth patterns are less well defined a low temperature (Fig.6.12a) than those observed at 300 K in Sec.5.3.1. Applying an in-plane field seems to orient the domains, and turn them into parallel stripes around 400 mT (Fig.6.12c). We could not sustain that value for long without overheating the power source of the electromagnet, so the image was done at zero field. In these images, the out-of-plane field does not significantly affect the structures, thus we do not know what happens when skyrmions form.

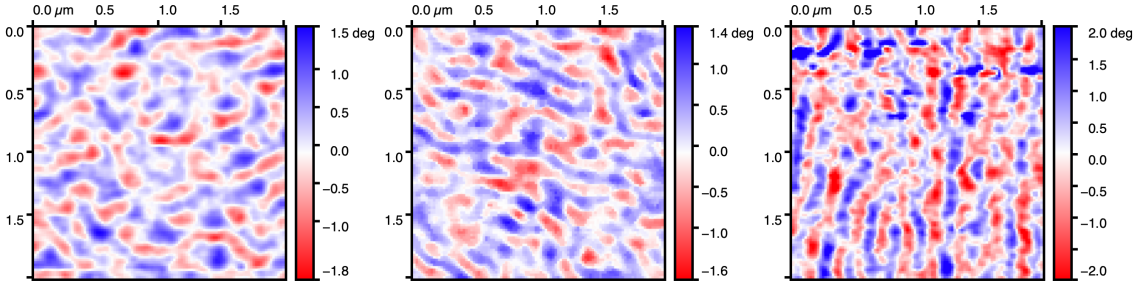

(a) 0 mT⊥ ; 0 mT ∥ (b) 20 mT⊥ ; 20 mT ∥ (c) 0 mT after 400 mT∥

Figure 6.12: **MFM images in Pt/Co/Ru (77 K)**
The in-plane field component is applied vertically in the images.

We also carried imaging on the Co/Pt multilayers, shown in 6.13. These show that $H_{\parallel}$ does not significantly alter the domain structures within the accessible field range. This multilayer is less sensitive to in-plane fields than Pt/Co/Ru. This is also

what transport experiment suggested (higher angles to see changes in R_{xy}). This is surely due to the higher out-of-plane anisotropy compared to the other multilayer.

Nevertheless, we could not explore a range of field and angles in which the odd transverse resistance is maximum. The images give an idea of how responsive they are to $H_{\parallel}$, but not exactly how they would look when the odd R_{xy} is maximum. To find more evidence, we carried out micromagnetic simulations, which we present next.

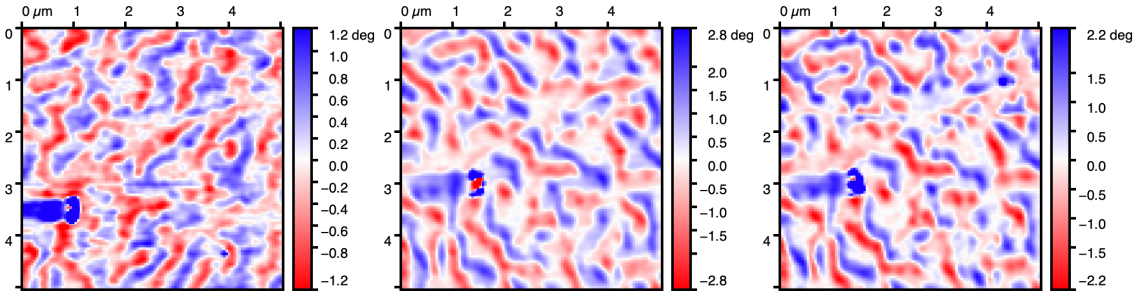

(a) 0 mT ⊥ ; 0 mT ∥ (b) 20 mT ⊥ ; 35 mT ∥ (c) 20 mT ⊥ ; 150 mT ∥

Figure 6.13: **MFM images in Co/Pt (77 K)**

6.4.2 Micromagnetic simulations in a tilted field

To complement the previously shown MFM images, we did micromagnetic simulations of the domain structures. The detailed parameters and methods are covered in Sec.6.2.4. We simulated the behavior of both the Co/Pt and Pt/Co/Ru multilayers, for several angles. In Fig.6.14, we present the curves of $m_z(H_z)$ of both, to compare with what we obtained previously in the Hall effect.

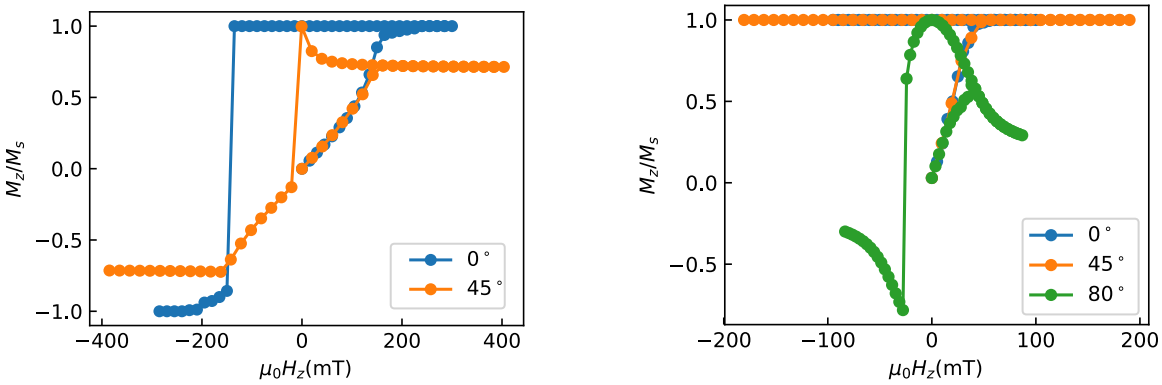

(a) $(Pt/Co/Ru)_4$ (b) $(Co/Pt)_5$

Figure 6.14: **Simulated magnetization loops**

The cycles of the Pt/Co/Ru model sample have a slightly higher saturation field, and hold their saturated magnetization harder than the real sample. Otherwise, the curves starting from $m_z = 0$ look quite similar to those found in experiments. In the Co/Pt sample, starting from $m_z = 0$, the magnetization increase is more

gradual than in the real sample. In addition, the saturated magnetization does not reverse within the field range we applied. These differences with the cycle in the real multilayers originate, at least in part, from the absence of defects. These may facilitate the nucleation of domains, and also pin the domain walls, through which the magnetization changes. When the field is tilted from the perpendicular direction, the loop becomes warped due to the effect of the in-plane field. At saturation, if $H_{\parallel}$ is high enough, the magnetization is inclined and $m_z < 1$.

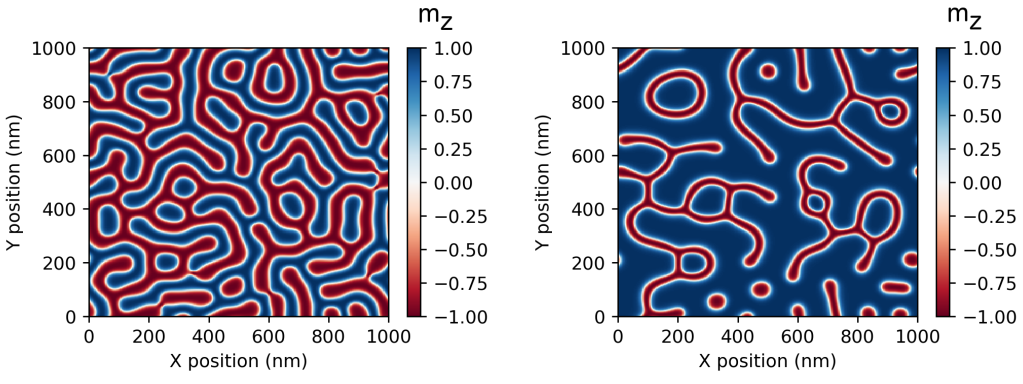

(a) B_z=0 ; m_z=0

(b) B_z=120mT ; m_z=0.53

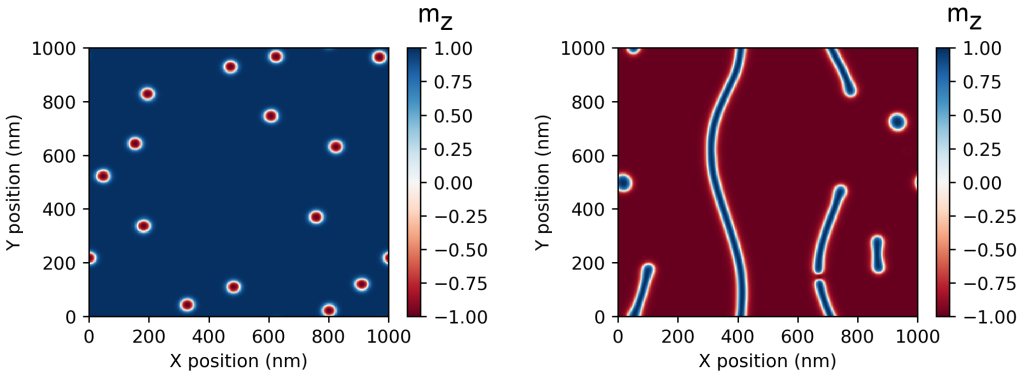

(c) B_z=150 ; m_z=0.95

(d) B_z=-150mT ; m_z=-0.86

Figure 6.15: **Micromagnetic simulations of the Ru/Co/Pt layers (θ =0°)**

In the following, we present the results of these simulations. The color map all represent the m_z component in the top magnetic layer.

Simulations of Pt/Co/Ru multilayers

In Fig.6.15, we present selected maps of m_z at 0°, for the Pt/Co/Ru sample. It starts from a 80-100 nm wide labyrinthine domain structure, that narrows and turn into magnetic skyrmions when the field increases(Fig 6.15b and6.15c), up to saturation. These do not show a specific order, and are relatively isolated from each other. At the coercive field, the magnetization reverses abruptly and forms isolated worms and skyrmions (Fig.6.15d). These structures and behavior resemble those observed at 300 K (Fig.5.5).

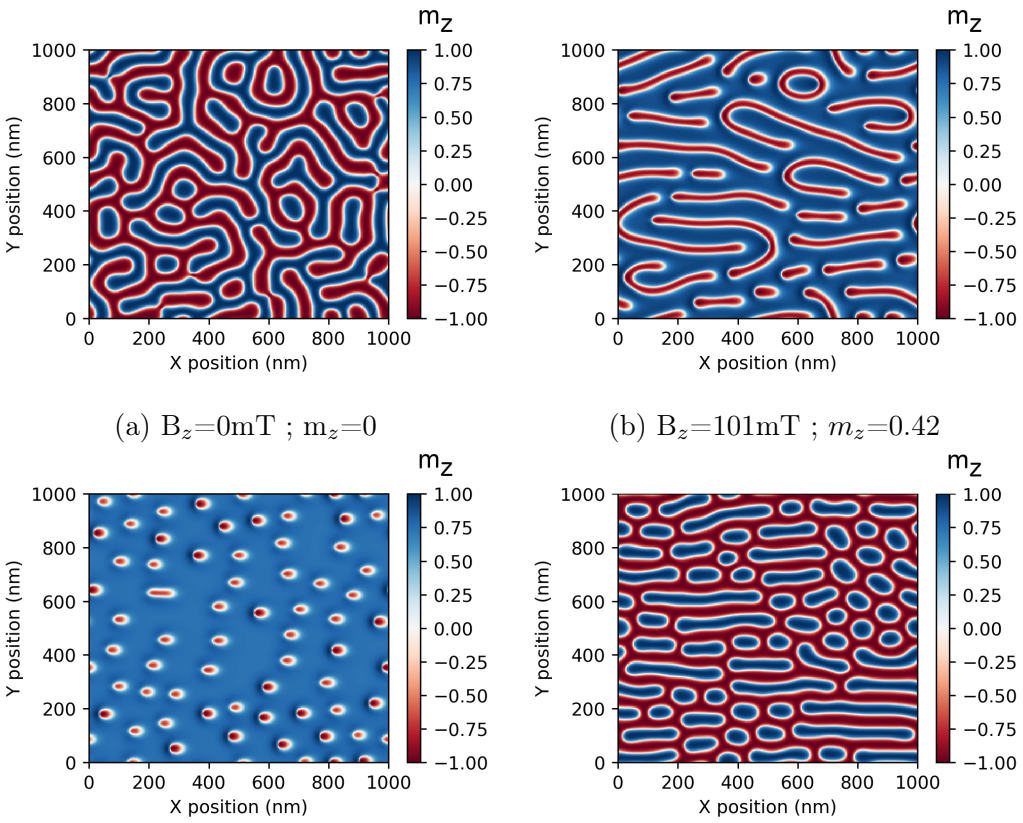

(a) B_z=0mT ; m_z=0

(b) B_z=101mT ; m_z=0.42

(c) B_z=141mT ; m_z=0.66

(d) B_z=-21mT ; m_z=0.13

Figure 6.16: **Micromagnetic simulations of the Ru/Co/Pt layers (θ =45°)**
The in-plane field component is applied horizontally in the simulations.

We then did the same cycle, with the field angled at 45° along x. As shown in the maps of Fig.6.16, a tilted field orients the domain structures in the direction of $H_{\parallel}$. At higher fields, the stripes also collapse into skyrmion-like structures, with a considerably higher density than at 0°. However, not all of them are truly skyrmions. In Fig.6.17b, we show the m_x, m_y, m_z components of the lower right quadrant of Fig.6.16c. Some of the bubbles wrap all directions of magnetization, and qualify as skyrmions. Some others do not have a negative m_x component, and are not skyrmions. These may be spotted on the m_z maps by their lighter color at the center. In the physical samples, we are not sure whether these exist or are true skyrmions instead. When the field is swept backwards, the magnetization reverses, and forms dense and organized arrays of stripes and skyrmionic bubbles (Fig.6.16d). They turn into the same arrays as in Fig.6.16c for a strong enough negative field. In addition, if the magnetic field is purely in-plane (θ =90°, Fig.6.17a), the domains align in parallel stripes. These never turn into skyrmions.

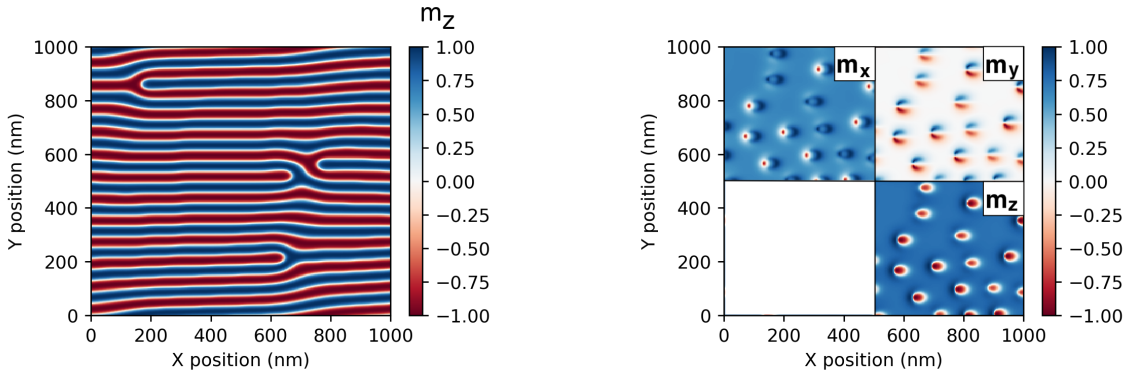

(a) Stripes at 90°

(b) Trivial bubbles and skyrmions

Figure 6.17: **Stripes and bubble/skyrmion arrays in Ru/Co/Pt layers** *A strong field applied in-plane creates parallel stripes that hold at zero field (Fig.6.17a). At angled fields, elongated worms and skyrmions appear (Fig.6.17b). Many are trivial bubbles, not skyrmions, as they do not have a negative m_x component.*

Simulations of Co/Pt multilayers

We then did simulations for the Co/Pt multilayer, presented in Fig.6.18. In these, the typical domains size at $m_z = 0$ is approximately twice that of Pt/Co/Ru. It is smaller than that in the real sample, though. When the field increases, the oppositely magnetized domains mostly shrink in thickness (Fig.6.18b). They collapse into isolated skyrmions when approaching the saturation field (Fig.6.18c).

The same simulations with fields angled at 45° and 60° yield strictly identical results. To observe a difference, we had to angle the field at 80°. The results are shown in Fig.6.19. The starting domain structure is identical as in Fig.6.18a. Further increasing the field forms more elongated domains than at lower angles (Fig.6.19a), that later turn into bubbles close to saturation (Fig.6.19b). The structures in the map do not have a negative m_x component. Therefore, they are topologically trivial bubbles, and not skyrmions, like the ones in Fig.6.17b.

As in the MFM, higher in-plane fields/angles are required to affect the domains in Co/Pt than in Pt/Co/Ru. This is surely due to the stronger perpendicular anisotropy in these layers. Nevertheless, both domain structures tend to align with the in-plane component, and favor the apparition of skyrmions or bubbles close to saturation.

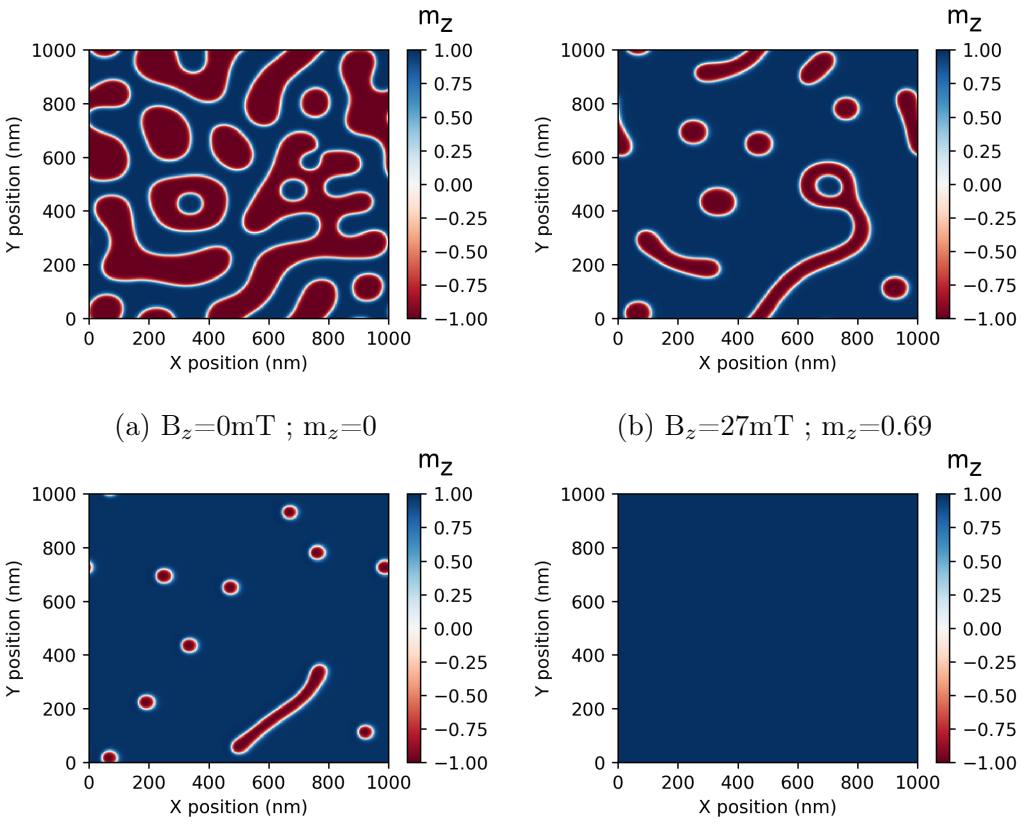

(a) B_z=0mT ; m_z=0

(b) B_z=27mT ; m_z=0.69

(c) B_z=40mT ; m_z=0.91

(d) B_z>57mT ; m_z=1

Figure 6.18: **Micromagnetic simulations of the Co/Pt layers (θ =45°)** *The evolution of the domain structure with the applied field is strictly identical for fields angled between 0° and 60° from the out-of-plane direction. It depends exclusively on H_z.*

6.5 Summary and discussion

First, let us first summarize our findings. The transport in the bare superconductor is unaffected by in-plane fields. It only depends on H_z, which is expected for a thin film ($d_s \ll \lambda$). In the bilayers, the presence of domains affects both R_{xx} and R_{xy}, creating magnetic hysteresis. Like in the bare superconductor, R_{xx} mostly depends on H_z, and is always *even*. R_{xy} on the other hand, is angle-dependent, and can be split in *even* and *odd* components. The even part depends mostly on H_z and vanishes progressively as the field is tilted from the perpendicular direction. In contrast, the odd one is maximal at intermediate angles, and vanishes at 0° and 90°. That contribution is the most interesting, since it is not accompanied by similar changes in the R_{xx} or m_z curves. Its sign is also peculiar, since it changes with the magnetic history, not directly the field polarity like the Hall effect. It is also indifferent to whether $j \perp H_\parallel$ or $j \parallel H_\parallel$.

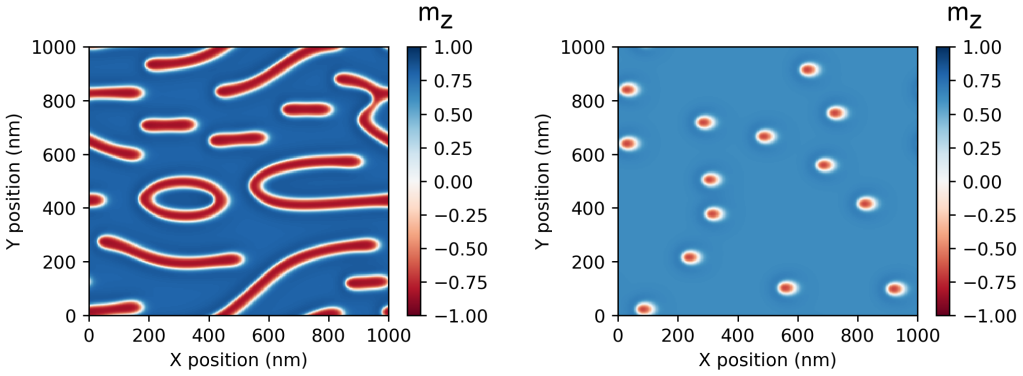

(a) B_z=28mT ; m_z=0.46 (b) B_z=38mT ; m_z=0.60

Figure 6.19: **Micromagnetic simulations of the Co/Pt layers (θ =80°)** *The starting domain structure is identical to that in Fig.6.18a. For fields applied at 80°, the domains become more elongated along $H_\parallel$, and turn into non-skyrmion bubbles close to saturation.*

Now, we shall discuss the possible phenomena from which the different R_{xy} components may spawn. Vortex dynamics are a very likely cause, as they dictate the transport properties in Mo_4Si. They could explain the odd part of R_{xy}, and why the effects do not depend monotonously on the bias. At low values, pinning strongly hinders the vortices, whereas for high enough currents (flux flow), it becomes insufficient to compete with the Lorentz force and affect the motion significantly. Both limits should result in a reduction of the hysteresis features, as observed in Fig.6.7b.

The origin of such a pinning is the domain structure, as the effects only appear in its presence ($|m_z| \neq 1$). However, $m_z(H_z)$ curves do not change strongly when tilting the field, unlike the odd component of R_{xy}. Thus, the difference might come from the domain morphology. This is supported by the simulations and MFM images, indicating that domains align into parallel stripes due to $H_\parallel$. Thus, guided vortex motion along the domain-walls is likely to occur.

However, measuring a transverse resistance implies that vortices are deflected from the direction of the Lorentz force. For $\mathbf{j} \perp \mathbf{H}_\parallel$, as in Fig.6.20a, the stripes are along the Lorentz force, and do not hinder the vortices. Conversely, for $\mathbf{j} \parallel \mathbf{H}_\parallel$, they should block the motion. However, in both cases, vortices are not deviated, and there should be no transverse electric field :$E_y = 0$. To observe a finite one is possible if the stripes are misaligned with $\mathbf{j}$, as in Fig.6.20b. In that case, the vortices are guided sideways, and $E_y \neq 0$. From the measurements, we estimated the deviation θ_H to have values around 1°, which is quite small (see App.B.3 for the estimation).

This scenario explains the angular dependency, as the stripes go from disordered at 0° to parallel when $H_\parallel \neq 0$. It also accounts for presence of a maximum at intermediate fields, as stripes turning into skyrmions should reduce the guiding. It also fits with the higher angles needed in Co/Pt, as the domains are less sensitive to in-plane fields (stronger out-of-plane anisotropy).

(a) Perpendicular stripes

(b) Tilted stripes

Figure 6.20: **Guided motion in the presence of stripes.**
Stripes perpendicular (or parallel) to $\mathbf{j}$ *do not deviate vortices (Fig.6.20a), thus* $E_y = 0$*. When these are tilted, vortices are deviated creating transverse electric fields* $E_y \neq 0$ *(Fig.6.20b).*

Explaining the sign is more delicate, though. In positive and negative fields regions of a single sweep (hysteresis branch), the sign is the same. It is coherent, since vortices of opposite polarities also have opposite velocities, but result in the same electric field $\mathbf{E} = \mathbf{B} \times \mathbf{v_l}$ (see Sec.2.1.4). Nonetheless, to account for the the sign changes when reversing the sweep, the deflection angle θ_H must also change sign. This is peculiar, as there is no indication of that in the imaging and simulation. In order to find out whether this is possible, we are developing a collaboration to make low-temperature MFM images of the domains (MIPT, Russian Federation).

We also considered effects related to the S and F layers being electrically in parallel. Transverse voltages, either due to vortices or the anomalous Hall effect, generate closed current loops so that the voltage in both layers remains equal (equipotential) [243, 244]. These effects, together with a small Hall contact misalignment in the bridge could explain the even component [63, p. 154]. However, they do not account for the apparition of the *odd* signal, since R_{xx} below T_c and R_{xy} at 10 K (the anomalous Hall effect) do not change much when the field is tilted at 45°.

It was also recently proposed that the vortex flow could drag skyrmions along [53], which in turn could create a Hall effect. This is plausible, since skyrmions may move due to magnetic field gradients [245], which are quite steep in neighborhood of the core.[1] That possibility is also under investigation with the help of theoreticians (LOMA, France).

[1] Using the values in Tab.6.1 and the profile of Eqn.2.5 yields a field in the core about 0.3 mT, and gradients of a few mT.μm^{-1}.

Chapter 7

General conclusion

7.1 Summary

In the present thesis, we studied superconductor/ferromagnet systems from two different angles. One is proximity effect, with the formation and propagation of triplet superconductivity in oxide heterostructures. Another one is magnetism, by attempting to detect the presence of magnetic skyrmions using vortex dynamics. In the following, we present a brief summary of our findings, accompanied by some comments on the outlook.

7.1.1 Proximity effect and triplet states at YBCO/LCMO interfaces

Tunneling in YBCO/LCMO/YBCO vertical junctions

First, we studied the proximity effect in oxide heterostructures involving thin films of the half-metallic manganite $La_{0.7}Ca_{0.3}MnO_3$ sandwiched between two superconducting layers of the high-temperature cuprate $YBa_2Cu_3O_7$ (T_c = 92 K). In vertical devices, we observed conductance oscillations that are in part related to the propagation of superconducting correlations in LCMO, up to 24 nm. This excludes singlet proximity effect, since LCMO is half-metallic. Hence, these correlations are very likely of the equal-spin triplet kind. The mechanism by which they manifest, McMillan-Rowell resonances, also suggests that the bottom YBCO/LCMO interface is reflective, at least partially. Analyzing the frequency of these oscillations yielded values of the Fermi velocity in both YBCO and LCMO that are reasonable, given those found in the literature. We observed that the Fermi velocity of LCMO diminishes when its thickness is reduced. That trend is consistent with earlier observations [27], and accentuates in layers as thin as 6nm. We suspect that it is due to interface effects, that are known to affect the electronic properties of LCMO, and likely become prominent in such thin layers.

Perspectives

In the trilayers, enhancing the quality of the Au/YBCO did not suffice to observe the Josephson effect. As in earlier work [27, 33], it might be due to the bottom YBCO/LCMO interface being opaque, preventing triplets from crossing and mediating the Josephson effect. It is also possible that the tunneling Au/YBCO contact prevents to observe the effect. To find out, we started the fabrication of 4-points junctions, in which that contact is not measured. The activity has been carried over in the group, and led to results possibly indicating that the Josephson effect exists but is inhomogeneous. That possibility is still under investigation at the moment of writing.

In the case of the bottom interface being truly opaque, one would need an alternative approach. A possibility is to find out what makes it opaque, and work on the growth to enhance the quality. It does not seems easy, though. Another possibility is to use only the top interface, by making planar devices in YBCO/LCMO bilayers. In these, the current would propagate through the ferromagnet from one superconducting electrode to another. This would be delicate too, since it involves patterning or irradiating the YBCO without damaging the LCMO below.

However, progress in that matter would be an important step to fabricate a π-Josephson junction in a high-temperature superconductor system, or a magnetic memory device like a spin-valve.

7.1.2 Coupling of vortices and skyrmions in bilayers

The second part investigated the interactions between a superconductor and ferromagnetic multilayers hosting domains and skyrmions. The latter are small chiral spin textures, that are promising for applications to high-density memory devices. Given that one could detect and manipulate them, they may be useful in superconducting devices as well. For that, we proposed to use vortices in a type II superconductor, which might interact with skyrmions through stray magnetic fields. We were especially motivated, since only a handful of papers alluded to the possibility when we started in 2016 [56, 246], while no experimental work was available. Since then, a few theoretical proposals emerged [229, 52, 53, 228]. During the thesis, we fabricated bilayers with the low-pinning superconductor Mo_4Si, and Pt/Co/X (X=Ru,Ir,Pt) ferromagnetic multilayers that can host skyrmions. We then looked for footprints of interactions between the two in magneto-transport measurements.

Critical currents

We found that similarly as regular magnetic domains, skyrmions enhance the critical current of the bilayers. As the domain structure changes irreversibly with the external field, the transport in the superconductor also becomes field-dependent and hysteretic. We could explain qualitatively the scaling of the critical current curves with a simple magnetic pinning model on stripes. However, the formation of close-packed skyrmions in Pt/Co/Ru multilayers resulted in a lesser enhancement of

j_c compared to expectations from the stripe model. Their core magnetization here opposes the flux, and thus repels vortices. We proposed that their small size hinders vortex motion less efficiently than the wider, more elongated magnetic domains.

Magneto-resistances and Hall effect

We also studied the magneto-resistance of these bilayers. Equivalently, the presence of magnetic structures reduces the longitudinal magneto-resistance R_{xx}, and induces magnetic hysteresis. The bilayer in the saturated state is also more resistive than the bare superconductor. It may hint at extra superconducting vortices being stabilized, due to a magneto-static coupling of their flux to the magnetization, lowering the nucleation barrier [161].

The most peculiar feature we found in these samples was in the Hall effect (R_{xy}) of Pt/Co/Ru and Co/Pt bilayers. We found that exclusively at angled fields, an *odd parity* resistance component appears in the presence of domains. This is puzzling, since no comparable features are visible in the R_{xx} curves, nor in the anomalous Hall effect above T_c (related to m_z). It is also indifferent to whether $H_{\parallel}$ is perpendicular or parallel to the applied current. We found evidence in images and simulations that in-plane fields can organize the domain structure, and ease the skyrmion formation. A possibility is that the domain structure might guide the vortex motion, resulting in our observations. Nonetheless, it is difficult to relate to the sign changes of the odd signal. These would imply that the guiding direction reverses depending on the way the field is swept. It could also result from the motion of skyrmions, dragged along by the vortex flow [53].

Perspectives

Explaining the origin of the measured Hall effect is the most immediate perspective. We are currently investigating two possibilities. One one hand, we are working with collaborators from the group of V.Stolyarov (Moscow Institute of Physics and Technology, Russian Federation) to make low-temperature imaging. Since the images can be done in conditions comparable to the transport experiments, they should help to find out whether morphology differences explain our observations. On the other hand, we are working with A.Buzdin (LOMA Bordeaux, France) on the theoretical side to find out whether it is possible that vortices can move skyrmions, resulting in a measured topological/skyrmion Hall effect.

On a farther horizon, it could be interesting to do the experiment with vortices and skyrmions of the same polarity. In that case, the coupling would be attractive, which should make the simultaneous motion of both easier to realize. This also means finding a material in which they are metastable when the field reverses. Moreover, we investigated it only through magneto-static interactions. Proximity effects is an equally interesting angle of approach, since the swirling spin texture could favor the formation of triplet states. Skyrmions in Josephson junctions is also a possibility [67], especially since they can also be created with current pulses [59].

Appendix A

Devices recipe

A.1 Hall cross-bar

- **Spin-coating**
  spin coating : SPR700 1.2 ; 6000rpm for 30 s
  baking : 90°C ; 1min

- **Bridge definition**
  UV illumination : 50 mJ
  baking : 110°C ; 1 min
  development : MF318 15 s shaking ; rinse in water
  ion beam etching : 500 V/150 mA ; beam at 30° angle, 5°C

- **Resist stripping**
  oxygen plasma : 2mn 100 sccm O_2, 14.5 sccm Ar, 200 mT, 27°C
  stripping : strip in acetone, rinse in isopropanol then water

A.2 3-points vertical junctions

A.2.1 Pillar definition

- **Spin-coating**
  spin coating : Microposit primer ; 30 s at 4000 rpm
  resist spin-coating : SPR700 1.2 photoresist, 30 s at 4000 rpm
  baking : 1min at 105 °C

- **Border removal**
  UV illumination : 100 mJ·cm^{-2}
  development : MF319 30 s, rinse in water

- **Pillars definition**
  UV illumination : 45 mJ/cm^2
  baking : 1 min at 105 °C
  development : MF319 30 s, rinse in water

ion beam etching : 300 V/40 mA, 5 °C, 30° angle with beam, rotating holder (see Fig.A.1)

- **Resist stripping**
  oxygen plasma : 2 mn 100 sccm O_2, 14.5 sccm Ar, 200 mT, 27°C stripping : strip in acetone, rinse in isopropanol then water

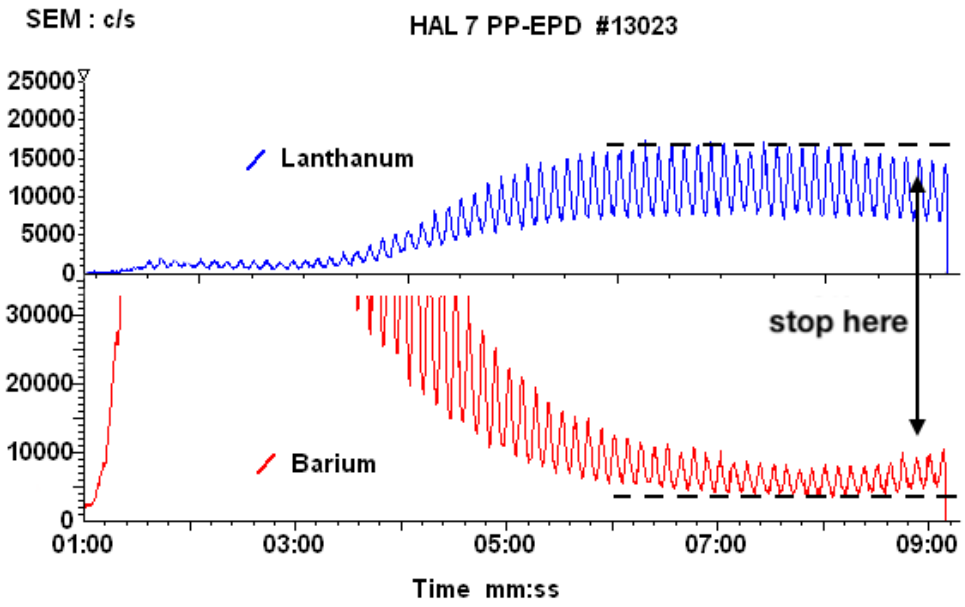

Figure A.1: **Sample SIMS spectrum for pillar etching**

A.2.2 Bottom electrode definition

- **Spin-coating**
  spin coating : Microposit primer ; 30 s at 4000 rpm (optional)
  resist spin-coating : S1813 photoresist, 30 s at 6000 rpm
  baking : 1 min at 90 °C

- **Electrode definition**
  UV illumination : 45 mJ/cm^2
  baking : 1 min at 110 °C
  development : MF319 ; 50 s, rinse in water
  ion beam etching : 300 V/40 mA, 5 °C, 30 ° angle with beam, rotating holder (see Fig.A.1)

- **Resist stripping**
  oxygen plasma : 2 mn 100 sccm O_2, 14.5 sccm Ar, 200 mT, 27°C
  stripping : strip in acetone, rinse in isopropanol then water

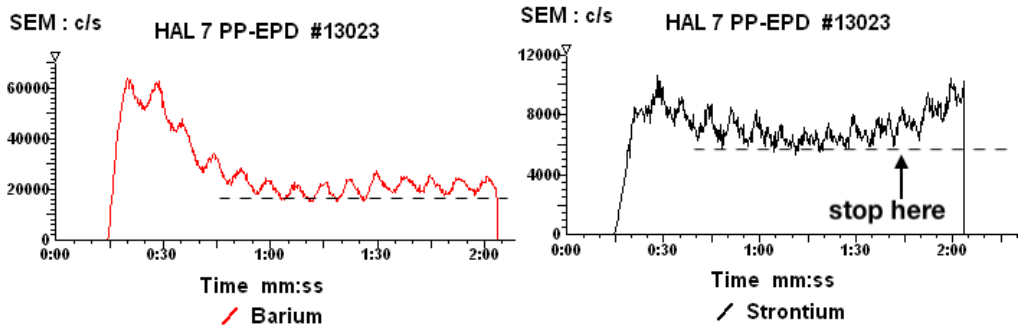

Figure A.2: **Sample SIMS spectrum for bottom electrode etching**
Ideally stop etching either when YBCO drops or STO increases (the earliest). Do not wait, the resistance of STO drops very fast once etched.

A.2.3 Permanent resist

- **Spin-coating**
  resist spin-coating : S1805 photoresist, diluted 50/50 with solvent, 30s at 6000rpm
  baking : 1 min at 110 °C

- **Holes definition**
  UV illumination : 30 mJ·cm^{-2}
  annealing : 1 min at 110 °C
  development : MF319 3 s, rinse in water (re-develop if holes are closed)
  permanent baking : 170 °C 1 min

A.2.4 Gold contacts

- **Spin-coating**
  resist spin-coating : SPR700 1.2 photoresist, 30 s at 4000 rpm
  baking : 1 min at 110 °C
  bathing : chlorobenzene, 10 mn, rinse in water *well*

- **Electrode definition**
  UV illumination : 100 mJ·cm^{-2}
  development : MF319 12 s, rinse in DI water

- **Gold evaporation**
  plasma etching (in the chamber) : 200 eV 45 s
  gold deposition : Ti 10 nm ; Au 200 nm
  lift-off : heated acetone (35-40 °C), blow acetone using pipette with thin head
  rinsing : isopropanol then water

A.3 4-points vertical junctions

A.3.1 Alignment marks definition

- **Spin-coating**
  spin-coating : SPR700 1.2 photoresist, 30s at 6000 rpm
  baking : 110 °C ; 60 s
  bathing : chlorobenzene, 10 mn, rinse in water *well*
  UV illumination : 100 mJ.cm^{-2}
  development : MF319 40 s, rinse in water

- **Gold evaporation**
  plasma etching (in the chamber) : 200 eV 45 s
  gold deposition : Au 200 nm (no titanium)
  lift-off : heated acetone (35 °C), blow acetone using pipette with thin head
  rinsing : isopropanol then water

A.3.2 Pillar definition

- **Spin-coating**
  spin coating : Microposit primer ; 30 s at 4000 rpm
  resist spin-coating : SPR700 1.2 photoresist, 30 s at 4000 rpm
  baking : 1min at 105°C

- **Border removal**
  UV illumination : 100 mJ·cm^{-2}
  development : MF319 40 s, rinse in water

- **Pillars definition**
  UV illumination : 45 mJ·cm^{-2}
  baking : 1 min at 105 °C
  development : MF319 30 s, rinse in DI water
  ion beam etching : 300 V/40 mA, 5 °C, 30° angle with beam, rotating holder

- **Resist stripping**
  oxygen plasma : 2 mn 100 sccm O_2, 14.5 sccm Ar, 200 mT, 27 °C
  stripping : strip in acetone, rinse isopropanol then water

A.3.3 Bottom electrode definition

- **Spin-coating**
  spin coating : Microposit primer ; 30 s at 4000 rpm (optional)
  resist spin-coating : S1813 photoresist, 30 s at 6000 rpm
  baking : 1 min at 90 °C

- **Electrode definition**
  UV illumination : 45 mJ·cm^{-2}

baking : 1 min at 110 °C
development : MF319 50 s, rinse in DI water
ion beam etching : 300 V/40 mA, 5 °C, 30° angle with beam, rotating holder

- **Resist stripping**
  oxygen plasma : 2 mn 100 sccm O_2, 14.5 sccm Ar, 200 mT, 27 °C
  stripping : strip in acetone, rinse isopropanol then water

A.3.4 Permanent resist

- **Spin-coating**
  resist spin-coating : S1805 photoresist, diluted 50/50 with solvent, 30 s at 6000 rpm
  baking : 1 min at 110 °C

- **Holes definition**
  UV illumination : 30 mJ·cm^{-2}
  annealing : 1 min at 110 °C
  development : MF319 3 s, rinse in DI water
  permanent baking : 170°C 1 min

A.3.5 Gold contacts

- **Spin-coating**
  resist spin-coating : SPR700 1.2 photoresist, 30 s at 4000 rpm
  baking : 1 min at 110 °C
  bathing : chlorobenzene, 10 mn, rinse in water *well*

- **Electrode definition**
  UV illumination : 45 mJ·cm^{-2}
  development : MF319 12 s, rinse in DI water

- **Gold evaporation**
  plasma etching (in the chamber) : 200 eV 45 s
  gold deposition : Au 200 nm (no titanium)
  lift-off : heated acetone (35 °C), blow acetone using pipette with thin head
  rinsing : isopropanol then water

Appendix B

Superconductor-ferromagnet bilayers

B.1 Domain-wall superconductivity model

We used a simple resistor circuit model to simulate inhomogeneous superconductivity. We modeled the superconductor with a square grid circuit of 250×250 nodes, as represented in Fig.B.1. In that circuit, each unit cell is composed of a central node and 4 resistors. All the four resistances are equal, and field-dependent. These are modeled as a simple type-I superconductor that switches from $R = 0$ ($H < H_{c2}$) to $R = 1$ ($H \geq H_{c2}$).
To calculate the inhomogeneous magnetic field at the surface of the superconductor, we used the stray-field calculations mentioned in 5.2.2, which were interpolated on the 250×250 grid to fit the circuit model. That size is chosen so that the calculations time remains manageable by the computer.
Each cell of the square array is then affected to the corresponding pixel of the stray magnetic field map presented in Fig.5.3.1. The magnetic field in the superconductor is then locally defined as $H_{tot} = H_{ext} + H_{stray}$, and the local resistance is then calculated accordingly. As these maps were obtained from MFM images at ambient temperature (see Chap.5), the external field at which they appear below T_c is different (see Fig.5.2). We estimated it by looking at the corresponding magnetization value in the 10K Hall effect loops. Each resistance is then calculated accordingly.
The resulting resistor mapping is input into the Ngspice[247] circuit simulator using the PySpice [248] Python3 library. To "measure" the resistance, we include in the circuit a constant current source, of which the input and output are connected to all the nodes of respectively the first and last rows of unit cells, as shown in the schematic of Fig.B.1. A current of 1mA is applied, and the resistance is then calculated for each magnetic field.
For the Co/Pt and Pt/Co/Ru samples, we calculated the model magneto-resistances using that circuit model. The results are presented in Fig.B.2, for the field-increasing branches of the MR. In the figure, all the curves are normalized by the normal-state resistance (all resistances equal to 1).

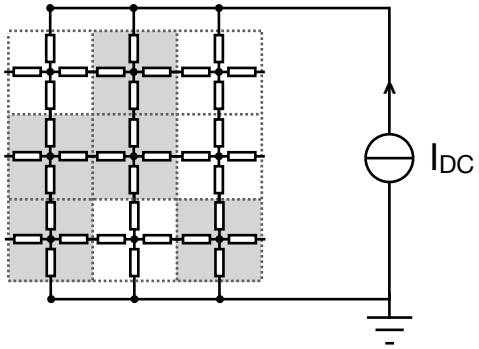

Figure B.1: **Simple resistor network model (3×3 cells)**
The bilayer is modeled as a network of resistances. Each resistance in the unit cell is initially equal to zero (white), and switches to 1 if the local field exceeds the critical field (grey). The real network has 250×250 cells.

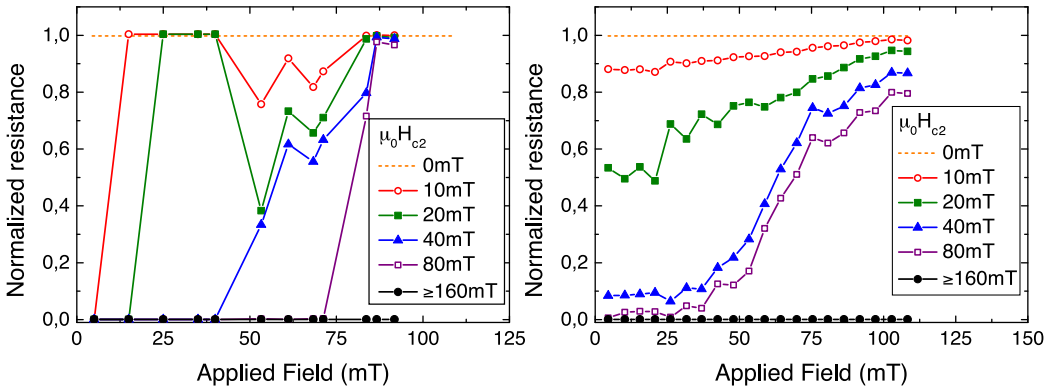

(a) $[Co_{0.6nm}/Pt_{1nm}]_{\times 5}$ (b) $[Pt_{1.2nm}/Co_{1.6nm}/Ru_{1.4nm}]_{\times 4}$

Figure B.2: **Inhomogeneous superconductor model**

For both samples, we observe a pattern that evolves similarly as the increasing resistance branch of the magnetoresistance measurements. In Co/Pt, we observe a re-entrance of superconductivity as observed in the measurements when domains appear ($\approx 40 - 50$ mT). Similarly, it slowly increases with the field in Pt/Co/Ru. For both systems, the effect is the largest when the critical field is comparable to the typical value of the stray magnetic field in the domains (respectively 20 mT and 80 mT). These suggest that the critical field should be of that order for DWS-related phenomena to occur. It is much lower than the estimations of H_{c2}, around 8 T at 3.5 K. These values are not realistic, since the samples are still well in the superconducting state ($R/R_N \ll 1$).

B.2 Effect of the insulating AlOx interlayer

In Chap.5 and 6, we presented results in bilayers that included a 3 nm alumina interlayer between the superconducting MoSi and the ferromagnetic multilayer. The point of that layer is to suppress proximity effects and ensure the interactions are magnetic. Here, we compare magneto-resistance measurements in bilayers with and without the alumina interlayer.These include Co/Pt layers in Fig.B.3a, and Ir/Co/Pt in Fig.B.3b. These were measured at 500 mA around 3 K. We do not have exactly comparable measurements, however the effect is similarly present in both. Since the hysteresis is not weakened by the insulating layer, proximity effect does not play a role in the observed magnetic hysteresis.

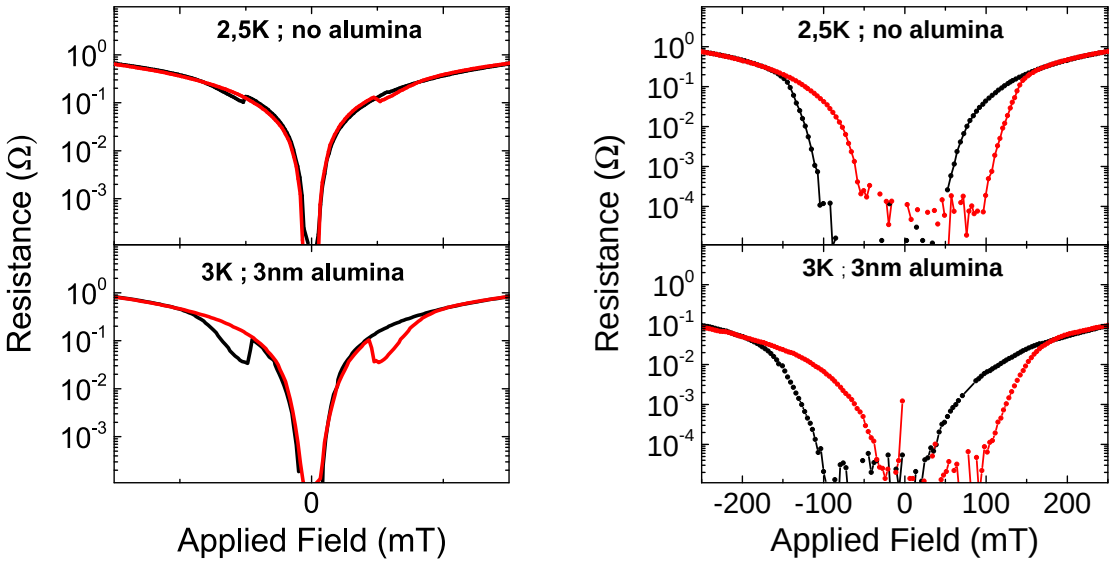

(a) $(Co_{0.6nm}/Pt_{1nm})_{\times 5}$ (b) $(Ir_{1nm}/Co_{0.6nm}/Pt_{1nm})_{\times 5}$

Figure B.3: **MR in bilayers with and without alumina (500 μA)**
A barrier of 3 nm alumina between the superconductor and ferromagnetic layers does not suppress the hysteresis.

B.3 Estimation of the deflection angle

Measuring a transverse resistance implies that, on average, vortices are deflected from the direction of the Lorentz force by an angle θ_H. The vortex velocity and resulting electric field relate through $\mathbf{E} = \mathbf{B_z} \times \mathbf{v_l}$ in the case of a thin film ($\mathbf{B} = \mathbf{B_z}$ in the superconductor). Thus, one can easily calculate the deflection angle using the ratio of the electric fields $E_\perp$ and $E_\parallel$ relative to the current. This is expressed in Eqn.B.1. L_x=200 μm and L_y=40 μm are the dimensions of the bridge. It is also equivalently expressed using the longitudinal and transverse resistances.

$$\theta_H = \arctan\left(\frac{E_\perp}{E_\parallel}\right) = \arctan\left(\frac{R_{xy}}{R_{xx}}\frac{L_x}{L_y}\right) \tag{B.1}$$

For the Pt/Co/Ru sample, at the maximum in the 45° curve (Fig.6.3b and 6.4b) and, we have $R_{xx} \approx 0.5\ \Omega$ and $R_{xy,odd} \approx 2\ \text{m}\Omega$. This results in a deflection angle of $\theta_H = 1.1°$.

List of Tables

List of Figures

References

[1] D. van Delft and P. Kes, "The discovery of superconductivity," *Physics Today*, vol. 63, no. 9, pp. 38–43, Sep. 2010.

[2] "Technological applications of superconductivity," *Wikipedia*, Feb. 2019, page Version ID: 884046460.

[3] S. W. Shin, G. Smith, J. A. Smolin, and U. Vazirani, "How" quantum" is the D-Wave machine?" *arXiv preprint*, 2014.

[4] D. S. Holmes, A. L. Ripple, and M. A. Manheimer, "Energy-Efficient Superconducting Computing—Power Budgets and Requirements," *IEEE Transactions on Applied Superconductivity*, vol. 23, no. 3, pp. 1 701 610–1 701 610, Jun. 2013.

[5] M. A. Manheimer, "Cryogenic Computing Complexity Program: Phase 1 Introduction," *IEEE Transactions on Applied Superconductivity*, vol. 25, no. 3, pp. 1–4, Jun. 2015.

[6] "November 2018 | TOP500 Supercomputer Sites," https://www.top500.org/lists/2018/11/.

[7] "Summit (OLCF-4) - Supercomputers - WikiChip," https://en.wikichip.org/wiki/supercomputers/olcf-4.

[8] "Portes de Champagne," https://www.edf-renouvelables.com/project/porte-de-champagne/.

[9] D. C. Brock, "Will the NSA Finally Build Its Superconducting Spy Computer?" https://spectrum.ieee.org/tech-history/silicon-revolution/will-the-nsa-finally-build-its-superconducting-spy-computer, Feb. 2016.

[10] S. Chen, "Can China build a superconducting computer to change the world?" https://www.scmp.com/news/china/society/article/2161390/can-china-build-us145-million-superconducting-computer-will, Aug. 2018.

[11] S. K. Tolpygo, "Superconductor digital electronics: Scalability and energy efficiency issues (Review Article)," *Low Temperature Physics*, vol. 42, no. 5, pp. 361–379, May 2016.

[12] "Flash memory," *Wikipedia*, May 2019, page Version ID: 896319372.

[13] C. Suplee, "Hybrid Memory Device for Superconducting Computing," https://www.nist.gov/news-events/news/2015/01/hybrid-memory-device-superconducting-computing, Jan. 2015.

[14] V. V. Ryazanov, V. A. Oboznov, A. Y. Rusanov, A. V. Veretennikov, A. A. Golubov, and J. Aarts, "Coupling of Two Superconductors through a Ferromagnet: Evidence for a π Junction," *Physical Review Letters*, vol. 86, no. 11, pp. 2427–2430, Mar. 2001.

[15] T. Kontos, M. Aprili, J. Lesueur, and X. Grison, "Inhomogeneous Superconductivity Induced in a Ferromagnet by Proximity Effect," *Physical Review Letters*, vol. 86, no. 2, pp. 304–307, Jan. 2001.

[16] V. V. Ryazanov, V. V. Bol'ginov, D. S. Sobanin, I. V. Vernik, S. K. Tolpygo, A. M. Kadin, and O. A. Mukhanov, "Magnetic Josephson Junction Technology for Digital and Memory Applications," *Physics Procedia*, vol. 36, pp. 35–41, 2012.

[17] S. S. P. Parkin, M. Hayashi, and L. Thomas, "Magnetic Domain-Wall Racetrack Memory," *Science*, vol. 320, no. 5873, pp. 190–194, Apr. 2008.

[18] A. Fert, V. Cros, and J. Sampaio, "Skyrmions on the track," *Nature Nanotechnology*, vol. 8, no. 3, pp. 152–156, Mar. 2013.

[19] F. S. Bergeret, A. F. Volkov, and K. B. Efetov, "Odd triplet superconductivity and related phenomena in superconductor-ferromagnet structures," *Reviews of Modern Physics*, vol. 77, no. 4, pp. 1321–1373, Nov. 2005.

[20] M. N. Baibich, J. M. Broto, A. Fert, F. N. Van Dau, F. Petroff, P. Etienne, G. Creuzet, A. Friederich, and J. Chazelas, "Giant Magnetoresistance of (001)Fe/(001)Cr Magnetic Superlattices," *Physical Review Letters*, vol. 61, no. 21, pp. 2472–2475, Nov. 1988.

[21] J. C. Slonczewski, "Conductance and exchange coupling of two ferromagnets separated by a tunneling barrier," *Physical Review B*, vol. 39, no. 10, pp. 6995–7002, Apr. 1989.

[22] R. S. Keizer, S. T. B. Goennenwein, T. M. Klapwijk, G. Miao, G. Xiao, and A. Gupta, "A spin triplet supercurrent through the half-metallic ferromagnet CrO2," *Nature*, vol. 439, no. 7078, pp. 825–827, Feb. 2006.

[23] T. S. Khaire, M. A. Khasawneh, W. P. Pratt, and N. O. Birge, "Observation of Spin-Triplet Superconductivity in Co-Based Josephson Junctions," *Physical Review Letters*, vol. 104, no. 13, Mar. 2010.

[24] M. S. Anwar, F. Czeschka, M. Hesselberth, M. Porcu, and J. Aarts, "Long-range supercurrents through half-metallic ferromagnetic CrO 2," *Physical Review B*, vol. 82, no. 10, Sep. 2010.

[25] J. W. A. Robinson, J. D. S. Witt, and M. G. Blamire, "Controlled Injection of Spin-Triplet Supercurrents into a Strong Ferromagnet," *Science*, vol. 329, no. 5987, pp. 59–61, 2010.

[26] V. Peña, Z. Sefrioui, D. Arias, C. Leon, J. Santamaria, M. Varela, S. J. Pennycook, and J. L. Martinez, "Coupling of superconductors through a half-metallic ferromagnet: Evidence for a long-range proximity effect," *Physical Review B*, vol. 69, no. 22, Jun. 2004.

[27] C. Visani, Z. Sefrioui, J. Tornos, C. Leon, J. Briatico, M. Bibes, A. Barthélémy, J. Santamaría, and J. E. Villegas, "Equal-spin Andreev reflection and long-range coherent transport in high-temperature superconductor/half-metallic ferromagnet junctions," *Nature Physics*, vol. 8, no. 7, pp. 539–543, Jul. 2012.

[28] Y. Kalcheim, T. Kirzhner, G. Koren, and O. Millo, "Long-range proximity effect in La 2 / 3 Ca 1 / 3 MnO 3 /(100)YBa 2 Cu 3 O 7 - δ ferromagnet/superconductor bilayers: Evidence for induced triplet superconductivity in the ferromagnet," *Physical Review B*, vol. 83, no. 6, Feb. 2011.

[29] Y. Kalcheim, I. Felner, O. Millo, T. Kirzhner, G. Koren, A. Di Bernardo, M. Egilmez, M. G. Blamire, and J. W. A. Robinson, "Magnetic field dependence of the proximity-induced triplet superconductivity at ferromagnet/superconductor interfaces," *Physical Review B*, vol. 89, no. 18, May 2014.

[30] M. Egilmez, J. W. A. Robinson, J. L. MacManus-Driscoll, L. Chen, H. Wang, and M. G. Blamire, "Supercurrents in half-metallic ferromagnetic La $_{0.7}$ Ca $_{0.3}$ MnO $_3$," *Europhysics Letters (EPL)*, vol. 106, no. 3, p. 37003, May 2014.

[31] V. Štrbík, Š. Beňačka, Š. Gaži, M. Španková, V. Šmatko, J. Knoška, N. Gál, Š. Chromik, M. Sojková, and M. Pisarčík, "Superconductor-ferromagnet-superconductor nanojunctions from perovskite materials," *Applied Surface Science*, vol. 395, pp. 237–240, Feb. 2017.

[32] Z. Sefrioui, D. Arias, V. Peña, J. E. Villegas, M. Varela, P. Prieto, C. León, J. L. Martinez, and J. Santamaria, "Ferromagnetic/superconducting proximity effect in La 0.7 Ca 0.3 MnO 3 / YBa 2 Cu 3 O 7 - δ superlattices," *Physical Review B*, vol. 67, no. 21, Jun. 2003.

[33] C. Visani, F. Cuellar, A. Pérez-Muñoz, Z. Sefrioui, C. León, J. Santamaría, and J. E. Villegas, "Magnetic field influence on the proximity effect at YB a 2 C u 3 O 7 / L a 2 / 3 C a 1 / 3 Mn O 3 superconductor/half-metal interfaces," *Physical Review B*, vol. 92, no. 1, Jul. 2015.

[34] W. J. Tomasch, "Geometrical Resonance and Boundary Effects in Tunneling from Superconducting In," *Physical Review Letters*, vol. 16, no. 1, pp. 16–19, Jan. 1966.

[35] T. Wolfram, "Tomasch Oscillations in the Density of States of Superconducting Films," *Physical Review*, vol. 170, no. 2, pp. 481–490, Jun. 1968.

[36] O. Nesher and G. Koren, "Measurements of Delta and vF from Andreev reflections and McMillan-Rowell oscillations in edge junctions of YBa2Cu3O6.6/YBa2Cu2.55Fe0.45Oy/YBa2Cu3O6.6," *Physical Review B*, p. 4, 1999.

[37] P. Seidel, M. Grajcar, A. Plecenik, and R. Hlubina, "Superconducting parameters of YBCO and BSCCO from 'tunneling' spectroscopy," *Physica B: Condensed Matter*, vol. 218, no. 1-4, pp. 224–227, Feb. 1996.

[38] J. M. Rowell and W. L. McMillan, "Electron Interference in a Normal Metal Induced by Superconducting Contracts," *Physical Review Letters*, vol. 16, no. 11, pp. 453–456, Mar. 1966.

[39] D. J. Singh and W. E. Pickett, "Pseudogaps, Jahn-Teller distortions, and magnetic order in manganite perovskites," *Physical Review B*, vol. 57, no. 1, pp. 88–91, Jan. 1998.

[40] T. Holden, H.-U. Habermeier, G. Cristiani, A. Golnik, A. Boris, A. Pimenov, J. Humlíc̆ek, O. I. Lebedev, G. Van Tendeloo, B. Keimer, and C. Bernhard, "Proximity induced metal-insulator transition in YBa 2 Cu 3 O 7 / La 2 / 3 Ca 1 / 3 MnO 3 superlattices," *Physical Review B*, vol. 69, no. 6, Feb. 2004.

[41] S. Yunoki, A. Moreo, E. Dagotto, S. Okamoto, S. S. Kancharla, and A. Fujimori, "Electron doping of cuprates via interfaces with manganites," *Physical Review B*, vol. 76, no. 6, Aug. 2007.

[42] S. Muhlbauer, B. Binz, F. Jonietz, C. Pfleiderer, A. Rosch, A. Neubauer, R. Georgii, and P. Boni, "Skyrmion Lattice in a Chiral Magnet," *Science*, vol. 323, no. 5916, pp. 915–919, Feb. 2009.

[43] Z. Yang, M. Lange, A. Volodin, R. Szymczak, and V. V. Moshchalkov, "Domain-wall superconductivity in superconductor–ferromagnet hybrids," *Nat.Mater.*, vol. 3, no. 11, pp. 793–798, Nov. 2004.

[44] L. Y. Zhu, T. Y. Chen, and C. L. Chien, "Altering the Superconductor Transition Temperature by Domain-Wall Arrangements in Hybrid Ferromagnet-Superconductor Structures," *Physical Review Letters*, vol. 101, no. 1, Jul. 2008.

[45] W. Gillijns, A. Y. Aladyshkin, A. V. Silhanek, and V. V. Moshchalkov, "Magnetic confinement of the superconducting condensate in superconductor-ferromagnet hybrid composites," *Physical Review B*, vol. 76, no. 6, Aug. 2007.

[46] M. Iavarone, A. Scarfato, F. Bobba, M. Longobardi, G. Karapetrov, V. Novosad, V. Yefremenko, F. Giubileo, and A. M. Cucolo, "Imaging the spontaneous formation of vortex-antivortex pairs in planar superconductor/ferromagnet hybrid structures," *Physical Review B*, vol. 84, no. 2, Jul. 2011.

[47] C. Visani, P. J. Metaxas, A. Collaudin, B. Calvet, R. Bernard, J. Briatico, C. Deranlot, K. Bouzehouane, and J. E. Villegas, "Hysteretic magnetic pinning and reversible resistance switching in high-temperature superconductor/ferromagnet multilayers," *Physical Review B*, vol. 84, no. 5, Aug. 2011.

[48] M. Lange, M. J. Van Bael, V. V. Moshchalkov, and Y. Bruynseraede, "Magnetic-domain-controlled vortex pinning in a superconductor/ferromagnet bilayer," *Applied Physics Letters*, vol. 81, no. 2, pp. 322–324, Jul. 2002.

[49] M. Lange, M. J. Van Bael, and V. V. Moshchalkov, "Vortex Matter in Superconductor / Ferromagnet Hybrids," *Journal of Low Temperature Physics*, vol. 139, no. 1, pp. 195–206, Apr. 2005.

[50] Z. Adamus, M. Z. Cieplak, M. Kończykowski, L. Y. Zhu, and C. L. Chien, "Influence of magnetic domain landscape on the flux dynamics in superconductor/ferromagnet bilayers," *Physical Review B*, vol. 93, no. 5, Feb. 2016.

[51] A. Belkin, V. Novosad, M. Iavarone, J. Pearson, and G. Karapetrov, "Superconductor/ferromagnet bilayers: Influence of magnetic domain structure on vortex dynamics," *Phys. Rev. B*, vol. 77, no. 18, May 2008.

[52] J. Baumard, J. Cayssol, F. S. Bergeret, and A. Buzdin, "Generation of a superconducting vortex via Néel skyrmions," *Physical Review B*, vol. 99, no. 1, Jan. 2019.

[53] R. M. Menezes, J. F. S. Neto, C. C. d. S. Silva, and M. V. Milošević, "Manipulation of magnetic skyrmions by superconducting vortices in ferromagnet-superconductor heterostructures," *Physical Review B*, vol. 100, no. 1, Jul. 2019.

[54] V. L. Vadimov, M. V. Sapozhnikov, and A. S. Mel'nikov, "Magnetic skyrmions in ferromagnet-superconductor (F/S) heterostructures," *Applied Physics Letters*, vol. 113, no. 3, p. 032402, Jul. 2018.

[55] K. M. D. Hals, M. Schecter, and M. S. Rudner, "Composite Topological Excitations in Ferromagnet-Superconductor Heterostructures," *Physical Review Letters*, vol. 117, no. 1, Jun. 2016.

[56] N. Del-Valle, S. Agramunt-Puig, A. Sanchez, and C. Navau, "Imprinting skyrmions in thin films by ferromagnetic and superconducting templates," *Applied Physics Letters*, vol. 107, no. 13, p. 133103, Sep. 2015.

[57] S. Kubo, "Superconducting properties of amorphous MoX (X=Si, Ge) alloy films for Abrikosov vortex memory," *Journal of Applied Physics*, vol. 63, no. 6, pp. 2033–2045, Mar. 1988.

[58] C. Moreau-Luchaire, C. Moutafis, N. Reyren, J. Sampaio, C. A. F. Vaz, N. Van Horne, K. Bouzehouane, K. Garcia, C. Deranlot, P. Warnicke, P. Wohlhüter, J.-M. George, M. Weigand, J. Raabe, V. Cros, and A. Fert, "Additive interfacial chiral interaction in multilayers for stabilization of small individual skyrmions at room temperature," *Nature Nanotechnology*, vol. 11, p. 444, Jan. 2016.

[59] W. Legrand, D. Maccariello, N. Reyren, K. Garcia, C. Moutafis, C. Moreau-Luchaire, S. Collin, K. Bouzehouane, V. Cros, and A. Fert, "Room-Temperature Current-Induced Generation and Motion of sub-100 nm Skyrmions," *Nano Lett.*, vol. 17, no. 4, pp. 2703–2712, Apr. 2017.

[60] W. Legrand, "Crafting magnetic skyrmions at room temperature: size, stability and dynamics in multilayers," Ph.D. dissertation, 2019.

[61] J. I. Martín, M. Vélez, A. Hoffmann, I. K. Schuller, and J. L. Vicent, "Artificially Induced Reconfiguration of the Vortex Lattice by Arrays of Magnetic Dots," *Physical Review Letters*, vol. 83, no. 5, pp. 1022–1025, Aug. 1999.

[62] J. R. Clem, "The Bardeen-Stephen theory," *J.Supercond.*, vol. 4, no. 5, pp. 337–339, Oct. 1991.

[63] M. Tinkham, *Introduction to Superconductivity*, 2nd ed. Dover books, 2004.

[64] S. Woo, K. Litzius, B. Krüger, M.-Y. Im, L. Caretta, K. Richter, M. Mann, A. Krone, R. M. Reeve, M. Weigand, P. Agrawal, I. Lemesh, M.-A. Mawass, P. Fischer, M. Kläui, and G. S. D. Beach, "Observation of room-temperature magnetic skyrmions and their current-driven dynamics in ultrathin metallic ferromagnets," *Nature Materials*, vol. 15, no. 5, pp. 501–506, May 2016.

[65] E. R. C. Dorf, *Electrical Engineering Handbook*. CRC Press, 2000.

[66] D. Maccariello, W. Legrand, N. Reyren, K. Garcia, K. Bouzehouane, S. Collin, V. Cros, and A. Fert, "Electrical detection of single magnetic skyrmions in metallic multilayers at room temperature," *Nature Nanotechnology*, vol. 13, no. 3, pp. 233–237, Mar. 2018.

[67] T. Yokoyama and J. Linder, "Josephson effect through magnetic skyrmions," *Physical Review B*, vol. 92, no. 6, Aug. 2015.

[68] S. S. Pershoguba, S. Nakosai, and A. V. Balatsky, "Skyrmion-induced bound states in a superconductor," *Physical Review B*, vol. 94, no. 6, Aug. 2016.

[69] X. Z. Yu, N. Kanazawa, Y. Onose, K. Kimoto, W. Z. Zhang, S. Ishiwata, Y. Matsui, and Y. Tokura, "Near room-temperature formation of a skyrmion crystal in thin-films of the helimagnet FeGe," *Nature Materials*, vol. 10, no. 2, pp. 106–109, Feb. 2011.

[70] J. Bardeen, L. N. Cooper, and J. R. Schrieffer, "Microscopic Theory of Superconductivity," *Physical Review*, vol. 106, no. 1, pp. 162–164, Apr. 1957.

[71] J. G. Bednorz and K. A. Müller, "Possible highT c superconductivity in the BaLaCuO system," *Zeitschrift für Physik B Condensed Matter*, vol. 64, no. 2, pp. 189–193, Jun. 1986.

[72] C. W. Chu, "Superconductivity at higher temperatures in the Hg-Ba-Ca-Cu-O compound system," *Journal of Superconductivity*, vol. 7, no. 1, pp. 1–7, Feb. 1994.

[73] J.-F. Ge, Z.-L. Liu, C. Liu, C.-L. Gao, D. Qian, Q.-K. Xue, Y. Liu, and J.-F. Jia, "Superconductivity above 100 K in single-layer FeSe films on doped SrTiO 3," *Nature materials*, vol. 14, no. 3, p. 285, 2015.

[74] A. Drozdov, M. Eremets, I. Troyan, V. Ksenofontov, and S. Shylin, "Conventional superconductivity at 203 kelvin at high pressures in the sulfur hydride system," *Nature*, vol. 525, no. 7567, p. 73, 2015.

[75] T. Lanting, A. J. Przybysz, A. Y. Smirnov, F. M. Spedalieri, M. H. Amin, A. J. Berkley, R. Harris, F. Altomare, S. Boixo, P. Bunyk, N. Dickson, C. Enderud, J. P. Hilton, E. Hoskinson, M. W. Johnson, E. Ladizinsky, N. Ladizinsky, R. Neufeld, T. Oh, I. Perminov, C. Rich, M. C. Thom, E. Tolkacheva, S. Uchaikin, A. B. Wilson, and G. Rose, "Entanglement in a Quantum Annealing Processor," *Physical Review X*, vol. 4, no. 2, May 2014.

[76] "Summit."

[77] "Aurora Supercomputer," https://www.intel.com/content/www/us/en/now/aurora-supercomputer/overview.html.

[78] M. Eschrig, "Spin-polarized supercurrents for spintronics," *Physics Today*, vol. 64, no. 1, p. 43, 2011.

[79] D. Einzel, "50 Years of Fluxoid Quantization: 2e or Not 2e," *J.LowTemp.Phys.*, vol. 163, no. 5-6, pp. 215–237, Jun. 2011.

[80] D. Dew-Hughes, "The critical current of superconductors: An historical review," *Low Temperature Physics*, vol. 27, no. 9, pp. 713–722, Sep. 2001.

[81] J. Pearl, "Current distribution in superconducting films carrying quantized fluxoids," *Applied Physics Letters*, vol. 5, no. 4, pp. 65–66, Aug. 1964.

[82] E. H. Brandt, "The flux-line lattice in superconductors," *Rep.Prog.Phys.*, vol. 58, no. 11, pp. 1465–1594, Nov. 1995.

[83] F. S. Wells, A. V. Pan, X. R. Wang, S. A. Fedoseev, and H. Hilgenkamp, "Analysis of low-field isotropic vortex glass containing vortex groups in YBa2Cu3O7-x thin films visualized by scanning SQUID microscopy," *Scientific Reports*, vol. 5, no. 1, Aug. 2015.

[84] A. Abrikosov, "The magnetic properties of superconducting alloys," *Journal of Physics and Chemistry of Solids*, vol. 2, no. 3, pp. 199–208, Jan. 1957.

[85] C. P. Bean, "Magnetization of Hard Superconductors," *Phys.Rev.Lett*, vol. 8, no. 6, pp. 250–253, Mar. 1962.

[86] C. P. Bean and J. D. Livingston, "Surface Barrier in Type-II Superconductors," *Phys.Rev.Lett*, vol. 12, no. 1, pp. 14–16, Jan. 1964.

[87] I. S. Veshchunov, W. Magrini, S. V. Mironov, A. G. Godin, J.-B. Trebbia, A. I. Buzdin, P. Tamarat, and B. Lounis, "Optical manipulation of single flux quanta," *Nature Communications*, vol. 7, no. 1, Dec. 2016.

[88] J. Bardeen and M. J. Stephen, "Theory of the Motion of Vortices in Superconductors," *Phys. Rev.*, vol. 140, no. 4A, pp. A1197–A1207, Nov. 1965.

[89] A. Campbell and J. Evetts, "Flux vortices and transport currents in type II superconductors," *Advances in Physics*, vol. 21, no. 90, pp. 199–428, Mar. 1972.

[90] M. Tinkham, "Viscous Flow of Flux in Type-ii Superconductors," *Physical Review Letters*, vol. 13, no. 26, pp. 804–807, Dec. 1964.

[91] B. Josephson, "Potential differences in the mixed state of type II superconductors," *Physics Letters*, vol. 16, no. 3, pp. 242–243, Jun. 1965.

[92] P. W. Anderson and Y. B. Kim, "Hard Superconductivity: Theory of the Motion of Abrikosov Flux Lines," *Rev.Mod.Phys.*, vol. 36, no. 1, pp. 39–43, Jan. 1964.

[93] P. W. Anderson, "Theory of Flux Creep in Hard Superconductors," *Phys.Rev.Lett*, vol. 9, no. 7, pp. 309–311, Oct. 1962.

[94] Y. B. Kim, C. F. Hempstead, and A. R. Strnad, "Critical Persistent Currents in Hard Superconductors," *Physical Review Letters*, vol. 9, no. 7, pp. 306–309, Oct. 1962.

[95] J. R. Waldram, *Superconductivity of Metals and Cuprates*. CRC Press, 1996.

[96] F. Irie and K. Yamafuji, "Theory of Flux Motion in Non-Ideal Type-II Superconductors," *Journal of the Physical Society of Japan*, vol. 23, no. 2, pp. 255–268, Aug. 1967.

[97] Y. B. Kim, C. F. Hempstead, and A. R. Strnad, "Flux-Flow Resistance in Type-II Superconductors," *Physical Review*, vol. 139, no. 4A, pp. A1163–A1172, Aug. 1965.

[98] P. H. Kes, J. Aarts, J. van den Berg, C. J. van der Beek, and J. A. Mydosh, "Thermally assisted flux flow at small driving forces," *Supercond. Sci. Technol.*, vol. 1, no. 5, p. 242, 1989.

[99] G. Blatter, M. V. Feigel'man, V. B. Geshkenbein, A. I. Larkin, and V. M. Vinokur, "Vortices in high-temperature superconductors," *Reviews of Modern Physics*, vol. 66, no. 4, pp. 1125–1388, Oct. 1994.

[100] A. Pautrat, J. Scola, C. Goupil, C. Simon, C. Villard, B. Domengès, Y. Simon, C. Guilpin, and L. Méchin, "Quantitative analysis of the critical current due to vortex pinning by surface corrugation," *Phys. Rev. B*, vol. 69, no. 22, p. 224504, Jun. 2004.

[101] J. Ekin, "Strain scaling law for flux pinning in practical superconductors. Part 1: Basic relationship and application to Nb3Sn conductors," *Cryogenics*, vol. 20, no. 11, pp. 611–624, Nov. 1980.

[102] E. J. Kramer, "Scaling laws for flux pinning in hard superconductors," *J.Appl.Phys.*, vol. 44, no. 3, pp. 1360–1370, Mar. 1973.

[103] D. Dew-Hughes, "Flux pinning mechanisms in type II superconductors," *Philosophical Magazine*, vol. 30, no. 2, pp. 293–305, Aug. 1974.

[104] L. Civale, "Vortex pinning and creep in high-temperature superconductors with columnar defects," *Superconductor Science and Technology*, vol. 10, no. 7A, pp. A11–A28, Jul. 1997.

[105] O. Daldini, P. Martinoli, J. L. Olsen, and G. Berner, "Vortex-Line Pinning by Thickness Modulation of Superconducting Films," *Physical Review Letters*, vol. 32, no. 5, pp. 218–221, Feb. 1974.

[106] V. V. Moshchalkov, M. Baert, V. V. Metlushko, E. Rosseel, M. J. Van Bael, K. Temst, Y. Bruynseraede, and R. Jonckheere, "Pinning by an antidot lattice: The problem of the optimum antidot size," *Physical Review B*, vol. 57, no. 6, pp. 3615–3622, Feb. 1998.

[107] J. E. Villegas, "A Superconducting Reversible Rectifier That Controls the Motion of Magnetic Flux Quanta," *Science*, vol. 302, no. 5648, pp. 1188–1191, Nov. 2003.

[108] K. Yu, T. W. Heitmann, C. Song, M. P. DeFeo, B. L. T. Plourde, M. B. S. Hesselberth, and P. H. Kes, "Asymmetric weak-pinning superconducting channels: Vortex ratchets," *Physical Review B*, vol. 76, no. 22, Dec. 2007.

[109] J. Trastoy, M. Malnou, C. Ulysse, R. Bernard, N. Bergeal, G. Faini, J. Lesueur, J. Briatico, and J. E. Villegas, "Freezing and thawing of artificial ice by thermal switching of geometric frustration in magnetic flux lattices," *Nature Nanotechnology*, vol. 9, no. 9, pp. 710–715, Sep. 2014.

[110] M. Vélez, J. Martín, J. Villegas, A. Hoffmann, E. González, J. Vicent, and I. K. Schuller, "Superconducting vortex pinning with artificial magnetic nanostructures," *Journal of Magnetism and Magnetic Materials*, vol. 320, no. 21, pp. 2547–2562, Nov. 2008.

[111] V. Rouco, R. Córdoba, J. De Teresa, L. A. Rodríguez, C. Navau, N. Del-Valle, G. Via, A. Sánchez, C. Monton, F. Kronast *et al.*, "Competition between superconductor–ferromagnetic stray magnetic fields in YBa 2 Cu 3 O 7- x films pierced with Co nano-rods," *Scientific reports*, vol. 7, no. 1, p. 5663, 2017.

[112] C. Reichhardt, G. T. Zimányi, and N. Grønbech-Jensen, "Complex dynamical flow phases and pinning in superconductors with rectangular pinning arrays," *Physical Review B*, vol. 64, no. 1, Jun. 2001.

[113] P. Nozières and W. F. Vinen, "The motion of flux lines in type II superconductors," *Philos.Mag.*, vol. 14, no. 130, pp. 667–688, Sep. 1966.

[114] E. B. Sonin, "Magnus force in superfluids and superconductors," *Phys. Rev. B*, vol. 55, no. 1, pp. 485–501, Jan. 1997.

[115] N. B. Kopnin, "Vortex dynamics and mutual friction in superconductors and Fermi superfluids," *Reports on Progress in Physics*, vol. 65, no. 11, pp. 1633–1678, Nov. 2002.

[116] P. Ao and D. J. Thouless, "Berry's phase and the Magnus force for a vortex line in a superconductor," *Phys.Rev.Lett*, vol. 70, no. 14, pp. 2158–2161, Apr. 1993.

[117] A. W. Smith, T. W. Clinton, C. C. Tsuei, and C. J. Lobb, "Sign reversal of the Hall resistivity in amorphous Mo3Si," *Phys. Rev. B*, vol. 49, no. 18, pp. 12 927–12 930, May 1994.

[118] C. Lobb, T. Clinton, A. Smith, p. Liu, p. Li, J. Peng, R. Greene, M. Eddp, and C. Tsuei, "Pinning, anisotropy, and the hall effect in superconductors," *Applied Superconductivity*, vol. 2, no. 10-12, pp. 631–637, Oct. 1994.

[119] Z. D. Wang, J. Dong, and C. S. Ting, "Unified theory of mixed state Hall effect in type-II superconductors: Scaling behavior and sign reversal," *Physical Review Letters*, vol. 72, no. 24, pp. 3875–3878, Jun. 1994.

[120] N. B. Kopnin and V. M. Vinokur, "Effects of Pinning on the Flux Flow Hall Resistivity," *Phys. Rev. Lett.*, vol. 83, no. 23, pp. 4864–4867, Dec. 1999.

[121] J. M. Harris, N. P. Ong, and Y. F. Yan, "Harris, Ong, and Yan Reply:," *Physical Review Letters*, vol. 74, no. 14, pp. 2839–2839, Apr. 1995.

[122] A. V. Silhanek, J. Van de Vondel, V. V. Moshchalkov, A. Leo, V. Metlushko, B. Ilic, V. R. Misko, and F. M. Peeters, "Comment on "Transverse rectification in superconducting thin films with arrays of asymmetric defects" [Appl. Phys. Lett. 91, 062505 (2007)]," *Applied Physics Letters*, vol. 92, no. 17, p. 176101, Apr. 2008.

[123] R. R. Hake, "Mixed-State Hall Effect in an Extreme Type-II Superconductor," *Physical Review*, vol. 168, no. 2, pp. 442–444, Apr. 1968.

[124] N. Kokubo, J. Aarts, and P. H. Kes, "Hall-conductivity sign change and fluctuations in amorphous Nb x Ge 1 - x films," *Physical Review B*, vol. 64, no. 1, Jun. 2001.

[125] N. Verellen, A. V. Silhanek, W. Gillijns, V. V. Moshchalkov, V. Metlushko, F. Gozzini, and B. Ilic, "Switchable magnetic dipole induced guided vortex motion," *Applied Physics Letters*, vol. 93, no. 2, p. 022507, Jul. 2008.

[126] J. E. Villegas, E. M. Gonzalez, M. I. Montero, I. K. Schuller, and J. L. Vicent, "Directional vortex motion guided by artificially induced mesoscopic potentials," *Physical Review B*, vol. 68, no. 22, Dec. 2003.

[127] A. V. Silhanek, L. Van Look, S. Raedts, R. Jonckheere, and V. V. Moshchalkov, "Guided vortex motion in superconductors with a square antidot array," *Physical Review B*, vol. 68, no. 21, Dec. 2003.

[128] J. Coey, *Magnetism and Magnetic Materials*. Cambridge: Cambridge University Press, 2010, oCLC: 819423378.

[129] A. Korkin and F. Rosei, *Nanoelectronics and Photonics: From Atoms to Materials, Devices, and Architectures*. Springer Science & Business Media, 2008.

[130] W. E. Pickett and J. S. Moodera, "Half Metallic Magnets," *Physics Today*, vol. 54, no. 5, pp. 39–44, May 2001.

[131] M. I. Katsnelson, V. Y. Irkhin, L. Chioncel, A. I. Lichtenstein, and R. A. de Groot, "Half-metallic ferromagnets: From band structure to many-body effects," *Reviews of Modern Physics*, vol. 80, no. 2, pp. 315–378, Apr. 2008.

[132] M. Duckheim and P. W. Brouwer, "Andreev reflection from noncentrosymmetric superconductors and Majorana bound-state generation in half-metallic ferromagnets," *Physical Review B*, vol. 83, no. 5, Feb. 2011.

[133] J. Alicea, "New directions in the pursuit of Majorana fermions in solid state systems," *Reports on Progress in Physics*, vol. 75, no. 7, p. 076501, Jul. 2012.

[134] P. F. Carcia, A. D. Meinhaldt, and A. Suna, "Perpendicular magnetic anisotropy in Pd/Co thin film layered structures," *Applied Physics Letters*, vol. 47, no. 2, pp. 178–180, Jul. 1985.

[135] P. F. Carcia, "Perpendicular magnetic anisotropy in Pd/Co and Pt/Co thin-film layered structures," *Journal of Applied Physics*, vol. 63, no. 10, pp. 5066–5073, May 1988.

[136] M. T. Johnson, P. J. H. Bloemen, F. J. A. den Broeder, and J. J. de Vries, "Magnetic anisotropy in metallic multilayers," *Reports on Progress in Physics*, vol. 59, no. 11, pp. 1409–1458, Nov. 1996.

[137] T. Tamegai, Y. Nakao, S. Mohan, and Y. Nakajima, "Experimental demonstration of shrinkage of magnetic domains in a superconductor/ferromagnet bilayer," *Superconductor Science and Technology*, vol. 24, no. 2, p. 024015, Feb. 2011.

[138] S. Seki and M. Mochizuki, *Skyrmions in Magnetic Materials*, ser. SpringerBriefs in Physics. Cham: Springer International Publishing, 2016.

[139] I. Dzyaloshinsky, "A thermodynamic theory of "weak" ferromagnetism of antiferromagnetics," *Journal of Physics and Chemistry of Solids*, vol. 4, no. 4, pp. 241–255, Jan. 1958.

[140] T. Moriya, "Anisotropic Superexchange Interaction and Weak Ferromagnetism," *Physical Review*, vol. 120, no. 1, pp. 91–98, Oct. 1960.

[141] P. F. Bessarab, G. P. Müller, I. S. Lobanov, F. N. Rybakov, N. S. Kiselev, H. Jónsson, V. M. Uzdin, S. Blügel, L. Bergqvist, and A. Delin, "Lifetime of racetrack skyrmions," *Scientific Reports*, vol. 8, no. 1, Dec. 2018.

[142] I. Kézsmárki, S. Bordács, P. Milde, E. Neuber, L. M. Eng, J. S. White, H. M. Rønnow, C. D. Dewhurst, M. Mochizuki, K. Yanai, H. Nakamura, D. Ehlers, V. Tsurkan, and A. Loidl, "Néel-type skyrmion lattice with confined orientation in the polar magnetic semiconductor GaV4S8," *Nature Materials*, vol. 14, no. 11, pp. 1116–1122, Nov. 2015.

[143] N. W. Ashcroft and N. D. Mermin, *Solid State Physics*. Brooks/Cole, 1976.

[144] N. Nagaosa, J. Sinova, S. Onoda, A. H. MacDonald, and N. P. Ong, "Anomalous Hall effect," *Rev. Mod. Phys.*, vol. 82, no. 2, pp. 1539–1592, May 2010.

[145] S. X. Huang and C. L. Chien, "Extended Skyrmion Phase in Epitaxial FeGe (111) Thin Films," *Physical Review Letters*, vol. 108, no. 26, Jun. 2012.

[146] N. Kanazawa, M. Kubota, A. Tsukazaki, Y. Kozuka, K. S. Takahashi, M. Kawasaki, M. Ichikawa, F. Kagawa, and Y. Tokura, "Discretized topological Hall effect emerging from skyrmions in constricted geometry," *Physical Review B*, vol. 91, no. 4, Jan. 2015.

[147] G. Binasch, P. Grünberg, F. Saurenbach, and W. Zinn, "Enhanced magnetoresistance in layered magnetic structures with antiferromagnetic interlayer exchange," *Physical Review B*, vol. 39, no. 7, pp. 4828–4830, Mar. 1989.

[148] I. Žutić, J. Fabian, and S. Das Sarma, "Spintronics: Fundamentals and applications," *Reviews of Modern Physics*, vol. 76, no. 2, pp. 323–410, Apr. 2004.

[149] C. Chappert, F. Nguyen Van Dau, and A. Fert, "The emergence of spin electronics in data storage," *Nat.Mater.*, vol. 6, 2007.

[150] J. M. Daughton and J. S. Huang, "Magnetoresistive memory including thin film storage cells having tapered ends," Patent, Mar., 1988, uS Patent 4,731,757.

[151] J. Akerman, "APPLIED PHYSICS: Toward a Universal Memory," *Science*, vol. 308, no. 5721, pp. 508–510, Apr. 2005.

[152] A. Yamaguchi, T. Ono, S. Nasu, K. Miyake, K. Mibu, and T. Shinjo, "Real-Space Observation of Current-Driven Domain Wall Motion in Submicron Magnetic Wires," *Physical Review Letters*, vol. 92, no. 7, Feb. 2004.

[153] A. H. Bobeck, P. I. Bonyhard, and J. E. Geusic, "Magnetic bubbles—An emerging new memory technology," *Proceedings of the IEEE*, vol. 63, no. 8, pp. 1176–1195, 1975.

[154] J. Iwasaki, M. Mochizuki, and N. Nagaosa, "Universal current-velocity relation of skyrmion motion in chiral magnets," *Nature Communications*, vol. 4, no. 1, Dec. 2013.

[155] A. Y. Aladyshkin, A. V. Silhanek, W. Gillijns, and V. V. Moshchalkov, "Nucleation of superconductivity and vortex matter in superconductor–ferromagnet hybrids," *Superconductor Science and Technology*, vol. 22, no. 5, p. 053001, May 2009.

[156] G. M. Maksimova, R. M. Ainbinder, and D. Y. Vodolazov, "Periodic vortex and current structures in superconductor-ferromagnet bilayer," *Physical Review B*, vol. 78, no. 22, Dec. 2008.

[157] A. Y. Aladyshkin, A. I. Buzdin, A. A. Fraerman, A. S. Mel'nikov, D. A. Ryzhov, and A. V. Sokolov, "Domain-wall superconductivity in hybrid superconductor-ferromagnet structures," *Physical Review B*, vol. 68, no. 18, Nov. 2003.

[158] A. Y. Aladyshkin and V. V. Moshchalkov, "Thin-film superconductor-ferromagnet hybrids: Competition between nucleation of superconductivity at domain walls and domains' centers," *Physical Review B*, vol. 74, no. 6, Aug. 2006.

[159] W. Gillijns, A. Y. Aladyshkin, M. Lange, M. J. Van Bael, and V. V. Moshchalkov, "Domain-Wall Guided Nucleation of Superconductivity in Hybrid Ferromagnet-Superconductor-Ferromagnet Layered Structures," *Physical Review Letters*, vol. 95, no. 22, Nov. 2005.

[160] R. Laiho, E. Lähderanta, E. B. Sonin, and K. B. Traito, "Penetration of vortices into the ferromagnet/type-II superconductor bilayer," *Physical Review B*, vol. 67, no. 14, Apr. 2003.

[161] S. Erdin, I. F. Lyuksyutov, V. L. Pokrovsky, and V. M. Vinokur, "Topological Textures in a Ferromagnet-Superconductor Bilayer," *Physical Review Letters*, vol. 88, no. 1, Dec. 2001.

[162] F. Bobba, C. Di Giorgio, A. Scarfato, M. Longobardi, M. Iavarone, S. A. Moore, G. Karapetrov, V. Novosad, V. Yefremenko, and A. M. Cucolo, "Vortex-antivortex coexistence in Nb-based superconductor/ferromagnet heterostructures," *Physical Review B*, vol. 89, no. 21, Jun. 2014.

[163] L. N. Bulaevskii, E. M. Chudnovsky, and M. P. Maley, "Magnetic pinning in superconductor-ferromagnet multilayers," *Appl.Phys.Lett.*, vol. 76, no. 18, pp. 2594–2596, May 2000.

[164] G. Karapetrov, A. Belkin, M. Iavarone, J. Fedor, V. Novosad, M. V. Milošević, and F. M. Peeters, "Anisotropic Superconductivity and Vortex Dynamics in Magnetically Coupled F/S and F/S/F Hybrids," *Journal of Superconductivity and Novel Magnetism*, vol. 24, no. 1-2, pp. 905–910, Jan. 2011.

[165] V. K. Vlasko-Vlasov, U. Welp, A. Imre, D. Rosenmann, J. Pearson, and W. K. Kwok, "Soft magnetic lithography and giant magnetoresistance in superconducting/ferromagnetic hybrids," *Physical Review B*, vol. 78, no. 21, Dec. 2008.

[166] D. B. Jan, J. Y. Coulter, M. E. Hawley, L. N. Bulaevskii, M. P. Maley, Q. X. Jia, B. B. Maranville, F. Hellman, and X. Q. Pan, "Flux pinning enhancement

in ferromagnetic and superconducting thin-film multilayers," *Applied Physics Letters*, vol. 82, no. 5, pp. 778–780, Feb. 2003.

[167] A. Garcıá-Santiago, F. Sánchez, M. Varela, and J. Tejada, "Enhanced pinning in a magnetic-superconducting bilayer," *Applied Physics Letters*, vol. 77, no. 18, pp. 2900–2902, Oct. 2000.

[168] J. I. Martín, M. Vélez, J. Nogués, and I. K. Schuller, "Flux Pinning in a Superconductor by an Array of Submicrometer Magnetic Dots," *Phys.Rev.Lett*, vol. 79, no. 10, pp. 1929–1932, Sep. 1997.

[169] C. Reichhardt, C. J. Olson, and F. Nori, "Commensurate and incommensurate vortex states in superconductors with periodic pinning arrays," *Physical Review B*, vol. 57, no. 13, pp. 7937–7943, Apr. 1998.

[170] M. Z. Cieplak, L. Y. Zhu, Z. Adamus, M. Kończykowski, and C. L. Chien, "Enhancement of vortex pinning in superconductor/ferromagnet bilayers via angled demagnetization," *Physical Review B*, vol. 84, no. 2, Jul. 2011.

[171] V. Vlasko-Vlasov, U. Welp, G. Karapetrov, V. Novosad, D. Rosenmann, M. Iavarone, A. Belkin, and W.-K. Kwok, "Guiding superconducting vortices with magnetic domain walls," *Physical Review B*, vol. 77, no. 13, Apr. 2008.

[172] M. A. Kayali and V. L. Pokrovsky, "Anisotropic transport properties of ferromagnetic-superconducting bilayers," *Physical Review B*, vol. 69, no. 13, Apr. 2004.

[173] T. M. Klapwijk, "Proximity Effect From an Andreev Perspective," *Journal of Superconductivity*, vol. 17, no. 5, pp. 593–611, Oct. 2004.

[174] G. E. Blonder, M. Tinkham, and T. M. Klapwijk, "Transition from metallic to tunneling regimes in superconducting microconstrictions: Excess current, charge imbalance, and supercurrent conversion," *Physical Review B*, vol. 25, no. 7, pp. 4515–4532, Apr. 1982.

[175] J. Y. T. Wei, N.-C. Yeh, D. F. Garrigus, and M. Strasik, "Directional Tunneling and Andreev Reflection on YBa 2 Cu 3 O 7 - δ Single Crystals: Predominance of d -Wave Pairing Symmetry Verified with the Generalized Blonder, Tinkham, and Klapwijk Theory," *Physical Review Letters*, vol. 81, no. 12, pp. 2542–2545, Sep. 1998.

[176] R. C. Dynes, V. Narayanamurti, and J. P. Garno, "Direct Measurement of Quasiparticle-Lifetime Broadening in a Strong-Coupled Superconductor," *Physical Review Letters*, vol. 41, no. 21, pp. 1509–1512, Nov. 1978.

[177] Y. Tanaka and S. Kashiwaya, "Theory of Tunneling Spectroscopy of d -Wave Superconductors," *Physical Review Letters*, vol. 74, no. 17, pp. 3451–3454, Apr. 1995.

[178] S. Kashiwaya, Y. Tanaka, M. Koyanagi, and K. Kajimura, "Theory for tunneling spectroscopy of anisotropic superconductors," *Physical Review B*, vol. 53, no. 5, pp. 2667–2676, Feb. 1996.

[179] C.-R. Hu, "Midgap surface states as a novel signature for d x a 2 - x b 2 -wave superconductivity," *Physical Review Letters*, vol. 72, no. 10, pp. 1526–1529, Mar. 1994.

[180] T. Löfwander, V. S. Shumeiko, and G. Wendin, "Andreev bound states in high- T_c superconducting junctions," *Superconductor Science and Technology*, vol. 14, no. 5, pp. R53–R77, May 2001.

[181] S. Kashiwaya and Y. Tanaka, "Tunnelling effects on surface bound states in unconventional superconductors," *Reports on Progress in Physics*, vol. 63, no. 10, pp. 1641–1724, Oct. 2000.

[182] M. Octavio, M. Tinkham, G. E. Blonder, and T. M. Klapwijk, "Subharmonic energy-gap structure in superconducting constrictions," *Physical Review B*, vol. 27, no. 11, pp. 6739–6746, Jun. 1983.

[183] W. L. McMillan and P. W. Anderson, "Theory of Geometrical Resonances in the Tunneling Characteristics of Thick Films of Superconductors," *Physical Review Letters*, vol. 16, no. 3, pp. 85–87, Jan. 1966.

[184] B. D. Josephson, "Coupled Superconductors," *Reviews of Modern Physics*, vol. 36, no. 1, pp. 216–220, Jan. 1964.

[185] C. Hamilton, R. Kautz, R. Steiner, and F. Lloyd, "A practical Josephson voltage standard at 1 V," *IEEE Electron Device Letters*, vol. 6, no. 12, pp. 623–625, Dec. 1985.

[186] S. Shapiro, "Josephson Currents in Superconducting Tunneling: The Effect of Microwaves and Other Observations," *Physical Review Letters*, vol. 11, no. 2, pp. 80–82, Jul. 1963.

[187] P. A. Warburton, "The Josephson effect: 50 years of science and technology," *Physics Education*, vol. 46, no. 6, pp. 669–675, Nov. 2011.

[188] N.-H. Kaneko, S. Nakamura, and Y. Okazaki, "A review of the quantum current standard," *Measurement Science and Technology*, vol. 27, no. 3, p. 032001, Mar. 2016.

[189] N. O. Birge, "Spin-triplet supercurrents in Josephson junctions containing strong ferromagnetic materials," *Philosophical Transactions of the Royal Society A: Mathematical, Physical and Engineering Sciences*, vol. 376, no. 2125, p. 20150150, Aug. 2018.

[190] R. J. Soulen Jr., "Measuring the Spin Polarization of a Metal with a Superconducting Point Contact," *Science*, vol. 282, no. 5386, pp. 85–88, Oct. 1998.

[191] P. M. Tedrow and R. Meservey, "Spin Polarization of Electrons Tunneling from Films of Fe, Co, Ni, and Gd," *Physical Review B*, vol. 7, no. 1, pp. 318–326, Jan. 1973.

[192] G. Deutscher, "Crossed Andreev Reflections," *Journal of Superconductivity*, p. 5, 2002.

[193] M. Eschrig, "Tailoring the Fulde-Ferrell-Larkin-Ovchinnikov state," *Annalen der Physik*, vol. 524, no. 3-4, pp. A65–A67, Apr. 2012.

[194] P. Fulde and R. A. Ferrell, "Superconductivity in a Strong Spin-Exchange Field," *Physical Review*, vol. 135, no. 3A, pp. A550–A563, Aug. 1964.

[195] A. Larkin and Y. N. Ovchinnikov, "Nonuniform state of superconductors," *Soviet Physics-JETP*, vol. 20, no. 3, pp. 762–762, 1965.

[196] M. Eschrig and T. Löfwander, "Triplet supercurrents in clean and disordered half-metallic ferromagnets," *Nature Physics*, vol. 4, no. 2, pp. 138–143, Feb. 2008.

[197] J. Linder, M. Cuoco, and A. Sudbø, "Spin-active interfaces and unconventional pairing in half-metal/superconductor junctions," *Physical Review B*, vol. 81, no. 17, May 2010.

[198] L. Bulaevskii, V. Kuzii, and A. Sobyanin, "Superconducting system with weak coupling to the current in the ground state," *JETP Letters*, vol. 25, no. 7, pp. 290–294, 1977.

[199] A. Bauer, J. Bentner, M. Aprili, M. L. Della Rocca, M. Reinwald, W. Wegscheider, and C. Strunk, "Spontaneous Supercurrent Induced by Ferromagnetic π Junctions," *Physical Review Letters*, vol. 92, no. 21, May 2004.

[200] H. Sellier, C. Baraduc, F. Lefloch, and R. Calemczuk, "Half-Integer Shapiro Steps at the 0 - π Crossover of a Ferromagnetic Josephson Junction," *Physical Review Letters*, vol. 92, no. 25, Jun. 2004.

[201] T. Kontos, M. Aprili, J. Lesueur, F. Genêt, B. Stephanidis, and R. Boursier, "Josephson Junction through a Thin Ferromagnetic Layer: Negative Coupling," *Physical Review Letters*, vol. 89, no. 13, Sep. 2002.

[202] R. Grein, T. Löfwander, G. Metalidis, and M. Eschrig, "Theory of superconductor-ferromagnet point-contact spectra: The case of strong spin polarization," *Physical Review B*, vol. 81, no. 9, Mar. 2010.

[203] A. I. Buzdin, L. Bulaevskii, and S. Panyukov, "Critical-current oscillations as a function of the exchange field and thickness of the ferromagnetic metal (F) in an SFS Josephson junction," *JETP Letters*, vol. 35, no. 4, p. 147, 1982.

[204] N. Banerjee, J. Robinson, and M. G. Blamire, "Reversible control of spin-polarized supercurrents in ferromagnetic Josephson junctions," *Nature Communications*, vol. 5, no. 1, Dec. 2014.

[205] M. Houzet and A. I. Buzdin, "Long range triplet Josephson effect through a ferromagnetic trilayer," *Physical Review B*, vol. 76, no. 6, Aug. 2007.

[206] I. Sosnin, H. Cho, V. T. Petrashov, and A. F. Volkov, "Superconducting Phase Coherent Electron Transport in Proximity Conical Ferromagnets," *Physical Review Letters*, vol. 96, no. 15, Apr. 2006.

[207] A. Iovan, T. Golod, and V. M. Krasnov, "Controllable generation of a spin-triplet supercurrent in a Josephson spin valve," *Physical Review B*, vol. 90, no. 13, Oct. 2014.

[208] C. Bell, S. Milikisyants, M. Huber, and J. Aarts, "Spin Dynamics in a Superconductor-Ferromagnet Proximity System," *Physical Review Letters*, vol. 100, no. 4, Feb. 2008.

[209] Z. Zhong-xian, M. Ru-ling, Z. Ping, and L. Lin, "Amorphous phase formation of Mo $_{1-x}$ Ge $_{x}$, Mo $_{1-x}$ Si $_{x}$ films and their superconducting properties," *Chinese Physics Letters*, vol. 1, no. 1, pp. 23–26, Aug. 1984.

[210] Y. P. Korneeva, M. Y. Mikhailov, Y. P. Pershin, N. N. Manova, A. V. Divochiy, Y. B. Vakhtomin, A. A. Korneev, K. V. Smirnov, A. G. Sivakov, A. Y. Devizenko, and G. N. Goltsman, "Superconducting single-photon detector made of MoSi film," *Superconductor Science and Technology*, vol. 27, no. 9, p. 095012, Sep. 2014.

[211] "Why the wind industry should cheer superconductivity," https://www.windpowerengineering.com/business-news-projects/uncategorized/why-the-wind-industry-should-cheer-superconductivity/.

[212] "Magnetische Materialien| emg," https://www.emg.tu-bs.de/forschung/material/lanthan_e.html.

[213] D. Zheng, A. Campbell, J. Johnson, J. Cooper, F. Blunt, A. Porch, and P. Freeman, "Magnetic susceptibilities, critical fields, and critical currents of Co-and Zn-doped YBa 2 Cu 3 O 7," *Physical Review B*, vol. 49, no. 2, p. 1417, 1994.

[214] O. Nesher and G. Koren, "Observation of Tomasch oscillations and tunneling-like behavior in oxygen-deficient edge junctions," *Applied Physics Letters*, vol. 74, no. 22, pp. 3392–3394, May 1999.

[215] A. Hoffmann, S. G. E. te Velthuis, Z. Sefrioui, J. Santamaría, M. R. Fitzsimmons, S. Park, and M. Varela, "Suppressed magnetization in La 0.7 Ca 0.3 MnO 3 / YBa 2 Cu 3 O 7 - δ superlattices," *Physical Review B*, vol. 72, no. 14, Oct. 2005.

[216] T. Hu, H. Xiao, C. Visani, Z. Sefrioui, J. Santamaria, and C. C. Almasan, "Evidence from magnetoresistance measurements for an induced triplet superconducting state in La 0.7 Ca 0.3 MnO 3 / YBa 2 Cu 3 O 7 - δ multilayers," *Physical Review B*, vol. 80, no. 6, Aug. 2009.

[217] R. C. Jaeger, *Introduction to Microelectronic Fabrication*, 2nd ed., ser. Modular Series on Solid State Devices. Prentice Hall, 2002, vol. 5.

[218] H. Gross, N. Bansal, Y.-S. Kim, and S. Oh, "*In Situ* study of emerging metallicity on ion-bombarded $SrTiO_3$ surface," *Journal of Applied Physics*, vol. 110, no. 7, p. 073704, Oct. 2011.

[219] J. Linder and J. W. A. Robinson, "Superconducting spintronics," *Nature Physics*, vol. 11, no. 4, pp. 307–315, Apr. 2015.

[220] M. Eschrig, "Spin-polarized supercurrents for spintronics: A review of current progress," *Reports on Progress in Physics*, vol. 78, no. 10, p. 104501, Oct. 2015.

[221] A. Singh, S. Voltan, K. Lahabi, and J. Aarts, "Colossal Proximity Effect in a Superconducting Triplet Spin Valve Based on the Half-Metallic Ferromagnet CrO 2," *Physical Review X*, vol. 5, no. 2, May 2015.

[222] "Keithley 622X user manual."

[223] C. Renner and B. Revaz, "Pseudogap Precursor of the Superconducting Gap in Under- and Overdoped Bi2Sr2CaCu2O81d," *Physical Review Letters*, vol. 80, no. 1, p. 4, 1998.

[224] A.-M. Tremblay, "Supraconductivité à haute température dans les cuprates et les organiques : où en est-on ?" https://www.college-de-france.fr/site/antoine-georges/guestlecturer-2015-03-16-17h00.htm.

[225] S. Kashiwaya, Y. Tanaka, M. Koyanagi, H. Takashima, and K. Kajimura, "Origin of zero-bias conductance peaks in high- T c superconductors," *Physical Review B*, vol. 51, no. 2, pp. 1350–1353, Jan. 1995.

[226] G. Deutscher, "Andreev–Saint-James reflections: A probe of cuprate superconductors," *Reviews of Modern Physics*, vol. 77, no. 1, pp. 109–135, Mar. 2005.

[227] P. Aronov and G. Koren, "Signature of a crossed Andreev reflection effect in the magnetic response of Y Ba 2 Cu 3 O 7 - δ junctions with the itinerant ferromagnet Sr Ru O 3," *Physical Review B*, vol. 72, no. 18, Nov. 2005.

[228] S. M. Dahir, A. F. Volkov, and I. M. Eremin, "Interaction of Skyrmions and Pearl Vortices in Superconductor-Chiral Ferromagnet Heterostructures," *arXiv:1810.09908 [cond-mat]*, Oct. 2018.

[229] K. M. D. Hals, "Magnetoelectric coupling in superconductor-helimagnet heterostructures," *Physical Review B*, vol. 95, no. 13, Apr. 2017.

[230] D. Nečas and P. Klapetek, "Gwyddion: An open-source software for SPM data analysis," *Central European Journal of Physics*, vol. 10, no. 1, pp. 181–188, 2012.

[231] A. Vansteenkiste, J. Leliaert, M. Dvornik, M. Helsen, F. Garcia-Sanchez, and B. Van Waeyenberge, "The design and verification of MuMax3," *AIP advances*, vol. 4, no. 10, p. 107133, 2014.

[232] G. S. Abo, Y.-K. Hong, J. Park, J. Lee, W. Lee, and B.-C. Choi, "Definition of Magnetic Exchange Length," *IEEE Transactions on Magnetics*, vol. 49, no. 8, pp. 4937–4939, Aug. 2013.

[233] C. Moreau-Luchaire, "Tailoring the interfacial properties of magnetic multilayers for the observation of skyrmions at room temperature," Ph.D. dissertation, Université Paris-Saclay, Dec. 2016.

[234] J. C. Russ and F. B. Neal, *The Image Processing Handbook*, 7th ed. CRC Press, 2016.

[235] M. J. Van Bael, M. Lange, S. Raedts, V. V. Moshchalkov, A. N. Grigorenko, and S. J. Bending, "Local visualization of asymmetric flux pinning by magnetic dots with perpendicular magnetization," *Physical Review B*, vol. 68, no. 1, Jul. 2003.

[236] C. Kittel, *Introduction to Solid State Physics*, 8th ed. Wiley, 2004.

[237] P. H. Kes and C. C. Tsuei, "Collective-Flux-Pinning Phenomena in Amorphous Superconductors," *Physical Review Letters*, vol. 47, no. 26, pp. 1930–1934, Dec. 1981.

[238] ——, "Two-dimensional collective flux pinning, defects, and structural relaxation in amorphous superconducting films," *Physical Review B*, vol. 28, no. 9, pp. 5126–5139, Nov. 1983.

[239] M. Zehetmayer and J. Hecher, "Testing V3Si for two-band superconductivity," *Superconductor Science and Technology*, vol. 27, no. 4, p. 044006, 2014.

[240] W. Jiang, G. Chen, K. Liu, J. Zang, S. G. te Velthuis, and A. Hoffmann, "Skyrmions in magnetic multilayers," *Physics Reports*, vol. 704, pp. 1–49, Aug. 2017.

[241] J. M. Harris, Y. F. Yan, O. K. C. Tsui, Y. Matsuda, and N. P. Ong, "Hall Angle Evidence for the Superclean Regime in 60 K Y Ba 2 Cu 3 O 6 + y," *Physical Review Letters*, vol. 73, no. 12, pp. 1711–1714, Sep. 1994.

[242] J. E. Villegas, A. Sharoni, C.-P. Li, and I. K. Schuller, "Anomalous, hysteretic, transverse magnetoresistance in superconducting thin films with magnetic vortex arrays," *Applied Physics Letters*, vol. 94, no. 25, p. 252507, Jun. 2009.

[243] W. J. Xu, B. Zhang, Z. X. Liu, Z. Wang, W. Li, Z. B. Wu, R. H. Yu, and X. X. Zhang, "Anomalous Hall effect in Fe/Gd bilayers," *EPL (Europhysics Letters)*, vol. 90, no. 2, p. 27004, Apr. 2010.

[244] W. J. Xu, B. Zhang, Z. Wang, S. S. Chu, W. Li, Z. B. Wu, R. H. Yu, and X. X. Zhang, "Scaling law of anomalous Hall effect in Fe/Cu bilayers," *The European Physical Journal B*, vol. 65, no. 2, pp. 233–237, Sep. 2008.

[245] S. L. Zhang, W. W. Wang, D. M. Burn, H. Peng, H. Berger, A. Bauer, C. Pfleiderer, G. van der Laan, and T. Hesjedal, "Manipulation of skyrmion motion by magnetic field gradients," *Nature Communications*, vol. 9, no. 1, Dec. 2018.

[246] C. Olson Reichhardt, S. Lin, D. Ray, and C. Reichhardt, "Comparing the dynamics of skyrmions and superconducting vortices," *Physica C: Superconductivity and its Applications*, vol. 503, pp. 52–57, Aug. 2014.

[247] P. Nenzi and H. Vogt, "Ngspice Users Manual Version 30," 2019.

[248] F. Salvaire, "PySpice."

université PARIS-SACLAY
ÉCOLE DOCTORALE
Physique en Île-de-France (EDPIF)

Titre : Effets de proximité et piégeage de vortex dans des hybrides supraconducteur-ferromagnétique

Mots clés : Supraconductivité, Ferromagnétisme, Effet de proximité, Piégeage de vortex, Skyrmion, Etats triplets

Résumé : Les systèmes hybrides supraconducteur-ferromagnétique présentent souvent de nouveaux phénomènes physiques, et pourraient également être utiles pour concevoir de nouvelles mémoires non-volatiles et haute densité pour les circuits supraconducteurs. Cette thèse étudie deux types différents d'hybrides SF, chacun suivant une approche possible de dispositif mémoire, en se focalisant sur les aspects fondamentaux. L'un porte sur l'effet de proximité dans des hétérostructures d'oxydes. Dans celles-ci, des corrélations *triplet* apparaissent, qui sont à la fois supraconductrices *et* polarisées en spin. Elles permettraient d'utiliser des effets de la spintronique comme la GMR, mais sont également très sensibles aux propriétés d'interface. Nous les avons étudiées dans des tricouches SFS d'oxydes, par des mesures de conductance. Celles-ci montrent des oscillations, en partie liées à ces états triplets. Nous observons également que les effets d'interface affectent les propriétés électroniques du ferromagnétique, en particulier lorsque cette couche est mince.
Un autre genre d'interaction se produit par les champs de fuite provenant des structures de domaines. Des propositions théoriques récentes ont suggéré que de petites structures en tourbillon appelées *skyrmion* peuvent interagir avec la supraconductivité par ce mécanisme Nous avons étudié ce couplage dans des bicouches, dans lesquelles les propriétés de transport sont dominées par la dynamique des vortex supraconducteurs. Nous avons vu une augmentation du courant critique en présence de skyrmions comme de domaines. Celles-ci créent également un effet Hall inhabituel dans l'état supraconducteur. La plupart de ces propriétés peuvent être expliquées qualitativement par la dynamique et le mouvement guidé des vortex.

Title : Proximity and flux pinning effects in superconductor-ferromagnet hybrids

Keywords : Superconductivity, Ferromagnetism, Proximity effect, Vortex pinning, Skyrmion, Triplet states

Abstract : Superconductor-ferromagnet hybrid systems often bring about new physics and may as well be useful to design new non-volatile, high-density memory devices for superconducting electronics. In this thesis, we study two different types of SF hybrids, each following a possible approach to memory devices, but focusing on fundamental aspects. One is about the proximity effect in oxide heterostructures. In these, *triplet* correlations appear, that are both superconducting *and* spin-polarized. These enable using effects from spintronics like GMR, but are also very dependent on interface properties. We investigated these in SFS oxide trilayers by conductance measurements. These showed oscillations which may, in part, be related to these triplet states. We also observed that interface effects affect the electronic properties of the ferromagnet, especially when that layer is thin.
Another type of interaction occurs through stray magnetic fields from the domain structures. Recent theoretical proposals suggested that small swirling spin textures called *skyrmions* could similarly interact with superconductivity through this mechanism. We investigated such coupling in bilayers, in which the superconducting vortex dynamics dominate the transport properties. We found that the presence of skyrmions and domains alike enhances the critical current. It also leads to an unusual Hall effect in the superconducting state. Most of these properties can be explained qualitatively in terms of vortex pinning and guided motion.

Université Paris-Saclay
Espace Technologique / Immeuble Discovery
Route de l'Orme aux Merisiers RD 128 / 91190 Saint-Aubin, France